Alma Mater Studiorum - Università di Bologna

Scuola di Scienze
Dipartimento di Fisica e Astronomia
Corso di Laurea Magistrale in Astrofisica e Cosmologia

Testing the methods to reconstruct and model the Baryonic Acoustic Oscillations of different tracers using N-body simulations

Tesi di Laurea Magistrale

Presentata da:
Giovanni Aricò

Relatore:
Chiar.mo Prof. **Lauro Moscardini**
Correlatore:
Dr. **Federico Marulli**
Dr. **Alfonso Veropalumbo**

Sessione III
Anno Accademico 2015-2016

"We succeeded in taking that picture, and, if you look at it, you see a dot. That's here. That's home. That's us. On it, everyone you ever heard of, every human being who ever lived, lived out their lives on a mote of dust, suspended in a sunbeam. The Earth is a very small stage in a vast cosmic arena. Think of the rivers of blood spilled by all those generals and emperors so that in glory and in triumph they could become the momentary masters of a fraction of a dot. Our posturings, our imagined self-importance, the delusion that we have some privileged position in the universe, are challenged by this point of pale light."

Carl Sagan (1934-1996)

"Don't you hear my call though you're many years away
Don't you hear me calling you
Write your letters in the sand
For the day I take your hand
In the land that our grandchildren knew."

Queen, '39, A Night at the Opera (1975)

To anyone who still looks up and asks questions about the Universe.

Contents

List of Figures

List of Tables

Sommario

L'espansione accelerata dell'Universo e la natura dell'Energia Oscura sono tuttora questioni aperte in cosmologia. Realizzare una mappatura su grande scala dell'Universo può aiutare a studiare questi problemi, determinando il tasso di espansione dell'Universo e di crescita delle strutture cosmiche. In particolare, le oscillazioni acustiche barioniche (BAO) propagatesi all'epoca della ricombinazione originano un picco nella funzione di correlazione delle galassie sulla scala caratteristica dell'orizzonte sonoro ($r_s \approx 150\,\mathrm{Mpc}$, una scala sufficientemente grande da "proteggere" il segnale dalle forti non linearità), oppure una serie di oscillazioni nello spettro di potenza, la cui lunghezza d'onda è proporzionale a $\lambda_s \simeq 2\pi/r_s$. Dato che la scala dell'orizzonte sonoro può essere determinata con grande precisione dalla posizione del primo picco nello spettro di potenza angolare del fondo cosmico a microonde (CMB, le cui oscillazioni hanno le stesse origini fisiche del BAO, in quanto fino alla ricombinazione vi era un unico plasma di barioni e fotoni), il picco del BAO nella funzione di correlazione delle galassie può essere utilizzato come un "righello standard" per estrarre informazione cosmologica fondamentale, come l'evoluzione nel tempo del parametro di Hubble, $H(z)$, e la distanza angolare $D_A(z)$.

Scopo di questa tesi è quello di testare sistematicamente, e possibilmente migliorare, gli strumenti di investigazione statistica utilizzati ad oggi per modellare il picco BAO, tenendo conto dell'evoluzione non lineare delle strutture, delle distorsioni dovute alle velocità peculiari delle galassie e del *bias* dei traccianti cosmici utilizzati per mappare la materia oscura. Per poter fare questo, abbiamo analizzato cataloghi di galassie, nuclei galattici attivi (AGN) ed ammassi di galassie ottenuti da una delle più grandi simulazioni idrodinamiche cosmologiche disponibili, le *Magneticum Simulations* (http://www.magneticum.org/), considerando un ampio intervallo di redshift, $0.2 \leq z \leq 2$.

Nonostante il picco BAO sia a grandi scale, l'evoluzione non lineare e le velocità peculiari fanno sì che il segnale del BAO sia smussato e allargato rispetto alle predizioni della teoria lineare. in particolare a bassi redshift. La *ricostruzione* del campo di densità lineare è un metodo per risolvere il problema. Uno degli obiettivi principali di questa tesi è l'implementazione e la verifica di un codice di ricostruzione, analizzando le sue prestazioni in funzione del redshift e degli oggetti cosmici usati come traccianti. La grande maggioranza delle analisi presentate in questo lavoro è stata realizzata tramite le CosmoBolognaLib, una raccolta di librerie C++/Python specificatamente pensata per calcoli cosmologici (Marulli, Veropalumbo, and Moresco, 2016).

Abstract

The accelerated expansion of the Universe and the nature of the Dark Energy are still open questions in cosmology. One of the most powerful ways to investigate these issues is to map the large-scale structure of the Universe, to constrain its expansion history and growth of structures.

In particular, baryon acoustic oscillations (BAO) occurred at recombination make a peak in the correlation function of galaxies at the characteristic scale of the sound horizon ($r_s \approx 150\,\mathrm{Mpc}$, a sufficiently large scale to "protect" the signal from strong non-linearities), or alternatively a series of oscillations in the power spectrum, whose wavelength is related to $\lambda_s \simeq 2\pi/r_s$. Since the sound horizon can be estimated with a great precision from the position of the first peak in the angular power spectrum of the Cosmic Microwave Background (which has the same physical origin of BAO, oscillations of the baryons-photons plasma), the BAO peak in the correlation function can be used as a *standard ruler*, providing paramount cosmological information, as the redshift evolution of the Hubble parameter, $H(z)$, and the angular distance parameter, $D_A(z)$.

The aim of this thesis is to systematically test and possibly improve the state-of-the-art statistical methods to model the BAO peak, taking into account the non-linear evolution of matter overdensities, redshift-space distortions and the bias of cosmic tracers. To do that, we analyse mock samples of galaxies, quasars and galaxy clusters extracted from one of the largest available cosmological hydrodynamical simulations of the standard ΛCDM model (`http://www.magneticum.org/`). We extract cosmological constraints from the BAO peak through different statistical tools in the redshift range $0.2 < z < 2$.

Although the BAO peak is at large scales, non-linear growth and galaxy peculiar velocities make the BAO signal smoothed and broader with respect to linear predictions, especially at low redshifts. A possible method to overcome these issues is the so-called *reconstruction* of the density field: one of the primary goals of this work is to implement a reconstruction method, to check its performances as a function of sample selections and redshift.

All the analyses presented in this thesis are performed by using the CosmoBolognaLib, a large set of Open Source C++/Python numerical libraries for cosmological calculations (Marulli, Veropalumbo, and Moresco, 2016).

Introduction

"It is my supposition that the Universe in not only queerer than we imagine, is queerer than we can imagine."

John B. S. Haldane (1892-1964)

At the end of the 19th century there was the conviction that almost everything was discovered in physics. Michelson, especially known for his experiment with Morely to measure the speed of light, and awarded with the Nobel Prize in Physics in 1907, said that "most of the grand underlying principles have been firmly established" and that "the future truths of physical science are to be looked for in the sixth place of decimals". Philipp von Jolly, professor of Physics in Munich, advised his young student Max Planck not to go into physics, because "in this field, almost everything is already discovered, and all that remains is to fill a few unimportant holes". These few unimportant holes, probably the same of the "two clouds" which for William Thomson, best known as Lord Kelvin, "obscure the beauty and clearness of the dynamical theory", are specifically the same Michelson-Morely's experiment, which couldn't detect the luminous ether, and the black body radiation effect known as ultraviolet catastrophe.

Well, exactly from these dark clouds, in the earliest years of 20th century, that a young student, Max Planck, and another german-born physicist, Albert Einstein, put the bases of the two most important and most experimentally tested theories of our times, the Quantum Mechanics and the General Relativity (just think about the last confirmed General Relativity's prediction, the detection of the gravitational waves, B. P. Abbott et al., 2016). Solutions of the Einstein's equations provide several cosmological models of the Universe: the pure gravitational field equation suggests a dynamical Universe, in contrast with the model accepted at the time; Einstein himself added a term to the equation, the Cosmological Constant Λ, to describe a static Universe. After Hubble discovery of the Universe expansion, Einstein admitted that the Cosmological Constant was "the biggest blunder of his life": if he would trust his pure equation, he could "rewind" the space-time expansion developing a Big Bang theory years before that Edwin Hubble measured the recession velocities of spiral galaxies.

Nowadays, in the early years of 21st century, the same equations of General Relativity, together with observational data, tell us that we are really far away from a complete understanding of the reality. With the discovery of the accelerated expansion of the Universe through the study of distant type Ia Supernovae (see Riess et al., 1998), for which Perlmutter, Schmidt and Riess won the Nobel prize in 2011, a lot of open questions arise: which force is driving the expansion? Is gravity different on

large scale? The Cosmological Constant appears again in the equations of the current standard cosmological model, the Λ Cold Dark Matter (ΛCDM) model. Independent measurements from distant supernovae, the Cosmic Microwave Background and the large-scale structure of the Universe, attest that the 69% of the content in energy of the Universe is made of Dark Energy, 26% of Cold Dark Matter, 5% of baryons and 10^{-5}% of radiation (P. Ade et al., 2016), where the adjective "dark" is an elegant way to say "we really don't know what it is". In just a century, we passed from knowing everything excepted for a few holes to knowing only the 5% of the Universe!
With this work we want to take a small step toward the understanding of the nature of the Dark Energy, by testing and possibly improving the modeling of a standard ruler used to constrain paramount cosmological parameters, the Baryonic Acoustic Oscillations (BAO) peaks.
At first time, after the Big Bang, the Universe was hotter and denser than today, the baryonic matter was completely ionized and photons were coupled with baryons through continuos Thomson scattering; Cold Dark Matter, on the contrary, for its low interaction was already decoupled.
Initial fluctuations in the Dark Matter density distribution drove acoustic oscillations of the baryon-photon plasma, trapped in the dark matter gravitational potential. With the expansion of the Universe the temperature of baryons was getting lower, until it was low enough to form first atoms, at the so-called "recombination time" (although it was more properly the first combination of atoms). By consequence there was the baryon-photon decoupling, and the photon waves were free to stream away (technically their mean free path was of the order of the scale of the Universe), but the baryon density waves expanded until the dark matter gravitational attraction made them return into the center of the potential well. Despite of this, we expected a residual overdensity in the matter distribution at the scale of the sound horizon, i.e. the BAO peak, as well as a series of oscillation in the Cosmic Microwave Background (CMB), the first radiation we get from recombination time.
Both oscillations were detected and measured: the BAO peak in the Two-Point Correlation Function of galaxies and galaxy clusters (D. J. Eisenstein, Zehavi, et al., 2005), and the acoustic peaks in the power spectrum of the CMB (Torbet et al., 1999, G. Hinshaw et al., 2007) .
Since we can measure with great precision the scale of the sound horizon from the first peak position in the CMB, we can use the BAO peak position as a standard ruler to constrain the most important cosmological parameters, as the Hubble parameter, in order to understand the expansion history of the Universe and so the nature of the Dark Energy.
The most precise is the BAO detection, the best are the constraints to the cosmological parameters; since non-linearity and peculiar velocities can smooth the BAO peak, technique as the reconstruction of the linear density filed are applied to enhance the signal (D. J. Eisenstein, H.-J. Seo, Sirko, et al., 2007). In this work we test all the techniques and tools to get the best detection of the BAO, using N-body simulations.
This work is organized as follow:

The first chapter presents the Einstein's theory of gravity and discusses the principles on which modern cosmology is based on. It also exposes the main cosmological models.

The second chapter , after a brief exposure of the history of the Universe, shows the cosmological structure formation and growth, exploring both linear and non-linear regime.

The third chapter introduces the clustering of cosmic structures and the main tools to analyse it, in order to extract cosmological information.

The forth chapter gives a brief introduction to numerical N-body and hydrodynamical simulations.

The fifth chapter exposes the Baryonic Acoustic Oscillations theory and the reconstruction technique, showing several observational results.

The sixth chapter after a brief introduction to the Magneticum Simulations, that we have analysed in this work, it exposes in details the methods adopted in the analysis.

The seventh chapter presents and discusses the obtained results.

The eighth chapter gives the conclusions and discusses about the future perspectives.

Chapter 1

Cosmological Models

"He used to do surgery
For girls in the eighties
But gravity always wins"

Radiohead, Fake Plastics Trees, The Bends (1995)

Cosmology (from the greek $\kappa\acute{o}\sigma\mu o\varsigma$ "Universe" and $\lambda o\gamma\acute{\iota}\alpha$ "study of") is the study of the origin, evolution, and fate of the Universe. Studying the Universe as a whole means as a matter of fact studying gravity (excluding the very first moments after the Big Bang), as it is the dominant force on large scales. The strong and the weak interaction, in fact, work on sub-atomic scales and the electromagnetic force, that in theory scales as the inverse of the squared distance exactly as the gravitational force, in practice isn't effective for the total neutral charge of cosmic bodies.

1.1 Elements of General Relativity

General Relativity (Einstein, 1915) is a geometrical theory: as in the Special Relativity (Einstein, 1905), time is not considered as an absolute, but just the forth coordinate of the spacetime. The genial idea of Einstein was to consider gravity not as a force, but as the effect of the geometrical distortion of the spacetime.
In Special Relativity, the separation in spacetime of two different events, $E1 = (t, x, y, z)$ and $E2 = (t + dt, x + dx, y + dy, z + dz)$, is defined as

$$ds^2 = c^2dt^2 - (dx^2 + dy^2 + dz^2), \tag{1.1}$$

where ds^2 is invariant for coordinate change. The integral over the path of a massive particle gives stationary values, so

$$\int_{path} ds = 0. \tag{1.2}$$

In a flat spacetime, as the Minkowski spacetime, this means that the shortest path between two points is a straight line.

This is no more strictly true in General Relativity, when the spacetime may be curved: we have that

$$ds^2 = g_{ij}dx^i dx^j, \tag{1.3}$$

where the indices i and j span between 0 and 3, being $x^0 = ct$ and $x^{1,3}$ the space coordinates. An interval $ds^2 > 0$ is called *time-like*, and ds/c represents the time difference measured by a clock which moves freely between the two points x^i and $x^i + dx$. A *space-like* interval is when $ds^2 < 0$; it measures the distance between the two points from the point of view of an observer at rest. An interval $ds^2 = 0$ is called *light-like*, and it represents the interval which a photon may crosses, from a point x^i to another $x^i + dx$.
The *metric tensor* g_{ij} describes the geometry of the spacetime; the shortest path between two points, called *geodesic*, for non-Euclidean geometries is not a straight line. The general equation of a geodesic is

$$\frac{d^2x^i}{ds^2} + \Gamma^i_{kl} + \frac{dx^k}{ds}\frac{dx^l}{ds} = 0, \tag{1.4}$$

where Γ^i_{kl} is the *Christoffel symbol*, defined as

$$\Gamma^i_{kl} \equiv \frac{1}{2}g^{lm}\left[\frac{\partial g_{mk}}{\partial x^l} + \frac{\partial g_{ml}}{\partial x^k} + \frac{\partial g_{kl}}{\partial x^m}\right], \tag{1.5}$$

and

$$g^{im}g_{mk} = \delta^i_k, \tag{1.6}$$

where δ^i_k is the Kronecker delta.
Starting from *Christoffel symbols*, we can define another tensor which well describes the geometrical properties of the spacetime: the *Riemann–Christoffel tensor*

$$R^i_{klm} \equiv \frac{\partial \Gamma^i_{km}}{\partial x^l} - \frac{\partial \Gamma^i_{kl}}{\partial x^m} + \Gamma^i_{nl}\Gamma^n_{km} - \Gamma^i_{nm}\Gamma^n_{kl}, \tag{1.7}$$

and the *Ricci tensor* $R_{ik} \equiv R^l_{ilk}$. The *Ricci scalar* $R \equiv g^{ik}R_{ik}$ gives a measure of the curvature of the spacetime.
We can now define the *Einstein tensor*

$$G_{ik} \equiv R_{ik} - \frac{1}{2}g_{ik}R. \tag{1.8}$$

The fundamental equation of Einstein's gravity may be written as follow:

$$G_{ik} = \frac{8\pi G}{c^4}T_{ik}, \tag{1.9}$$

where G is the Universal Gravitational Constant. T_{ik} is the so-called *Energy-Momentum Tensor*, which describes the matter distribution for a perfect fluid:

$$T_{ik} = (p + \rho c^2)U_i U_k - p g_{ik}, \tag{1.10}$$

where p is the pressure, ρ is the density and U_i is the four-velocity

$$U_i = g_{ik}U^k = g_{ik}\frac{dx^k}{ds}, \tag{1.11}$$

x^k being the spacetime trajectory of the fluid element.
The matter-energy distribution incurves the spacetime, and the spacetime distorts the

matter-energy distribution.
In the weak gravitational field limit, as we expect, Einstein's equation returns the Poisson's equation describing Newton's gravity,

$$\nabla^2\phi = 4\pi G\rho. \tag{1.12}$$

General Relativity's field equation, written as above, doesn't admit a cosmological static solution: as we already told, Einstein added a term to equilibrate the gravity, the *Cosmological Constant*:

$$G_{ik} \equiv R_{ik} - \frac{1}{2}g_{ik}R - \Lambda g_{ik} = \frac{8\pi G}{c^4}T_{ik}. \tag{1.13}$$

Note that we can add the term both in the *Einstein tensor* or in the *Energy-Momentum Tensor*: in the first case we modify the properties of the spacetime itself, in the second way we add a component of energy-matter with particular properties, i.e. the *Dark Energy*.

1.2 Cosmological Principles

General Relativity is one of the most tested physical theory and until now it was confirmed in all the experiments, from the deviation of the light rays in proximity of the sun disk by Sir Arthur Eddington (1919) to the gravitational waves detection by LIGO and Virgo collaborations (B. P. Abbott et al., 2016).
However, it is very hard to solve the Einstein's field equations to make a completed model of the Universe. Einstein himself and the first cosmologists proposed a principle to simplify the models, specifically the complexity of a general matter distribution, lowering the degrees of freedom of the system with the hypothesis of symmetries of the energy-matter distribution.
In particular, the *Cosmological Principle*, on which the whole modern cosmology is built, asserts that the Universe is homogenous and isotopic. The homogeneity is the translational invariance, the isotropy the rotational invariance; isotropy does not imply homogeneity without the assumption of not being in a special position of the Universe, the so-called *Copernican Principle*. According to these principles, the properties of the Universe at sufficiently large scales should be the same in each point.
Since from General Relativity we know that we are not in a three-dimensional space, but in a four-dimensional spacetime, the *Cosmological Principle* can be extended to the Perfect Cosmological Principle: the properties of the Universe are the same in all regions, all directions and at all times. This principle was originally formulated by Bondi and Gold (H. Bondi and T. Gold, 1948), and it led Hoyle to develop a steady-state cosmological model, in which the expansion of the Universe was contrasted by a small amount of matter created continuously. This model was later abandoned by the scientific community, after the discover of the Cosmic Microwave Background by Penzias and Wilson (Penzias and Wilson, 1965).
When it was formulated, the *Cosmological Principle* had not even the smallest observational confirmation, but it was fundamental to lead to simple cosmological models. Nowadays, we know from CMB that that the primordial Universe was isotropic with a precision of one part over 10^5 (Smoot et al., 1992); moreover, the magnitude-distance relation of the type Ia Supernovae shows that the Universe is isotropic on the very large scales (Campanelli et al., 2011, Lin et al., 2016); we have also indirect tests of the homogeneity of the Universe (see Heavens et al., 2011). So far, all the observations are in agreement with the *Cosmological Principle*.

1.3 The Robertson-Walker metric

Once we assume the *Cosmological Principle*, from pure geometrical considerations, we get a univocal metric, called the *Robertson-Walker metric*:

$$ds^2 = (cdt)^2 - a(t)^2 \left[\frac{dr^2}{1 - Kr^2} + r^2(d\theta^2 + \sin^2\theta d\varphi^2) \right], \tag{1.14}$$

where θ, φ and r are polar, comoving coordinates. The comoving coordinates are at rest with the Universe expansion: by consequence the *comoving distance* between two objects does not change with time, not taking account of peculiar velocities of the two objects.
The $a(t)$ parameter is called the *expansion parameter* or *cosmic scale factor*: it has the dimension of a length and it is expressed as a function of the proper time t, measured by a clock moving with the object. The *curvature parameter*, K, could have three different values:

- $K = 1$, the spacetime is a hypersphere: closed, without boundaries but with finite volume;
- $K = 0$, the spacetime is Euclidean, flat;
- $K = -1$, the spacetime has a negative curvature, i.e. it is open;

We will see how these three different values of K lead to different fates of the Universe in the Friedmann cosmological models.

1.4 About Cosmological Distances

In a Universe in which spacetime is expanding, carrying on all its content (*Hubble Flow*), and the information travels with a finite speed which is at least several order of magnitude smaller than the measurement you're interest in, it is not easy to define the distance between two points. As a consequence, there is not a univocal definition of distance in cosmology.

- The *proper distance*, D_P, is the distance measured in a hypersurface of constant proper time ($dt = 0$), i.e., with a *Robertson-Walker* metric:

$$D_P(r,t) = a(t) \int \frac{dr}{\sqrt{1 - Kr^2}} = a(t) f(r) = a(t) \begin{cases} \sin^{-1}(r) & K = 1 \\ \sinh^{-1}(r) & K = -1 \\ r & K = 0 \end{cases} . \tag{1.15}$$

- The *comoving distance*, D_C, is then the proper distance at present time t_0:

$$D_C(r) = a_0 f(r) = \frac{a_0}{a(t)} D_P. \tag{1.16}$$

  Proper and comoving distances cannot be directly measured by observations, because the light we received from distant objects travels with a finite speed and so it needs a different amount of time to arrive to our telescopes; we cannot therefore make measurements along a surface of constant proper time, but only along the set of light paths travelling to us from the past -our past-light cone (P. Coles and Lucchin, 2002).
  We can define distances that are directly related to observations:

- The *luminosity distance*,D_L, is defined assuming the flux conservation, that is

$$D_L = \left(\frac{L}{4\pi l}\right)^{1/2} = a_0^2 \frac{r}{a}, \tag{1.17}$$

where L is the luminosity of the source, l is the flux received by the observer, r the coordinate distance and a the cosmic scale factor. It is clear from this equation the importance of identifying *Standard Candles*, objects with known absolute magnitudes, such as Supernovae of type Ia, to measure cosmological distances.

- The *angular distance*, D_A, on the contrary preserves the geometrical properties of the space, in particular the angular size of an object seen from a certain distance. If D_ϑ is the proper diameter of the object and $\Delta\vartheta$ is the subtended angle, the angular distance is defined as

$$D_A \equiv a_0 \frac{D_\vartheta}{\Delta\vartheta} = ar. \tag{1.18}$$

In this case, it is fundamental to have an object of fixed and known proper diameter, i.e. a "Standard Ruler". The BAO feature, as we will see, it is a perfect candidate.

A possible way of testing the Robertson-Walker metric is through the *duality equation*:

$$D_A = a(t)r = D_L \frac{a^2}{a_0^2}; \tag{1.19}$$

any consistent violation of this relation would highlight deviations from the assumed homogeneity and isotropy of the Universe. Until now, we have no evidence of deviation from the duality relation.

1.5 The Hubble Law

The proper distance between an observer and any source changes with time, because of the expansion of the Universe: the source will have a radial velocity with respect to the observer

$$v_r = \frac{dD_P}{dt} = \dot{a} f(r) = \frac{\dot{a}}{a} D_P. \tag{1.20}$$

This radial velocity, that Edwin Hubble measured, pointing the Hooker Telescope of Mt. Wilson to a group of spiral galaxies, led him to the discovery of a Universe in expansion, with a velocity proportional to the distance. The equation (1.20) is so called *Hubble Law*, and the parameter

$$H(t) \equiv \frac{\dot{a}}{a} \tag{1.21}$$

is called *Hubble parameter*. The value of the Hubble parameter at the present time is a paramount cosmological information; the last measurement, released from the Planck Collaboration (Planck Collaboration, Adam, et al., 2016), is

$$H_0 = 67.8 \pm 0.9\,\mathrm{km\,s^{-1}Mpc^{-1}}. \tag{1.22}$$

This value expresses the isotropic expansion rate of the Universe, and it is the same in all the space at fixed cosmic time. We can also define the *reduced* Hubble constant, that is

$$h \equiv \frac{H_0}{100\,\mathrm{Km\,s^{-1}Mpc^{-1}}} \tag{1.23}$$

1.5.1 The Deceleration Parameter

The Hubble parameter represents the first derivative of the cosmic scale factor. Expanding $a(t)$ in power series around today, t_0, we can see how $H(t)$ varies with the content of the Universe. Up to the second derivative, we have:

$$a(t) = a_0[1 + H_0(t - t_0) - \frac{1}{2}q_0H_0^2(t - t_0)^2 + ...], \tag{1.24}$$

the *Deceleration Parameter* can then be the defined as:

$$q \equiv -\frac{\ddot{a}(t)a(t)}{\dot{a}(t)^2}, \tag{1.25}$$

and we will call q_0 the present time value of q.

1.5.2 Redshift

The Hubble Law can be used to measure galaxy distances: the radial velocity of galaxies due to the expansion of the Universe causes in fact a measurable redshift in the galaxy spectra.
In the relativistic Doppler effect we have that

$$1 + z = \gamma(1 + \frac{v_\parallel}{c}), \tag{1.26}$$

where

$$\gamma = \left(1 - \frac{v^2}{c^2}\right)^{-1}. \tag{1.27}$$

However, until galaxy recession velocities are non-relativistic ($v \ll c$), equation (1.26) can be reduced to

$$z \approx \frac{v_\parallel}{c}. \tag{1.28}$$

The redshift is defined as follows:

$$z \equiv \frac{\lambda_0 - \lambda_e}{\lambda_e}, \tag{1.29}$$

where λ_e is the wavelength of the radiation emitted by the source and λ_0 is the wavelength received by the observer. From equation (1.14), integrating over the path of a light-like interval, it is demonstrated that

$$\frac{a}{\lambda_e} = \frac{a_0}{\lambda_0}, \tag{1.30}$$

and then

$$1 + z = \frac{a_0}{a}. \tag{1.31}$$

Combining equations (1.20) and (1.28) we can write the Hubble Law, in the non-relativistic limit, as

$$cz \approx H(z)D_P. \tag{1.32}$$

Of course, the radial component of peculiar velocities of the galaxies degenerates with the radial velocity due to the expansion of the Universe, so the uncertainty on the distance calculated with the redshift grows-up, as we will discuss in section 3.5.1.

Note that the Hubble parameter, $H(t)$, has the dimension of the inverse of time and the deceleration parameter, $q(t)$, is dimensionless. If we combine the equations (1.31) and (1.24), we obtain that

$$z = H_0(t - t_0) + (1 + \frac{1}{2}q_0)H_0^2(t_0 - t)^2 + ..., \tag{1.33}$$

which inverted gives

$$t_0 - t = \frac{1}{H_0}\left[z - \left(1 + \frac{1}{2}q_0\right)z^2 + ...\right], \tag{1.34}$$

where t_0 is so-called *Hubble Time* and represents the Universe age ($t_H \approx 13.7Gyr$).

1.6 Cosmological Models

Combining the Einstein equations (1.9) and (1.10) with the Robertson-Walker metric (1.14), we can derive the two *Friedmann equations*

$$\ddot{a} = -\frac{4\pi}{3}G\left(\rho + \frac{3p}{c^2}\right)a^2 \tag{1.35}$$

$$\dot{a}^2 + Kc^2 = \frac{8}{3}\pi G\rho a^2. \tag{1.36}$$

Solving these two equations, joined to the *adiabatic condition*, it is possible to describe the expansion of the spacetime. The adiabatic condition is the assumption that the Universe is a closed system: if it doesn't loose energy, then

$$dU = -pdV, \tag{1.37}$$

where $U = \rho c^2 a^3$ is the internal energy, p is the pressure and $V = a^3$ is the volume. The eq. (1.37) can be written also as

$$d(\rho c^2 a^3) = -pda^3 \tag{1.38}$$

or equivalently as

$$\dot{\rho} + 3\left(\rho + \frac{p}{c^2}\right)\frac{\dot{a}}{a} = 0. \tag{1.39}$$

Note that equations (1.35), (1.36), (1.38) are not independent: from two of these we can determine the third one.
It's moreover remarkable the *Birkhoff's theorem* (1923): *any spherically symmetric vacuum solution of Einstein's equations is locally isometric to a region in Schwarzschild spacetime.* The Schwarzschild's solution of the Einstein field equations describes the geometry of the spacetime around a spherical neutral mass, without any angular

moment. Its corollary demonstrates that the spacetime inside a homogeneous and isotropic spherical distribution of mass-energy, M, and radius, r, can be described by a Minkowski metric. That is, the spacetime is flat, so we can work in the Newtonian limit, until the condition

$$\frac{GM}{rc^2} \ll 1, \tag{1.40}$$

is valid.

1.6.1 Einstein Universe

If we recall the first Friedmann equation (1.35), we can note that a static Universe, that is $\ddot{a} = \dot{a} = 0$, is possible only if

$$\rho = -\frac{3p}{c^2}. \tag{1.41}$$

This means that either the density or the pressure should be negative! To solve this problem, Einstein introduced the Cosmological Constant Λ in his field equation (1.13). A similar approach consists in modifying the Energy-Momentum Tensor as follow:

$$R_{ik} - \frac{1}{2}g_{ik}R = \frac{8\pi G}{c^4}\tilde{T}_{ik}, \tag{1.42}$$

where $\tilde{T}_{ik}$ is obtained by substituting the effective pressure and density, $\tilde{p}$ and $\tilde{\rho}$, to preserve the form of the Friedmann equations (1.35) and (1.36):

$$\tilde{T}_{ik} = -\tilde{p}g_{ij} + (\tilde{p} + \tilde{\rho}c^2)U_iU_j = T_{ij} + \frac{\Lambda c^4}{8\pi G}g_{ij}, \tag{1.43}$$

where

$$\tilde{p} = p - \tfrac{\Lambda c^4}{8\pi G}; \quad \tilde{\rho} = \rho + \tfrac{\Lambda c^2}{8\pi G}; \tag{1.44}$$

Equations (1.35) and (1.36) are then

$$\ddot{a} = -\frac{4\pi}{3}G\left(\tilde{\rho} + \frac{3\tilde{p}}{c^2}\right)a^2 \tag{1.45}$$

$$\dot{a}^2 + Kc^2 = \frac{8}{3}\pi G\tilde{\rho}a^2. \tag{1.46}$$

If we consider a "dust Universe", where the pressure is negligible ($p = 0$), we obtain

$$\Lambda = \tfrac{K}{a^2}, \quad \rho = \tfrac{Kc^2}{4\pi G a^2}. \tag{1.47}$$

The density must be positive, so $K = 1$ and $\Lambda > 0$: the *Einstein Universe* is static (but not stable!) and it is spherical.

1.6.2 De Sitter and Lemaître models

The *de Sitter Universe* is a model formulated in 1917, in which the Universe is empty and flat ($p = 0$; $\rho = 0$; $K = 0$), completely dominated by the Cosmological Constant; from equations (1.44) and (1.46) we have that

$$\dot{a}^2 = \frac{1}{3}\Lambda c^2 a^2, \tag{1.48}$$

from which we can note that Λ is positive. The solution of the equation (1.48) is

$$a = A \exp\left[\left(\frac{1}{3}\Lambda\right)^{1/2} ct\right], \tag{1.49}$$

which gives a Hubble parameter constant in time:

$$H(t) = \frac{\dot{a}}{a} = c\left(\frac{\Lambda}{3}\right)^{1/2}. \tag{1.50}$$

The de Sitter model is actually used to describe the inflationary epoch of the Universe, when for a certain period of time the Universe was exponentially expanding.
The *Lemaître Universe* is a model formulated in 1927. In this model the parameter of curvature is positive too, and the cosmic scale factor always increases, excepted for a short period in which it results constant ("stagnation"). The stagnation was explaining the apparent surplus of quasars and galaxies at $z \approx 2$ until it was discovered that it was just an apparent effect.

1.6.3 The Friedmann Model

The Russian cosmologist Alexander Friedmann solved the equations (1.35) and (1.36) for a general case, giving the description of the properties of the main cosmological models (Friedmann, 1922). He was however almost completely ignored, either because he wrote in german or because he died soon after the publications. The two Friedmann equations depend on three parameters: $a(t)$, p and ρ; we can add an equation of state to solve the system. When a cosmological component has a particles mean free path smaller than the scale of the cosmic structure physical phenomena, we can describes it as a perfect fluid, that is fully characterised by the following equation of state:

$$p = w\rho c^2, \tag{1.51}$$

where w is a constant parameter which, in a Universe without any Cosmological Constant, spans the so-called *Zel'dovich Interval* $0 \leq w \leq 1$. The w parameter is linked to the adiabatic sound speed in the fluid as follow:

$$v_s = \left(\frac{\partial p}{\partial \rho}\right)_S^{1/2} = c\sqrt{w}. \tag{1.52}$$

We can assign at the various components of the Universe the following w parameters:

- $w = 0$, the "dust" case, with $p = 0$, to describe non-relativistic and non-degenerate matter;
- $w = \frac{1}{3}$ for ultra-relativistic particles in thermal equilibrium, both not degenerated matter and radiation;
- $w = -1$, for the Cosmological Constant equation of state;

The Energy-Momentum Tensor can therefore be written as a sum of different components:

$$T_{\mu\nu} \equiv \sum_i T^{(i)}_{\mu\nu}. \tag{1.53}$$

From equations (1.37) and (1.51) we can get the relation

$$\rho a^{3(1+w)} = \rho_{0w} a_0^{3(1+w)}. \tag{1.54}$$

where the suffix "0" indicates, as usual, the parameter measured at present time.
We can rewrite the equation (1.36) to highlight the dependence of Robertson-Walker metric's curvature on the Universe content:

$$\frac{K}{a^2} = \frac{1}{c^2}\left(\frac{\dot{a}}{a}\right)^2\left(\frac{\rho}{\rho_c} - 1\right), \tag{1.55}$$

where the ρ_c parameter is the *critical density*

$$\rho_c \equiv \frac{3H^2(t)}{8\pi G}. \tag{1.56}$$

If the total density of the Universe is equal to the critical density, then the geometry of the spacetime is Euclidean. We can define also a *density parameter*

$$\Omega(t) \equiv \frac{\rho(t)}{\rho_c(t)}. \tag{1.57}$$

We will indicate the density parameter of a single component, having equation of state with w, Ω_w, while the total density parameter will be $\Omega_{tot} = \sum_i \Omega_{w_i}$.
The density parameter provides information on the geometry of the spacetime:

- if $\Omega_{tot} = 1$, the Universe is flat;
- if $\Omega_{tot} < 1$, the Universe is open;
- if $\Omega_{tot} > 1$, the Universe is closed;

It is interesting to calculate the time dependencies of cosmological parameters, to study the expansion history of the Universe. Equivalently, we can study how the parameters depend on redshift, because there is a univocal time-redshift relation for a fixed cosmology. From the adiabatic expansion condition (1.37) we can obtain the equation

$$\rho_w(z) = \rho_{0w}(1+z)^{3(1+w)}, \tag{1.58}$$

while combining the Hubble Law (1.20) with the Second Friedmann Equation (1.36) we obtain that

$$H^2(z) = H_0^2(1+z)^2\left[1 - \sum_i \Omega_{0w_i} + \sum_i \Omega_{0w_i}(1+z)^{1+3w_i}\right]. \tag{1.59}$$

Moreover, from the first Friedmann Equation (1.35) we can get the second derivative of the cosmic expansion parameter

$$\ddot{a} = -\frac{4\pi}{3} G\rho(1+3w)a. \tag{1.60}$$

Since we know from observations that $H_0 > 0$, and so $\dot{a} > 0$, these two equations show that in a homogeneous and isotropic Universe where w is within the Zel'dovich Interval the cosmic scale factor $a(z)$ grows monotonically with the redshift. As a consequence, as we can see in figure (1.1), there must be an initial singularity, where the cosmic

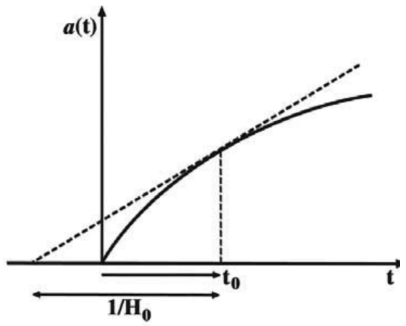

Figure 1.1: The cosmic scale factor monotonically increases with the time; the concavity makes the curve crosses the time axis, and so there must be an initial singularity or Big Bang. Figure from (P. Coles and Lucchin, 2002).

scale factor is zero and the redshift, the density and the temperature are infinite: the *Big Bang* cannot be avoided, unless we consider a strong Cosmological Constant, which would introduce a flection point in the cosmic scale factor curve.

If we measure the values of the cosmological density parameters today, we can reconstruct the time evolution of the parameters. Considering just the dominant component in the different ages simplifies a lot the calculations: equation (1.59), for example, is reduced to

$$H^2(z) = H_0^2(1+z)^2\left[1-\Omega_{0w}+\Omega_{0w}(1+z)^{1+3w}\right], \tag{1.61}$$

thus from equation (1.58), we have that

$$\Omega_w(z) = \frac{\Omega_{0w}(1+z)^{1+3w}}{1-\Omega_{0w}+\Omega_{0w}(1+z)^{1+3w}}, \tag{1.62}$$

which can be rewritten as

$$\Omega_w^{-1}(z) - 1 = \frac{\Omega_0^{-1}-1}{(1+z)^{1+3w}}. \tag{1.63}$$

This equation, valid for a single component Universe, shows that the geometry of the spacetime cannot change with time: a closed Universe will be always closed, and so a flat or an open one. Moreover, as we can see in Figure (1.2), at high redshift the spacetime tends to the flatness.

Assuming a flat single-component Universe (*Einstein - de Sitter Model* , hereafter EdS), the equations are even more simplified; for instance, equation (1.61) reduces ulteriorly to

$$H(z) = H_0(1+z)^{\frac{3(1+w)}{2}}; \tag{1.64}$$

the various parameters can be determined just substituting the equation-of-state parameter w. Furthermore, it can be shown that

$$q = \frac{1+3w}{2}; \tag{1.65}$$

this means that an EdS Universe, composed either by matter or by radiation, is in constant deceleration.

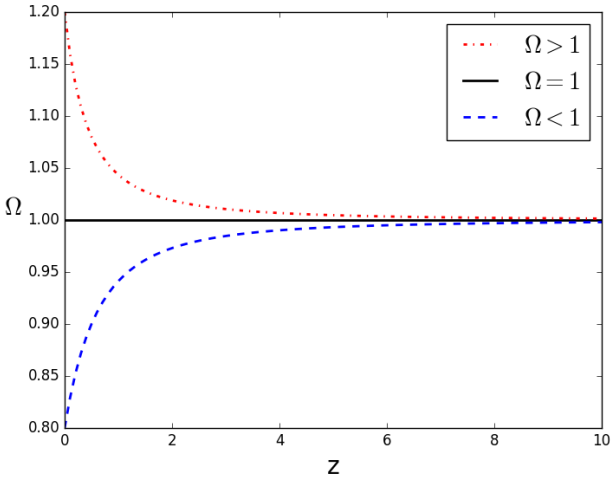

Figure 1.2: Three different evolutions of the density parameter Ω in redshift; it emerges that the geometry of the spacetime cannot change in time: the curves under and over $\Omega = 1$ never cross the line. It is also evident that an open or a closed Universe tend to the flatness with the redshift; this means that to observe today $|\Omega(t_0) - 1| \leq 0.01$, at the *Planck time* t_P ($\approx 5.39 \times 10^{-44}$ s after the Big Bang) it should be $|\Omega(t_P) - 1| = 10^{-62}$.

A cosmological model provides information on the past evolution of the Universe, and on the future trend of the cosmological parameters, thus constraining the actual age and fate of the Universe. In figure (1.3) we see how models that have in common the same cosmic scale factor observed today (a_0) can have completely different origins and fates (depending also on H_0):

- a flat Universe composed only by matter ($\Omega_m = 1$) has an age of about 10 Gyr, and will asymptotically expand until the so-called "heath death" ;
- an open Universe ($\Omega_T < 1$) has an age that is greater than a flat Universe, while its end will be very similar, even if its size per cosmic time will be a little greater;
- a closed Universe ($\Omega_T > 1$) is younger than a flat Universe. The expansion of the spacetime will reach a turning point, beyond which there will be a contraction until another singularity, the so-called *Big Crunch*;
- the ΛCDM model is a flat Universe, which today is made of 30% of matter and 70% of Cosmological Constant. This Universe has an age of 13.7 Gyr, and the cosmic scale factor presents a flection point; as a consequence, the size of the Universe diverges.

1.6.4 The Standard Cosmological Model

The cosmological model most in agreement with observations nowadays is the flat ΛCDM model. The main component today is the Cosmological Constant ($\approx 70\%$), which is driving the accelerated expansion of the Universe. The 25% of the total energy

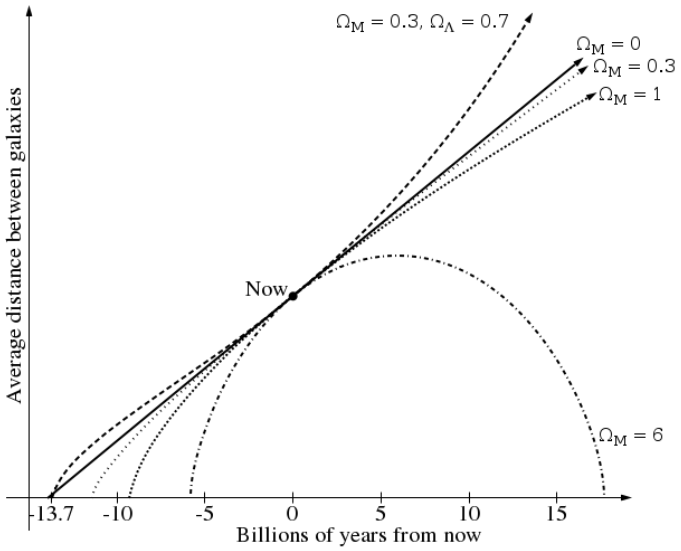

Figure 1.3: Different evolutions of the cosmic scale factor (i.e. the size of the Universe) as a function of the time, for different values of the density factor. The time axis is centered at 0, i.e. today. We can note as all the curves without Cosmological Constant are concave and cross the time axis. As a consequence, in all of these models the Big Bang cannot be avoided. We can also note that the bigger is Ω_m, the younger is our Universe. Closed Universes ($\Omega_m > 1$) expands up to a maximum size, then collapse to another singularity, the so called *Big Crunch*. As we can see from the dashed line, models with the cosmological constant, even if $\Omega_T = 1$, have a flection point and then diverge. Figure from https://en.wikipedia.org/wiki/Hubble's_law.

budget is made by cold dark matter, that is not fully understood yet. Nevertheless, we have several and independent evidences of its existence and some theories on its nature (e.g. Bertone et al., 2005). Only 5% of the energy content of the Universe is made of baryons and radiation. The sum of all the components has, to a very high level of approximation, the value 1 (see Table (1.1)), so the spacetime is flat.
From equation (1.63) it is evident that the distance between Ω and the value 1 gets lower with the redshift, as Figure (1.2) shows. At the *Planck time* t_P ($\approx 5.39 \times 10^{-44}$ s after the Big Bang), it should be $|\Omega(t_P) - 1| = 10^{-62}$ to have $|\Omega(t_0) - 1| \leq 0.01$ at present time! This apparent *fine tuning problem*, known as *flatness problem*, may be resolved by inflationary models [1].

In table (1.1) we resume the values of the main cosmological parameters for the ΛCDM model, as released from the Planck collaboration, from CMB Power Spectra, plus lensing reconstruction and external data as BAO (P. Ade et al., 2016).

H_0 $(Km\,s^{-1})$	Ω_Λ	Ω_m	$Age(Gyr)$
67.90 ± 0.55	0.6935 ± 0.0072	0.3065 ± 0.0072	13.796 ± 0.029

Table 1.1: Cosmological parameters plus best-fit 68% confidence levels, obtained combining data from the *Planck* Satellite CMB temperature power spectra, data from the reconstruction of lensing and other large-scale structures external data (P. Ade et al., 2016).

1.6.5 Cosmological Horizons

Let us consider a sphere, centered at a generic point of the Universe, with a radius equivalent to the maximum distance from which a signal could have reached that point in the spacetime, that is

$$R_H(t) = a(t) \int_0^t \frac{c\,dt'}{a(t')}. \tag{1.66}$$

The distance $c\,dt'$ travelled by a photon between t' and $t' + dt'$ is multiplied by a factor $a(t)/a(t')$ to take into account the expansion of the Universe. If this integral converges, this sphere is called *particle horizon*: all the points inside the particle horizon could in principle have interacted in some way with the center; on the contrary, it is impossible for the central point to receive a signal or any kind of information coming from outside the particle horizon. If the integral diverges, in theory it is possible that this point has received signals from the whole Universe.
For $\Omega_w = 1$, the integral can be approximated to

$$R_H(t) \approx 3\frac{1+w}{1+3w}ct. \tag{1.67}$$

In particular, $R_H(t) = 3ct$ for a dust Universe and $R_H(t) = 2ct$ for a radiative model. In the other hand, in a pure de Sitter cosmological model, there is no particle horizon,

[1] see Evrard and P. Coles (1995) for the demonstration that the flatness problem may be only an apparent fine tuning problem, due to wrong assumptions.

because the integral of equation (1.66) diverges. Different cosmological models have different particle horizons, comoving sizes and angles (see Figure (1.4)); measuring the angle that subtends the particle horizon at a time t of known proper size gives information on the spacetime geometry.
It is important not to confuse the particle horizon with the *Hubble sphere*, or *speed of light sphere*: its radius, the so-called *Hubble radius*, is the distance travelled by a particle at the speed of light in the Hubble flow, that is

$$R_c = c\frac{a}{\dot{a}} = \frac{c}{H}. \tag{1.68}$$

The Hubble radius can also be seen as the proper distance travelled by light in a Hubble time. It is easy to see that for a flat spacetime it coincides approximately to the particle horizon:

$$R_c = \frac{3}{2}(1+w)ct = \frac{1}{2}(1+3w)R_H \approx R_H. \tag{1.69}$$

However, once a point enters the particle horizon, it cannot ever go out of it; the particle horizon at time t takes into account all the past history of the Universe, while the Hubble sphere is defined with the proper distance, so it is instantly defined at a time t. By consequence, a point can be in the particle horizon but not in the Hubble sphere, or can enter in the Hubble sphere, go out and re-enter.
It is interesting to notice that, for the Hubble Law (1.20), points where proper distance is larger than $R_c = c/H_0$ recess with velocities greater than the speed of light.
Observations of the CMB temperature show great homogeneity between points that apparently should be out of each other particle horizons. Inflationary theories explain how physical properties of two points that apparently were never been casually connected are so similar (*horizon problem*) and other issues as the *magnetic monopoles problem* [2] or the *flatness problem*, making use of the Hubble spheres.
Finally, despite it is more used in black hole studies than in cosmology, for completeness we introduce the *event horizon*, that is the complementary of the particle horizon: it is the sphere that separates the points of the spacetime which could, in principle, emit a signal that can reach the center in a future, from ones which cannot. Its radius is

$$R_E(t) = a(t)\int_t^{t_{max}} \frac{c\,dt'}{a(t')}. \tag{1.70}$$

Friedmann models with w belonging to the Zel'dovich interval do not have a event horizon, contrary to the de Sitter models.

[2] GUTs models predict a magnetic monopoles density such that the Universe would be closed, with a very high density parameter, which is totally in contrast with the observations.

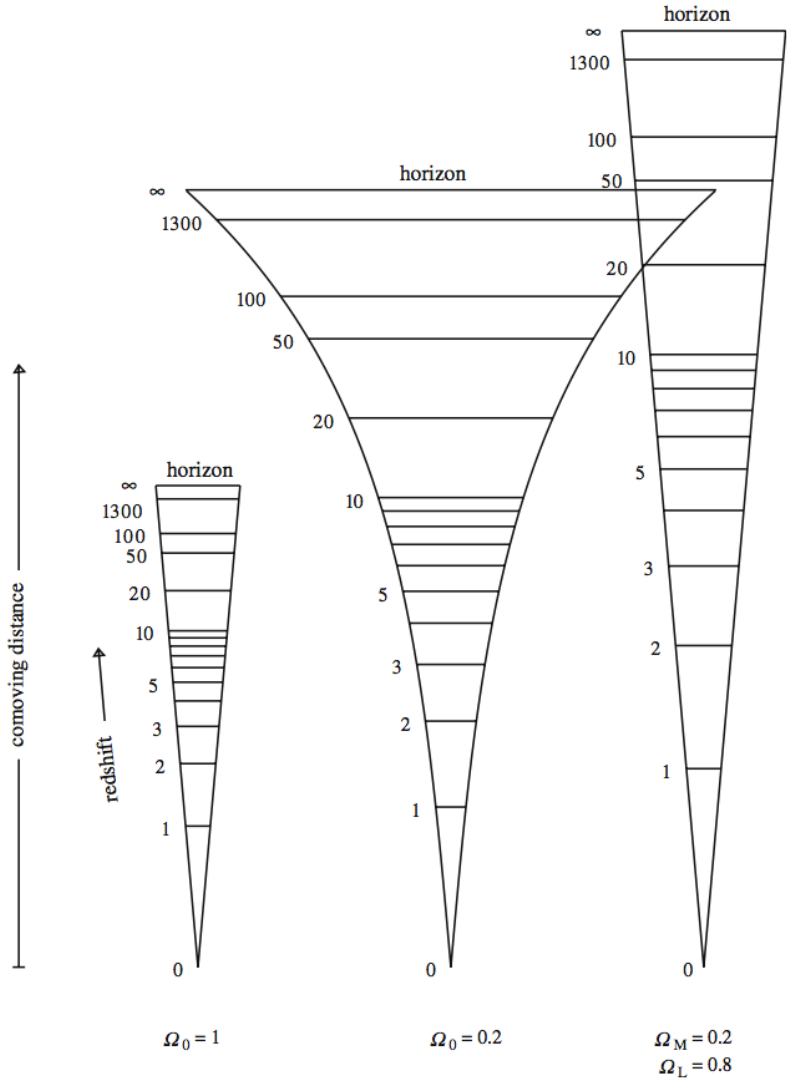

Figure 1.4: This figure shows how the spacetime geometry of the Universe makes cosmological models differ in angles, horizons and comoving distances. In particular, models of open Universe have larger horizons and distances, but tinier angles; flat models with a Cosmological Constant has larger sizes, but smaller horizons. Figure from (Hamilton, 1998).

Chapter 2

Cosmic Structures

> "In the darkness something was happening at last. A voice had begun to sing. Sometimes it seemed to come from all directions at once. There were no words. There was hardly even a tune. But it was, beyond comparison, the most beautiful noise he had ever heard. It was so beautiful he could hardly bear it."
>
> C.S.Lewis, The Magician's Nephew (1955)

2.1 Short history of the Universe

Ironically, the Big Bang model describes and predicts well the Universe until a tiny fraction of second before the Big Bang itself: precisely, 10^{-43} seconds, the *Planck time*, before the singularity. Over this time, that is established by the Heisenberg's *indetermination principle*, the size of the Universe is small enough to present both quantum and gravitational effects. Nobody was capable to formulate a completely satisfying quantum gravity theory, despite all the tentatives made by the theoretical physicists since Einstein's times. It is even possible that a quantum gravity theory allows to avoid the primordial singularity, describing the Universe also before the Big Bang, like the *loop quantum gravity* (e.g. Bojowald, 2008).
The CMB provides a direct evidence that the Universe at $z \approx 1000$ was hotter than now. For this reason the standard cosmological model is also known as *Hot Big Bang*. It is proved that at high temperature the electromagnetic force is joined to the weak interaction in the so-called electroweak interaction (S. Weinberg, 1967); this symmetry is broken at low temperature. There are theories aimed at unifying the strong interaction (GUTs, Grand Unified Theories) and the gravitational force (supersymmetry theories) to the electroweak force. In some GUT models superheavy (10^{15} GeV) bosons mediate the unified interaction. The Higgs boson would brake the GUT symmetry; however there are not strong observational evidences for any of these models. The idea that all the fundamental forces are just different sides of the same interaction is very attractive, but scientists could not yet formulate the so-called Theory of Everything.
The break of a symmetry is called *transition phase*: during the GUT transition phase, that is when the Universe had a temperature of 10^{15} GeV and the strong interaction

was separated from the electroweak force, the baryon number was not conserved. This minimum difference between matter and antimatter could explain the *baryogenesis*, that is the actual matter-antimatter discrepancy.

About 10^{-32} - 10^{-33} after the Big Bang, the Universe is believed to have experienced an instantaneous and exponential expansion called "inflation". Nowadays there are many inflationary models, originally developed by Alan Guth (A. H. Guth, 1981) to solve some main cosmological problems, such as the flatness problem and the horizon problem. It also solves the magnetic monopoles problem and explains the Gaussian anisotropies of the primordial Universe. Moreover, the assumed initial scalar field (*inflaton*) spontaneously leads to the baryogenesis. The inflationary models, nowadays, are accepted by the largest part of the scientific community, and strongly confirmed by the CMB data from the Planck satellite A. H. Guth et al., 2014. Nevertheless, these models are contested by a few scientists, which consider inflation as a scientific paradigm and claim untestable predictions and lack of empirical evidences (P. J. Steinhardt, 2011; Ijjas et al., 2013; Ijjas et al., 2014).

Figure (2.1) shows the redshift evolution of the density parameters. At the beginning, the radiation was the main component of the Universe. After the transition phase period, while the temperature was getting lower, quarks started to bounded into hadrons (the "hadron epoch"), and after about 10 seconds from the Big Bang, during the primordial nucleosynthesis, almost all the hydrogen and helium nuclei of the Universe were formed, with a small percentage of other light elements.
About 47000 years after the Big Bang ($z \approx 3600$), soon after the so-called *equivalence time*, the matter started to be dominant. Approximatively 380000 years after the Big Bang ($z \approx 1088$), at the *recombination time*, the Universe had a temperature of ≈ 4000 K, which is sufficiently low to start to bind electrons and protons in hydrogen atoms, making the Universe transparent to the radiation (more precisely, "optically thin"). Residual interaction between the matter and photons continued until $z \approx 400$ (*matter-radiation decoupling*). Later, after the *re-heating* operated by the luminous structures, matter and radiation will be locally coupled again.
The matter epoch finished when the Dark Energy started to be the dominant component of the Universe ,"just" 4 billion years ago, about 9,8 billion years after the Big Bang.

2.2 Cosmological Structures Formation

One of the main goals of a cosmological model is to make a link between the past Universe and the present one. The Universe today contains in fact galaxies, clusters, and, on larger scales, filaments and voids. In fact it looks inhomogeneous, at scales of tens Mpc, and it shows effects of the non-linear evolution of its structures. The Universe looks homogeneous today only at the largest scales that can be mapped with the actual surveys, of the order of hundreds Mpc. On the other hand, the Universe at the time of recombination looked smooth and homogeneous as we can see from the CMB light produced 13,7 billions of years ago.
In the *Jeans Theory*, the structures are formed by the gravitational collapse of small perturbations in a homogeneous mean fluid. Nevertheless, the distribution of photon-matter plasma constrained by the CMB appeared, in the first observations, homogeneous with a precision of 10^{-4}. Eventual anisotropies of the order of 10^{-5}, predicted by the Jeans theory, would lead to clusters with a mass of $\approx 10^{13}\, M\odot$, formed in

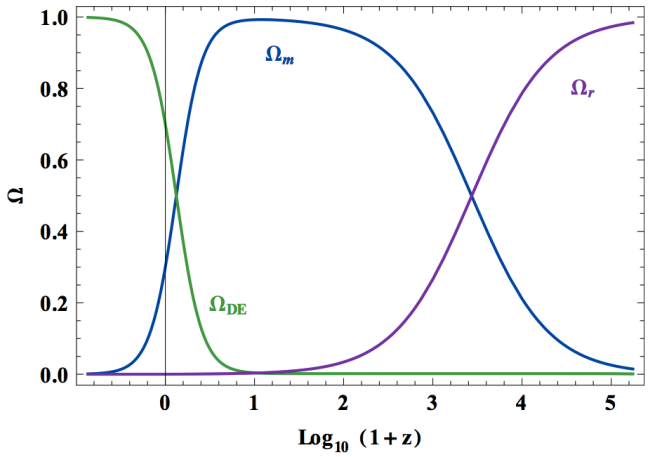

Figure 2.1: Typical behaviours of the density parameters, as a function of the redshift, in Dark Energy cosmological models. The radiation (purple line) was the dominant component for the first 50,000 years after the Big Bang. For most of the time the matter (blue line) was the main component, until the Dark Energy (green line) took its place about 4 billion years ago. Figure from Bamba et al. (2014).

the redshift range $\approx 2 - 20$ (Zel'dovich, 1972). The discovery of small, Gaussian anisotropies of the order of 10^{-5} in the CMB (Smoot et al., 1992), thus, gave an important observational confirmation to the Jeans Theory.

At first, we need to define the *punctual density contrast*:

$$\delta(x) \equiv \frac{\rho(x) - \bar{\rho}}{\bar{\rho}}, \tag{2.1}$$

where $\rho(x)$ is the punctual density field, and $\bar{\rho}$ is the mean density of the Universe. In the Fourier space, we have that

$$\hat{\delta}(k) = \frac{1}{(2\pi)^3} \int d^3x \, \delta(x) \, e^{ikx}, \tag{2.2}$$

where $k = 2\pi/x$. It is impossible to model the density contrast field *exactly*, because it is made by stochastic processes. We are interested instead to the statistical information contained in it. Since we have just one Universe from which we can obtain statistical samples, we will work on the hypothesis of *Fair Sample*: the parts of the Universe sufficiently distant from each other evolved independently.
The first central moment of the punctual density contrast, that is the mean, is null by construction; if we consider just Gaussian fluctuations, the only non-null moment is the *variance*:

$$\sigma^2 \equiv \frac{1}{V_\infty} \int d^3x < \delta^2(x) >, \tag{2.3}$$

or equivalently, in the Fourier space:

$$\sigma^2 \equiv \frac{1}{(2\pi)^3 \, V_\infty} \int d^3k < \delta^2(k) >, \tag{2.4}$$

where V_∞ is virtually the volume of the Universe, and the symbol <> means an average on all the sub-volumes in which the Universe is divided. We can also define the *power spectrum* , $P(k)$, as

$$P(k) \equiv < \delta^2(k) > . \tag{2.5}$$

The power spectrum gives a measure of the contribution of a scale k to the total density fluctuation $\delta(x)$; its real-space corresponding quantity is the *two-point correlation function*, defined as follows:

$$\xi(r) \equiv \frac{1}{(2\pi)^3} \int d^3k P(k) e^{ik\cdot r}. \tag{2.6}$$

The power spectrum and the two-point correlation function are linked by the *Wiener-Khintchine theorem*:

$$P(k) = \int \xi(r) e^{ik\cdot r} dr. \tag{2.7}$$

The inflation theory predicts an initial power spectrum of the following form:

$$P(k) = Ak^n, \tag{2.8}$$

where n is the so-called *spectral index*. Zel'dovich and Harrison proposed independently to set $n = 1$ (Harrison, 1970, Zel'dovich, 1970): in this way, the *Harrison-Zel'dovich Spectrum* has the property to be scale-invariant, and the resultant anisotropies on the CMB are smaller than 10^{-4} , that is the precision achieved at that epoch. The observations today provides values consistent with $n = 1$ (Planck Collaboration, P. A. Ade, et al., 2014), a value that is also predicted by inflationary models. We will discuss more specifically about the two-point correlation functions in the Chapter 3.
To compare theory and observations, we need to trace the contrast field in some way. The easiest one is to count luminous objects as galaxies, that constitute a discrete distribution, and to make an average on a given volume. Specifically, for an object of mass M, we have to pick a minimum radius R to have a mean density $\bar{\rho} \propto M/R^3$. We define the *Mass Variance* as the convolution of the power spectrum with a window function $\tilde{W}_R(k)$, that is used to filter all the information on scales smaller than R:

$$\sigma_M^2 \equiv \frac{1}{(2\pi)^3 V_\infty} \int d^3k < \delta^2(k) > \tilde{W}_R^2(k). \tag{2.9}$$

It is often used σ_8^2, the mass variance computed with $R = 8\,h^{-1}$ Mpc, for historical reasons:

$$\sigma_8^2 \equiv \frac{1}{(2\pi)^3 V_\infty} \int d^3k < \delta^2(k) > \tilde{W}_{R=8}^2(k), \tag{2.10}$$

in particular, in the galaxy distribution $\sigma_8^2(z = 0) \approx 1$.

2.3 Linear theory

Since, as we already discussed in section 2.2, CMB temperature fluctuations are of the order of

$$\frac{\delta T}{T} = 10^{-5}, \tag{2.11}$$

we can use the perturbation's linear theory to describes the initial evolution of the cosmic structures, finding analytical solutions that are valid until $\delta(x) < 1$.

Jeans demonstrated that small density and velocity fluctuations in a homogenous and isotropic mean fluid can grow, accreting mass until the gravitational collapse. The condition for the collapse is simply that the initial perturbation's length must be larger than a certain scale, called the *Jeans Length*, λ_J. We can evaluate the forces acting on a spherical density fluctuation $\delta\rho$, of mass M and length λ, in a homogeneous fluid of mean density ρ, to have a simple order-of-magnitude idea of the situation:

$$F_g \approx \frac{GM}{\lambda^2} \approx \frac{G\rho\lambda^3}{\lambda^2} = F_p \approx \frac{p\lambda^2}{\rho^3} \approx \frac{c_s^2}{\lambda}. \tag{2.12}$$

The overdense region will collapse if the self-gravitational force per unit of mass, F_g, is greater than the pressure force per unit mass, F_p, that is if $\lambda > c_s(G\rho)^{-1/2}$, where c_s is the speed of sound in the fluid; the Jeans length is then

$$\lambda_J \simeq c_s\sqrt{\frac{1}{G\rho}}. \tag{2.13}$$

A similar result is achievable by equilibrating the self-gravitational energy, U, of the overdensity with the kinetic energy, K, of the thermal gas, which tends to spread the perturbation,

$$U \approx \frac{G\rho\lambda^3}{\lambda} = K \approx c_s^2, \tag{2.14}$$

or the gravitational free-fall time, τ_{ff}, with the hydrodynamical time, τ_h:

$$\tau_{ff} \approx \frac{1}{(G\rho)^{1/2}} = \tau h \approx \frac{\lambda}{c_s}. \tag{2.15}$$

If $\lambda < \lambda_J$, the self-gravity of the overdensity is not sufficient for the mass infall in the gravitational well, and the perturbation propagates as an acoustical wave.

2.3.1 Jeans Theory in a static Universe

We consider here a homogeneous, isotropic, adiabatic and static Universe with time-independent matter density. We can set the following hydrodynamical equation system for a Newtonian, collisional fluid:

Continuity Equation	$\frac{\partial\rho}{\partial t} + \nabla\cdot(\rho v) = 0$	(2.16)
Euler Equation	$\frac{\partial v}{\partial t} + (v\cdot\nabla)v = -\frac{1}{\rho}\nabla\rho - \nabla\Phi$	(2.17)
Poisson Equation	$\nabla^2\Phi = 4\pi G\rho$	(2.18)
Equation of State	$p = p(\rho, S)$	(2.19)
Entropy Conservation	$\frac{\partial s}{\partial t} + v\cdot\nabla s = 0$	(2.20)

where ρ is the density, v the velocity, Φ the gravitational potential, s the entropy. Once we solved this set of equations for the Universe's background, we introduce a small perturbation, imposing that the perturbed solutions are still valid; if we look for solutions in the form of plane waves, we get the following *dispersion relation* in Fourier space:

$$\omega^2 - c_s^2k^2 + 4\pi G\rho_0 = 0, \tag{2.21}$$

where ω is the wave frequency and k is the wave number. In this way we obtain the Jeans length as follows:

$$\lambda_J = c_s \sqrt{\frac{\pi}{G\rho}}. \tag{2.22}$$

Considering a collisionless fluid, where the particle's pressure is null, we have to substitute equations (2.16) and (2.17) with the *Liouville equation*:

$$\frac{\partial f}{\partial t} + \nabla \cdot f v + \nabla_v \cdot f \dot{v} = 0, \tag{2.23}$$

where f is the phase-space distribution function and $\nabla_V \equiv (\partial/\partial v)$. The Jeans length in this case is

$$\lambda_J = c_* \sqrt{\frac{\pi}{G\rho}}, \tag{2.24}$$

where c_* replaces the sound speed in equation (2.22):

$$c_*^{-2} = \frac{\int v^{-2} f d^3 v}{\int f d^3 v} \equiv < v^{-2} > . \tag{2.25}$$

In particular, for a Maxwellian distribution

$$f(v) = \frac{\rho}{(2\pi\sigma^2)^{3/2}} \exp\left(\frac{-v^2}{2\sigma^2}\right), \tag{2.26}$$

we have that $v_* = \sigma$. In a collisionless fluid (as the dark matter one), if the scale of a perturbation is shorter than the Jeans length, the fluctuation will dissipate in a time of the order of $\tau \approx \lambda / c_*$, a process called *free streaming*, very similar to the *Landau damping* in a collisionless plasma.

2.3.2 The Jeans Theory in a Universe in expansion

In an expanding Universe the background density, ρ_B, is not constant, but time dependent; the peculiar velocities of cosmic structures follow the Hubble Law (1.20). By substituting opportunely these terms in equation (2.16) we get

$$\dot{\rho}_B + 3H(t)\rho_B = 0; \tag{2.27}$$

we can obtain again a dispersion relation:

$$\ddot{\delta}_k + 2H(t)\dot{\delta}_k + (k^2 c_s^2 - 4\pi G \rho_b)\delta_k = 0. \tag{2.28}$$

Both the expansion of the Universe, represented by the *Hubble friction* term $2H(t)\dot{\delta}_k$, and the peculiar velocity field of the fluid, $k^2 c_s^2 \delta_k$, are opposite to the gravitational collapse of the perturbation.
The Jeans length in this case is

$$\lambda_J = c_s \sqrt{\frac{\pi}{G\rho_B}}. \tag{2.29}$$

These results are valid only on scales inside the particle horizon: outside the horizon, in fact, for the absence of causal connection between particles, there cannot be microphysical processes; only gravitational effects are influent. This means that

outside the particle horizon the perturbations always grow due to the absence of the pressure that can oppose the gravitational collapse. Moreover, all the components of the Universe are gravitationally bounded. This means that it is sufficient to study only the behaviour of the main component of the Universe at a time t: the other components will follow the dominant one. As already discussed in section 2.1, at first the main component of the Universe was the radiation; after the equivalence it was the matter. Since the dark matter is dominant on the baryonic matter, in an EdS Universe we have that

$$\delta_R \propto \delta_B \propto \delta_{DM} \propto a(t)^2 \qquad \text{if } z > z_{eq}; \tag{2.30}$$

$$\delta_{DM} \propto \delta_B \propto \delta_R \propto a(t) \qquad \text{if } z < z_{eq}; \tag{2.31}$$

where δ_R, δ_B, δ_{DM} are fluctuations of radiation, baryons and dark matter respectively, and a is the cosmic scale factor.
Figure (2.2) shows the time evolution of the density fluctuations, in ΛCDM model. The accretion of an overdensity continue until the scales of the perturbation enter into the particle horizon; the microphysical processes are again effective, and different components behave in different way:

- The radiation fluctuations have a Jeans scale larger than the horizon particle: because of their speed, these fluctuations never collapse, neither before nor after the equivalence time.
- The growth of dark matter fluctuations time is "frozen" before the equivalence due to the so-called *Meszaros Effect* or *stagnation*: the lack of the radiation pressure after the equivalence makes the dark matter to collapse again, after the equivalence, with $\delta_{DM} \propto a(t)$.
- The baryon fluctuations follow the radiation ones, oscillating like acoustic waves until the decoupling, a_{dec}; after that epoch, the baryons fall into the dark matter's potential wells (*baryons catch-up*), with $\delta_B = \delta_{DM}(1 - a_{dec}/a)$.

Let δ_+ be the density perturbation growing modes in time. It can be demonstrated that, generically,

$$\delta_+(t) = H(t) \int_0^t \frac{dt}{a^2 H^2(t)} = -H(z) \int_\infty^z \frac{(1+z)dz}{a_0^2 H^3(z)}; \tag{2.32}$$

this equation cannot be solved analytically. Nevertheless, in a EdS Universe, where $\Omega_{0,m} = 1$, through equation (1.64) we can get that

$$\delta_+(z) \propto (1+z)^{-1} \propto a. \tag{2.33}$$

In general, the cosmic structures form faster in closed models, and slower in open ones, relative to a flat Universe, i.e. the higher is the matter content of the Universe, the faster is the growth of overdensities. We can define *the linear growth rate* parameter as:

$$f \equiv \frac{d\ln\delta_+}{d\ln a}, \tag{2.34}$$

It is valid the approximation

$$f \approx \Omega_m(z)^\gamma + \frac{\Omega_\Lambda}{70}\left(1 + \frac{1}{2}\Omega_m\right); \tag{2.35}$$

where the *growth index*, γ, is predicted by the GR, $\gamma = 0.545$ (L. Wang and P. J. Steinhardt, 1998a, Linder, 2005). Notice that, when the Cosmological Constant, Λ, is negligible, equation (2.35) reduces to

$$f \approx \Omega_m(z)^{\gamma}. \tag{2.36}$$

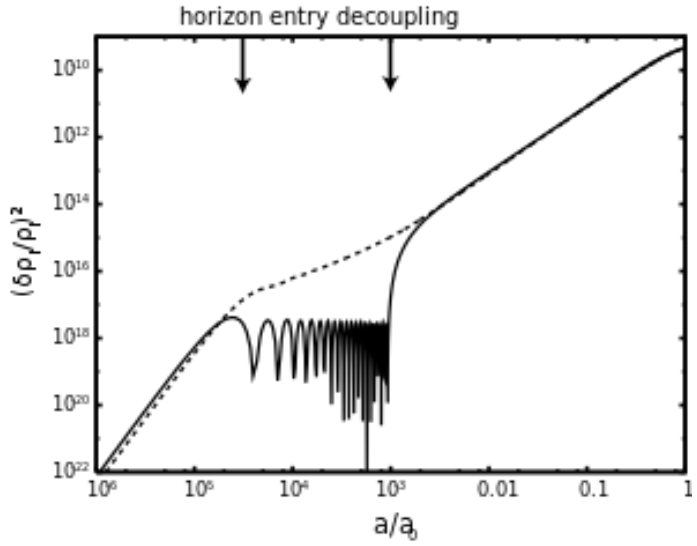

Figure 2.2: Evolution of dark matter (solid line) and baryon (dashed line) perturbations in a ΛCDM model. Outside the particle horizon all the components are gravitationally bounded and grow together; after entering the particle horizon, the dark matter perturbation keeps growing, while the baryon-photon fluid oscillates. After the decoupling, the radiation keeps oscillating, while the baryons fall in the dark matter wells, in the so-called baryon catch-up. Figure from https://en.wikipedia.org/wiki/Structure_formation.

2.3.3 Critical Masses and Structure Formation Scenarios

We introduce now some critical lengths and masses that define the evolution of a perturbation:

- Starting from the *Jeans length* given by equation (2.29), we can define the *Jeans Mass*:

$$M_J \equiv \frac{4}{3}\pi\rho\lambda_J^3; \tag{2.37}$$

  an overdensity of mass $M > M_J$ will collapse for its self-gravity; if $M < M_J$ the perturbation keeps oscillating.

- The *free-streaming length* is the path travelled by a dark matter particle in a time t:

$$\lambda_{fs}(t) = a(t)\int_0^t \frac{v(t')}{a(t')}dt'; \tag{2.38}$$

where v is the velocity of the perturbation. The *free-streaming mass* is then

$$M_{fs} \equiv \frac{4}{3}\pi\rho\lambda_{fs}^3; \tag{2.39}$$

A dark matter perturbation with $M_{DM} < M_{fs}$ streams away, completely erased.

- The comoving *mean squared displacement* of baryons in a photon-baryon plasma is:

$$< dx^2 > \propto c\frac{l}{a^2}d\tau, \tag{2.40}$$

where $l \propto a^3$ is the mean free path of the baryons. The baryon total displacement at a time t is then

$$x^2(t) = \int_0^t \frac{c\,l\,dt}{a^2} \propto c\int_0^t a\,dt; \tag{2.41}$$

the *Silk length* and the *Silk Mass* are defined, respectively, as

$$\lambda_S \equiv a(t)x \tag{2.42}$$

$$M_S \equiv \frac{4}{3}\pi\rho\lambda_S^3. \tag{2.43}$$

Before the decoupling, a baryon perturbation with $M_B < M_S$ is damped by the Thomson scatter with the photons (Silk, 1967).

The Jeans Mass for the dark matter at the equivalence time is a paramount quantity, providing the masses of the initial dark matter haloes that will form the cosmic structures. This value, though, is dependent on the mass of the dark matter particles: -The cold dark matter (CDM) particles are already non-relativistic before the decoupling from the radiation; the Jeans Mass for the CDM at the equivalence is $M_J^{(CDM)}(z_{eq}) \approx 10^{7-8}M_\odot$; the formation scenario with CDM is the so-called *Bottom-Up*: as the power is larger at the small scales, small objects formed at first (galaxies, groups), and clusters and superclusters formed for aggregation of the smaller structures. -The hot dark matter (HDM) is composed by light, relativistic particles at the decoupling; the Jeans Mass for HDM at the equivalence is $M_J^{(HDM)}(z_{eq}) \approx 10^{14-15}M_\odot$; the power is larger at the large scales, the first objects to collapse are the biggest ones. The small objects have to form for fragmentations: it is the *Top-Down* scenario. Nowadays, observations indicate that the Bottom-Up is the most reliable formation scenario: galaxy clusters are younger than the galaxies themselves.

2.4 Non-Linear Theory

Galaxies, clusters and filaments are all non-linear structures: to describe their formation, we can use the Jeans Theory only until $\delta \lesssim 1$; for $\delta > 1$ the assumptions of the Jeans Theory are no more valid, and we have to develop non-linear techniques. Nowadays, we do not have any analytical solution for the gravitational collapse of non-linear anisotropies, unless we consider very simplified models with particular boundary conditions (Shandarin and Zeldovich, 1989, Sahni and P. Coles, 1995); another possibility to study the non-linear regime of structure formation is to rely on numerical simulations, that will be treated in the Chapter 4.

2.4.1 Spherical "TopHat" Collapse

The simplest case we can consider is a spherical perturbation. This perturbation can be thought as a spherical Friedmann Universe, expanding in an EdS Universe. This system has three main phases:

- the initial expansion, following the EdS background Universe;
- the collapse: after it has reached the maximum expansion in a time t_M, the gravitational force of the overdensity leads to the collapse, as a spherical Universe;
- the virialization: after $2t_M$, the collapse is contrasted by the matter internal pressure, and after an oscillating phase the structure will be virialized at $t \approx 3t_M$.

Although this is a very simplified model, it can be demonstrated that a similar result is obtained with an initial ellipsoidal fluctuation. Moreover, the paramount contribution of this model is to show how different cosmology models lead to different scenarios: the turn-around time, t_M, depends on the cosmological model:

$$t_M = \frac{\pi}{2H_i} \frac{\Omega_p(t_i)}{(\Omega_p(t_i) - 1)^{3/2}}; \tag{2.44}$$

the periods of time involved in the structures formation depend significantly on the cosmological parameters, moreover the values of the density fluctuations at the time of collapse, δ_c, can be substantially different, in contrast with the linear theory case. To have an idea of the values involved, in the linear theory $\delta_c = 1.686$, for an EdS Universe, while the non-linear theory predicts density fluctuations, at the collapse time, of the order of hundreds.

2.4.2 The Press & Schechter Theory

Press & Schechter developed a theory to extract cosmological information from the halo mass function, that is the comoving number of objects as a function of mass and at a given redshifts (W. H. Press and Schechter, 1974). We can assume that the initial distribution of the perturbations was Gaussian (with a cut on $\delta = -1$ by definition of δ), as the inflationary models predict. The shape of the distribution changes in time. The idea of the Press & Schechter model is to compute the probability of having a perturbation with $\delta > \delta_c$ in a time t, that is the probability of a structure to collapse, in linear regime, where the Gaussianity of the distribution is preserved. From this probability, Press & Schechter derived the halo mass function:

$$n(M, z)dM = \sqrt{\frac{2}{\pi}} \frac{\delta_c}{\sigma_M(z)} \frac{\bar{\rho}_M(z)}{M^2} \left| \frac{d \ln \sigma_M}{d \ln M} \right| \exp\left(-\frac{\delta_c^2}{2\sigma_M^2(z)} \right) dM, \tag{2.45}$$

where σ_M is the mass variance (equation (2.9)). The shape of the Press & Schechter halo mass function, shown in Figure (2.3), is a power-law with a cut-off at higher masses for lower redshift. To compare the theory with the observations we have to link the mass distribution (CDM and baryons) with the distribution of luminous tracers that we can observe; assuming a linear bias factor between CDM and baryons, the halo mass function can be used to constrain the product $\sigma_M \Omega_M$. Since the growth of overdensities is slower in open models (and also in a ΛCDM model) than in a flat EdS Universe, we expect that in the last model the structures formed later. In other

words, in an open Universe, which has a lower growing rate with respect to a flat EdS Universe, it takes more time to reach the same value of δ observed today, i.e. the structures formed earlier.

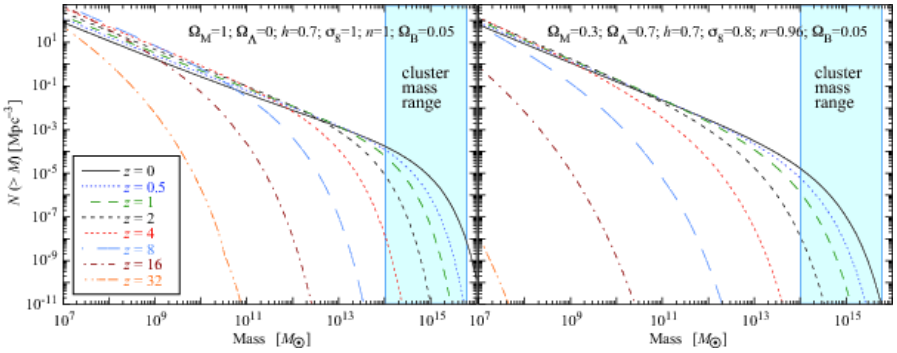

Figure 2.3: Press & Schechter mass function for a flat EdS Universe of pure matter (left panel) and for the ΛCDM model (right panel), as a function of redshift. The shape of the mass function is a power-law, with a cut-off at higher masses for lower redshifts. The cluster mass ranges, close to the cut-off, are highlighted. Figure from Lima Neto et al., 2014.

2.5 Perturbation Theory

More generically, we can follow the non-linear evolution of matter density fluctuations in the cosmological Perturbation Theory (PT). This theory can be developed either in an Eulerian perspective (EPT), fixing a local system in space and watching the fluid flows in time, or in a Lagrangian perspective, following each fluid volume trajectory through space and time (LPT). We will briefly expose the fundamentals of LPT; our notation and formalism is closed to that in Padmanabhan, M. White, and Cohn (2009), to which we refer the reader for further details.
The current (or Eulerian) comoving coordinate, $\mathbf{x}$, of each fluid volume, is related to the initial (or Lagrangian) position, $\mathbf{q}$, through a displacement vector field $\mathbf{\Psi}$:

$$\mathbf{x}(\mathbf{q}, t) = \mathbf{q} + \mathbf{\Psi}(\mathbf{q}, \mathbf{t}). \tag{2.46}$$

It is evident that $\mathbf{\Psi}(\mathbf{q}, \mathbf{t_0}) = \mathbf{0}$. Hereafter, the dependencies of the quantities will not be explicit anymore. The displacement field can be related to the overdensities as follows:

$$\delta(\mathbf{x}) = \int d^3\mathbf{q}\delta^{(\mathbf{D})}(\mathbf{x} - \mathbf{q} - \mathbf{\Psi}) - \mathbf{1}, \tag{2.47}$$

where $\delta^{(D)}$ is the three-dimensional Dirac δ function. Analogously, in the Fourier space

$$\delta(\mathbf{k}) = \int d^3\mathbf{q} e^{-i\mathbf{k}\cdot\mathbf{q}} \left(e^{-i\mathbf{k}\cdot\mathbf{\Psi}} - 1\right). \tag{2.48}$$

In LPT, as also in EPT, the displacement field is expanded in powers of the linear density field:

$$\mathbf{\Psi} = \mathbf{\Psi}^{(1)} + \mathbf{\Psi}^{(2)} + ... \tag{2.49}$$

where $\mathbf{\Psi}^{(n)}$ is n^{th}-order in δ. Expanding the exponential in the equation (2.48), we can obtain a perturbative series for the overdensity:

$$\delta = \delta^{(1)} + \delta^{(2)} + ... \tag{2.50}$$

The density field is linked to the gravitational potential, Φ, through a Poisson-like equation. From equation (2.28), we have that

$$\frac{d^2\mathbf{\Psi}}{dt^2} + 2H\frac{d\mathbf{\Psi}}{dt} = -\nabla_x \Phi[q + \mathbf{\Psi}]. \tag{2.51}$$

The displacement field has the general form

$$\mathbf{\Psi}^{(n)}(\mathbf{k}) = \frac{i}{n!}\int \prod_{i=1}^{n}\left[\frac{d^3\mathbf{k}_i}{(2\pi)^3}\right] \times (2\pi)^3\delta^{(D)}\left(\sum_i \mathbf{k}_i - \mathbf{k}\right) \times \\ \times \mathbf{L}^{(n)}(\mathbf{k}_1, ..., \mathbf{k}_n, \mathbf{k})\delta_l(\mathbf{k}_1)...\delta_l(\mathbf{k}_n), \tag{2.52}$$

where the $\mathbf{L}^{(n)}$ terms have closed form expression, generated by recurrence relations.
Let J be the Jacobian of the transformation between Lagrangian and Eulerian coordinates, defined as

$$J \equiv \left|\frac{\partial \mathbf{x}}{\partial \mathbf{q}}\right|. \tag{2.53}$$

We have that

$$J = |det\ D| = |\det(I + R)|. \tag{2.54}$$

That is, we can decompose the deformation tensor D in the identity tensor I plus the shear of the displacement , $R \equiv \partial\mathbf{\Psi}/\partial\mathbf{q}$. We can obtaining the Jacobian through the Eulerian and Lagrangian densities, by requiring the *mass conservation*:

$$\rho(\mathbf{x})d^3\mathbf{x} = \rho(\mathbf{q})d^3\mathbf{q}, \tag{2.55}$$

from which

$$\bar{\rho}[\delta(\mathbf{x})]d^3\mathbf{x} = \bar{\rho}d^3\mathbf{q}; \tag{2.56}$$

$\bar{\rho}$ is the mean density of the Universe. Hence, we have that

$$J(\mathbf{q}) = \frac{1}{1 + \delta(\mathbf{x})}. \tag{2.57}$$

Notice that, when the Jacobian vanishes, we expect a singularity, that is a collapse to an infinity density. Thus, this results is valid until the shell-crossing occurs. At the first crossing of trajectories, in fact, fluid elements with different initial positions, $\mathbf{q}$, end up to the same Eulerian positions, $\mathbf{x}$, according to the mapping of equation (2.46).

2.5.1 The Zel'dovich approximation

At the first order, we have that the relation between the Eulerian and the Lagrangian gradient is $J\,\nabla_{\mathbf{x}} \approx \nabla_{\mathbf{q}}$, where $J \approx 1 + \nabla_{\mathbf{q}} \cdot \mathbf{\Psi}$.
The evolution of fluid elements at linear order is *local*, i.e. it does not depend on the behaviour of the rest of the fluid elements. Moreover, we assume the displacement field as irrotational, $\nabla_{\mathbf{q}} \times \mathbf{\Psi}(\mathbf{q}) = 0$. Since we have not vorticity,

$$\mathbf{\Psi}^{(1)}(\mathbf{q}) = -\delta_+^{(1)}\nabla_{\mathbf{q}}\Phi^{(1)}(\mathbf{q}), \tag{2.58}$$

where $\delta_+^{(1)}$ is the first-order growing mode of the density fluctuations. From equation (2.55) we have the following relation:

$$\Psi^{(1)}(\mathbf{q}) \equiv \nabla_{\mathbf{q}} \cdot \mathbf{\Psi}^{(1)}(\mathbf{q}) = -\delta^{(1)}(\mathbf{q}). \tag{2.59}$$

Combining the equations (2.58) and (2.59), we get:

$$\nabla_{\mathbf{q}} \cdot \mathbf{\Psi}^{(1)}(\mathbf{q}) = \nabla_{\mathbf{q}}^2 \Phi^{(1)}(\mathbf{q}) = \delta^{(1)}(\mathbf{q}), \tag{2.60}$$

where

$$\delta^{(1)}(\mathbf{q}) = \delta_+^{(1)}(\mathbf{q})\delta(\mathbf{q}). \tag{2.61}$$

The first-order Poisson-like equation is, then:

$$\nabla_{\mathbf{q}}^2 \Phi^{(1)}(\mathbf{q}) = \delta^{(1)}(\mathbf{q}), \tag{2.62}$$

From these results, we can obtain the first-order $\mathbf{L}$ term of equation (2.52),

$$\mathbf{L}^{(1)} = \frac{\mathbf{k}}{k^2}; \tag{2.63}$$

the displacement field, hence, can be calculated directly from the Fourier transform of the density field, combining the equations (2.52) and (2.63):

$$\mathbf{\Psi}^{(1)} = -\frac{i\mathbf{k}}{k^2}\delta^{(1)}(\mathbf{k}). \tag{2.64}$$

This is the so-called *Zel'dovich approximation* (Zel'dovich, 1970; M. White, 2014), that is a first-order LPT expansion of the displacement field.
In particular, combining the equations (2.46) and (2.58), we find that

$$r(t, \mathbf{q}) = a(t)[\mathbf{q} - \delta_+^{(1)} \nabla_{\mathbf{q}} \Phi^{(1)}(\mathbf{q})], \tag{2.65}$$

where $r = a(t)\mathbf{x}$.
We can show that, from a certain point of view, the Zel'dovich approximation is a non-linear Eulerian approximation. In the Eulerian dynamics, non-linearity is encoded in the Poisson equation, which is equivalent to the Eulerian Zel'dovich approximation. From equation (2.65) we can write the velocity field, taking into account the Universe expansion, as

$$\mathbf{u} = \frac{d\mathbf{r}}{dt} - H\mathbf{r} = a\frac{d\mathbf{x}}{dt} = -a\dot{\delta}_+^{(1)} \nabla_{\mathbf{q}} \Phi^{(1)}(\mathbf{q}), \tag{2.66}$$

that is, the velocity field is curl-free. Thus, it can be written as a gradient of a velocity potential, V:

$$\mathbf{u} = -\frac{\nabla_{\mathbf{x}} V}{a}. \tag{2.67}$$

We can postulate various velocity potential forms. It can be shown that within the Zel'dovich approximation:

$$V = \frac{2f}{3\Omega_m H}\Phi. \tag{2.68}$$

(Munshi et al., 1994; Hui and Bertschinger, 1996; Roman Scoccimarro, 1997). The Zel'dovich approximation is therefore equivalent to the replacement of the Poisson equation by

$$\mathbf{u} = \frac{2f}{3\Omega_m a H}\nabla\Phi. \tag{2.69}$$

We can check this result by considering the equation of motion in Lagrangian coordinates:

$$a\frac{\partial \mathbf{u}}{\partial t} + aH\mathbf{u} = -\nabla_{\mathbf{x}}\Phi; \tag{2.70}$$

combining the equations (2.70) and (2.69) we get

$$\frac{\partial \mathbf{u}}{\partial t} + H\mathbf{u} = \frac{3\Omega_m H}{2f}\mathbf{u}. \tag{2.71}$$

Noting that

$$\nabla_{\mathbf{q}} \cdot \mathbf{u} = \Psi' \equiv \frac{\partial \Psi}{\partial \tau}, \tag{2.72}$$

where $d\tau = dt/a$, we can obtain the differential equation

$$a^{-1}\Psi'' + H\Psi' = \frac{3\Omega_m H}{2f}\Psi'. \tag{2.73}$$

It is possible to prove that the Zel'dovich solution, $\Psi = -\delta_+^{(1)}\delta(\mathbf{q})$, indeed solves this equation. The final position of each particle depends only on the initial position and on the displacement field; the equation (2.69) means that the particles move on straight lines (in comoving coordinates), in the direction of their initial velocities, as a kind of inertial motion.
From equation (2.57),

$$\rho(\mathbf{q}, t) = \frac{\bar{\rho}}{(1 - \delta_+^{(1)}\lambda_1)(1 - \delta_+\lambda_2)(1 - \delta_+\lambda_3)}, \tag{2.74}$$

where λ_n are the eigenvalues of the displacement shear, R, we can describe the geometry of the gravitational collapse:

- if none of the eigenvalues is positive, there is no collapse, the cosmic voids expand;
- if just one eigenvalue is positive the geometry of the collapse is one-dimensional (the so-called "pancakes");
- if two eigenvalues are positive the collapse is two-dimensional: as a consequence, it will form a cosmic filament;
- if three eigenvalues are positive there is a three-dimensional collapse, that leads to the formation of a cosmic node (cluster);

According to the N-body simulations, the most reliable collapse is the two-dimensional one; the cosmic web is thus mainly constituted by cosmic filaments, as clustering measurements confirm.
The Zel'dovich approximation is more accurate in a lower dimensional collapse, and it is exactly valid for one-dimensional collapsing system, until the shell-crossing (Buchert, 1993). Since the gravitational collapse preferentially proceeds along the direction of the strongest gravitational acceleration, and it becomes progressively lower dimensional with the passage of time (Yoshisato et al., 2006), we can conclude that the Zel'dovich approximation is quite accurate, and incorporates the essence itself of the non-linear gravitational collapse.

2.5.2 Second-order LPT

We expose now some of the results of the second-order LPT (2LPT). The 2LPT improves remarkably the Zel'dovich approximation in describing the global properties of density and velocity field (Weiss et al., 1996). The 2LPT takes into account the non-locality of the gravitational collapse, i.e. it considers the correction to the Zel'dovich approximation due to the tidal effects. The second-order density field, obtained by expanding equation (2.48), is

$$\delta(\mathbf{k})^{(2)} = \int d^3\mathbf{q} e^{-i\mathbf{k}\cdot\mathbf{q}} \left[-i\mathbf{\Psi}^{(2)} - \frac{(\mathbf{k}\cdot\mathbf{\Psi}^{(1)})^2}{2} \right], \tag{2.75}$$

(Padmanabhan, M. White, and Cohn, 2009) or, equivalently, through the equation (2.52),

$$\delta^{(2)} = \frac{1}{2}\int \frac{d^3k_1 d^3k_2}{(2\pi)^3}\delta^{(D)}\left(\mathbf{k}_1+\mathbf{k}_2-\mathbf{k}\right)\times$$
$$\times\delta_l(\mathbf{k}_1)\delta_l(\mathbf{k}_2)\left[\mathbf{k}\cdot\mathbf{L}^{(2)}(\mathbf{k}_1,\mathbf{k}_2,\mathbf{k}) + \mathbf{k}\cdot\mathbf{L}^{(1)}(\mathbf{k}_1)\mathbf{k}\cdot\mathbf{L}^{(1)}(\mathbf{k}_2)\right]. \tag{2.76}$$

The divergence of the second-order displacement describes the tidal effects:

$$\Psi^{(2)}(\mathbf{q}) \equiv \nabla_{\mathbf{q}}\cdot\mathbf{\Psi}^{(2)}(\mathbf{q}) = \frac{1}{2}\frac{\delta_+^{(2)}}{\delta_+^{(1)2}}\sum_{i\neq j}\left[\mathbf{\Psi}^{(1)}_{i,i}\mathbf{\Psi}^{(1)}_{j,j} - \mathbf{\Psi}^{(1)}_{i,j}\mathbf{\Psi}^{(1)}_{j,i}\right], \tag{2.77}$$

where

$$\mathbf{\Psi}^{(1)}_{k,l} = \frac{\partial\mathbf{\Psi}^{(1)}_k}{\partial\mathbf{q}_l}, \tag{2.78}$$

and $\delta_+^{(2)}$ is the second-order growing mode of the density fluctuations.
The second-order Poisson-like equation is

$$\nabla^2_{\mathbf{q}}\Phi^{(2)} = \sum_{i>j}\left[\Phi^{(1)}_{ii}\Phi^{(1)}_{jj} - \left(\Phi^{(1)}_{ij}\right)^2\right], \tag{2.79}$$

while the 2PT equation equivalent to the first-order relation (2.58) is

$$\mathbf{\Psi}^{(2)}(\mathbf{q}) = -\delta_+^{(2)}\nabla_{\mathbf{q}}\Phi^{(2)}(\mathbf{q}). \tag{2.80}$$

Thus, we find that the mapping from Eulerian to Lagrangian in the 2LPT is

$$\mathbf{x} = \mathbf{q} - \delta_+^{(1)}\nabla_{\mathbf{q}}\Phi^{(1)}(\mathbf{q}) + \delta_+^{(2)}\nabla_{\mathbf{q}}\Phi^{(2)}(\mathbf{q}). \tag{2.81}$$

Chapter 3

Clustering

"...and everything under the sun is in tune
but the sun is eclipsed by the moon.
There is no dark side of the moon really.
Matter of fact it's all dark."

Pink Floyd , Eclipse, The Dark Side of the Moon (1973)

The Friedmann models, and the theories of the formation and evolution of cosmic structures, should be now linked in some way to the observations. Measuring clustering means to study the statistical properties of the Universe, by analysing three-dimensional maps traced by the cosmic structures. In order to extract the most accurate cosmological information from the clustering of extragalactic sources, through the statistical tools that we will describe in this chapter, the survey should be the largest possible, to be statistically representative of the Universe and thus to minimise the so-called *cosmic variance*, a source of uncertainty discussed in section 3.3.

3.1 Correlation Functions

We can re-define the two-point correlation function of the matter distribution, starting from equation (2.6), as

$$\xi(r) \equiv \langle \delta(x)\delta(x+r) \rangle, \tag{3.1}$$

where, as usual, the $\langle\rangle$ symbol means a spatial average, while δ is the punctual contrast field (2.1). The two-point correlation function measures the discrepancy of a population with respect to a random distribution: the joint probability P_{12} of finding a couple of objects in two comoving volumes, dV_1 and dV_2, separated by a comoving distance r, is

$$dP_{12} = \bar{n}_V^2 [1 + \xi(r)] dV_1 dV_2, \tag{3.2}$$

where $\bar{n}_V$ is the mean density of the matter distribution over a volume representative of the Universe. If the distribution is perfectly random, then $\xi(r) = 0$; if objects are

clustered, $\xi(r) > 0$; if $\xi(r) < 0$ the objects are avoiding each others at that scale.
From equation (3.2) we can compute the mean number of objects expected at a certain distance from another object, that is

$$\langle n \rangle_r = \frac{4}{3}\pi\bar{n}r^3 + 4\pi\bar{n}\int_0^r \xi(r'_{12})r'^2_{12}dr'_{12}. \tag{3.3}$$

The second term of the right-hand side of equation (3.3) represents the excess (or the defect) relative to a random distribution; according to the definition of the mean density of the Universe, at the limit of $r \to \infty$, this term must be zero:

$$\lim_{r\to\infty}\int_0^r \xi(r'_{12})r'^2_{12}dr'_{12} = 0. \tag{3.4}$$

For two-dimensional distributions, we can similarly measure the angular correlation function $\omega(\theta)$:

$$dP_{12} = \bar{n}^2_\Omega[1 + \omega(\theta_{12})]d\Omega_1 d\Omega_2; \tag{3.5}$$

where $\bar{n}_\Omega$ is the mean density over a solid angle in the sky. The angular correlation function measures then the excess probability of finding a couple of objects in two small solid angles $d\Omega_1$ and $d\Omega_2$, separated by an angle θ_{12}.
In analogous way to equation(3.2) we can define higher-order correlation functions; for example, the probability of finding three objects in three disjoint volumes is

$$dP_3 \equiv \bar{n}^3_V[1 + \xi(r_{12}) + \xi(r_{13}) + \xi(r_{23}) + \zeta(r_{12}, r_{13}, r_{23})]dV_1 dV_2 dV_3, \tag{3.6}$$

where $\zeta(r_{12}, r_{13}, r_{23})$ is called *connected three-point correlation function*. It is hard to extract cosmological information from the higher-order correlation functions, since they depend on more the one parameter, differently from the two-point correlation function. It has been demonstrated that a *hierarchical model*, in which all $\xi_{(N)}$ have a self-similar behavior, describes fairly well the higher-order correlation functions. In this way, the Nth-point correlation function is related to the (N-1)th correlation function through simple scaling rules, and so on until the two-point correlation function. The model of the three-point correlation function is

$$\zeta(r_{12}, r_{13}, r_{23}) \equiv \xi_{(3)}(r_{12}, r_{13}, r_{23}) = Q(\xi_{12}\xi_{13} + \xi_{13}\xi_{23} + \xi_{23}\xi_{12}), \tag{3.7}$$

where Q is a constant. The observations agree with this result, finding that $Q \approx 1$ at scales $50\ h^{-1}$ kpc $< r < 5\ h^{-1}$ Mpc (P. Coles and Lucchin, 2002). This equation can be generalised to higher orders, but this is beyond the aims of this thesis. For further information on this topic, see e.g. P. Coles and Lucchin (2002).

3.2 The bias factor

Until now, we have considered the correlation function of the matter distribution. The largest fraction of the matter in the Universe is composed by CDM, which interacts with the baryons substantially through gravitational forces. To extract cosmological information from galaxy redshift surveys it is necessary to link the matter distribution to the spatial properties of cosmic tracers. In section 2.3.2, we described how the baryons fell in the CDM potential wells. Contrary to the CDM, baryon fluctuations undergo also non-gravitational astrophysical processes, as, for example, the radiative

transfer.Thus, the matter distribution is linked to the astrophysical objects that we can observe now via a complex function, f (M. Davis and Geller, 1976):

$$\delta_{obj}(x) = f(\delta_m(x)). \tag{3.8}$$

This function should take into account all the physical processes occurred in the formation history of the tracers. This request is translated in multiple dependences, e.g. with quantities such as the mass, the magnitude, the density of the environment, the richness, colours, morphological and spectral types, as well as non-locality, and non-linear evolution of the observable objects (e.g. M. Davis and Geller, 1976; Loveday et al., 1995; Norberg, Baugh, Hawkins, et al., 2001; Christodoulou et al., 2012; Marulli, Bolzonella, et al., 2013). In its general form, f can be stochastic and non-local. Stochasticity, however, has small effects except for adding a little extra variance (R. Scoccimarro, 2000). The link between matter and its tracers can be modeled with a non-linear and non-local relation, as follows (McDonald and Roy, 2009):

$$\delta_{obj}(x) = b_1\delta_m(x) + \frac{1}{2}b_2\left[\delta_m^2(x) - \delta^2\right] + \frac{1}{2}b_{s^2}\left[s^2(x) - \langle s^2\rangle\right] + O\left(s^3(x)\right), \tag{3.9}$$

where b_1 and b_2 are the linear and second-order non-linear bias terms, while b_{s^2} is the non-local bias term. The non-locality is originated by the tidal tensor term, s, while the σ^2 and $\langle s^2\rangle$ terms ensure that the condition $\langle\delta_{obj}\rangle = 0$ is verified (for further information, see McDonald and Roy, 2009).
In some cases, we can simplify the equation (3.9) at the first order, assuming only a linear bias factor:

$$\delta_{obj} = b\delta_m; \tag{3.10}$$

we can notice that the linear bias is scale-independent, contrary to the non-linear and non-local bias terms of equation (3.9). This bias factor gives information on the clustering level of the tracers; for instance, a bias $b > 1$ means a higher clustering of the tracers with respect to the underlying matter. Combining the equations (3.10) and (3.1), we have:

$$b = \sqrt{\frac{\xi_{obj}(r)}{\xi_m(r)}}. \tag{3.11}$$

The correlation function of both matter and tracers has positive values at small scales, and a power-law shape:

$$\xi(r) = \left(\frac{r}{r_0}\right)^{-\gamma}, \tag{3.12}$$

with $\gamma \approx 1.8$ in the range $0.1h^{-1}\,\mathrm{Mpc} \leq r \leq 10h^{-1}\mathrm{Mpc}$ (e.g. Shanks et al., 1989) . Being positive at small scales, the correlation function must be negative at larger scales (see equation (3.4)). The so-called *correlation length*, r_0, represents the physical scale at which the correlation is equal to 1. In general, the correlation length is dependent on the properties of tracers used to measure the correlation function. In the local Universe ($z \approx 0$), for instance, it has been measured, from the Metcalife and the Parker galaxy redshift surveys (Metcalfe et al., 1989; Q. A. Parker et al., 1986), that $r_0 \approx 5$ Mpc for galaxies (Shanks et al., 1989) and $r_0 \approx 10 - 25$ Mpc for the Abell galaxy clusters (P. Coles and Lucchin, 2002). There are evidences of a redshift evolution of the correlation length. Marulli, Bolzonella, et al. (2013), for instance, showed that r_0 increases with time between $z \approx 1$ and $z \approx 0.6$, and, moreover, that r_0 grows faster for faint galaxies compared to brightest ones.

Galaxy clusters have larger biases than galaxies, and, in general, the clustering level of the massive objects is higher than the bias of low massive ones. This is expected in the standard cosmological scenario of the hierarchical growth of cosmic structures, described in section 2.3.3. We can easily understand this relation looking at the Figure (3.1):

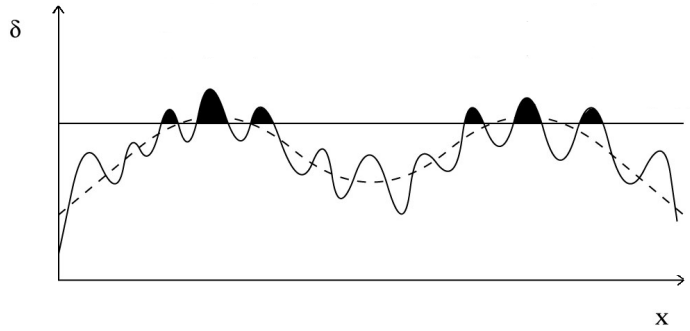

Figure 3.1: Illustrative picture of the density field, decomposed in planar waves. The small-scale fluctuations (solid sinusoid) have wavelengths of the order of galaxy sizes, while the dashed line are the largest wavelength component. The horizontal line represents the threshold beyond which a density peak can collapse. The peaks above this threshold, evidenced with the shades, will form the rarest, most massive and clustered objects of the density field. Original figure from https://ned.ipac.caltech.edu/level5/Sept03/Peacock/Peacock6_2.html

if we decompose the density field in planar waves with different wavelengths, and impose a threshold to the collapse of the structures (in some way, as in the Press & Schechter Theory, section 2.4.2), the rare, highest density peaks are naturally closer, forming, by collapse, massive objects strongly clustered (Kaiser, 1984). Fry (1996) and Tegmark and P. J. Peebles (1998) showed theoretically that the bias depends on the redshift; in particular, the bias is larger at high redshift. Figure (3.2) clearly shows how the bias depends on stellar masses and redshifts, as measured from the galaxy VIMOS Public Extragalactic Redshift Survey (VIPERS, Guzzo et al., 2014), by Marulli, Bolzonella, et al. (2013).

As we already discussed, the bias is scale dependent; Mann et al. (1998) showed that this dependence is weaker at large scales, where the bias tends to a constant value. We will discuss about the advantages and disadvantages of using a particular cosmic tracer in section 5.6.2.

3.3 The cosmic variance

Since the distribution of objects is discrete and finite, the accuracy of clustering measurements will be limited by the *cosmic variance*, that arises from the finite volume of the cosmic tracer sampling, compared to the underlying large-scale matter density fluctuations. This usually represents a significant source of uncertainty, especially in deep surveys, which tend to cover relatively small areas. Assuming $P(N)$ as the probability of finding N objects in a volume V, $\langle N \rangle$ as the mean and $\langle N^2 \rangle$ as the variance of the sample, we can define the *relative* cosmic variance as follows:

$$\sigma_{cv}^2 \equiv \frac{\langle N^2 \rangle - \langle N \rangle^2}{\langle N \rangle^2} - \frac{1}{\langle N \rangle}, \tag{3.13}$$

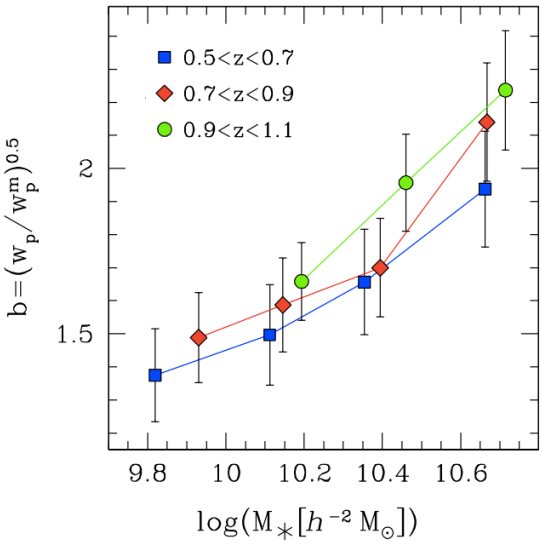

Figure 3.2: Bias of the VIPERS galaxy survey as a function of the stellar masses. The symbols and the colours refer to different redshift ranges, as shown in the legend: the blue squares refer to $0.5 < z < 0.7$, the red diamonds $0.7 < z < 0.9$ and the green circles $0.9 < z < 1.1$. The bias increases both with the mass and the redshift, as expected from the theory. Figure from Marulli, Bolzonella, et al. (2013).

where the last term is the *Poissonian shot noise* (Somerville et al., 2004), that cannot be avoided, as it is due to the discreteness of the distribution.
It can be shown that the relative cosmic variance of a population of known two-point correlation function, $\xi(r)$, is

$$\sigma^2_{cv} = \frac{1}{V^2} \int_0^R \xi(|r_1 - r_2|) dV_1 dV_2. \tag{3.14}$$

If the correlation function has a power-law form, as in equation (3.12), then equation (3.14) is reduced to

$$\sigma^2_{cv} = J_2 \left(\frac{r}{r_0} \right)^{\gamma}, \tag{3.15}$$

where $J_2 = 72/[(3-\gamma)4-\gamma)(6-\gamma)2^{\gamma}]$ (see e.g. P. J. E. Peebles, 1980).

3.4 Two-point correlation function estimators

In order to estimate the two-point correlation function of a distribution of objects, we have to compare the pair count of our data catalogue with a random distribution, that should reproduce the angular and radial selection function of the data catalogue. We can define a simple estimator as follows. Let N and N_r be the number of data and random points, respectively. We can count all the data and random pairs within the distance bin range $(r - \Delta r, r + \Delta r)$, $DD(r)$ and $RR(r)$. Since the total number of pairs is $N_{DD} = N_D(N_D - 1)/2$ for the data and $N_{RR} = N_R(N_R - 1)/2$ for the random

sample, we can derive that

$$dP_{12} = \frac{DD(r)}{N_{DD}}; \tag{3.16}$$

$$\bar{n}^2 dV_1 dV_2 = \frac{RR(r)}{N_{rr}}. \tag{3.17}$$

The *Peebles-Hauser* estimator, also called *natural* estimator, can be obtained by substituting equations (3.16) and (3.17) in (3.2) (P. J. Peebles and Hauser, 1974):

$$\hat{\xi}_{PH}(r) = \frac{N_{RR}}{N_{DD}} \frac{DD(r)}{RR(r)} - 1. \tag{3.18}$$

Since this estimator is heavily affected by shot noise at large scales (Labatie et al., 2010), more accurate estimators have been proposed. In this work we will use the *Landy-Szalay* estimator (Landy and Szalay, 1993):

$$\hat{\xi}_{LS}(r) = 1 + \frac{N_{RR}}{N_{DD}} \frac{DD(r)}{RR(r)} - 2\frac{N_{RR}}{N_{DR}} \frac{DR(r)}{RR(r)}, \tag{3.19}$$

where $DR(r)$ represents the number of the data-random pairs. Such a estimator is almost unbiased, and its variance is nearly Poisson; for these characteristics the Landy-Szalay estimator is preferred with respect to several other estimators (see e.g. Kerscher et al., 2000).

3.5 Dynamical and geometrical distortions

As we already discussed, in order to perform clustering analyses, we need first to construct three-dimensional maps of the Universe. In general, for each object in the map we have the angular coordinates on the sky, and the redshift. Thus, to obtain a three-dimensional map in comoving coordinates, we have to convert angles, and redshift, into comoving distances.

3.5.1 Dynamical distortions

We can calculate the comoving distance, $D_{c,\perp}$, between two points on the sky separated by an angle $\Delta\vartheta$, by using equation (1.16) and assuming a fiducial cosmological model:

$$D_{c,\perp} = (1+z) D_A \Delta\vartheta, \tag{3.20}$$

where D_A is the angular distance described in equation (1.18). In order to convert redshift measurements into comoving distances along the line-of-sight, we can combine equations (1.16) and (1.32):

$$D_{c,\parallel} = \frac{cz(1+z)}{H(z)}. \tag{3.21}$$

The cosmological redshift, z_c, (see equation (1.20)), is caused by the Hubble flow. However, also the peculiar velocities of the cosmic tracers, precisely the radial component of such velocities, can add an extra redshift term. In general, we have that the observed redshift can be written as follows:

$$z_{obs} = z_c + \frac{v_\parallel}{c}(1+z_c) + \frac{\sigma_z}{c}, \tag{3.22}$$

where the cosmological redshift, z_c, is due to the expansion of the Universe, $v_\parallel$ is the line-of-sight component of the peculiar velocity of the observed object, and σ_z is the error on the redshift measure.
If z_{obs} is used in equation (3.21) to estimate the comoving distance, even if we do not consider the redshift errors, the three-dimensional cosmic structure map will be distorted, because of the radial peculiar velocities. This effect is called *dynamical distortion*, or equivalently Redshift Space Distortion (RSD). We can distinguish between two different types of RSD:

- the so-called *Fingers of God* are the effects of peculiar velocities at the small scales ($r \leq 5$ Mpc). At these scales, the dominant velocities are the random motions of the galaxies inside the clusters, that act like an extra uncertainty in the redshift measurement (e.g. Marulli, Veropalumbo, Moscardini, et al., 2015);
- the *Kaiser effect* is the result of the large-scale peculiar velocities, that represent the coherent infalling of galaxies into the cluster potential wells (Kaiser, 1987).

In general, the RSD are more effective in sample of "small" objects, like galaxies, which have higher peculiar velocities, both random and coherent. It is possible to model the RSD, to remove the contribution of peculiar velocities to the cosmological redshift, as we will briefly see in section 3.6.1. Hereafter, we will talk about *redshift space* when we refer to the space where cosmological distances are affected by RSD; on the contrary, we will talk about *real space* if we have corrected for the dynamical distortions. Moreover, r will refer to the distances in the real space, while s to the ones in the redshift space. These two distances are related by the following equation:

$$s = r + \frac{v_\parallel(r)\hat{e}_\parallel}{aH(a)}, \tag{3.23}$$

where $\hat{e}_\parallel$ is the line-of-sight unit vector. We can thus link the real and the redshift density fields, as follows:

$$\delta(s) = [1 + \delta(r)] \left| \frac{d^3 s}{d^3 r} \right| - 1. \tag{3.24}$$

3.5.2 Geometrical distortions

Even if we remove the RSD, thus working in the real space, we can have other distortion effects. The most significant ones, called *geometrical distortions*, are caused by eventual errors on the assumed fiducial cosmology. Let us consider two observed objects, separated by an angle $\Delta\vartheta$ and with a cosmological redshift difference Δz, assumed small ($\Delta z \ll$). The radial and the transverse components of the comoving distance between the two objects, obtained from equations (3.21) and (3.20), are respectively:

$$r_\parallel = \frac{c}{H(z)}\Delta z; \tag{3.25}$$

$$r_\perp = (1+z)D_A(z)\Delta\vartheta, \tag{3.26}$$

where the angular distance can be written as

$$D_A(z) = \frac{1}{1+z}\int_0^z \frac{dz'}{H(z')}. \tag{3.27}$$

The two distance components have different dependencies on the Hubble parameter, thus on the adopted cosmological model. This means that, if we assume different

cosmological models, the transversal and the radial distance vary in a different way, causing the geometrical distortions. In particular, we have that

$$\frac{r_{\parallel,1}}{r_{\parallel,2}} = \frac{H_2(z)}{H_1(z)}; \tag{3.28}$$

$$\frac{r_{\perp,1}}{r_{\perp,2}} = \frac{D_{A,1}(z)}{D_{A,2}(z)}; \tag{3.29}$$

where the subscripts $1, 2$ refer to different cosmological models.

3.5.3 The Alcock-Paczynski test

The geometrical distortions can be modeled and thus corrected. Moreover, we can use the geometrical distortions to infer constraints on cosmological parameters. This can be done by using the so-called *Alcock-Paczynski test* (AP test, Alcock and Paczynski, 1979). This test is based on the idea of observing an object of known shape. Specifically, since the shapes of the observed objects are different from the one expected, due to geometrical distortions, the cosmological parameters that induce the distortions can be "adjusted" to restore the right geometry. As an example, we can consider a flat ΛCDM model, neglecting the radiation density contribution and imposing $w_\Lambda = -1$. In this case, since $\Omega_\Lambda = 1 - \Omega_m$, the equation (1.59) can be reduced as follows:

$$H(z) = H_0(1+z)\left[\Omega_{0,m}(1+z) + (1-\Omega_{0,m})(1+z)^{-2}\right]^{1/2}. \tag{3.30}$$

We can notice that the geometrical distortions depend on the redshift of the observation. A wrong value of the $\Omega_{0,m}$ parameter will introduce geometric distortions. This effect can be described by the following parameter:

$$F_{AP}(z) \equiv \frac{(r_\parallel/r_\perp)_f}{(r_\parallel/r_\perp)_t} = \frac{[D_A(z)H(z)]_f}{[D_A(z)H(z)]_t}; \tag{3.31}$$

where the f and t subscripts refer to the fiducial and the test cosmological models assumed, respectively. If $F_{AP} = 1$, the test cosmological model coincides with the fiducial one, i.e. there are no geometrical distortions. If $F_{AP} > 1$, the radial distortion is larger than the transversal one (*line-of-sight stretching*); vice versa, if $F_{AP} < 1$, the largest distortion is in the transversal component (line-of-sight shrinking).
In general, the effect of the geometrical distortions increases at higher redshifts. In particular, in cosmological models where $\Omega_{m,t} > \Omega_{m,f}$, the line-of-sight shrinking increases; on the contrary, when $\Omega_{m,t} > \Omega_{m,f}$ the line-of-sight stretching is higher.

3.6 Anisotropic correlation functions

We introduce now the *two-dimensional correlation function*, $\xi(r_\parallel, r_\perp)$, obtained by decomposing the distance r, in the radial and transversal components. We can extend the Landy-Szalay estimator, of equation (3.19), for the two-dimensional correlation function, as follow:

$$\hat{\xi}_{LS}(r_\parallel, r_\perp) = 1 + \frac{N_{RR}}{N_{DD}}\frac{DD(r_\parallel, r_\perp)}{RR(r_\parallel, r_\perp)} - 2\frac{N_{RR}}{N_{DR}}\frac{DR(r_\parallel, r_\perp)}{RR(r_\parallel, r_\perp)}. \tag{3.32}$$

Under the assumption of the Cosmological Principle, being the Universe isotropic, the correlation function should be isotropic too. Thus, the iso-correlation curves of the

two-dimensional correlation function should be circular. Nevertheless, dynamical and geometrical distortions can brake the circular symmetry, adding anisotropies that can be modeled to extract cosmological information. In the following sections, we will summarise the effects of the distortions on the correlation function and how to extract cosmological information.

3.6.1 Effects of RSD on the two-point correlation function

Let us consider two objects, with observed redshifts corresponding to the velocities v_1 and v_2. The separation in the redshift space is then $s = v_1 - v_2$, and the observer's line-of-sight can be defined as $l \equiv (v_1 + v_2)/2$. Thus, the components parallel and perpendicular to the line-of-sight, are

$$\pi = \frac{s \cdot l}{|l|}, \tag{3.33}$$

and

$$r_p = \sqrt{s \cdot s - \pi^2}, \tag{3.34}$$

respectively. The redshift space two-dimensional correlation function is then $\xi(r_p, \pi)$. In redshift space, the large-scale distances along the line-of-sight tend to be underestimated, due to the Kaiser effect; thus, the iso-correlation curves are elliptic instead of circular; at small scales, on the contrary, the random motion of the objects stretches the iso-correlation curves, the so-called Fingers of God. In Figure (3.3) it is shown how the iso-correlation curves, circular in the real space, are deformed by the Kaiser effect and by the Fingers of God. If the two effects are present at the same time, the iso-correlation curves appear as squashed circles (due to the coherent motions) elongated on the line-of-sight (for the random motions of the objects).

We cannot model the Finger of God effect in linear theory, but we can use non-linear methods. For instance, we can use the conservation of particles pairs,

$$\frac{\partial \xi}{\partial t} = \frac{1}{ax^2} \frac{\partial}{\partial x} \left[x^2 (1 + \xi) v_{12} \right], \tag{3.35}$$

where x is the comoving coordinates and $v_{12} = |s|$. Equation (3.35) is just the first one of an infinite set of equations called BBGKY hierarchy (M. Davis and P. J. Peebles, 1977), which describe the evolution of the galaxy correlation functions in an expanding universe. To close the hierarchy, we have to make the assumption that the two-point correlation function has a power-law form, as in the equation (3.12); moreover, the three-point correlation function must have the hierarchical model form of equation (3.7). Under these assumptions, the so-called *cosmic virial theorem* applies (P. J. Peebles, 1976):

$$\langle v_{12}^2(r) \rangle = C_\gamma H_0^2 Q \Omega_m r_0^2 r^{2-\gamma}, \tag{3.36}$$

where $C_\gamma \approx 23.8$ if $\gamma = 1.8$. Assuming that the radial small-scale anisotropy in $\xi(r_p, \pi)$ is due to the Fingers of God, caused by the peculiar velocity v_{12}, we can estimate Ω_m. The Kaiser effect on the correlation function depends on the cosine of the angle, μ, between the line-of-sight, l, and the separation, s. Kaiser (1987) showed that it is easier to model this directional dependence in the power spectrum; in particular, the relation between the power spectra in redshift and real space, in linear regime and by assuming parallel plane is

$$P_s(k) = P_r(k) \left[1 + f\mu^2 + f^2 \mu^4 \right]. \tag{3.37}$$

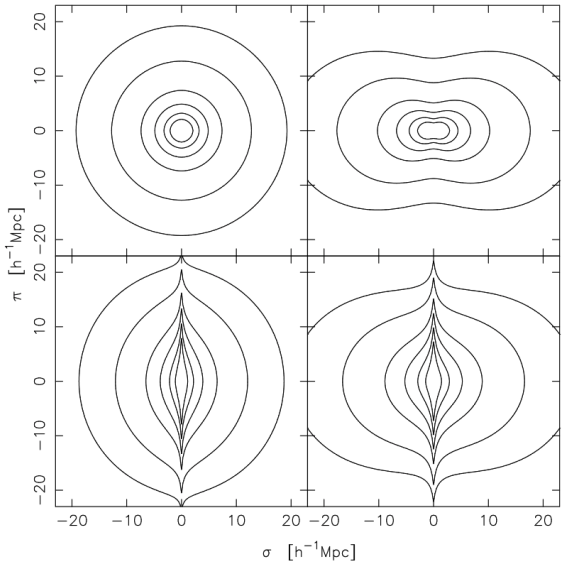

Figure 3.3: Figure from Hawkins et al. (2003), which shows RSD effects on the iso-correlation curves in the two-dimensional correlation function, $\xi(\sigma, \pi)$, where $\sigma \equiv r_p$ and π are the transversal and the radial components of the separation, respectively. On the top-left panel, we have the real-space correlation function, i.e. the undistorted, circular, curves. On the top-right panel, the squashing effect of the coherent motions at large scales distorts the iso-contours. On the bottom-left, the stretching is caused by random peculiar velocities at small scales. On the bottom right panel, the joint result of the Fingers of God and the Kaiser effect on $\xi(\sigma, \pi)$ is shown.

Notice that, when modeling the power spectrum in such a way, different assumptions are made. It is assumed the value of the linear regime, the plane parallel approximation, that is we assume the position vectors of a galaxy pair can be treated as parallel, and the distance observer approximation, where we assume that the displacement due to RSD is much smaller than the galaxy distance (Beutler et al., 2014).
In configuration space, from equation (3.37) we can derive a simple relation between the angle-averaged correlation function in real and in redshift space (Kaiser, 1987; Hamilton, 1992), that is:

$$\xi(s) = \xi(r)\left(1 + \frac{2}{3}f + \frac{1}{5}f^2\right). \tag{3.38}$$

To study the correlation anisotropy, it is more advantageous to expand the two-dimensional correlation function $\xi(r_p, \pi)$ into spherical harmonics:

$$\xi_l(r) = \frac{2l+1}{2}\int_{-1}^{+1} \xi(r\sin\theta, r\cos\theta)P_l(\cos\theta)d\cos\theta, \tag{3.39}$$

where $P_l(\cos\theta)$ is the Legendre polynomial of the multipole l. The quadrupole-monopole ratio gives a robust test for the RSD:

$$\frac{\xi_2}{\xi_0} = \frac{\frac{4}{3}f + \frac{4}{7}f^2}{1 + \frac{2}{3}f + \frac{1}{5}f^2}; \tag{3.40}$$

again, we can estimate Ω_m from the growth rate parameter f. We can take into account the bias in equations (3.37), (3.38), (3.39) and (3.40) by substituting f with the *effective growth parameter*, or *distortion parameter*, β:

$$\beta(z) \equiv \frac{f(z)}{b(z)}. \tag{3.41}$$

Equation (3.41) assumes a linear bias, that is a reliable approximation at large scales, where the Kaiser effect is dominant.
Figure (3.4) shows how this model fits the anisotropic galaxy two-point correlation function of the 2dF Galaxy Redshift Survey (Hawkins et al., 2003). Fixing the cosmological model, it is possible to constrain the β parameter; alternatively, having an estimation of the growth rate factor, f, we can obtained the linear bias, b.

The RSD can be also corrected by integrating the $\xi(r_p, \pi)$ along the line-of-sight, thus defining the *projected correlation function*:

$$w_p(r_p) = \int_{-\infty}^{\infty} \xi(r_p, \pi)d\pi. \tag{3.42}$$

The linear bias, b, can be estimated with the following simple equation:

$$b = \sqrt{\frac{w_p^t(r_p)}{w_p^m(r_p)}}, \tag{3.43}$$

where $w_p^t(r_p)$ is the projected correlation function of the cosmic tracer and $w_p^m(r_p)$ is the projected correlation function of the underlying matter distribution.
As an alternative statistics, the *clustering wedges*, $\xi_\perp(s)$ and $\xi_\parallel(s)$, have been proposed

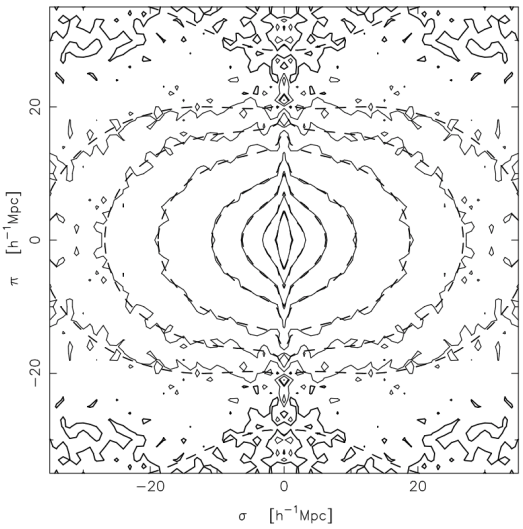

Figure 3.4: Contours of $\xi(\sigma, \pi)$, of the 2dF Galaxy Redshift Survey (solid lines). π and σ are the radial and the transversal components of the separation, respectively. The best-fit model (dashed line) well reproduces the features caused by the dynamical distortions. Figure from Hawkins et al. (2003).

to extract the anisotropic cosmological information (Kazin et al., 2012). The latter are the average of $\xi(\mu, s)$ over the intervals $\Delta\mu$ $0 \leq \mu \leq 0.5$ and $0.5 \leq \mu \leq 1$, respectively, that is:

$$\xi_{\Delta\mu}(s) \equiv \frac{1}{\delta\mu} \int_{\mu_{min}}^{\mu_{max}} \xi(\mu, s) d\mu \,. \tag{3.44}$$

The clustering wedges are related to the multipoles, as follow:

$$\xi_{\perp}(s) = \xi_0(s) - \frac{3}{8}\xi_2(s) + \frac{15}{128}\xi_4(s), \tag{3.45}$$

$$\xi_{\parallel}(s) = \xi_0(s) - \frac{3}{8}\xi_2(s) - \frac{15}{128}\xi_4(s). \tag{3.46}$$

For more details on models and fit methods used to correct the RSD, in both configuration and Fourier space, see e.g. de la Torre and Guzzo (2012) and de la Torre, Guzzo, et al. (2013).

3.6.2 Geometrical distortions on the correlation function

Geometrical distortions, as well as dynamical distortions, warp the iso-correlation curves of the two-point correlation function, $\xi(r_{\parallel}, r_{\perp})$. Since we can model the shape of $\xi(r_{\parallel}, r_{\perp})$, we can apply the AP test, described in section 3.5.3, to study the expansion of the Universe and its geometry. This method has the great advantage not to be dependent on structure evolution.
Since the AP test consists in comparing a known object shape in fiducial and test cosmologies, and we know how RSD warp the shape of iso-correlation contours (thanks to the models described in section 3.6.1), we can do an AP test on the dynamical distorted two-dimensional correlation function. Figures (3.5) and (3.6) show the

effects of geometrical distortions in the galaxy two-point correlation function, in real and redshift space, respectively. The analysis was made by using the Magneticum Simulations, a series of hydrodynamical simulations that will be described in detail in section 6.1. Figures (3.5) and (3.6), from Gaspari (2016), highlight the dependence of geometrical distortions on the redshift; in particular, the contours are more warped at higher redshift. It is also evident that, for cosmological models where $\Omega_{m,t} > \Omega_{m,f}$, the line-of-sight shrinking increases; vice versa, the line-of-sight stretching is higher for $\Omega_{m,t} > \Omega_{m,f}$. In the redshift space, we can appreciate the combined effects of geometrical and dynamical distortions, both at the small and large scales.

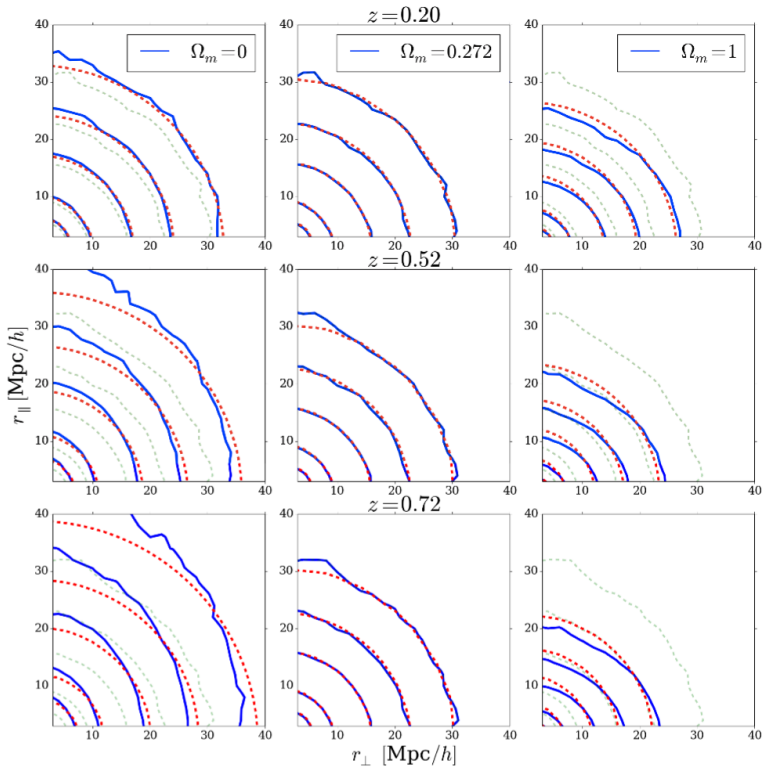

Figure 3.5: Iso-correlation contours, relative to the levels $\xi(r_\perp, r_\parallel) = [1, 0.5, 0.2, 0.1, 0.05]$ of the Magneticum Simulations galaxy catalogue, in real space. The top panels refer to $z = 0.2$, the middle to $z = 0.52$, the bottom to $z = 0.72$, as reported on the top of the central boxes. In the left panels, the test cosmological model has $\Omega_m = 0$, in the middle $\Omega_m = 0.272$, in the right panel $\Omega_m = 1$. The fiducial cosmological model has $\Omega_m = 0.272$. The solid blue lines are the measured correlation functions, the dashed red lines represent the best-fit models computed at the test cosmology, while the dashed green lines show the models at the fiducial cosmology. Figure from Gaspari (2016).

3.7 Errors estimation

The errors of a clustering measurement are expressed through the *covariance matrix*. The covariance matrix measures all the correlations between the values of the

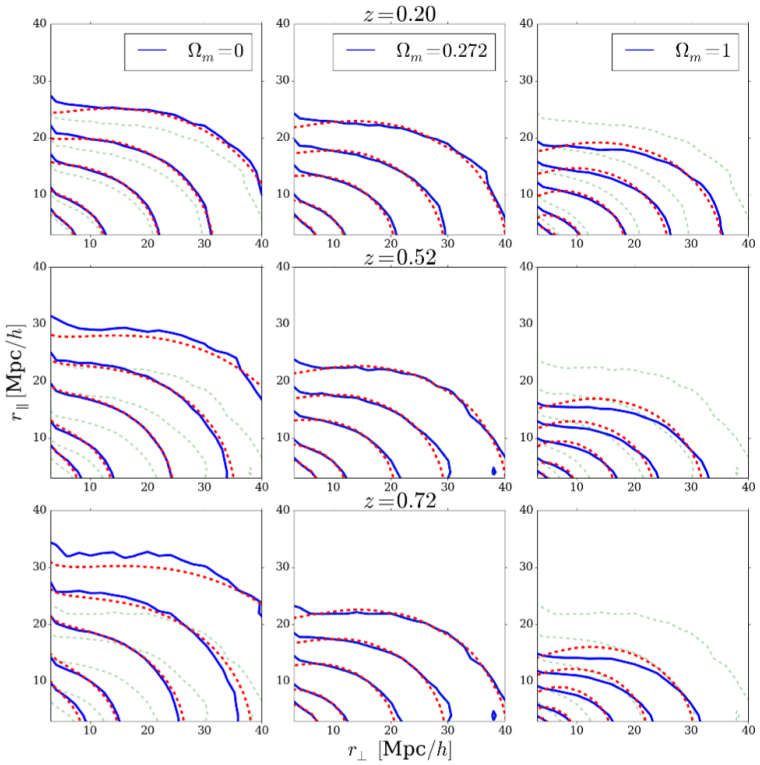

Figure 3.6: Same as Figure (3.5), but in the redshift space. The Fingers of God and the Kaiser effect are clearly visible, warping the circular shape of both measured correlations and models. The geometrical distortions make the red dashed lines not to coincide with the green dashed lines. Figure from Gaspari (2016).

correlation function at different separations.
A first, rough method to estimate the correlation function errors is to consider data and random pair distributions as Poissonian processes. If the expected value is N, then the variance is N too. The Poissonian errors, δ_{DD}, of the data pair counts, DD, will be then $\delta_{DD} = \sqrt{DD}$. By propagating the Poissanian errors of data and random pair counts, in a correlation estimator as the one in equation (3.19), gives as a result an estimate of the correlation function errors. At small scales this is a fair estimate, while at larger scales this estimate significantly underestimates the real errors, not taking into account the cosmic variance.
There are so-called "internal" and "external" methods to estimate the error covariance matrix. The external method consists in using a sufficiently large number N of independent mock galaxy catalogues, similar to the original dataset, and to measure the correlation function in each mock catalogue. The covariance matrix is then

$$C(\xi_i, \xi_j) = \frac{1}{N} \sum_{k=0}^{N} (\xi_i^k - \bar{\xi}_i)(\xi_j^k - \bar{\xi}_j), \tag{3.47}$$

where i, j iterate the correlation function bins, and ξ^k is the correlation function of the k^{th} mock. $\bar{\xi}_j$ is the mean correlation function, in the j^{th} bin, averaged over the mocks. It is challenging to reproduce faithful mocks of a dataset, and furthermore it is very expensive in terms of computational time.
The internal methods, such as Jackknife and Bootstrap, perturb in someway the original dataset itself, to generate statistically relevant subsamples (see Norberg, Baugh, Gaztañaga, et al., 2009 and references therein). In particular, in the Jackknife resampling, the dataset is split in N_{sub} sub-volumes. By omitting, in turn, each sub-volume, we can consider $N_{sub} - 1$ sub-samples, each one composed of $N_{sub} - 1$ sub-volumes. The final volume of each new catalogue is $(N_{sub} - 1)/N_{sub}$ times the volume of the original one. The covariance matrix for N_{sub} Jackknife resampling is

$$C_{jack}(\xi_i, \xi_j) = \frac{(N_{sub} - 1)}{N_{sub}} \sum_{k=1}^{N_{sub}} (\xi_i^k - \bar{\xi}_i)(\xi_j^k - \bar{\xi}_j)\,, \tag{3.48}$$

where ξ_i^k is the measure of the correlation function in the k^{th} sub-sample and i^{th} bin. $\bar{\xi}_i$ is the mean value of the correlation function over the sub-samples, that is

$$\bar{\xi}_i = \sum_{k=1}^{N_{sub}} \frac{\xi_i^k}{N}. \tag{3.49}$$

The $(N_{sub} - 1)$ factor in the equation (3.48) takes into account the lack of independence of the N_{sub} resampling of the original dataset. Indeed, only two sub-volumes are different (or, equivalently, $N_{sub} - 2$ sub-volumes are identical) from a copy to another. The Bootstrap resampling is instead performed by selecting randomly N_R of N_{sub} subsamples. In the original dataset, all sub-volumes have equal weight; in the resampling, the weight is the number of times each sub-volume has been selected. We can have $(N_{sub} + N_r - 1)!/(N_{sub} - 1)!N_r!$ different possible Bootstrap resamplings, but usually it is set a number of realizations, N, of the order of a hundred, for reasons of computational time. In general it is set $N_R = N_{sub}$. The covariance matrix for N Bootstrap resampling is

$$C_{boot}(\xi_i, \xi_j) = \frac{1}{(N - 1)} \sum_{k=1}^{N} (\xi_i^k - \bar{\xi}_i)(\xi_j^k - \bar{\xi}_j)\,. \tag{3.50}$$

Notice that there is not the (N-1) factor of the equation (3.48), because the Bootstrap copies should be more independent than the Jackknife resampling.

Chapter 4

Numerical simulations

"No Time, No Space
another Race of vibrations
the Sea of the Simulation
keep your feelings in memories..."

Franco Battiato, No Time No Space, Mondi Lontanissimi (1985)

Numerical simulations allow to treat problems that have no analytical solutions, as the gravitational N-body problem or the non-linear growing of matter density fluctuations. N-body simulations follow the evolution of a gravitational system composed by N particles, computing the forces acting on each particle, by calculating the gravitational potential of the density field. One of the main issues of numerical simulations is to balance the resolution, i.e. the mass of each particle, with the computational time. The CDM evolution can be accurately described through N-body simulations, because CDM are collisionless particles which interact substantially only through gravitational forces. On the other hand, to describe the evolution of baryonic matter we need hydrodynamical codes, which solve the hydrodynamical equations. Furthermore, we have to model astrophysical processes such as the dynamics of gas cooling, the galaxy building by consecutive merging events, the spectroscopic and chemical evolution of stellar population, etc. In this chapter we briefly discuss about the several approaches one can follow to develop such codes.

4.1 N-body simulations

From equations (2.18), (2.28) and (2.69) we get the following analytic system of equations we want to solve:

$$\begin{cases} \ddot{\mathbf{x}}_i + 2H\dot{\mathbf{x}}_i = -\frac{\nabla\phi}{a^2} = -\frac{GM_i}{a^3}\sum\limits_{j\neq i,j} M_j \frac{\mathbf{x}_i-\mathbf{x}_j}{|\mathbf{x}_i-\mathbf{x}_j|^3} = \frac{\mathbf{F}_i}{a^3} \\ \nabla^2\Phi = 4\pi G\delta(t,\mathbf{x}_i)\bar{\rho}(t) = \frac{3H_0^2\Omega_0\delta}{2a} \end{cases}, \tag{4.1}$$

where M_i, x_i, F_i are the mass, the comoving coordinates and the gravitational force on the i-th particle, respectively. N-body simulations can describe the evolution of a gravitational system, by computing the position and the velocity of each massive

particle measuring the gravitational force acting on it. To do this, N-body codes have to solve the following set of equations:

$$\begin{cases} F_i = GM_i \sum_{i \neq j} M_j \mathbf{r}_{ij}^{-2} \\ \dot{\mathbf{v}}_i = \mathbf{F}_i M_i^{-1} \\ \dot{\mathbf{x}}_i = \mathbf{v}_i \end{cases}, \tag{4.2}$$

where v_i is the velocity of the i-th particle, and r_{ij} the comoving distance between the i-th and j-th particles. These equations have to be integrated for each particle and time interval:

$$\mathbf{v}_i(t + \Delta t) = \mathbf{v}_i(t) + \frac{\mathbf{F}_i}{M_i}\Delta t + O(\Delta t^2); \tag{4.3}$$

$$\mathbf{x}_i(t + \Delta t) = \mathbf{x}_i(t) + \mathbf{v}_i \Delta t + O(\Delta t^2); \tag{4.4}$$

the position and velocity at t_1 will be the initial conditions for the integration at t_2. The various N-body algorithms can be classified according to the specific method they use to compute F_i. In the following sections we describe the main methodologies proposed to implement N-body simulations.

4.1.1 Particle-Particle method

The most direct way to solve the equation system (4.2) is to compute, for each time interval Δt, the gravity force acting on each particle by adding all the contributes due to the other particles. This implies to compute the forces acting on all the $N(N-1)/2$ particle pairs, integrating then the equations of motion. A numerical issue of this method is that the gravitational forces tend to infinite when the distance tends to zero. Thus, a *softening* parameter, ϵ, is introduced, such that

$$F(r) \simeq (r^2 + \epsilon^2)^{-1}. \tag{4.5}$$

The softening parameter can be interpreted as the physical dimension of the particles. Nevertheless, in cosmological simulations the particles are not physical objects, such as galaxies, so the ϵ value has not a strictly physical meaning. In general its value is chosen to ensure sufficiently good performances of the codes.

The method described above, called Particle-Particle (PP), is easy to implement, and very accurate. However, it requires to compute $\simeq N^2$ forces at each time step, so the computational time scales with the squared number of the particles. This implies that such a code can be used with a relatively small number of objects, reducing the mass resolution, compared to the other methods described in the following sections.

4.1.2 Particle-Mesh method

In order to reduce the computational time, one can compute the field quantities, such as the gravitational potential and the density field, on a spatial grid. The consequence is to reduce the spatial accuracy, especially at small scales, because of the averaging of the density field. This method is called Particle-Mesh (PM). After the computation of the density field through particle interpolation (different interpolation techniques can be exploited), the fast Fourier transform can be used to calculate the gravitational potential through the Poisson equation, and then Fourier anti-tranform to have the force field in configuration space. It can be demonstrated that the computational time

of this method scales as $\simeq N + 5M^3 \log M^3 \ll N^2$,where M is the number of the grid nodes (see G. Efstathiou et al., 1985 and references therein). In conclusion, the PM is fast in terms of computational time, at the expense of a low spatial accuracy due to the use of the grid cells.

4.1.3 Particle-Particle-Particle-Mesh method

The Particle-Particle-Particle-Mesh (P^3M) method joins together the best characteristics of PP and PM methods. The gravitational force acting on the i-th particle is decomposed in two contributions. The contribution of the particles inside a sphere of a given critical radius r_c, centered on the i-th particle, is computed with the PP method, ensuring a good resolution at small scales. Outside this sphere, the force contribution is computed with the PM method, which ensures a short computational time. In this case, the PP scales as $N \cdot N_{rc} < N^2$, being N_{rc} the mean number of particles inside the spheres with radius r_c, while the PM method scales as $\simeq N + 5M^3 \log M^3 \ll N^2$. The critical radius must be accurately chosen, because a large -or a short- radius would imply that the P^3M method will be too close to the PP or to the PM method, respectively, with their consequent problematics. Moreover, simulating, for instance, the growth of structures, as the clustering level gets higher, more particles enter inside the critical radius, thus reducing the efficiency of the method.

4.1.4 Hierarchical Tree method

The force computation in the Hierarchical Tree (HT) method is done by direct sum only for the closest particles, as in the P^3M method. On the contrary, the gravitational contribute of the farthest particles is computed by expanding in multipoles the potential. At each time step a *hierarchical tree* is generated. There are different types of trees; for instance, in the *Barnes-Hut* tree (Barnes and Hut, 1986), the entire volume of the simulation is divided in cells, and each cell is divided is sub-cells, and so on until each cell contains only one particle or zero. The not-empty cells are the tree nodes. According to a required criterion on the distances, a given node can be either considered as a single, or grouped with the closest nodes. For large distances, the gravitational force can be computed considering the particles group as a unique virtual particle, situated on the mass center of the cell. Also, the gravitational forces of the virtual particles can be expanded in multipoles, filtering the high terms. On the other hand, for short distances, where the approximation in multipoles is less accurate, one can consider the sub-nodes, substantially calculating the gravitational force as in the PP method.
This method is quite accurate and fast, scaling as $N \log N$.

4.2 Hydrodynamical simulations

The aim of hydrodynamical codes is to solve the system of equations treated in section 2.3.1, and following reported:

$$\text{Continuity Equation} \qquad \frac{\partial \rho}{\partial t} + \nabla \cdot (\rho v) = 0 \tag{4.6}$$

$$\text{Euler Equation} \qquad \frac{\partial v}{\partial t} + (v \cdot \nabla) v = -\frac{1}{\rho} \nabla \rho - \nabla \Phi \tag{4.7}$$

$$\text{Poisson Equation} \qquad \nabla^2 \Phi = 4\pi G \rho \tag{4.8}$$

$$\text{Equation of State} \qquad p = p(\rho, S) \tag{4.9}$$

$$\text{Entropy Conservation} \qquad \frac{\partial s}{\partial t} + v \cdot \nabla s = 0 \tag{4.10}$$

Analogously to the discussion in section 2.5, two different approaches can be followed to solve this set of equations:

- Eulerian methods. In this approach, a grid is used to compute the mean values of the quantities. The grid can be either fixed or adaptive. A better resolution can be obtained by refining the grid dynamically, in the regions where the density is high. The conservation equations are solved by using finite-differences methods. Codes of this type can accurately describe shocks and discontinuities, and are especially efficient for magnetohydrodynamic studies (e.g. Stone and M. L. Norman, 1992). Furthermore, they can be easily coupled with Eulerian N-body simulations that use grids (e.g. the PM method).

- Lagrangian methods. In this approach the hydrodynamical quantities are computed at particles positions. One of the most used Lagrangian methods is the so-called Smoothed Particle Hydrodynamics (SPH, see e.g. Gingold and Joseph J Monaghan, 1977 and Joe J Monaghan, 1992). This method computes the properties of the fluid, such as temperature, density and pressure, at each position, as a weighted average of these properties around the point. It is clear that, in this treatment, the continuous properties of the fluid are traced by a discrete number of particles, i.e. the integrals become sums. For these reasons, these codes are less indicated to treat shocks and discontinuities. The sums can be performed over a small subsample of close particles, because the hydrodynamical forces vanish at large distances. In general, Lagrangian methods are easier to implement with respect to Eulerian, and have higher spatial resolution, at the expense of a lower mass resolution.

4.3 Other Astrophysical processes

In addiction to the CDM physics simulated through N-body simulations, and baryon hydrodynamics described with Eulerian or Lagrangian methods, we might want to consider also other astrophysical processes, which in general are significant on scales smaller than resolution scale of the simulation. The main physical processes are the following: cooling (i.e. radiative losses), star formation, AGN feedback, stellar population evolution, chemical enrichment, magnetic fields, thermal conduction, turbulence, winds, viscosity, etc. It is not the aim of this thesis to develop these arguments in detail; however, some of them will be briefly treated in the specific context of the Magneticum simulations, in section 6.1.

Chapter 5

BAO theory and Reconstruction technique

"Sounds of laughter, shades of life
are ringing through my opened ears
inciting and inviting me.
Limitless undying love, which
shines around me like a million suns,
it calls me on and on across the Universe"

The Beatles, Across the Universe, No One's Gonna Change Our World (1969)

5.1 Acoustic oscillations in the baryon-photon plasma

The earliest Universe was not perfectly isotropic; quantum fluctuations of the spacetime metric, expanded by the inflation (Marochnik and Usikov, 2015, Cao et al., 2004), are presumably the seeds of primordial overdensities, made of CDM particles, photons, baryons and neutrinos, in approximately equal fractions. Neutrinos, being extremely weak interactive particles, decoupled first from the other components and streamed away. After the CDM decoupling, only photons and baryons were coupled, through continuous Thomson scattering. This lasted until the recombination time. When, for the first time, electrons and protons formed hydrogen atoms, the photon mean free path became larger than the size of the Universe, due to the small number of free electrons. The baryon-photon plasma was gravitationally attracted by the CDM potential wells, but the overdensities growth and the plasma, fallen into the wells, heated up the photons and provided a radiation pressure that pushed away the baryon-photon fluid, equilibrating the gravitational force. The interaction of these two forces produced spherical sound waves within the plasma, though smoothed by the Silk damping on comoving scales of $\approx 8 - 10$ Mpc (Silk, 1967). These acoustic oscillations travelled around the primordial Universe, expanding until the recombination time. Figure (5.1) describes the main phases of this evolution. The radius of the baryon-photon acoustic shell is proportional to the mean distance travelled by a sound wave in the time period between the Big Bang and the recombination. This distance, hereafter

called *acoustic scale* or *sound horizon*, is given by:

$$r_s = \int_0^{t_{rec}} \frac{c_s(t)}{a(t)} dt = \int_{z_{rec}}^{\infty} \frac{c_s(z)}{H(z)} dz. \tag{5.1}$$

The Hubble parameter, $H(z)$, depends on the values of the matter-radiation density parameters; on the other hand, the speed of sound, c_s, is dependent on the *baryon-to-photon ratio*, η. In the standard cosmological model, we assume that the Hubble parameter depends only on $\Omega_m h^2$. After the recombination, the characteristic time of the Thomson scatter between photons and electrons is greater than the Hubble time: photons are free to stream away, carrying the information of the acoustic features to us; the "earliest light" of the Universe which we could ever observe comes from the so-called *last scattering surface*, and forms the CMB.

5.2 The Cosmic Microwave Background

The CMB is a black-body radiation permeating the entire Universe, with a density of $\rho_0 \approx 415$ cm^{-3} photons. Even if the initial black-body temperature was ≈ 4000 K, at $z \approx 1100$, the cosmic background is detected in the microwaves because of the cosmological redshift caused by the expansion of the Universe, that brings the black-body temperature down to 2.726 K today. This is, precisely, the mean temperature of the CMB over the whole sky. As we already mentioned in section 2.2, in fact, the CMB is not perfectly isotropic. There are indeed small temperature fluctuations,

$$\frac{\delta T}{T} \equiv \frac{T(\theta, \varphi) - \bar{T}}{\bar{T}} = 10^{-5}, \tag{5.2}$$

where θ and φ are the angular coordinates in the sky. We can expand the temperature fluctuations on the celestial surface as a sum of spherical harmonics:

$$\frac{\delta T}{T} = \sum_{l=0}^{\infty} \sum_{m=-l}^{l} a_{lm} Y_{lm}(\theta, \varphi), \tag{5.3}$$

where

$$Y_{lm}(\theta, \varphi) = \sqrt{\frac{2l+1}{4\pi} \frac{(l-m)!}{(l+m)!}} P_l^m(\cos\theta) e^{i\varphi}, \tag{5.4}$$

being P_l^m the Legendre polynomial of the multipole l, and $-l \leq m \leq l$. Analogously to the matter Power Spectrum (2.5) case, we can define the Angular Power Spectrum of the CMB as

$$C_{l,m} \equiv < |a_{lm}|^2 > \equiv (2l+1)^{-1} \sum_{m=-l}^{l} a_{lm}^2. \tag{5.5}$$

The monopole ($l = 0$) represents the mean value of the temperature, averaged over all the possible observers. The dipole ($l = 1$) measures the redshift of the CMB photons due to the Earth motion. Opportunely subtracting the Earth orbital motion around the Sun, the Solar System revolution around the Milky Way, and our galaxy motion towards the centre of the Local Group, it provides the speed and direction of the Local Group with respect to a comoving cosmological frame, in which the CMB is isotropic. The result is a velocity of ≈ 600 km/s toward the point of galactic coordinates l =

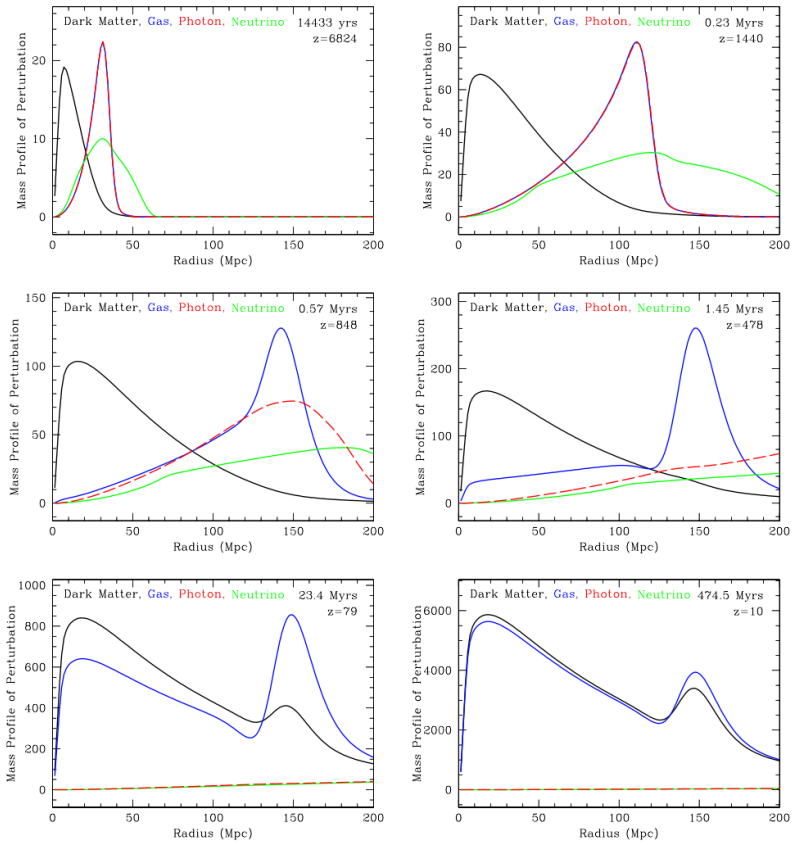

Figure 5.1: Time evolution of a single point-like perturbation generated at the origin, composed by CDM (black), baryons (blue), radiation (red) and neutrinos (green). In each panel both the cosmic time and the redshift are reported. The panels show the mass profiles of the fractional perturbations of each species versus the comoving radii. The energy density of relativistic components are multiplied by a factor 3/4 to have the same scale. In the top panels, we can see how the baryon-photon plasma perturbation is propagating at the sound speed, while the neutrino perturbation, already decoupled, is quickly spreading out. The CDM perturbation, on the other hand, is growing due to gravitational collapse. In the central panels, the recombination decoupled baryons and radiation; neutrino and photon perturbations are spreading, while the baryon overdensity stays at the acoustic scale. In the bottom panels, the neutrino and photon fluctuations are completely erased, while the CDM and the baryons are gravitationally interacting, with a significant baryon infalling in the CDM well, and a rising of the CDM overdensity at the sound horizon. Figure from D. J. Eisenstein, H.-J. Seo, and M. White (2007).

268°, b = 27°, in the direction of the Hydra-Centaurus (Rowan-Robinson et al., 1990).

Figure (5.2) shows the Angular Power Spectrum of the CMB, as measured by the ESA's satellite *Planck*. The acoustic features are immediately evident; they are the product of the oscillations of the baryon-photon fluid in the CDM potential wells. The symmetry of the amplitude of the oscillations, due to the equilibrium between

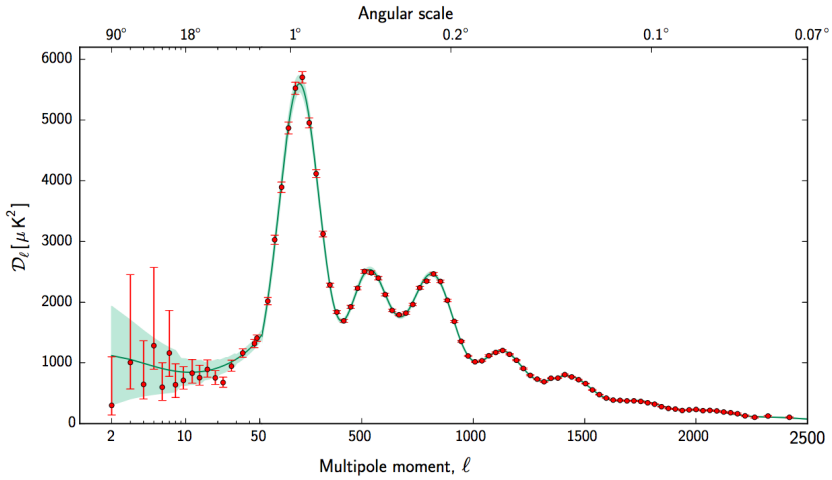

Figure 5.2: CMB Angular Power Spectrum from ESA's satellite Planck. The first acoustical peak marks the sound horizon at the last scattering time and thus the geometry of the Universe, while the fraction between the first and the second peak provides a measure of the baryon density. At higher l, that is at shorter scales, the Silk dumping smooths the oscillations. At the largest scales there is a plateau, which implies that the primordial spectrum is approximately a Harrison-Zel'dovich Spectrum. Figure from Planck Collaboration, P. A. Ade, et al. (2014).

kinetic energy of radiation pressure and gravitational potential energy, is broken by the *baryon drag* which makes the CDM potential wells deeper (leading to higher temperatures of the baryon-photon plasma). This, combined to the different phases ($\Delta\varphi = \pi/2$) between the velocity field and the gravitational field, leads to higher peaks corresponding to the maximum compression, and lower peaks corresponding to the maximum rarefaction of the baryon-photon fluid.
In particular, the largest allowed wavelength has the size of the sound horizon; this means that the first acoustic peak (often called the *Doppler peak* in a misleading way), which corresponds to the first maximum compression, signs the angle which subtends the acoustic scale. Moreover, the difference of the amplitudes between compression and rarefaction peaks provides a measure of Ω_b; since the CMB Angular Power Spectrum is also sensitive to Ω_m, through the equation (5.1), we can assess both the angle and the comoving size of the sound horizon. As shown in section 1.6.5, this provides a measure of the geometry of the Universe, that is the curvature parameter, K, or equivalently the total density parameter, Ω_T. In a flat Universe, where $K = 0$, the first acoustic peak would be centered at $l \approx 200$ (or $\approx 1°$). Until now all the observations are in agreement with this value (Planck Collaboration, Adam, et al., 2016). The comoving size of the sound horizon at the last scattering time has a weak dependence on the cosmology; its estimated value is $r_s \approx 150$ Mpc.
We can notice that the third peak is not as high as the first one, nor the forth compared to the second one, and so on; this effect is due to the Silk damping, that is the diffusion of the baryons caused by the scattering with the photons, as discussed in section 2.3.3. At scales larger than the first acoustic peak (lower l), outside the particle horizon at the last scattering time, the absence of causal connection between particles makes the microphysical processes ineffective. This means that we can measure the primordial power spectrum, which, being scale-invariant, forms a plateau, in agreement with the

predicted Zel'dovich spectral index, introduced in section 2.2.
The anisotropies that occurred at the last scattering time, that is the so-called primary anisotropies, are not the only ones imprinted in the CMB. Physical processes occurred during the photon travel from the last scattering surface to us cause the so-called secondary anisotropies. Phenomena such as the integrated *Sachs–Wolfe effect* (Sachs and Wolfe, 1967), the *Rees-Sciama effect* (Rees and Sciama, 1968), the thermal and kinetic *Sunyaev-Zel'dovich effects* (R. A. Sunyaev and Zeldovich, 1970), that will not be treated here, perturb the primary signal. Nevertheless, if opportunely treated, these effects provide paramount information on the evolution of cosmic structures.
Constraints on the main cosmological parameters provided by the analysis of the CMB anisotropies, from the *Planck* satellite, have been previously reported in Table (1.1).

5.3 The Baryonic Acoustic Oscillations

The lack of radiation pressure after the recombination rapidly decreases the sound speed in the baryon fluid essentially to zero, freezing the baryonic sound wave at the acoustic scale. Despite the successive infall into the CDM wells, a residual baryonic overdensity remains at the sound horizon, attracting also the CDM (see Figure (5.1)). The probability of gravitational collapse is thus higher at the acoustic scale, and so the formation of structures. As a consequence, there will be a preferred galaxy separation scale, corresponding to the sound horizon, detectable as a small bump in the galaxy correlation function.
The spherical perturbations are initially generated in different positions, and the interference of the different sound waves is on average destructive. Nevertheless, we still expect to have a signal, because of the large radius of the BAO shells: for this reason, the acoustic overdensities have a non-negligible weight in comparison to the low intrinsic large-scale correlation in the CDM (D. J. Eisenstein, 2005b).
Since the baryon-photon fluid of the primordial Universe was relativistic, with a sound speed of $c_s \approx c/\sqrt{3}$, the acoustic scale is very large, about 150 Mpc, as derived from the CMB (section 5.2). The BAO signal, due to its intrinsic size, is "protected" from non-linearities in the low-redshift Universe. Moreover, it depends only weakly on the cosmology, and the acoustic feature scale is quite stable. Indeed, both theoretical works and numerical simulations infer an accuracy better than 1% (see D. H. Weinberg et al. (2013) and references therein). These facts make the BAO a perfect standard ruler. Thus, it is one of the best probes to study the geometry of the Universe and to investigate the Dark Energy properties.
In the Fourier space, each crest of the initial sound wave generates a planar wave that travels a distance equal to the sound horizon (e.g. Hu and Sugiyama, 1996; D. J. Eisenstein and Hu, 1998). If the baryon perturbation ends on a CDM crest, the interference is constructive. On the other hand, if the baryon crest ends on a CDM trough, the interference is destructive. As a result, the matter power spectrum presents a series of harmonic oscillations, that depend on the relation between the perturbation wavelength and the acoustic scale ($\lambda_s \simeq 2\pi/r_s$). Mathematically, a Dirac delta in the correlation function corresponds, through the theorem (2.7), to a sinusoid. The Silk diffusion (see section 2.3.3), that smooths the peak in the correlation function, damps the higher harmonics in the power spectrum.

5.3.1 How to detect the BAO

The acoustic oscillations were theorised as a potential effect in the CMB in the late 1960s (Sakharov, 1966). Further studies (Bond and G. Efstathiou, 1984; G. Efstathiou and Bond, 1986; Hu and M. White, 1996) investigated possible methods to use the acoustic scale as a standard ruler (Kamionkowski et al., 1994; Jungman et al., 1996). These works were later extended to the matter power spectrum. Pure baryon cosmologies predict a very strong matter acoustical oscillations (P. J. Peebles and Yu, 1970; R. A. Sunyaev and Zeldovich, 1970). However, since the signal is significantly weaker in CDM models, the chances of detecting these features seemed very low. After the discovery of the accelerated expansion of the Universe through type Ia Supernovae (Riess et al., 1998; Perlmutter et al., 1999; Schmidt, 1999), the interest on the BAO started to increase again (D. J. Eisenstein, 2005a). The BAO feature, in fact, being a standard ruler (Hu and Sugiyama, 1996; D. J. Eisenstein and Hu, 1998), can break the distance scale degeneracy between Ω_m and $H(z)$ at different redshifts, constraining the Dark Energy equation of state (D. Eisenstein, 2002; Blake and Glazebrook, 2003; H.-J. Seo and D. J. Eisenstein, 2003). Nevertheless, the large size of the acoustic scale and the weakness of the signal (10% contrast in the power spectrum) imply significant statistical issues, making it necessary to survey very large volumes, of the order of $\approx 1\,\mathrm{h}^{-3}\,\mathrm{Gpc}^3$ (Tegmark, 1997). After several theoretical and observational investigations (e.g. W. J. Percival et al., 2001), the BAO was finally detected both in the galaxy correlation function and in the power spectrum (D. J. Eisenstein, Zehavi, et al., 2005, S. Cole et al., 2005), using the Sloan Digital Sky Survey (SDSS, York et al., 2000). Figure (5.3) shows the correlation function measured by D. J. Eisenstein, Zehavi, et al. (2005), from a sample of 46748 luminous red galaxies, that provided the first detection of the BAO peak, with 3.4 σ significance.
They defined a spherically-averaged distance measurement, $D_V(z)$:

$$D_V(z) \equiv \left[D_M(z)^2 \frac{cz}{H(z)} \right]^{1/3}, \tag{5.6}$$

where D_M is the *comoving angular distance*, obtained by combining the equations (1.18) and (1.16):

$$D_M = (1+z)\, D_A(z). \tag{5.7}$$

They defined also the ratio, R, of the angle-averaged distance at the redshift of the measurements, to the comoving angular distance at $z = 1089$ (the redshift of decoupling, C. L. Bennett et al., 2003):

$$R(z) \equiv \frac{D_V(z)}{D_M(z_{dec})}. \tag{5.8}$$

This robust distance measurement is predicted by linear perturbation theory, and links the matter with the photon acoustic waves.
To constrain the Dark Energy models, they defined another parameter, independent of the acoustic scale in the CMB and so useful especially at low redshifts:

$$A \equiv D_V(z) \frac{\sqrt{\Omega_m H_0^2}}{zc}. \tag{5.9}$$

We can notice that this parameter is also independent on the Hubble constant, H_0, since $D_V \propto H_0^{-1}$. Assuming the following fiducial cosmological parameters, $\Omega_m = 0.3$, $\Omega_\Lambda = 0.7$ and $h = 0.7$, they found that $D_V(z = 0.35) = 1334$ Mpc with a 1σ uncertainty of 4.7%, while $R(z = 0.35)$ and $A(z = 0.35)$ were measured with uncertainties of 3.7%

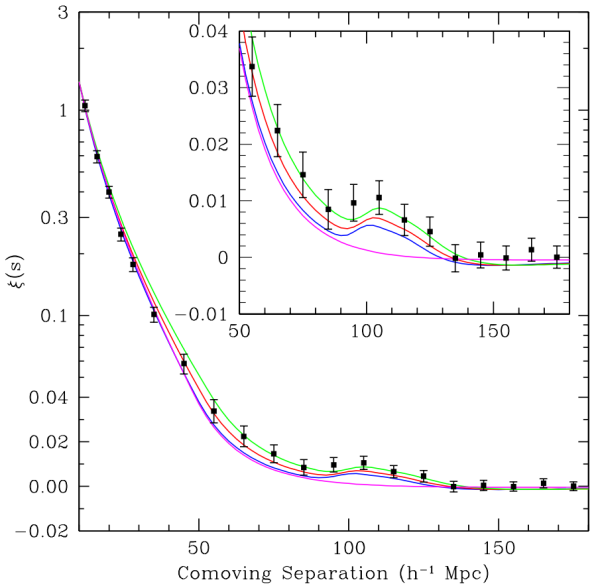

Figure 5.3: Galaxy two-point correlation function, from a spectroscopic sample of 46748 luminous red galaxies from the SDSS (York et al., 2000). Notice that the y-axis is partially linear and partially logarithmic. The inset panel is a zoom of the BAO peak, at comoving separation $s \approx 100\ h^{-1}$ Mpc. The colored solid lines represent models computed with different cosmological parameters: $\Omega_m h^2 = 0.12$ (green), $\Omega_m h^2 = 0.13$ (red), $\Omega_m h^2 = 014$ (blue), all with $\Omega_b h^2 = 0.024$; the magenta line indicates a pure CDM model, with $\Omega_m h^2 = 0.105$. Figure from D. J. Eisenstein, Zehavi, et al. (2005).

and 3.6%, respectively. Further observational results and general considerations on the BAO surveys will be reported in section 5.6.

5.3.2 Non-linearity in the BAO theory

Despite of the large scales of the BAO, there are still some effects that can slightly distort this standard ruler, especially at low redshift. The growth of structures, the peculiar velocities and the bias, behave differently from how the linear theory predicts (Meiksin et al., 1999; H.-J. Seo and D. J. Eisenstein, 2005; Angulo, Baugh, et al., 2008). Different theoretical approaches can be used to describe the non-linear evolution of the BAO feature. In particular, the most widely-used models are the following ones:

- the 2PT, with the possibility of combining its analytic results with numerical simulations, in order to compute the mean pairwise displacement of tracers within the Zel'dovich approximation (D. J. Eisenstein, H.-J. Seo, and M. White, 2007; Padmanabhan and M. White, 2009);

- the renormalised perturbation theory (RPT, M. Crocce and R. Scoccimarro, 2008). This theory describes the non-linear growth of structures by decomposing it into a linear propagation plus interactions, and summing over all possibilities. To do this, one makes a resummation of an infinite subset of contributions to the perturbation theory expansion, getting a new series expansion, which is not a perturbative expansion in the amplitude of fluctuations. A treatment of this theory is above the aim of this thesis, for further details see M. Crocce and Román Scoccimarro (2006).

These theories are all in agreement, and show that non-linear effects cause both a broadening and a shift of the BAO peak toward smaller scales, in the correlation function, or equivalently in the power spectrum. In particular, the maximum shift in the correlation function, at $z = 0$, is of the order of $0.5 - 1\%$, ensuring a high stability of the BAO scale.
Figure (5.4) compares the predictions of the linear theory and RPT. In the RPT, the BAO peak is smoothed and shifted on smaller scales, with respect to the linear theory prediction, in excellent agreement with measurements from numerical simulations (M. Crocce and R. Scoccimarro, 2008).

The width of the final BAO peak in the correlation function, σ_{bao}, can be seen as the quadrature sum between the initial width, σ_{IC}, due to the Silk dumping, and the mean-squared displacement between pairs, Σ_{NL} (Orban and D. H. Weinberg, 2011):

$$\sigma^2_{bao} = \sigma^2_{IC} + \Sigma^2_{NL}, \tag{5.10}$$

where

$$\Sigma^2_{NL} = r^2_{12} \int_0^\infty \frac{k^2 dk}{2\pi^2} P(k) f_\parallel(kr_{12}), \tag{5.11}$$

being r_{12} the separation and

$$f_\parallel(x) = \frac{2}{x^2}\left(\frac{1}{3} - \frac{\sin(x)}{x} - \frac{2\cos(x)}{x^2} + \frac{2\sin(x)}{x^3}\right). \tag{5.12}$$

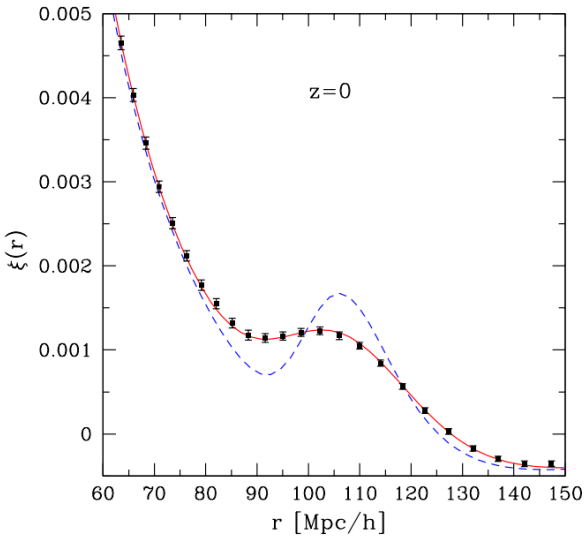

Figure 5.4: The effects of non-linearities in the correlation function, at redshift $z = 0$. The data points with error bars are measurements from a numerical simulation, the red solid line is the prediction given by the RPT (M. Crocce and R. Scoccimarro, 2008), while the blue dashed line represents the linear theory prediction. Figure from M. Crocce and R. Scoccimarro (2008).

In the limit of $r_{12} \to \infty$, the equation (5.11) becomes

$$\Sigma_L^2 = \frac{1}{3\pi^2} \int_0^\infty P_L(q) dq, \tag{5.13}$$

that is the rms displacement of particles in the PT, including the contribution from bulk motions, that shifts coherently all the particles at large scales. In other words, the rms pairwise displacement, Σ_{NL}, is asymptotic to the Zel'dovich displacement. However, in this work, Σ_{NL} was not computed through equation (5.11)), but it was considered as a fixed parameter of the model. It can be shown that the non-linear evolution damps the harmonics oscillations in the power spectrum by a factor $\exp(-k^2\Sigma_{NL}^2)$:

$$P_{NL}(k) = P_L(k) e^{-k^2 \Sigma_{NL}^2}. \tag{5.14}$$

Figure (5.5) shows a comparison between the power spectrum predicted by the linear theory, and the non-linear power spectrum computed through N-body simulations. Alternatively, the so-called Boltzmann codes can be used to get accurate predictions of both linear and non-linear matter power spectra (see e.g. CAMB, Lewis and Challinor, 2011; CLASS, Lesgourgues, 2011). The RSD, and in particular the Kaiser effect, causes an extra broadening of the BAO peak, blurring the clustering measurements along the line-of-sight and creating anisotropies in the broadband clustering. The bias can also change the amplitudes of both the correlation function and the power spectrum, with minor effects on their shapes. The non-linear evolution can alter the relative weights of overdense and underdense regions, shifting the scale of the BAO peak. Numerical simulations predict a BAO shift of $0.1\% - 0.8\%$, at $z = 1$, depending on the strength of the bias (Mehta, H.-J. Seo, et al., 2011).

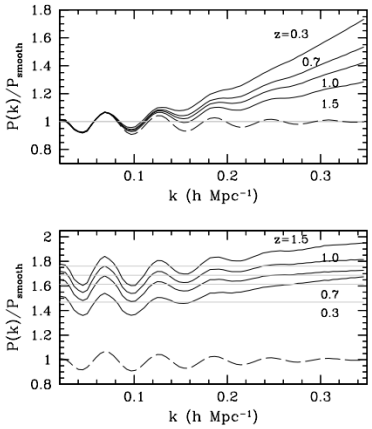

Figure 5.5: Non-linearities in the power spectrum, in real (top) and in redshift space (bottom), as a function of the redshift (from H.-J. Seo, Siegel, et al., 2008). The solid black lines are computed with numerical simulations, while the dashed lines are the linear predictions. The grey lines represent the large-scale amplitudes expected in linear theory. In redshift space, the power spectra are shifted for clarity purpose.

5.4 Reconstruction of the BAO

As discussed in the previous section, the non-linear evolution of cosmic structures smooths and shifts the BAO peak, possibly introducing systematics in the acoustic scale constraints, if these effects are not properly modelled.
A possible method to overcome this issue is the so-called *reconstruction* of the linear density field (D. J. Eisenstein, H.-J. Seo, Sirko, et al., 2007). The idea of the method is quite simple: to move back galaxies from where we observe them now to where they were at the beginning, before structures growth. Since the acoustic scale is very large, we expect that the motion of galaxies can be reliably modelled by the PT. The connection between the velocity and the density fields at these scales is almost linear, thus the density fluctuations that we measure are the ones that generate the bulk flows. We can so predict the velocity field, and thus compute the reverse motion of the galaxies.
Figure (5.6) shows the main effects of such a method, in a two-dimensional cosmological density field. In the initial linear density field, the BAO shell coincides with the acoustic scale, which has a radius of ≈ 150 Mpc. Evolving the density field in time, with the Zel'dovich approximation (discussed in section 2.5.1) the BAO feature is distorted, and its rms width is broader. Thus, we loose accuracy in estimating the acoustic scale. Nevertheless, once obtained the displacement field from the actual density field, we can apply a reverse Zel'dovich approximation to move back the objects, restoring the linearity. In this way, the BAO feature marks better the acoustic scale and the width of the shell is narrower. Thus it is possible to infer a more precise constraint on the sound horizon.

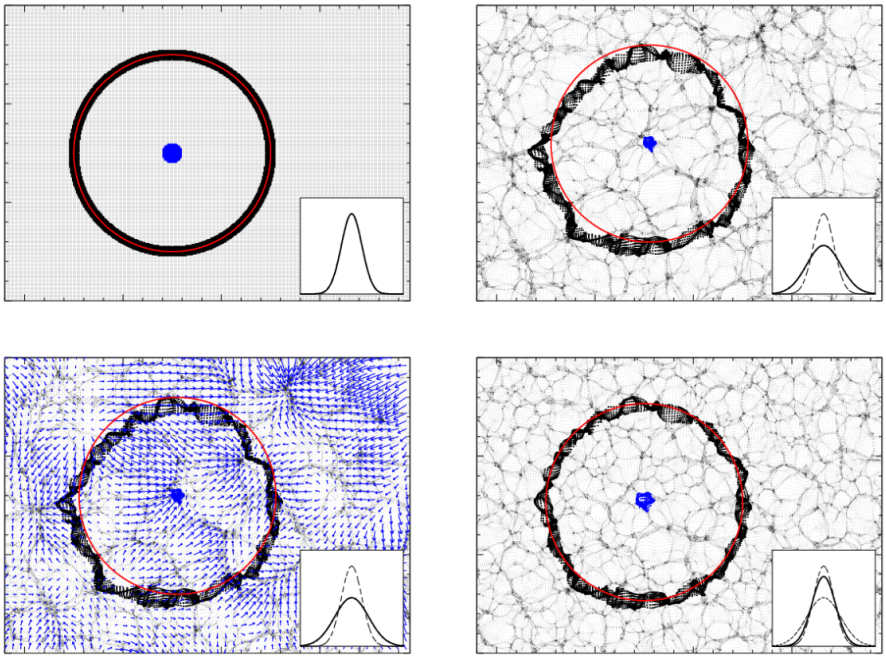

Figure 5.6: Illustrative picture of the BAO reconstruction method. Each panel shows a slice of a simulated cosmological density field, highlighting the acoustic scale with a red circle. The boxes contain a Gaussian having the same width as the rms radial distribution of the BAO feature (black points) with respect to the centroid (blue points). Top-left: at the beginning, in linear regime, the density field was smooth. The BAO shell is a symmetrical sphere, with radius ≈ 150 Mpc, that perfectly marks the acoustic scale. Top-right: evolving the density field within the Zel'dovich approximation up to the present time, the BAO shell is distorted and broadened, due to the large-scale velocity field. The actual Gaussian (solid line) became wider than the initial one (dashed line). Bottom-left: the Lagrangian displacement field is overplotted on the previous panel. From an estimation of the actual displacement field, the reconstruction "rewinds the gravity" reversing the Zel'dovich approximation, to obtain the linear density field. Bottom-right: reconstructed density field. Again, the BAO feature marks well the acoustic scale. The new Gaussian (solid line), representing the rms radius, is narrower compared to the previous one (short-dashed line), and quite similar to the initial one (long-dashed line). This means that it is easier to extract accurately the acoustic scale from the BAO feature in the reconstructed density field. Figure from Padmanabhan, Xu, et al. (2012)

5.4.1 The Zel'dovich approximation in redshift space

With the Zel'dovich approximation we can estimate the large-scale velocity field. From the density field, in the redshift space, we can correct the Kaiser effect, which degrades the measurement of the acoustic scale along the line of sight, and the effects of the linear bias.
The treatment of RSD is easier with LPT than with ELT (Matsubara, 2008). In LPT, in fact, we have that

$$\mathbf{\Psi}_s = \mathbf{\Psi} + \frac{\hat{s} \cdot \dot{\mathbf{\Psi}}}{H} \hat{s}, \tag{5.15}$$

where $\mathbf{\Psi}$ is the displacement in real space, Ψ_s is the displacement in redshift space and $\hat{s}$ is the unit vector in the line-of-sight direction. This relation is exactly linear even in non-linear regimes, on the contrary of its Eulerian counterpart.
It can be shown that the PT equation (2.60), in redshift space, can be expanded at the first order as follows:

$$\nabla \cdot \mathbf{\Psi}^{(1)} + f \nabla \cdot (\Psi_s \hat{s}) = -\frac{\delta}{b}, \tag{5.16}$$

where $\Psi_s \equiv \mathbf{\Psi}^{(1)} \cdot \hat{s}$ is the displacement in the line-of-sight direction, and f is the linear growth rate parameter (Nusser and M. Davis, 1994; Padmanabhan, Xu, et al., 2012; Burden, W. J. Percival, Manera, et al., 2014). Hereafter, unless contrary statements, we will use the notation $\mathbf{\Psi} \equiv \mathbf{\Psi}^{(1)}$. The second term of equation (5.16) is the correction due to the coherent infall of galaxies into larger structures. Assuming $\mathbf{\Psi}$ as irrotational (see section 2.5.1), $\mathbf{\Psi} = \nabla \Phi$, we have that

$$\nabla^2 \Phi + f \nabla \cdot (\nabla \Phi_s)\, \hat{s} = -\frac{\delta}{b}. \tag{5.17}$$

We can solve equation (5.17) for the scalar field Φ, fixing the linear bias, b, and the linear growth factor, f, by using the finite difference method to approximate the derivatives (see Padmanabhan, Xu, et al., 2012 for further details). Alternatively, it is possible to solve the displacement field by using the Fast Fourier Transform method (FTT). Following Burden, W. J. Percival, and Howlett (2015), we can decompose the $\Psi_s \hat{s}$ term of equation (5.16), through the Helmholtz's Theorem, into a solenoidal and an irrotational component:

$$\Psi_s \hat{s} = \nabla A + \nabla \times B, \tag{5.18}$$

where A and B are scalar and vector potential fields, respectively. By substituting equation (5.18) in equation (5.16) , we obtain that

$$\nabla(\Phi + fA) = -\nabla \nabla^{-2} \frac{\delta}{b}. \tag{5.19}$$

Equation (5.19) does not allow to solve equation (5.16), to find the displacement field, using FFTs. However, assuming the approximation made by Burden, W. J. Percival, Manera, et al. (2014), that $\Psi_s \hat{s}$ is irrotational,

$$\Psi_s \hat{s} \approx \nabla A, \tag{5.20}$$

equation (5.19) becomes

$$\mathbf{\Psi} + f\,(\Psi_s \hat{s}) = -\nabla \nabla^{-2} \frac{\delta}{b}. \tag{5.21}$$

We can compute the right-hand side of equation (5.21) using the FFTs [1]; the displacement field is then

$$\mathbf{\Psi} = \text{IFFT}\left[-\frac{i\mathbf{k}\delta(\mathbf{k})}{k^2 b}\right] - \frac{f}{1+f}\left\{\text{IFFT}\left[-\frac{i\mathbf{k}\delta(\mathbf{k})}{k^2 b}\right]\cdot\hat{\mathbf{s}}\right\}\mathbf{s}, \tag{5.22}$$

where IFTTs are the inverse of FFTs.

5.4.2 A simple reconstruction algorithm

In this section we describe the fundamental steps of a generic reconstruction algorithm (D. J. Eisenstein, H.-J. Seo, Sirko, et al., 2007; Padmanabhan, Xu, et al., 2012; Burden, W. J. Percival, Manera, et al., 2014):

- Compute the density field using mass tracers.
- Fourier transform the density field.
- Smooth the density field to filter out the high-k non-linearities (generally at k equivalent to $10 - 20\,h^{-1}$ Mpc), harder to model. This is equivalent to multiply by a function *S(k)*, that monotonically decreases from unity, at low k, to zero, at high k:
$$\delta_{smooth}(\mathbf{k}) = S(k)\delta(\mathbf{k}), \tag{5.23}$$
where $\delta_{smooth}(\mathbf{k})$ is the smoothed density field. Generally, it is used a Gaussian filter:
$$S(k) = e^{-k^2R^2/2}. \tag{5.24}$$
- Estimate the displacement field $\mathbf{\Psi}$; the simplest way is to use the Zel'dovich Approximation (equation 2.64), that relates the displacement field to the density field in Fourier space. Taking into account the smoothing (equation (5.23)), we have that
$$\mathbf{\Psi} = -\frac{i\mathbf{k}}{k^2}\delta_{smooth}(\mathbf{k}). \tag{5.25}$$
- Fourier anti-transform to compute the displacement field in configuration space.
- Shift the galaxy comoving positions by $-\mathbf{\Psi}$, thus inverting equation (2.46), to get:
$$\mathbf{q} = \mathbf{x}(\mathbf{q}, \mathbf{t_0}) - \mathbf{\Psi}(\mathbf{q}, \mathbf{t_0}), \tag{5.26}$$
where $\mathbf{x}(\mathbf{q}, t_0)$ are the galaxy comoving coordinates measured at $t = t_0$, and $\mathbf{q}$ are their initial Lagrangian positions.
- In case, add the term $-f\,(\mathbf{\Psi}\cdot\hat{s})\,\hat{s}$, to correct for RSD (this exactly removes the Kaiser effect at first order, see equation (5.16)):
$$\mathbf{q} = \mathbf{x}(\mathbf{q}, \mathbf{t_0}) - \mathbf{\Psi}(\mathbf{q}, \mathbf{t_0}) - f\,(\mathbf{\Psi}(\mathbf{q}, \mathbf{t_0})\cdot\hat{\mathbf{s}})\,\hat{\mathbf{s}}. \tag{5.27}$$

Figures (5.7) and (5.8) show the final effect of such a method on the angular power spectrum and two-point correlation function, respectively. The two figures report the clustering measurements before and after the reconstruction, at $z = 0.3$, compared with

[1] Burden, W. J. Percival, and Howlett (2015) suggest also an extra 3/7 factor on the growth factor, f, to take into account the solenoidal component. This correction, however, is not well tested yet

the initial ones, at $z = 49$. These figures, from D. J. Eisenstein, H.-J. Seo, Sirko, et al. (2007), show the averaged measurements over 30 simulations, in both real and redshift space. In real space, two different Gaussian filters are applied, with radii 10 and 20 h^{-1} Mpc. The reconstruction with the 10 h^{-1} Mpc Gaussian smoothing restores better the higher harmonic oscillations in the power spectra, damped by the non-linear effects. Moreover, with this filter, the acoustic peak in the correlation function is nearly fully restored.
Until now, we have discussed about how to correct the reconstruction method only for the large-scale velocity distortions. As discussed in section (3.6.1), the Fingers of God stretch the iso-correlation contours along the line-of-sight, degrading the accuracy of the acoustic scale measurements. To take into account this further effect, we should also compress the Fingers of God to their original position in real space. The real-space measurements shown in Figures (5.7) and (5.8) highlight the effects of this Finger-of-God compression, realised by moving all cluster particles to the center of mass of the host cluster, and then applying the reconstruction in such a compressed density field. The improvement on the constraints of the acoustic scale is clear, in both correlation function and power spectra. D. J. Eisenstein, H.-J. Seo, Sirko, et al. (2007) found that a $1h^{-3}\mathrm{Gpc}^3$ survey should provide a distant measurement of 1.4% in real space and 1.9% in redshift space, at $z = 0.3$. The reconstruction method improves these measurements to 0.75% and 0.95% in real and redshift space, respectively. In principle, with a perfect reconstruction, it is possible to achieve a 0.5% distance (although shot noise from reasonable galaxy samples would degrade this to $0.55 - 0.60\%$). As a consequence, the actual precision is a factor of 3.5 worse than the cosmic variance, but the reconstruction method improves the measurement accuracy by a factor of 2. Once that the errors are below the rms width of the acoustic peak, that is $8h^{-1}$ Mpc, the possible improvements of the measure of the acoustic scales get lower. The reconstruction is less effective at high redshifts: the displacement are smaller, so we can get good results using only the largest scales. We expect the best improvements (a factor 2-3) at low redshifts, where the non-linearities are larger.

Padmanabhan, Xu, et al., 2012 applied the reconstruction technique on the clustering measurements from the SDSS Data Release 7 (SDSS DR7) Luminous Red Galaxy sample (W. J. Percival et al., 2010), at $z = 0.35$, after testing it on 160 LasDamas N-body simulations (C. McBride et al., 2009). Figure (5.9) shows how well the reconstruction restores the isotropy of the two-dimensional correlation function, by correcting the RSD, in the LasDamas simulations. The measured correlation functions, from real data, before and after the reconstruction, are shown on Figure (5.10). In this case the reconstruction technique reduces the non-linear smoothing scale from $\Sigma_{NL} = 8.1\,h^{-1}$Mpc to $\Sigma_{NL} = 4.4\,h^{-1}$Mpc. The BAO detection significance improves from 3.3σ to 4.2σ. Furthermore, the errors in the angle-averaged distance measurement, pre and post reconstruction, are 3.5% and 1.9%, respectively, equivalent to survey a volume three times larger. The final angle averaged distance, assuming a sound horizon of 154.25 Mpc, is $D_V(z = 0.35) = 1.356 \pm 0.025\,\mathrm{Gpc}$.
In general, the reconstruction technique increases the statistical accuracy of the BAO detection by a factor of 1.5-2, which is equivalent to have a factor 2-4 gain in the size of the survey (D. H. Weinberg et al., 2013).

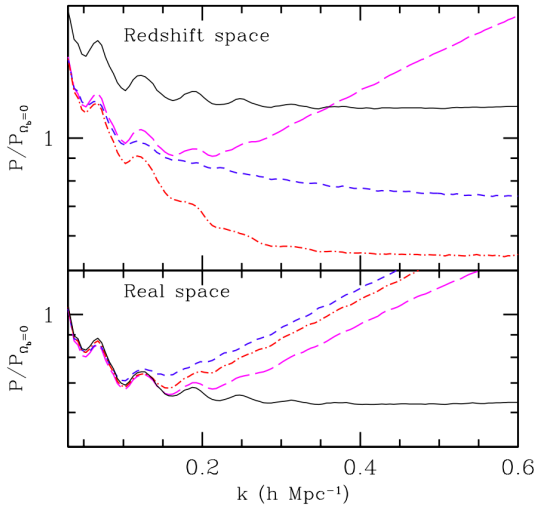

Figure 5.7: Angle-averaged matter power spectra, in redshift (top panel) and real (bottom panel) space. The black solid lines are at $z = 47$, while the blue dashed lines at $z = 0.3$. At low redshifts, the BAO peaks are clearly smoothed, due to large-scale velocity field. In real space, the reconstruction has been applied with two Gaussian filters of 10 h^{-1} Mpc (magenta long dashed line) and 20 h^{-1} Mpc (red dot-dashed line). The reconstruction restores the highest harmonics, damped by the non-linear evolution. In redshift space, both the magenta and red lines have been obtained with a 10 h^{-1} Mpc filtering; the magenta long-dashed line includes the Fingers of God compression, contrary to the red dot-dashed line. The increase of power at large k is essentially irrelevant to the accuracy of the acoustic signature, as it can marginalise over these broadband changes. Figure from D. J. Eisenstein, H.-J. Seo, Sirko, et al. (2007).

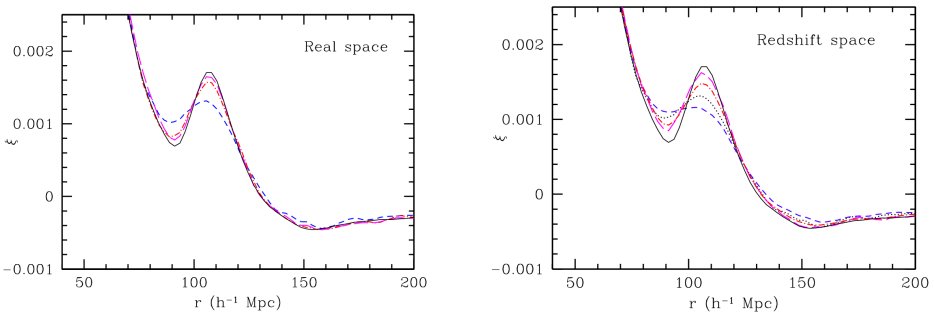

Figure 5.8: Real-space (left panel) and redshift-space (right panel) matter correlation functions. All the symbols are as in Figure (5.7) . After the the reconstruction, the BAO peak is enhanced, providing a better accuracy in the evaluation of the acoustic scale, around 100 h^{-1} Mpc. Figure from D. J. Eisenstein, H.-J. Seo, Sirko, et al. (2007).

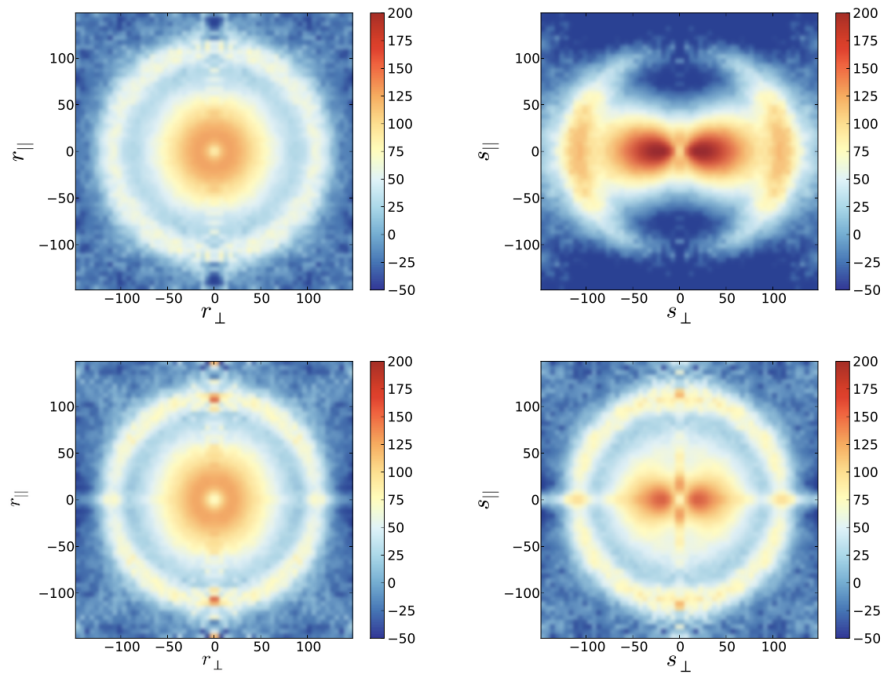

Figure 5.9: Two-dimensional galaxy correlation functions, averaged over 160 LasDamas N-body simulations. The line-of-sight separation is in the y-axis, while the transverse component in the x-axis, both in Mpc. The top panels show the correlation function pre-reconstruction, while the bottom panels refer to the post-reconstruction, in real (left) and redshift (right) space. The asymmetry of the BAO feature in redshift space, due to RSD and, in particular, to the Kaiser effect, is corrected with the reconstruction. Moreover, in both real and redshift spaces the BAO signal in the reconstructed galaxy density field is enhanced. Figure from Padmanabhan, Xu, et al. (2012).

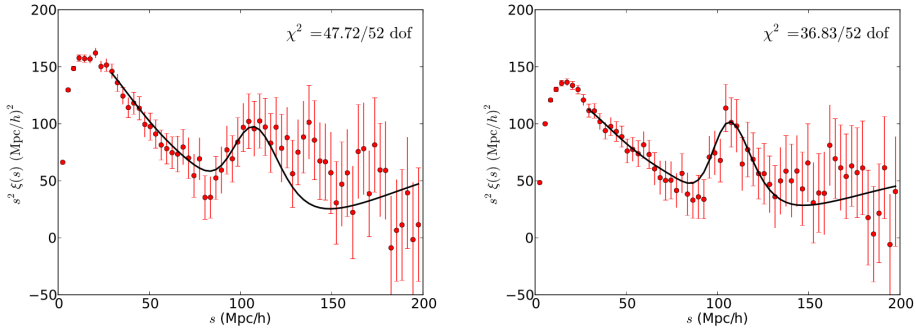

Figure 5.10: Unreconstructed (left panel) and reconstructed (right panel) galaxy two-point correlation functions, from the SDSS DR7 Luminous Red Galaxy sample, at $z = 0.35$. The s^2 factor, multiplied to the $\xi(s)$, enhances the BAO peak in the plot. The error bars are the standard deviation of the 160 LasDamas simulations. Figure from Padmanabhan, Xu, et al. (2012).

5.4.3 Reconstruction in the 2LPT

D. J. Eisenstein, H.-J. Seo, Sirko, et al. (2007) presented the BAO reconstruction method, and tested it with numerical simulations. Padmanabhan, M. White, and Cohn (2009) used the 2LPT to analytically describe the method (see also M. White, 2015 and Achitouv and Blake, 2015). Now we use the formalism developed in section 2.5, to describe the main points of the reconstruction method, described in the previous section.

- From equation (2.48), we can write a particle density field as follows:

$$\delta(\mathbf{k}) = \int d^3\mathbf{q} e^{-i\mathbf{k}\cdot\mathbf{q}} \left(e^{-i\mathbf{k}\cdot\mathbf{\Psi_0}} - 1\right). \tag{5.28}$$

- We can shift the original particles by Ψ_{rec}, the negative Zel'dovich displacement field of equation (5.25), obtaining the displaced density field:

$$\delta_d(\mathbf{k}) = \int d^3\mathbf{q} e^{-i\mathbf{k}\cdot\mathbf{q}} \left(e^{-i\mathbf{k}\cdot[\mathbf{\Psi_0}+\mathbf{\Psi_{rec}}]} - 1\right). \tag{5.29}$$

  Notice that if the original density field were linear, and $S(\mathbf{k}) = 1$ (see equation (5.23)), the reconstruction would undo the original displacement exactly, moving back the particles to their original positions and giving $\delta_d(\mathbf{k}) = 0$.

- Shifting a spatially uniform grid of particles by Ψ_{rec}, we can obtain the shifted density field, that is:

$$\delta_s(\mathbf{k}) = \int d^3\mathbf{q} e^{-i\mathbf{k}\cdot\mathbf{q}} \left(e^{-i\mathbf{k}\cdot\mathbf{\Psi_{rec}}} - 1\right); \tag{5.30}$$

  assuming a linear field, we have that $\delta_s(\mathbf{k}) = -\delta(\mathbf{k})$.

- The reconstruction density field, $\delta_{rec}(\mathbf{k})$, defined as $\delta_{rec}(\mathbf{k}) = \delta_d(\mathbf{k}) - \delta_s(\mathbf{k})$, is thus:

$$\delta_{rec}(\mathbf{k}) = \int d^3\mathbf{q} e^{-i\mathbf{k}\cdot\mathbf{q}} e^{-i\mathbf{k}\cdot\mathbf{\Psi_{rec}}} \left(e^{-i\mathbf{k}\cdot\mathbf{\Psi_0}} - 1\right). \tag{5.31}$$

  The reconstructed power spectrum is then

$$P_{rec}(\mathbf{k}) \propto \langle|\delta^2_{rec}|\rangle. \tag{5.32}$$

  Notice that since $S(\mathbf{k}) \propto \Psi_{rec}$, in the limit of $S(\mathbf{k}) \to 0$ the reconstruction is not effective.

Now we expand the reconstruction density field within the 2LPT, as in equation (2.50):

$$\delta_{rec} = \delta^{(1)}_{rec} + \delta^{(2)}_{rec} + ... \tag{5.33}$$

The reconstructed field is equal to the first-order linear density field. At second order, we have that

$$\delta^{(2)}_{rec} = \delta^{(2)} - \frac{1}{2}\int \frac{d^3k_1 d^3k_2}{(2\pi)^3}\delta^{(D)}\left(\mathbf{k}_1 + \mathbf{k}_2 - \mathbf{k}\right) \times$$
$$\times\delta_l(\mathbf{k}_1)\delta_l(\mathbf{k}_2)\mathbf{k}\cdot\mathbf{L}^{(1)}(\mathbf{k}_1)\mathbf{k}\cdot\mathbf{L}^{(1)}(\mathbf{k}_2)\left[S(\mathbf{k}_1) + S(\mathbf{k}_2)\right], \tag{5.34}$$

where $\delta^{(2)}$ is given by equation (2.76), reported here:

$$\delta^{(2)} = \frac{1}{2}\int \frac{d^3k_1 d^3k_2}{(2\pi)^3}\delta^{(D)}\left(\mathbf{k}_1+\mathbf{k}_2-\mathbf{k}\right)\times$$
$$\times\delta_l(\mathbf{k}_1)\delta_l(\mathbf{k}_2)\left[\mathbf{k}\cdot\mathbf{L}^{(2)}(\mathbf{k}_1,\mathbf{k}_2,\mathbf{k})+\mathbf{k}\cdot\mathbf{L}^{(1)}(\mathbf{k}_1)\mathbf{k}\cdot\mathbf{L}^{(1)}(\mathbf{k}_2)\right]. \tag{5.35}$$

We can notice that the second-order terms in the reconstructed density field do not vanish. The second-order density field, in fact, contains $\mathbf{L}^{(2)}$ terms, on the contrary of the reconstructed density field, which contains only $\mathbf{L}^{(1)}$ terms. Thus, we have demonstrated that the reconstruction method cannot fully cancel the non-linearity, i.e. it does not restore the linear density field, but provides a density field with second-order corrections. Furthermore, studying the reconstructed power spectrum within the 2LPT, one can show that the reconstruction method reduces the mode coupling terms, which introduces out-of-phase oscillations in the power spectrum, thus shifting the acoustic peaks (see D. J. Eisenstein, H.-J. Seo, Sirko, et al. (2007) for more details).

5.5 Extract cosmological informations from BAO

The BAO marks the acoustic scale indirectly. In fact, the decoupling of the baryon-photon fluid is consequent to the recombination. More precisely, the decoupling of the radiation from the baryons (and the resulting last scattering surface) happened earlier than the decoupling of matter from the photons. Moreover, the Silk dumping alters the effective recombination redshift, as a function of the wavelength, and the growing-modes after the recombination are due to the velocity perturbations at recombination, rather than to the density fluctuations. As a result, the sound horizon, defined in the equation (5.1), is not marked by the maximum of the BAO peak in the correlation function, and the harmonics in the power spectrum have not the same scales of the oscillations in the CMB. Nevertheless, all these effects can be accurately computed with Boltzmann codes, that provide precise predictions for power spectra in both matter and radiation. The appropriate method to extract cosmological information from the BAO peak in the two-point correlation function, i.e. to measure the acoustic scale using the BAO standard ruler, is to fit a fiducial cosmological model, as a template, to the data over a given range of scales, using the correct covariance matrix (see section 3.7) and likelihood.

5.5.1 Fundamentals of Bayesian methods in cosmology

Let X be a random variable and ϑ a set of a model parameters, which describe the observed data X, $\hat{x} = \{\hat{x}_1, \hat{x}_2, ..., \hat{x}_N\}$. Being $p(X|\vartheta)$ the probability density function (pdf), the likelihood function, $\mathcal{L}$, is defined as follows:

$$\mathcal{L}(\theta) = p(X = \hat{x}|\theta). \tag{5.36}$$

Thus, the likelihood represents the density probability of observing the data that have been measured, as a function of the model parameters. Let $\hat{x} = \{\hat{x}_1, \hat{x}_2, ..., \hat{x}_N\}$ be N independent measurements of a Gaussian-distributed quantity, and μ and σ the mean and the standard deviation of the distribution, respectively. Considering $\vartheta = \{\mu, \sigma\}$, we have that

$$\mathcal{L}(\mu,\vartheta) = p(X = \hat{x}|\mu,\sigma) = \prod_{i=1}^{N}\frac{1}{\sqrt{2\pi}\sigma}\exp\left(-\frac{1}{2}\frac{(\hat{x}_i-\mu)^2}{\sigma^2}\right). \tag{5.37}$$

Equation (5.37) is usually written as follows:

$$\mathcal{L}(\theta) = L_0 \exp(-\chi^2/2), \tag{5.38}$$

where the so-called *chi-squared* is defined as

$$\chi^2 \equiv \sum_{i=1}^{N} \frac{(\hat{x}_i - \mu)^2}{\sigma^2}. \tag{5.39}$$

We can estimate the model parameters maximising the probability of obtaining the data we got. To do this, we define the maximum likelihood estimator:

$$\theta_{ML} \equiv \max_\theta \mathcal{L}(\theta). \tag{5.40}$$

It can be shown that θ_{ML} converges to the true values of the parameters for infinite data points, and it is asymptotically the minimum variance estimator, i.e. the one with the smallest errors. To calculate the maximum likelihood estimator, we impose its first derivative to be null and its second derivative to be negative:

$$\frac{\partial \mathcal{L}(\theta)}{\partial \theta}\Big|_{\theta_{ML}} = 0; \tag{5.41}$$

$$\frac{\partial^2 \mathcal{L}(\theta^2)}{\partial \theta}\Big|_{\theta_{ML}} < 0. \tag{5.42}$$

Notice that this is not strictly equivalent to find the most probable parameters of the model. To do so, we introduce the *Bayes Theorem*:

$$P(\theta|X) = \frac{\mathcal{L}(\theta)P(\theta)}{P(X)}, \tag{5.43}$$

where $P(\theta|X)$ is the *posterior* probability for θ, that represents our degree of belief about the values of θ, when we already know the data, X. $P(\theta)$ is the *prior* probability distribution, that represents our degree of belief about the values of θ, ignoring the data. Finally, $P(X)$ is a normalising constant, called *the evidence* or *marginal likelihood*, that ensures that the posterior is normalised to unity:

$$P(X) = \int d\theta \mathcal{L}(\theta)P(\theta). \tag{5.44}$$

In general, the posterior and the likelihood do not coincides. Several methods can be used in order to compute the posterior. In this work, we used the so-called *Markov Chain Monte Carlo* (MCMC) methods, which generate chains having a sample density, in the space of the parameters, that is proportional to the posterior pdf. If the chain is not long enough, the Monte Carlo estimation is not sufficiently accurate, due to the low number of samples, thus the method does not converge. For more details on the MCMC methods, and in general on the Bayesian statistic applied in cosmology, see e.g. Trotta (2017).

5.5.2 Modeling and fitting the BAO in the correlation function

The non-linear matter two-point correlation function, $\xi_{DM}(r)$, can be obtained by Fourier transforming the matter power spectrum, $P_{DM}(k)$, as follows:

$$\xi_{DM}(r) = \frac{1}{2\pi^2} \int dk\, k^2 P_{DM}(k) \frac{\sin(kr)}{kr}. \tag{5.45}$$

In this work we used the so-called *de-wiggled* model, specifically designed to fit the BAO in the matter power spectrum (D. J. Eisenstein, H.-J. Seo, and M. White, 2007):

$$P_{DM}(k) = [P_L(k) - P_{nw}(k)]e^{-k^2\Sigma_{NL}^2/2} + P_{nw}(k), \tag{5.46}$$

where the linear power spectrum, $P_L(k)$, can be computed with a Boltzmann code, and P_{nw} is the power spectrum without the BAO feature (see for further details D. J. Eisenstein and Hu (1998) and Veropalumbo et al., 2016).
A robust theoretical model, that can be used to fit the BAO data in the two-point correlation function of cosmic tracers, is the following:

$$\xi(r) = B^2\xi_{DM}(\alpha r) + A(r), \tag{5.47}$$

where the B^2 factor describes the bias of the cosmic tracers, and the $A(r)$ function can be modelled as follows:

$$A(r) = A_0 + \frac{A_1}{r} + \frac{A_2}{r^2}\,, \tag{5.48}$$

where A_0, A_1,A_2 are nuisance parameters, used to minimize the effects of the unmodelled broadband signal, as the scale-dependent bias and residual geometrical and dynamical distortions (Xu, Padmanabhan, et al., 2012; Anderson, E. Aubourg, et al., 2012; Anderson, É. Aubourg, et al., 2014; Veropalumbo et al., 2016).
We can consider a Gaussian likelihood for this model. From equation (5.38) we have that

$$\mathcal{L}(\alpha, B, A_0, A_1, A_2) \propto \exp(-\chi^2/2). \tag{5.49}$$

In this case, equation (5.39) becomes

$$\chi^2 = \sum_{i=0}^{n}\sum_{j=0}^{n}(\xi_i - \xi_i^m)C_{ij}^{-1}(\xi_j - \xi_j^m), \tag{5.50}$$

where ξ_i and ξ_i^m are the measured two-point correlation function and the model in the i-th bin, respectively, and C_{ij}^{-1} is the inverted covariance matrix. By assuming the priors, we can use the MCMC technique to populate the parameter space, thus getting the posteriors. The main goal is to constrain the α parameter, that represents the isotropic shift of the BAO peak from the expected position, due to an incorrect assumption of the cosmological model. We can define the α parameter as

$$\alpha \equiv \frac{D_V(z)/r_s}{D_{V,f}(z)/r_{s,f}} = \left[\frac{D_A^2(z)}{D_{A,f}^2(z)}\frac{H_f(z)}{H(z)}\right]^{1/3}\frac{r_{s,f}}{r_s}\,, \tag{5.51}$$

where D_V is defined in equation (5.6). $\alpha = 1$ means that the fiducial cosmological model coincides with the true one. On the contrary, if $\alpha \neq 1$, the acoustic scale of the assumed model is incorrect, or the distance scale assumed is wrong. In particular, when $\alpha < 1$, the acoustic scale is shifted toward higher scales; on the other hand, when $\alpha > 1$ the sound horizon is shifted toward smaller scales. Several investigations have been performed to test the robustness of this method, using polynomials of different orders, and changing the values of the Σ_{NL} parameter (that enters the model through the non-linear dark matter power spectrum, see equations (5.14) and (5.46)) and the nuisance parameters (H.-J. Seo, Eckel, et al., 2010). It has been demonstrated, in particular, that the nuisance parameters do not impact significantly the constraints on

the α parameter.
From equation (5.6) it is also evident that the two quantities $H(z)$ and $D_A(z)$ are degenerate when cosmological constraints are extracted from $D_V(z)$. The information contained in clustering anisotropies can be exploited to break this degeneracy (Okumura et al., 2008; Chuang and Y. Wang, 2012; Kazin et al., 2012; Sánchez, Kazin, et al., 2013). Anisotropic BAO analyses apply implicitly the *Alcock-Paczynski* test, discussed in section 3.5.3, exploiting the difference between line-of-sight and transverse scales. The two-dimensional correlation function, $\xi(\mu, s)$, is the simplest statistics that can be used to extract information from clustering anisotropies (see section 3.6). However, the expected signal-to-noise ratio of $\xi(\mu, s)$ at large scales is low, even for large-volume surveys, and, in addition, the covariance matrix is hard to be computed due to the large number of bins (Okumura et al., 2008; Blake, Kazin, et al., 2011; Sánchez, Kazin, et al., 2013). Nevertheless, the information encoded in $\xi(\mu, s)$ can be condensed in one-dimensional projections, which can be measured with high signal-to-noise, and whose covariance matrices are easy to handle. Several statistical methodologies have been developed to extract anisotropic constraints (e.g. Okumura et al., 2008; Padmanabhan and M. White, 2008; Chuang and Y. Wang, 2012; Kazin et al., 2012; Xu, Cuesta, et al., 2013). In particular, Padmanabhan and M. White (2008) proposed to use the multipole expansion of the two-point correlation function in Legendre polynomials. The multipoles, opportunely modelled (see e.g. Xu, Cuesta, et al., 2013), provide an estimate of both radial and transversal components of the α parameter. The isotropic-averaged shift, α (equation (5.51)), in fact, can be decomposed into line-of-sight and transverse components, $\alpha_\parallel$ and $\alpha_\perp$, as follow:

$$\alpha = \alpha_\parallel^{1/3} \alpha_\perp^{2/3}, \tag{5.52}$$

where

$$\alpha_\parallel = \frac{D_M(z) r_{s,f}}{D_{M,f}(z) r_s}, \tag{5.53}$$

$$\alpha_\perp = \frac{H_f(z) r_{s,f}}{H(z) r_s}. \tag{5.54}$$

We can define the anisotropic BAO signal parameter, or anisotropic warping factor, ϵ, as:

$$1 + \epsilon \equiv \left(\frac{\alpha_\parallel}{\alpha_\perp}\right)^{1/3} = \left(\frac{D_{A,f}(z)}{D_A(z)} \frac{H_f(z)}{H(z)}\right)^{1/3}; \tag{5.55}$$

If there are no anisotropies, $\epsilon = 0$.
Combining equations (5.51) and (5.55), and using the value of r_s provided by CMB analysis (section 5.2), it is possible to disentangle $D_A(z)$ and $H(z)$, as follows:

$$\frac{D_A(z)}{r_s} = \frac{\alpha}{1+\epsilon} \frac{D_{A,f}(z)}{r_{s,f}}; \tag{5.56}$$

$$H(z)\, r_s = \frac{1}{\alpha(1+\epsilon)^2} H_f(z) r_{s,f}. \tag{5.57}$$

Alternatively, modeling the full-shape of the clustering wedges (see section 3.6.1), we can obtain the following two parameters, that can break the degeneracy between $D_A(z)$ and $H(z)$ (Kazin et al., 2012; Sánchez, Kazin, et al., 2013):

$$d_\perp \equiv \frac{D_A(z)}{r_s(z_{rec})}, \tag{5.58}$$

$$d_{\parallel} \equiv \frac{cz}{r_s(z_{rec})H(z)}. \tag{5.59}$$

Joining the BAO and CMB constraints, from the equation (1.59) we can obtain constraints on the Dark Energy equation-of-state, defined in the equation (1.51).

5.6 BAO surveys

The galaxy redshift surveys specifically designed for BAO investigations aim at balancing the shot noise and the cosmic variance terms at the wave-numbers where the acoustic oscillations are found, that is $k \approx 0.1 - 0.2h\mathrm{M}pc^{-1}$. These two quantities are directly related to the volume of the survey and the sample density, as showed in equation (3.13). In this section we discuss about the different characteristics of BAO surveys, focusing on the properties of cosmic tracers, sampling density, redshift ranges and accuracy of the measurements. Finally, we present the results obtained by several BAO surveys analyses.

5.6.1 Accuracy of redshift measurements

Larger errors on redshift measurements can compromise the evaluation of cosmological distances (see equation (3.22)), hampering a good evaluation of cosmological distances. This can also impact clustering at large scales, broadening the BAO feature. Photometric redshift surveys can collect data for a large number of galaxies, but are generically affected by large redshift errors (it is not trivial to derive good photometric redshifts). Spectroscopic redshift surveys, on the other hand, are much more accurate, at the expense of larger shot noise uncertainties (H.-J. Seo and D. J. Eisenstein, 2003; H.-J. Seo and D. J. Eisenstein, 2007). The difference between spectroscopic and photometric redshift errors can be very large: for instance, in the SDSS DR7, at redshift range $0.1 < z < 0.7$, the spectroscopic error is $\sigma_{z,sp} \approx 30$ km/s, while the photometric one is $\sigma_{z,ph} = 7000$ km/s. For $\sigma_z \geq 1000$ km/s the BAO peak is totally smeared, and cannot be used to constrain cosmological parameters. It has been calculated that redshift errors below 300 km/s are required to infer reliable constraints from BAO (D. H. Weinberg et al., 2013). Photometric redshift surveys could be a valid alternative at high redshifts, where they can sample large volumes and the accuracy of spectroscopic redshifts is worst. An intermediate approach such as using an instrument with several narrow bands, could be, in some regimes, an interesting solution (Benítez et al., 2009).

5.6.2 Cosmic tracers of the density field

We expand here the discussion of section 3.2, summarising the advantages and disadvantages of using different cosmic tracers for BAO analyses.

- The standard choice is to use galaxies as tracers. For instance, luminous red galaxies have been preferentially used at low redshift (e.g. D. J. Eisenstein, Zehavi, et al., 2005; Padmanabhan, Xu, et al., 2012). They have a high surface brightness, that allows trivial spectroscopy measurements, and a strong bias, $b \approx 2$. Moreover, it is relatively simply to select them using photometry (D. J. Eisenstein, Annis, et al., 2001). At $z \geq 1$, blue galaxies are better tracers. Indeed, red galaxies are fainter than the blue galaxies in the optical band, because of the

K correction (Glazebrook and Blake, 2005). Star forming galaxies, furthermore, can be selected exploiting their emission lines.

- Clusters of galaxies can also be used as tracers of the matter density field (Angulo et al., 2005; Hütsi, 2010). In fact, clusters surveys are subsamples of galaxy surveys, obtained by selecting only the brightest cluster galaxies (BCG). Thus, the shot noise errors are larger in cluster correlation function measurements, but this is well balanced by the higher bias, which enhances the clustering signal. In fact, it can be shown that the accuracy of the BAO detection is higher with respect to what can be obtained with galaxy samples of comparable number of objects (Veropalumbo et al., 2014; Veropalumbo et al., 2016). Galaxy clusters are almost insensitive to non-linear dynamical distortions at small scales. This reflects in a sharp, quasi-linear BAO peak; the reconstruction technique, thus, is expected to be less effective for this type of tracers. Moreover, galaxy clusters are detectable in a wide wavelength range, from radio to X-ray. As a consequence, several methods, that exploit different astrophysical processes, allow to measure the main properties of these objects, such as mass, temperature, and density profile. This information can be used to estimate the bias, since there is a tight correlation between cluster and CDM halo mass functions (for further details, see Tinker et al., 2010). As discussed in section 2.3.3, in the Bottom-Up scenario, small objects form at first. Since galaxy clusters are the largest collapsed structures in the present Universe, they are also the youngest. This means that we can observe these objects only at small redshifts, avoiding deep surveys.

- Active galaxy nuclei (AGN) have been used as large-scale structure tracers since many years (Sawangwit et al., 2012). Also AGN surveys can be considered as subsamples of galaxy surveys. AGN can be easily distinguished from normal galaxies, thanks to their particular spectra. Their clustering at small scales can be modelled by a power-law with a slope $\gamma \approx 1.8$, as for normal galaxies. Similarly to the cluster case, the reduced number of AGN is compensated by the high bias of these objects, which provides a strong clustering signal. Because of their high luminosity and easy selection, they are particularly indicated for wide-field surveys, at high redshifts.

- The Lyα forest is another interesting cosmic density tracer. It is a series of narrow lines, due to Lyα resonance absorption in hydrogen clouds, spread in wavelength because of the cosmological redshift, and observable in high-redshift quasar spectra. With the Lyα forest, it is possible to study three-dimensionally the BAO feature in the distribution of neutral hydrogen, even in a relatively object-poor sample of AGN. In fact, each spectrum provides hundreds of density measurements, in multiple line-of-sights, rather than just a single one (McDonald and D. J. Eisenstein, 2007; M. L. Norman et al., 2009; McQuinn and M. White, 2011). First detections of the BAO feature at high redshifts ($2 < z < 3.5$) have been already preformed (Busca et al., 2013; Slosar et al., 2013; Delubac et al., 2015).

- It is also possible to trace the large-scale structures with 21 cm intensity mapping (Peterson et al., 2006; Ansari et al., 2008; Chang et al., 2008; Wyithe et al., 2008; H.-J. Seo, Dodelson, et al., 2010). This technique does not sample the single

galaxies, but it measures the combined 21 cm emission of all the galaxies in a given region. The BAO information is contained in the large-scale density field, but it is hard to extract it because the signal is order-of-magnitudes weaker than the galactic and extragalactic backgrounds. Nevertheless, techniques such as cross-correlation between intensity maps and galaxy surveys can help to remove the foreground extra-signal, leaving the background intact. Furthermore, the reconstruction technique can enhance the signal, improving in principle the accuracy of $H(z)$ by $10 - 40\%$ (H.-J. Seo and Hirata, 2016).

- Finally, cosmic voids, that trace the minima of the density field, can be used for BAO analysis (Liang et al., 2016). Kitaura et al. (2016), for the first time, performed a $> 3\sigma$ detection of the BAO with cosmic voids. Their claim is that the isotropy of these expanding regions, joined to the absence of a strong gravitational pull ("void centers represent the most quiet places in the Universe"), can reduce the effect of non-linear evolution, avoiding the need of techniques such as the reconstruction. Further studies are necessary to demonstrate this claim.

5.6.3 State-of-the-art and future perspective

The actual largest cosmological survey, the Baryon Oscillation Spectroscopic Survey (BOSS, K. S. Dawson, Schlegel, et al., 2013), that is part of the SDSS III (D. J. Eisenstein, D. H. Weinberg, et al., 2011), provides a catalogue of 1.2 million massive galaxies in a volume of 18.7 Gpc^3. Usually, this survey is split in a low-redshift sample, LOWZ ($0.12 < z < 0.43$), and a high-redshift sample, CMASS ($0.43 < z < 0.70$). Several clustering analyses have been performed on this survey, achieving the aim of performing a 1% distant measurement. Figures (5.11) and (5.12) show the anisotropic clustering measurements, performed by Vargas-Magaña et al. (2016), superimposed to the mean values over 1000 BOSS mock samples. In this work, the survey has been divided in three redshift bins, partially overlapping, at mean redshifts of 0.38, 0.51, and 0.61. In particular, Figure (5.11) shows the first three galaxy multipoles, making a comparison before and after the reconstruction technique has been applied. While the hexadecapole has a mean value of zero at large scales, in spite of low signal-to-noise ratio, the pre-reconstruction quadrupole is negative. We can notice how the post-reconstruction quadrupole is significantly closer to zero, meaning that such a technique has partially removed the non-linear anisotropies in the correlation function. Figure (5.12) shows the clustering wedges, in the same redshift bins, both before and after the reconstruction. In this case, the reconstruction method clearly enhances the large-scale signal in $\xi_{\parallel}(r)$, while the clustering level of $\xi_{\perp}(r)$ is significantly lower after the reconstruction. In both the cases, however, after the reconstruction the BAO peak is sharper. Furthermore, Vargas-Magaña et al. (2016) performed an analysis of both statistical and systematic errors. They found that, in this analysis, systematics are significantly lower than statistical errors: the results of this work, obtained by only the BAO analysis, are reported in Table (5.1).

Veropalumbo et al. (2016) selected a number of 12910, 42215 and 11816 galaxy clusters, at median redshift $z = 0.2$, $z = 0.3$, $z = 0.5$, respectively, from the BOSS survey and the SDSS DR7 (Abazajian et al., 2009). Figure (5.13) shows the measured cluster angle-averaged correlation functions, with its best-fit model. As expected, despite of using the largest ever spectroscopic sample of galaxy clusters, the constraints on distance scales are not comparable with the BOSS galaxy ones. However, at all the

z	$D_V(z)(r_{s,f}/r_s)$ (Mpc)	$H(z)(r_s/r_{s,f})$ $(Km\,s^{-1}\,Mpc^{-1})$	$D_A(z)(r_{s,f}/r_s)$ (Mpc)
0.38	$1475 \pm 14 \pm 3$	$80.5 \pm 2.2 \pm 0.5$	$1092 \pm 16 \pm 4$
0.51	$1872 \pm 16 \pm 4$	$90.9 \pm 2.1 \pm 0.6$	$1308 \pm 18 \pm 5$
0.61	$2131 \pm 20 \pm 4$	$99.1 \pm 2.5 \pm 0.6$	$1423 \pm 23 \pm 5$
z	$D_M(z)(r_{s,f}/r_s)$ (Mpc)	α	ϵ
0.38	$1507 \pm 22 \pm 6$	0.9995 ± 0.0098	0.0152 ± 0.0125
0.51	$1975 \pm 27 \pm 8$	0.9928 ± 0.0084	-0.0036 ± 0.0107
0.61	$2291 \pm 37 \pm 8$	0.9820 ± 0.0091	-0.0109 ± 0.0125

Table 5.1: Results of the BAO analysis of the clustering measurements from the BOSS galaxy survey (Vargas-Magaña et al., 2016). The contribution of the systematic errors to the total budget is explicit, as $x \pm \sigma_{stat} \pm \sigma_{sys}$, where σ_{stat} are the statistical errors and σ_{sys} are the systematics. We can notice that the systematics are significantly lower than the statistical errors. The total error is then computed with summing the two contributes in quadrature, $\sigma^2_{tot} = \sigma^2_{stat} + \sigma^2_{sys}$. The α and ϵ parameters are quoted with their systematics errors.

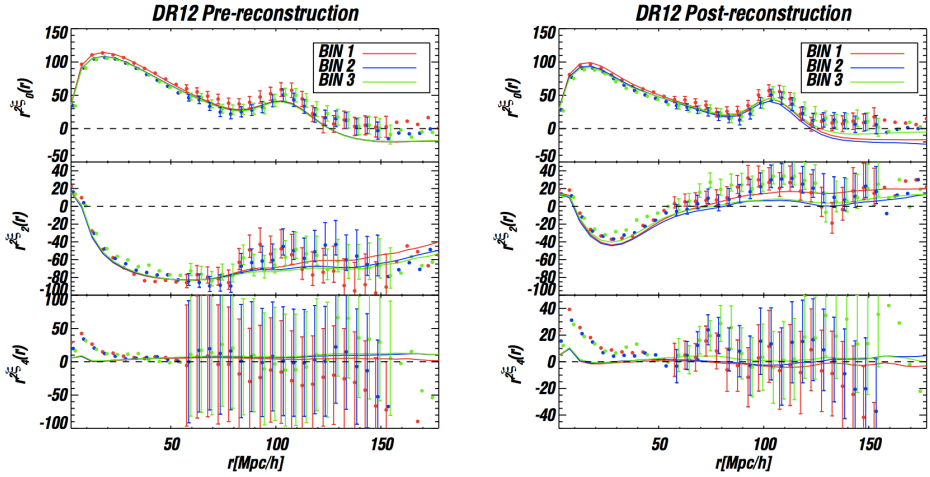

Figure 5.11: Correlation function multipoles, from the BOSS galaxy survey, before and after the reconstruction (left and right panels, respectively). The top panels show the monopoles, the middle panels the quadrupoles, the bottom panels the hexadecapoles. The points with the error bars are the data measurements, while the lines represent the mean values computed with 1000 BOSS mock samples. The colours are referred to different redshift bins: $0.2 < z < 0.5$ (red), $0.4 < z < 0.6$ (blue), $0.5 < z < 0.75$(green). Figure from Vargas-Magaña et al. (2016).

redshift bins considered, the BAO peak has been detected at significance larger than 2σ. Thanks to this, they could infer a 3% angle-averaged distance, $D_V(z)$, at redshift $z = 0.3$ and $z = 0.5$, while at $z = 0.2$ the accuracy is 6%.

Kitaura et al. (2016) used the BOSS survey to unveil a 3.2σ accuracy BAO detection from the cosmic voids, shown in Figure (5.14), inferring a 2.2% distance measurement.

Delubac et al. (2015) detected the BAO feature, with a 5σ significance, in the Lyα

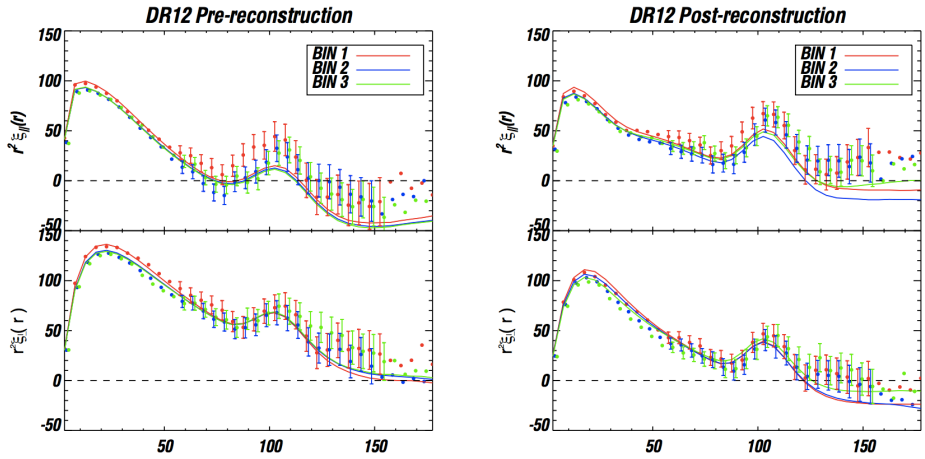

Figure 5.12: Clustering wedges, from the BOSS galaxy survey, before and after the reconstruction (left and right panels, respectively). The top panels show $r^2\xi_{\parallel}(r)$, while the bottom panels $r^2\xi_{\perp}(r)$. The points with the error bars are the data measurements, while the lines the mean values computed with 1000 BOSS mock samples. The colours are referred to different redshift bins: $0.2 < z < 0.5$ (red), $0.4 < z < 0.6$ (blue), $0.5 < z < 0.75$(green). Figure from Vargas-Magaña et al. (2016).

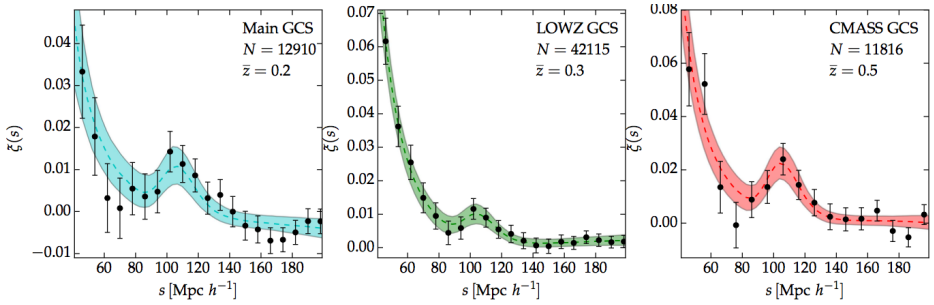

Figure 5.13: Angle-averaged correlation functions from spectroscopic cluster samples, obtained joining BOSS and SDSS DR7 catalogues of BCG. In each panel, the legend show the number of objects and the median redshift. The dashed lines are the best-fit models, while the shaded areas represent the 68% posterior uncertainties provided by the MCMC analysis (see section 5.5.1). Figure from Veropalumbo et al. (2016).

forest flux-correlation function of 137562 quasars, in the redshift range $2.1 < z < 3.5$, from the BOSS survey. Figure (5.15) shows the correlation functions measured in three different angular regions. From this clustering analysis, they obtained a 3% D_A/r_s measurement, and a 5.8% precision on D_H/r_s. Figure (5.16) shows clustering results from Lyα Forest data that have been used to constrain some main cosmological parameters of the $o\Lambda CDM$ model [2]. The combination of galaxy and Lyα forest data yields a marginalised constraint of $\Omega_\Lambda = 0.73^{+0.25}_{-0.68}$, at 99.9% confidence, implying a detection of the Dark Energy with an accuracy higher than 3σ, from BAO analysis

[2]this model assumes that the Dark Energy is a cosmological constant, but allows $\Omega_\Lambda = 0$ and an arbitrary Ω_T.

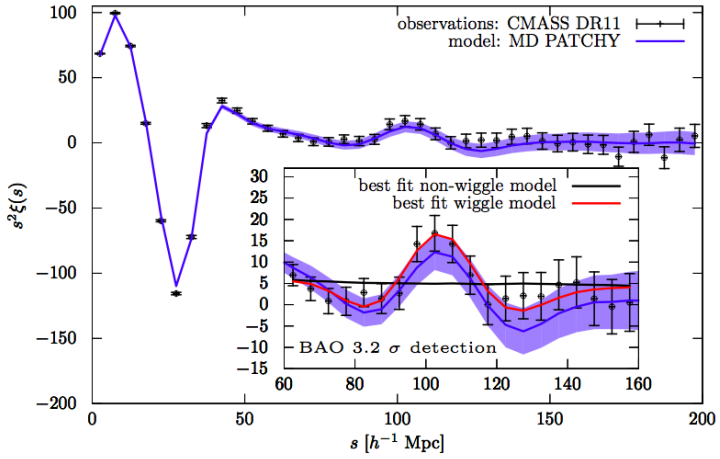

Figure 5.14: Angle-averaged correlation function from voids, using the BOSS luminous red galaxy sample. The black points with error bars are the data, the blue solid line and the blue shaded area are the mean, and the 1σ region, respectively, of 1000 mock voids catalogues. The inset shows the best-fit models, considering the BAO feature ("wiggle", red) or not ("non-wiggle", black), to estimate the significance of the BAO detection. Figure from Kitaura et al. (2016).

alone. Since the CMB provides the same acoustic scale, it works as a BAO experiment at higher redshift. Thus combining CMB and BAO the constraints are much tighter: $\Omega_\Lambda = 0.72^{+0.030}_{-0.034}$, at 68% confidence, implying a 20σ Dark Energy detection (É. Aubourg et al., 2015).

Alam et al. (2016) combined different BOSS analysis tools, including BAO, Alcock-Paczynski test and RSD distortions, in both configuration and Fourier spaces, with different statistics such as multipoles or clustering wedges, and various tracers, as Lyα Forest and galaxies. Figure (5.17) shows the two-point correlation function, $\xi(s_\parallel, s_\perp)$, as measured in the redshift space, compared to $\xi(\mu, s)$ obtained from an ensemble of BOSS mock catalogues (Sánchez, Kazin, et al., 2013). $\xi(s_\parallel, s_\perp)$ contains both the geometrical and dynamical distortions, which hold most of the anisotropic information used to disentangle $D_M(z)/r_s$, $H(z)r_s$ and $f\sigma_8$.

Figure (5.18) shows the post-reconstructions multipoles in both the power spectrum and the correlation function, in three different redshift bins: $0.2 < z < 0.5$, $0.4 < z < 0.6$, $0.5 < z < 0.75$. In particular, the top panels show the monopoles, the middle panels the quadrupoles, and the bottom panels the BAO rings, in the redshift range $0.4 < z < 0.6$, as reconstructed from the monopoles and the quadrupoles, thus filtering all the higher-order multipoles. Decomposing the radial and transversal components, it is displayed $x(p, \mu) = x_0(p) + L_2(\mu)x_2(p)$, where x represents either s^2 multiplied by the correlation function or $(P_l - P_{l,smooth})/P_{0,smooth}(k)$, where the subscript "smooth" denotes the best-fit model with no BAO feature. The parameter p represents either the separation, s, or the Fourier mode, k; L_2 is the second-order Legendre polynomial, $p_\parallel = \mu p$ and $p_\perp = \sqrt{p^2 - \mu^2 p^2}$. Such a display represents the angle-averaged BAO measurement, and the accuracy of the circular shapes of the BAO rings gives a measure of the geometrical distortions.

Figure (5.19) shows the constraints on $D_M(z)(r_{s,f}/r_s)$, $H(z)(r_s/r_{s,f})$, and $f(z)\sigma_8(z)$ clustering measurements, obtained by modelling the BAO and RSD in both correlation

function and power spectrum, in comparison with the Planck ΛCDM model. In this figure are also shown the constraints obtained by compressing the different cosmological information, provided by the anisotropic BAO and RSD investigations, into a unique set of parameters, through a brand new technique called *consensus* (for further details see Sánchez, Grieb, et al., 2017). The consensus constraints are $\approx 10 - 20\%$ tighter than the most accurate measurement from the original set.

Figure (5.20) shows the so-called "Hubble diagram", which displays three different distance measures, D_V/r_s, D_A/r_s, and D_H/r_s, where $D_H \equiv c/H(z)$, showing how these quantities converge at low redshifts. All the measurements are obtained from BAO surveys, such as the BOSS, the 6dF Galaxy Survey (Jones et al., 2004), at mean redshift of $z \approx 0.15$, the SDSS-II DR7 (W. J. Percival et al., 2010), whose clustering analysis provided a 2.7% D_V/r_s at $z = 0.275$ measurement, and the WiggleZ survey (Blake, Kazin, et al., 2011), in which a 4.9σ BAO detection at mean redshift $z = 0.6$ provided a 4.5% accurate measurement of the A parameter (see equation (5.9)). All these measurements are in agreement with the ΛCDM model predictions, over plotted in the figure.

In Table (5.2) are shown some of the final constraints on the main cosmological parameters obtained from the clustering analysis of the BOSS survey, combined with the data from the *Planck* Satellite CMB temperature power spectra (Alam et al., 2016)
.

H_0 $(Km\,s^{-1}\,Mpc^{-1})$	Ω_k	Ω_m	w
67.6 ± 0.5	0.0003 ± 0.0026	0.311 ± 0.006	-1.01 ± 0.06

Table 5.2: Constraints on four main cosmological parameters from the clustering analysis of the BOSS survey, combined with the data from the *Planck* Satellite CMB temperature power spectra (Alam et al., 2016).

The sensitivity of the BAO to the Dark Energy starts to decline at redshift $z \approx 3.5$. Sampling a sufficient fraction of the entire comoving volume over such redshift, with high sampling density, will ensure that the sample variance dominates over the shot noise. Sampling at the same redshift, with the same methods, different sky regions is thus not redundant. Since just a few percent of the sky, mainly at low redshift, has been covered until now, the BAO surveys have a great possibility of growth.
An on-going survey is the eBOSS (extended Baryon Oscillations Spectroscopic Survey, K. S. Dawson, Kneib, et al., 2016), which is sampling massive galaxies at redshifts $0.6 < z < 2.2$, providing Lyα forest measurements at redshift $z > 2.1$.
Future projects are the Hobby-Eberly Telescope Dark Energy Experiment (HETDEX, Hill and HETDEX Consortium, 2016), which plans to survey 800000 Lyα emission-line galaxies at redshifts $1.8 < z < 3.7$, with a large set of integral-field spectrographs; the Dark Energy Spectroscopic Instrument (DESI, Levi et al., 2013), which will survey 4 million red galaxies and 3 million quasars, creating three-dimensional galaxy maps at $z < 2$ and Lyα forest at $z > 2$; J-PAS (Benitez et al., 2014), that will measure $0.003(1 + z)$ photometric redshifts for 9×10^7 galaxies, 7×10^5 galaxy clusters and groups, plus several million AGN, in a effective volume of 14 Gpc^3 up to $z = 1.3$. the

ESA space mission *Euclid* (Laureijs et al., 2011), that will be composed by a wide and two deep surveys, providing both spectroscopic and photometric measurements. The wide survey will cover an area of 14000 deg^2 up to $z < 2.$, while the two deep fields will cover each one a 20 deg^2 area. In particular, Euclid will combine weak lensing and BAO analyses to improve the constraints on cosmological parameters. For the BAO analysis, Euclid will use a slitless spectrometer, that will detect million of Hα emission line galaxies in the near-infrared band, providing a redshift accuracy of $dz/(1+z) = 0.001$ (Cimatti et al., 2009).
There are many near-future experiments with the aim of detecting the BAO in 21 cm intensity maps, such as the Baryon Acoustic Oscillations Broadband and Broad-beam Array (BAOBAB, Pober et al., 2013), the Canadian Hydrogen Intensity Mapping Experiment (CHIME, Bandura et al., 2014) and the Hydrogen Intensity and Real-time Analysis eXperiment (HIRAX, Newburgh et al., 2016).
To approach the limit of the cosmic variance at $z > 1$, it requires $\approx 10^8$ galaxies. Next-generation interferometers, such as the Square Kilometer Array, should be capable to detect the 21 cm line of the neutral hydrogen in emission-line galaxies. Such interferometers could in principle sample spectroscopically 10^9 galaxies in the redshift range $z = 2 - 3$ (Abdalla and Rawlings, 2005), reaching the sample variance limit over half of the sky, thus probably being the most valuable BAO experiment in the very next future.

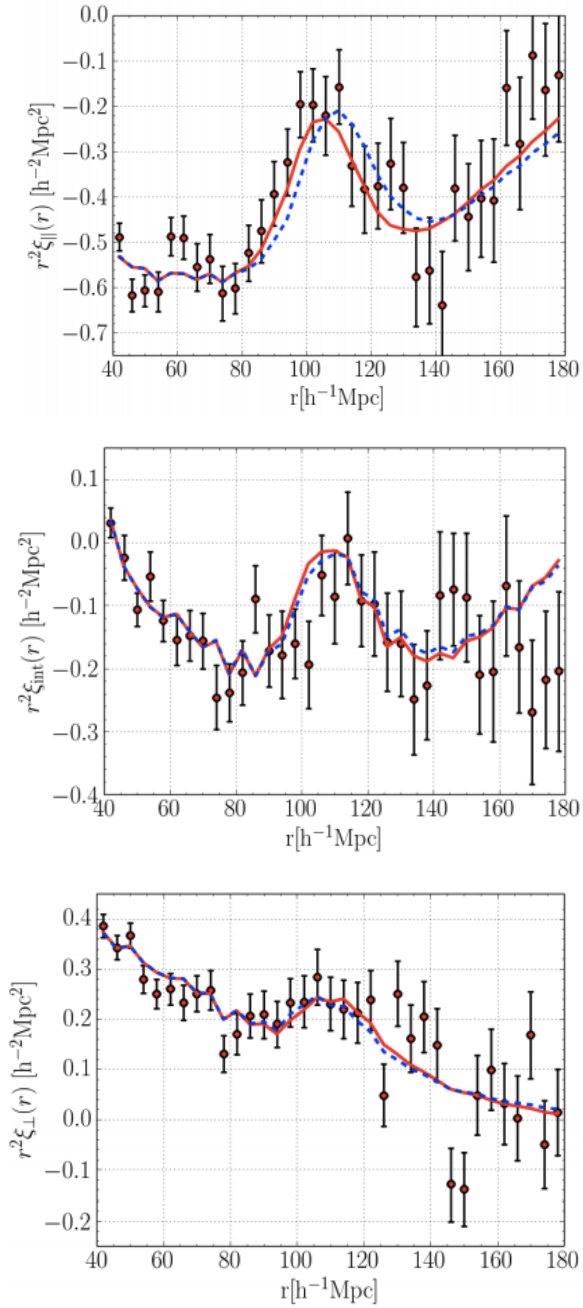

Figure 5.15: Lyα forest flux-correlation functions from a BOSS quasar catalogue, in the redshift range $2.1 < z < 3.5$. The measurements are in three different angular regions: $\mu > 0.8$ (top panel), $0.8 > \mu > 0.5$ (middle panel) and $0.5 > \mu > 0$, where μ is the central value of $r_{\parallel}/\sqrt{r_{\parallel}^2 + r_{\perp}^2}$ in each $(r_{\parallel}, r_{\perp})$ bin (bottom panel). The solid line is the best fit, while the dashed curve is the best fit keeping both the $\alpha_{\perp}$ and $\alpha_{\parallel}$ parameters (see section 5.5.2, equations (5.53) and (5.54)) set to the unity. Figure from Delubac et al. (2015).

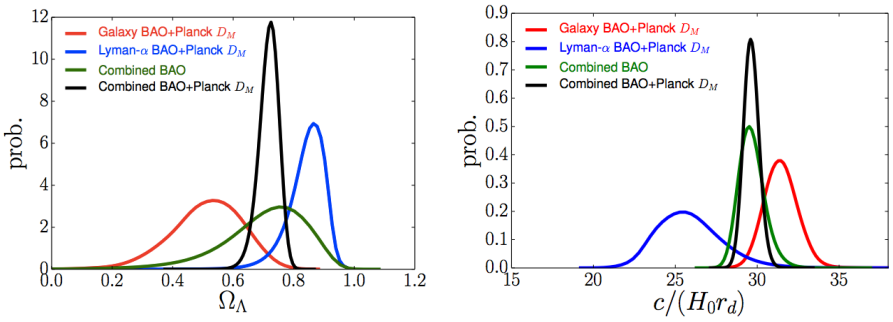

Figure 5.16: Constraints on Ω_Λ (left panel) and $c/(H_0 r_s)$ (right panel) in the $o\Lambda CDM$ model. Green curves show the combined constraints from galaxy and Lyα Forest BAO analysis. Black curves include also the measurement of $D_M(z = 1090)/r_s$ from the CMB acoustic scale, with no assumption on the value of r_s, except that is the same scale as the BAO. Blue and red curves represent the result of combining the CMB with Lyα Forest and galaxies, respectively. Figure from É. Aubourg et al. (2015).

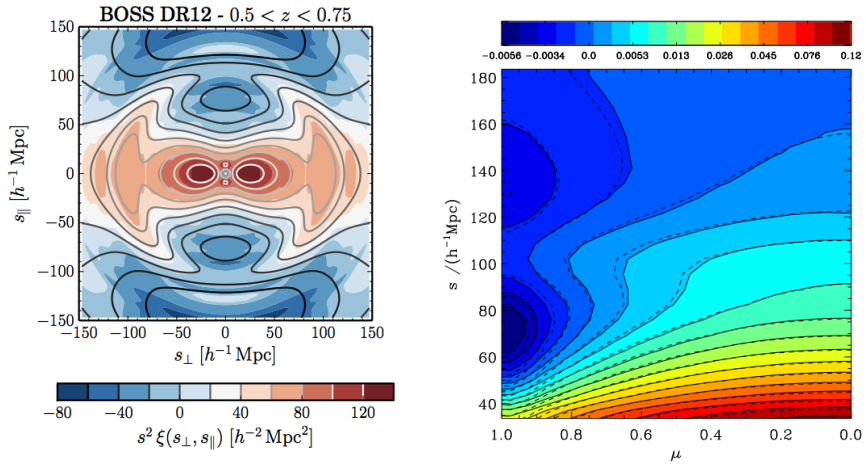

Figure 5.17: Left panel: unreconstructed $\xi(s_\parallel, s_\perp)$, measured from the BOSS galaxy survey, at redshifts $0.5 < z < 0.75$ (Alam et al., 2016). The color scale shows the data and the contours show the prediction of the best-fit model. The RSD shrink the iso-curves in the line-of-sight direction, and also the BAO ring, clearly visible. Right panel: $\xi(s, \mu)$ from an ensemble of BOSS mock catalogues (Sánchez, Kazin, et al., 2013). The solid contours lines follow the color scheme, while the dashed contour lines represent the multipoles expansion. The contours line are not horizontal, i.e. there is not isotropic clustering, due to RSD. The BAO feature can be noticed at $s \approx 110 h^{-1}$ Mpc.

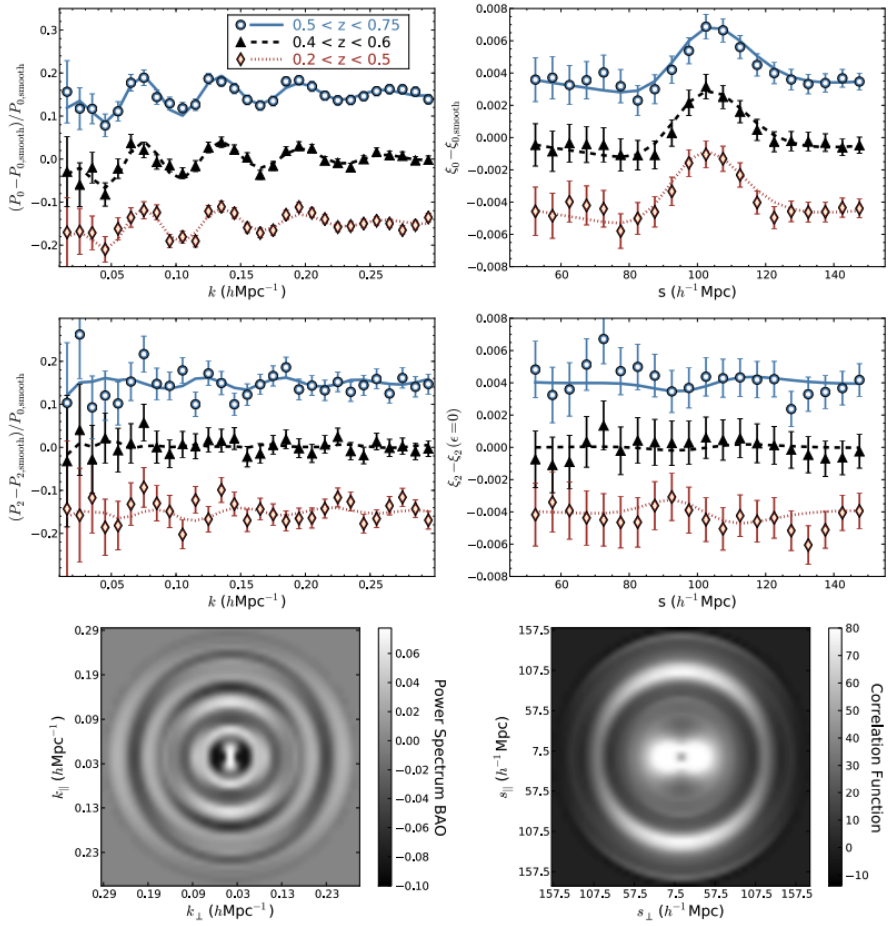

Figure 5.18: BAO signal in Fourier (left panels) and configuration (right panels) space. The top panels show the monopoles, data (points) and best-fit BAO models (curves), in three different redshift bins: $0.2 < z < 0.5$ (red diamonds), $0.4 < z < 0.6$ (black triangles), $0.5 < z < 0.75$ (blue circles), as shown in the legend. The power spectrum is visualised as $(P_0 - P_{0,smooth})/P_{0,smooth}$, while the correlation function $\xi_0 - \xi_{0,smooth}$, where the subscript "smooth" denotes the best-fit model with no BAO feature. For clarity, there is an offset between the data at the highest and lowest redshifts, of ± 0.15 in the power spectra and ± 0.004 in the correlation functions. The middle panels show the quadrupoles, displayed as $(P_2 - P_{2,smooth})/P_{2,smooth}$ in the power spectrum and $\xi_2 - \xi_2(\epsilon = 0)$. If the reconstruction was perfect, and the fiducial model corrected, both the curves and the points would be flat. The bottom panels show the measurements in the redshift range $0.4 < z < 0.6$ decomposed in the radial and transversal components. It is displayed $x(p, \mu) = x_0(p) + L_2(\mu)x_2(p)$, where x represents either s^2 multiplied by the correlation function or $(P_l - P_{l,smooth})/P_{0,smooth}(k)$. The parameter p represents either the separation, s, or the Fourier mode, k; L_2 is the second-order Legendre polynomial, $p_\parallel = \mu p$ and $p_\perp = \sqrt{p^2 - \mu^2 p^2}$. Figure from Alam et al. (2016).

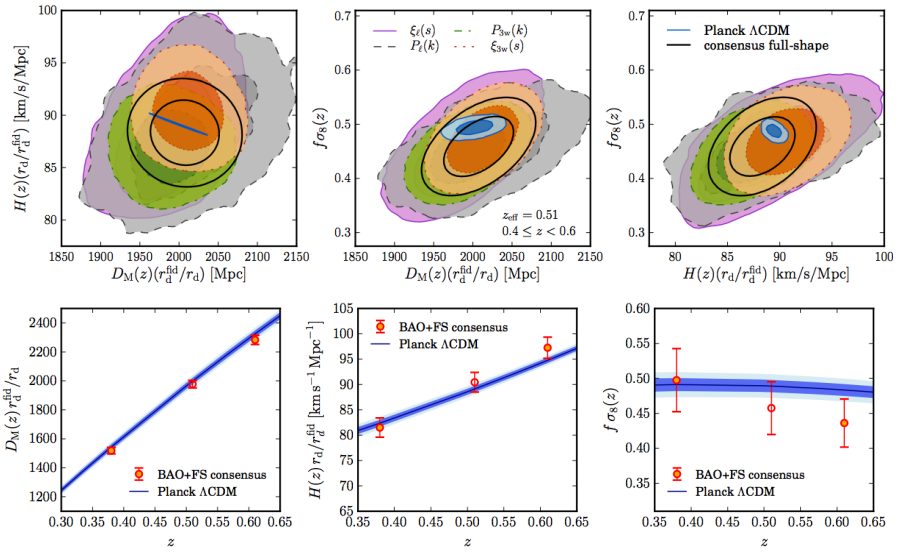

Figure 5.19: Top panels: two-dimensional 68% and 95% marginalized constraints on $D_M(z)(r_{s,f}/r_s)$, $H(z)(r_s/r_{s,f})$, and $f(z)\sigma_8(z)$, at middle redshift, in the BOSS survey. The blue solid contour lines represent the fiducial Planck ΛCDM model, while the black solid lines represent the consensus of the parameters. Bottom panels: the data points are the final consensus of the parameters, overplotted on the Planck ΛCDM model (blu line) as a function of the redshift. The results of the BOSS analysis are in good agreement with the fiducial Planck ΛCDM model. Figure from Alam et al. (2016).

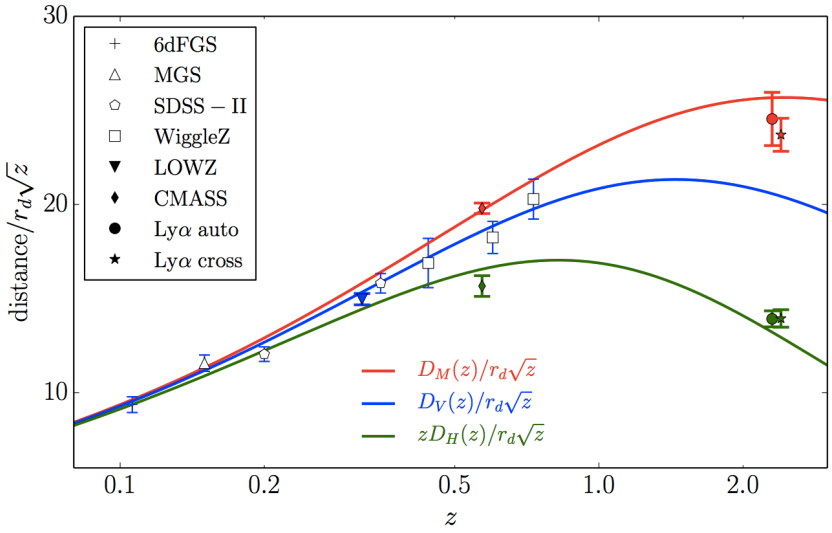

Figure 5.20: The "BAO Hubble diagram", from É. Aubourg et al., 2015. All the data points are BAO measurements of D_V/r_s (blue), D_M/r_s (red), and zD_H/r_s (green), where $D_H \equiv c/H(z)$. The sources of the measurements are showed in the legend; the filled points represents the BOSS data. The lines are the prediction of the fiducial Planck ΛCDM model. The $\sqrt{z}$ factor scaling factor is just for plot necessity.

Chapter 6

BAO analysis of Magneticum simulations

"Behind every man now alive stand 30 ghosts,
for that is the ratio by which the dead outnumber the living."

Arthur C. Clarke, 2001: A Space Odyssey (1968)

Nowadays, the reconstruction is a standard technique in clustering analysis. Future BAO surveys are specifically designed to take into account the potential improvements given by this method. Reconstruction is expected to be more effective at low redshifts, where non-linear evolution strongly affects the clustering of objects. Nevertheless, since previous works focused mainly on reconstructing the density field of specific galaxy surveys, we lack a general evaluation of the reconstruction performances in different regimes. This thesis aims at estimating the impact of the reconstruction method on the constraints of cosmological parameters, inferred through BAO analyses at different redshifts. Moreover, we want to investigate how the reconstruction efficiency varies for different cosmic tracers. So far, no one applied the reconstruction method on density fields traced by galaxy clusters. Thus, it is not clear whether the reconstruction can improve the accuracy of BAO from galaxy clusters or not. We investigate this, furthermore quantifying the gain obtained by the reconstruction at different redshifts, trying to constrain the limits beyond which this technique is not effective. To do this, we have performed a clustering analysis on the Magneticum simulations, a set of cosmological hydrodynamical simulations described in the next section. In particular, we have analysed the angle-averaged two-point correlation function of galaxy, galaxy cluster and AGN mocks catalogues, at the following redshifts: $z = 0.2$, $z = 0.52$, $z = 0.72$, $z = 1$, $z = 1.5$, $z = 2$.
The adopted procedure, exposed in details in this chapter, is schematically reported here:

- since the cosmological simulations provide real-space catalogues, we have turned our mock samples in redshift space, to simulate realistic observations;

- we have computed the angle averaged two-point correlation function, repeating the measurement at all the redshifts considered, for the different cosmic tracers;

- by computing and modelling the projected correlation function, we have estimated the bias of the tracers;
- we have implemented and tested a reconstruction code, and used it to "shift" the original catalogues, in order to restore the linear density field;
- after the reconstruction has been applied, we have re-computed the angle-averaged two-point correlation function;
- we have modelled the two-point correlation function both before and after the application of the reconstruction method, to estimate the differences on the constraints of the inferred best-fit model parameters.

6.1 Magneticum Simulations

The Magneticum simulations[1] (Dolag et al., in preparation), are a set of hydrodynamical simulations over different cosmological volumes, characterised by an excellent spatial resolution. They are based on the P-GADGET3 code (V. Springel, 2005), which solves the gravitational forces with an hybrid approach between HT and PM methods (i.e. the TREE-PM method), while the hydrodynamical part is implemented with an entropy-conserving formulation of a SPH formalism (see V. Springel and L. Hernquist, 2002). The adopted cosmological model is a flat ΛCDM scenario, with the parameters chosen to match the seven-year Wilkinson Microwave Anisotropy Probe (WMAP7, Komatsu et al., 2011) and reported in Table (6.1).

H_0 $(km\,s^{-1}\,Mpc^{-1})$	$\Omega_{0,m}$	$\Omega_{0,b}$	$\sigma_{0,8}$
70.4	0.272	0.0456	0.809

Table 6.1: Cosmological parameters of Magneticum simulations, within a ΛCDM Universe (from Komatsu et al., 2011).

The simulations cover a volume with periodic boundary conditions, initially filled with an equal number of CDM and baryon particles, which satisfy the relation

$$\frac{m_b}{m_{DM}} = \frac{\Omega_b}{\Omega_{DM}}. \tag{6.1}$$

In this way the different abundances of the two components are correctly taken into account, despite their number is the same.
The low viscosity of SPH codes helps to properly track turbulences (Dolag, Vazza, et al., 2005), and it also allows to treat radiative cooling, heating from a uniform time-independent background and star formation with the associated feedback. Radiative cooling rates are implemented following Wiersma et al. (2009), while the CMB and the X-ray background are taken into account following Haardt and Madau (2001). The contribute to the cooling from eleven elements (H, He, C, N, O, Ne, Mg, Si, S, Ca, Fe) have been pre-computed using the CLOUDY photoionization code (Ferland et al., 1998), within an optically thin gas in photoionization equilibrium.

[1] http://magneticum.org/index.html

The star formation model describes a multiphase structure (V. Springel and L. Hernquist, 2003); in particular, the intra-stellar medium (ISM) is considered as a two-phases medium. Cold clouds, formed from the cooling of hot gas, that are above a certain density threshold, are embedded in the hot gas phase, by assuming pressure equilibrium. The Supernovae feedback is also taken into account, by heating the two-phases medium and possibly evaporating the cold clouds. A fraction of 10% of massive stars are assumed to explode as type II Supernovae, each one releasing 10^{51} erg that trigger galactic winds at velocity of $v_{wind} = 350$ km/s, with a mass loading rate proportional to the star formation rate (SFR).
Metals are produced by type II and type Ia supernovae, and by stars in the asymptotic giant branch (AGB) phase, as a function of their lifetime, modeled according to the mass-lifetime function provided by Padovani and Matteucci (1993), following Woosley and Weaver (1995), Van den Hoek and Groenewegen (1997), Thielemann et al. (2003). The assumed initial mass function is from Chabrier (2003).
The black hole growth and AGN feedback are modeled following V. Springel, S. D. White, Jenkins, et al. (2005) and Di Matteo et al. (2005). The black holes are represented as collisionless *sink particles*, within the most massive objects, with an initial mass of 10 $M_{\odot}$. The black holes accrete gas according the Bondi-Hoyle-Lyttleton approximation (Hoyle and Lyttleton, 1939; Hermann Bondi and Hoyle, 1944; HJ Bondi, 1952) :

$$\dot{M}_{BH} = \frac{4\pi G^2 M_{BH}^2 f_{boost} \rho}{c_s^2 + v^2)^{3/2}}, \tag{6.2}$$

where ρ and c_s are the density and the sound speed within the surrounding gas, f_{boost} is a density boost factor, typically $f_{boost} \approx 100$, and v is the velocity of the black hole with respect to the surrounding gas. The radiated bolometric luminosity is

$$L_{bol} = \epsilon_r \dot{M}_{BH} c^2, \tag{6.3}$$

where the radiative efficiency, ϵ_r, is fixed to the value of 0.1 for a non-rapidly spinning black hole, according to Shakura and R. A. Sunyaev (1973).
When the simulation runs, CDM and baryon particles interact gravitationally. The self-gravitating CDM haloes are identified with a Friend-of-Friend (FoF) algorithm (see e.g. W. Press and M. Davis, 1982), which recognises the virialised groups which have at least 32 CDM particles within a distance $l < 0.16\bar{l}$, where $\bar{l}$ is the mean distance between particles (Dolag, Borgani, et al., 2009). At each time step, a modified version of the SUBFIND algorithm (V. Springel, S. D. White, Tormen, et al., 2001), identifies the substructures within self-gravitating CDM haloes. The physical properties, obtained from the hydrodynamics of the baryon particles within each substructure, determine the nature of the object: galaxy, AGN or galaxy cluster.
In particular, each substructure has a SFR associated, as a function of its mass, and consequently a number of "star-particles", according to the initial mass function. These particle will be recognized as galaxies. From Magneticum galaxy catalogues we have position, velocity, absolute magnitude in multi-bands, stellar mass and SFR of each galaxy.
AGN are active galaxies, selected according to the bolometric luminosity of their central black holes (see Hirschmann et al., 2014). A paramount quantity to describe the AGN evolution is the accretion rate, usually normalised to the Eddington accretion rate:

$$f_{Ed} \equiv \frac{\dot{M}_{BH}}{\dot{M}_{Ed}}, \tag{6.4}$$

where the Eddington accretion rate, $\dot{M}_{Ed}$, is calculated by balancing the radiation pressure with the gravitational attraction between the black hole and the surrounding gas, assuming a spherically symmetric accretion and a non-spinning black hole.
Galaxy clusters are identified as the matter substructures (both baryon and CDM) within the same virialised FoF halo. The central particle of the group determines the cluster position, while the cluster velocity is the mean velocity of all the particles within the halo. The galaxy cluster properties include also the mass and the temperature at the radius R_{500} (defined as the radius where the density is 500 times the critical density of the Universe) and the X-ray luminosity due to *bremsstrahlung* emission. It is important to notice that, within this *cluster* definition, we are considering not only real galaxy clusters, but also low-mass objects, as galaxy groups or just haloes. This is why we have such a large number of clusters at high redshifts, and we can perform clustering analysis up to $z = 2$, which is impossible with real galaxy-clusters. To consider the real galaxy clusters, we should impose a mass cut, as shown in the next chapter. However, to simplify the discussion, hereafter the word *cluster* will be referred to the Magneticum definition.
For further details on Magneticum simulations, see Marulli, Veropalumbo, Moscardini, et al. (2015) and references therein.

As already mentioned, the Magneticum set includes simulations of different volumes and resolutions (see http://magneticum.org/simulations.html). For this work we use the *Box1* volume, with *mr* resolution, hereafter Box1mr: the properties of this simulation are reported in Table (6.2), while a map of the snapshot at $z = 0$ is shown in Figure (6.1). Finally, Table (6.3) reports the mean properties of the galaxy, AGN and cluster catalogues used in this work, in six different snapshots, at $z = 0.2$, $z = 0.52$, $z = 0.72$, $z = 1$, $z = 1.5$, $z = 2$.

Table 6.2: Main characteristics of the Box1mr Magneticum simulation: cosmological volume, number of particles N, mass m of CDM and gas particles, and softening scales for CDM, gas and stars (ϵ_{CDM}, ϵ_{gas} and $\epsilon_\star$ respectively).

V (Mpc h^{-1})	N	m_{DM} ($M_\odot\, h^{-1}$)	m_{gas} ($M_\odot\, h^{-1}$)
896	$2 \cdot 1526^3$	$1.3 \cdot 10^{10}$	$2.6 \cdot 10^9$
ϵ_{CDM} (kpc h^{-1})	ϵ_{gas} (kpc h^{-1})	$\epsilon_\star$ (kpc h^{-1})	
10	10	5	

6.2 CosmoBolognaLib

For the clustering analysis of the simulation, we have used the CosmoBolognaLib (CBL) (Marulli, Veropalumbo, and Moresco, 2016), a large set of C++ libraries for cosmological computations, which can can be easily included in high-level language

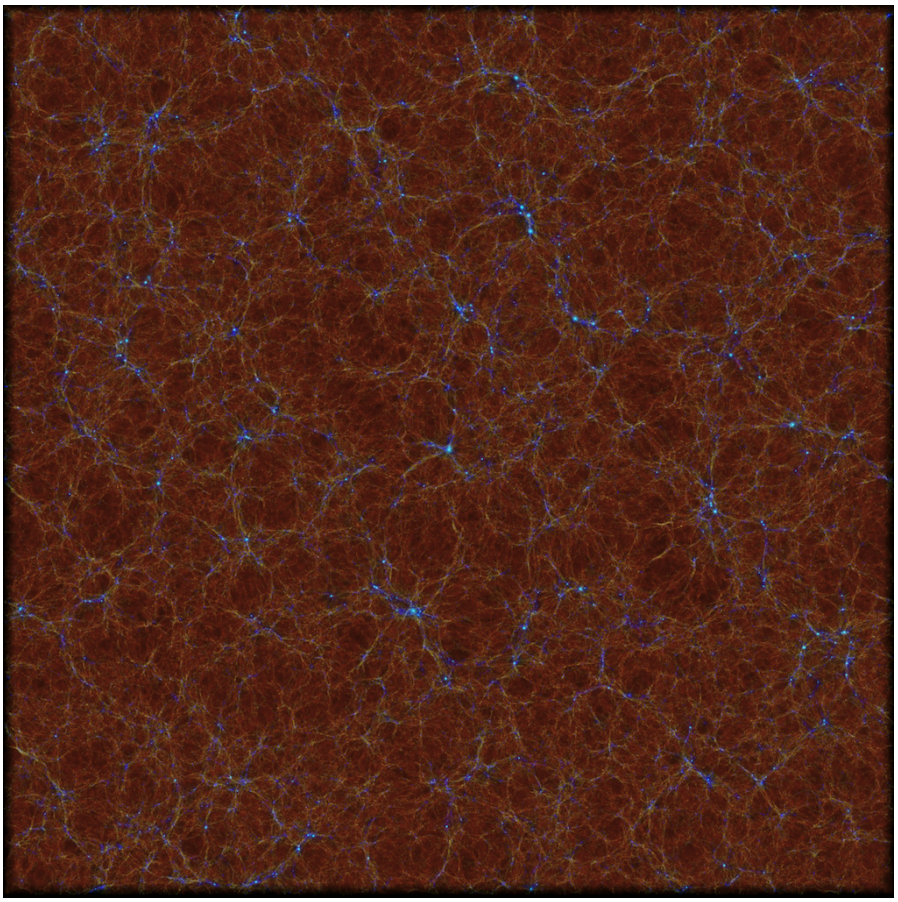

Figure 6.1: Snapshot of the Box1mr, one of the Magneticum simulations, at $z = 0$. The region shown spans a total size of 1300 Mpc, and contains 7×10^9 CDM, gas, star and black hole particles. The galaxies and the stars are colored in white. The gas, which fills the space between the galaxies, is colored according to its temperature, from cold/brown to hot/light blue. Figure from http://magneticum.org/media.html

codes, such as Python. CBL is a living project, fully publicly available [2], especially indicated for cosmological investigations of the large-scale structure. Among the other things, CBL allows to asset a cosmological framework, to handle astronomical catalogues and to measure two-point and three-point statistics in configuration space. Moreover, it is possible to estimate the errors through different covariance matrices and model the two-point correlation function, performing the MCMC likelihood sampling technique. For further details, see Marulli, Veropalumbo, and Moresco (2016).

[2] http://apps.difa.unibo.it/files/people/federico.marulli3/CosmoBolognaLib/Doc/html/index.html

Table 6.3: Mean properties of the catalogues from the Box1mr of Magneticum Simulations, at the redshifts of interest in this work: $z = 0.2$, $z = 0.52$, $z = 0.72$, $z = 1.$, $z = 1.5$, $z = 2$. For galaxy catalogues, we reported the mean stellar mass, $M_\star$, G-band magnitude and SFR. For cluster catalogues, we reported the total mass, M_{500}, the temperature, T_{500}, and the X-ray luminosity, L_{500}, at the r_{500} radius. For AGN catalogues, the mass of the black hole, M_{BH}, its bolometric luminosity, L_{bol}, and the normalised accretion rate, f_{Ed}.

Galaxies	N_{obj} (10^6)	$M_\star$ (10^{10} $M_\odot h^{-1}$)	G	SFR ($M_\odot h^{-1} yr^{-1}$)
z=0.20	3.24	8.9	-21.48	16.24
z=0.52	2.87	7.6	-21.19	21.72
z=0.72	2.60	6.8	-21.04	25.78
z=1.00	2.18	5.7	-20.87	32.77
z=1.50	1.64	4.4	-20.57	42.35
z=2.00	1.12	3.3	-20.27	48.33
Clusters	N_{obj} (10^5)	M_{500} (10^{12} $M_\odot h^{-1}$)	T_{500} (Kev)	L_{500} (10^{42} erg s^{-1})
z=0.20	5.3	8.3	0.239	6.11
z=0.52	4.8	7.2	0.240	7.76
z=0.72	4.3	6.5	0.227	9.52
z=1.00	3.5	5.5	0.226	10.80
z=1.50	2.4	4.4	0.203	13.14
z=2.00	1.4	3.4	0.170	14.33
AGN	N_{obj} (10^5)	M_{BH} (10^8 $M_\odot h^{-1}$)	L_{bol} (10^{45} erg s^{-1})	f_{Ed}
z=0.20	9.5	6.0	0.59	0.03
z=0.52	6.9	6.7	1.13	0.05
z=0.72	5.6	6.9	1.26	0.06
z=1.00	3.6	8.2	2.80	0.10
z=1.50	2.0	8.9	9.26	0.21
z=2.00	0.9	8.1	16.34	0.25

6.3 Reconstruction Algorithm

We have implemented a reconstruction algorithm in the CBL, that uses the Fast Fourier Transform method (FTT) to solve the displacement field in redshift space, as discussed in section 5.4.1. Such an algorithm is composed by the following steps:

- take in input the data and random catalogues;
- if the input catalogues are in redshift space, transform them in real-space, assuming a fiducial cosmological model, through equation (3.22);
- create a three-dimensional grid, computing the number of objects in each grid cell of a given size r_{cell}, by using the particle-in-cell method;
- compute the density field converting the grid in Fourier space, using the FFT;

$$\delta(\mathbf{k}) = \mathrm{FTT}[\mathrm{grid}(r_{cell}, \mathbf{q})], \tag{6.5}$$

  being $\mathbf{q} = (x, y, z)$ the comoving coordinates of catalogue objects;
- smooth the density field through a Gaussian filter, assuming a given radius r_{smooth}:

$$\delta_{smooth}(\mathbf{k}) = \delta(\mathbf{k}) \exp\left(-\frac{k^2 r_{smooth}^2}{2}\right); \tag{6.6}$$

- compute the displacement field in Fourier space, adopting the Zel'dovich approximation and using a given bias, b:

$$\mathbf{\Psi} = -\frac{i\mathbf{k}}{k^2}\frac{\delta_{smooth}(\mathbf{k})}{b}; \tag{6.7}$$

- compute the displacement field in configuration space, by using the IFFT:

$$\mathbf{\Psi} = \mathrm{IFFT}\left[-\frac{i\mathbf{k}\delta_{smooth}(\mathbf{k})}{k^2 b}\right]; \tag{6.8}$$

- eventually compute the displacement field corrected for RSD, hereafter $\mathbf{\Psi}_{RSD}$:

$$\mathbf{\Psi}_{RSD} = \mathbf{\Psi} - \frac{f}{1+f}\left\{\mathrm{IFFT}\left[-\frac{i\mathbf{k}\delta_{smooth}(\mathbf{k})}{k^2 b}\right] \cdot \hat{\mathbf{s}}\right\}\mathbf{s}, \tag{6.9}$$

  where the growth factor, f, is an input parameter;
- shift the data catalogue using the displacement field corrected for RSD:

$$\mathbf{q} = \mathbf{q} - \mathbf{\Psi}_{RSD}; \tag{6.10}$$

- shift the random catalogue using the displacement field, without RSD correction:

$$\mathbf{q} = \mathbf{q} - \mathbf{\Psi}; \tag{6.11}$$

6.4 Testing the reconstruction algorithm

We have tested the reconstruction algorithm implemented on the CBL using the Magneticum mock catalogues. At first, we investigate the impact of varying the input parameters on the reconstruction performances. To do this, we used the galaxy catalogue at $z = 0.52$. Moreover, we discuss about how to estimate (or choose) such parameters, exposing also the fiducial values used in this work. We also perform other tests, like a check of eventual velocity bias and a comparison with a different code, using different Magneticum catalogues depending on the type of test performed and its purpose.

6.4.1 The Gaussian smoothing scale

The smoothing scale is the parameter that impacts the most the reconstruction efficiency. In fact, if we smooth at scales too small, the reconstruction is heavily affected by the shot noise. On the contrary, by oversmoothing, the displacement is reduced, i.e. the reconstruction is less effective. For a sufficiently large number of tracers, the best choice would be to smooth at small scales, e.g. $r_{smooth} = 5h^{-1}\,\mathrm{Mpc}$. Moreover, such a small smoothing radius heavily distorts the correlation function at small scales. On the contrary, large smoothing scales, of the order of $r_{smooth} = 20h^{-1}\,\mathrm{Mpc}$, degrades the reconstructed BAO peak, although it is still enhanced with respect to the unreconstructed one. This is another proof that the large-scale bulk flows damp the BAO peak, because we can correct them even with large smoothing scales. Figure (6.2) shows the angle-averaged two-point correlation function, computed after the application of the reconstruction technique, by using three different Gaussian filters, with $r_{smooth} = 10h^{-1}\,\mathrm{Mpc}$, $r_{smooth} = 15h^{-1}\,\mathrm{Mpc}$, $r_{smooth} = 20h^{-1}\,\mathrm{Mpc}$, in the galaxy catalogue at $z = 0.52$. Modelling the BAO peak as shown in section 6.6, we have inferred a value of the α parameter $\alpha = 1.062 \pm 032$, $\alpha = 1.066 \pm 0.034$, $\alpha = 1.067 \pm 0.031$, respectively. Even if, as expected, the reconstruction is more effective with the $10h^{-1}\,\mathrm{Mpc}$ Gaussian filter, the values of the α parameters are widely within their errors. Nevertheless, we can notice that, at small scales, the reconstruction with a smoothing radius of $15h^{-1}\,\mathrm{Mpc}$ better corrects the RSD compared to the other two cases. For these reasons, our choice has been to perform a Gaussian smoothing at the fiducial scale of $15h^{-1}\,\mathrm{Mpc}$, a value widely used in previous works (e.g. Padmanabhan, Xu, et al., 2012).

6.4.2 The bias

The bias has a strong effect on the reconstruction. If we underestimate the bias, then we overestimate the density field and, as a consequence, the displacement field. On the contrary, overestimating the bias, we underestimate the density field and so the displacement field. We have inferred the linear bias by modelling the projected correlation function. After turning the Magneticum catalogues into redshift-space mocks, by using equation (3.22), the linear bias can be estimated through equation (3.43), reported here:

$$b = \sqrt{\frac{w_p^t(r_p)}{w_p^m(r_p)}}, \tag{6.12}$$

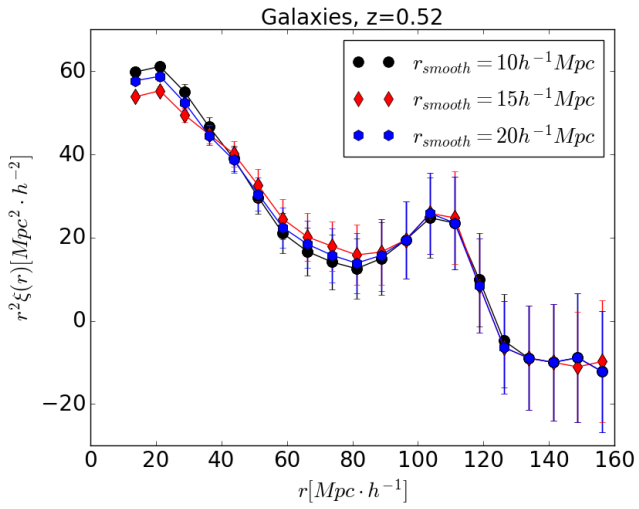

Figure 6.2: Galaxy two-point correlation function, at $z = 0.52$, computed reconstructing the density field with smoothing scales of $r_{smooth} = 10h^{-1}$ Mpc (black circles), $r_{smooth} = 15h^{-1}$ Mpc (red diamonds), $r_{smooth} = 20h^{-1}$ Mpc (blue hexagons). The error bars are computed with the Jackknife method. Notice how the reconstruction technique with a Gaussian filter at $r_{smooth} = 15h^{-1}$ Mpc corrects the RSD distortions, at small scales, better than using the other two filters.

where

$$w_p^m(r_p) = \int_{r_p^2}^{\sqrt{\pi_{max}^2 + r_p^2}} dr \frac{2r\xi(r)}{\sqrt{r^2 - r_p^2}} \tag{6.13}$$

(Veropalumbo et al., 2016), and the matter correlation function, $\xi(r)$, is given by equation (5.45). The projected correlation function of tracers, $w_p^t(r_p)$, has been measured by creating random catalogues 5 times larger than the data, to minimise the shot noise error, in 10 logarithmic bins within $1 - 50h^{-1}$ Mpc. The two-dimensional correlation function, $\xi(r_p, \pi)$, has been integrated up to $\pi_{max} = 50h^{-1}$ Mpc, a value that well balance the robustness with the need of excluding noisy bins at large scales. We have modelled the projected correlation function in the range of $5 - 50h^{-1}$ Mpc, by generating 100 MCMC chains of 10000 samples, with a Gaussian likelihood (equation 5.38). We have assumed a uniform bias prior of $b\sigma_8$ in the range of $1 - 5$. The value of the bias, given by equation (6.12), is then calculated by averaging all the values over the bins within the fit range. The modelled projected correlation functions, together with the bias values that we have estimated, are presented in the next chapter.

6.4.3 The growth factor

The growth factor is used to restore the isotropy of the correlation function (neglecting the impact of geometric and other distortions). Several investigations (e.g. Padmanabhan, Xu, et al., 2012) have demonstrated that the impact of this parameter on the accuracy of the reconstruction is marginal. In this thesis, we have compute the growth rate directly from the fiducial cosmological model, through equation (2.34),

following e.g. L. Wang and P. J. Steinhardt (1998b), Kiakotou et al. (2008) and Gong et al. (2009).

6.4.4 The cell radius

The cell radius defines the resolution of the three-dimensional grid used to computed the density field. We test the possible impact of different choices of r_{cell} to the reconstruction performances, by running three different methods, with $r_{cell} = 5h^{-1}$ Mpc, $r_{cell} = 10h^{-1}$ Mpc, $r_{cell} = 20h^{-1}$ Mpc. Figure (6.3) shows the result of this analysis: the measured two-point correlation functions appear almost identical for all the cases. By modelling the BAO peak, we have estimated the following α parameters: $\alpha = 1.071 \pm 033$, $\alpha = 1.071 \pm 0.033$, $\alpha = 1.066 \pm 0.033$ for $r_{cell} = 5h^{-1}$ Mpc, $r_{cell} = 10h^{-1}$ Mpc, $r_{cell} = 20h^{-1}$ Mpc respectively . Since the accuracy of the α parameter is equivalent for all the cell radii considered, we set our fiducial cell radius value to the intermediate scale considered, $r_{cell} = 10h^{-1}$ Mpc. In conclusion, the effect of varying r_{cell} is marginal on the efficacy of the reconstruction.

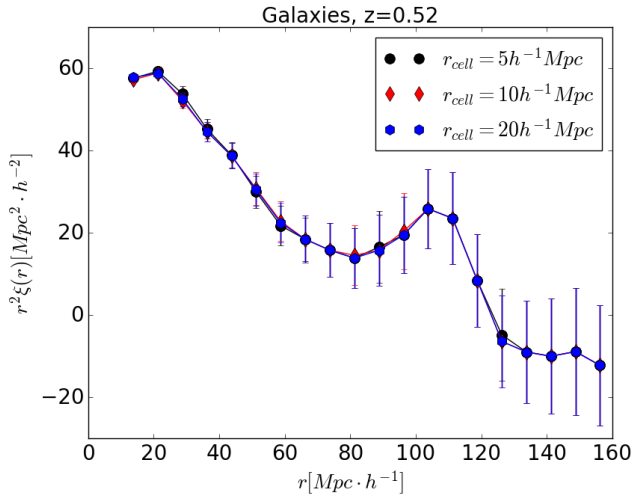

Figure 6.3: Same of Figure (6.2), but varying r_{cell} instead of r_{smooth} . In particular, the different curves refer to $r_{cell} = 5h^{-1}$ Mpc, $r_{cell} = 10h^{-1}$ Mpc, $r_{cell} = 20h^{-1}$ Mpc. The measured correlation function measured for these three different cases is almost identical.

6.5 The velocity bias

As discussed, the observable cosmic objects do not trace precisely the density field of the underlying matter. This means that it can be possible they do not trace fairly also the matter velocity field. Since we know the true velocity field of the mock catalogues, we can compare it to the displacement field computed by the reconstruction. Figure (6.4) shows the relation between velocity and displacement fields, for galaxy mocks at low ($z = 0.2$) and high ($z = 2$) redshifts. Figure (6.5), instead, shows the velocity and

displacement fields of galaxy cluster as a function of the mass, at $z = 0.2$, $z = 0.52$ and $z = 2$. We used in the first case galaxy catalogues, to show the velocity bias of the objects with the expected highest peculiar velocities, at the extremes of the redshift range considered. In the second case, we used the galaxy cluster catalogues because of the known viral mass, M_{500}. As expected, small objects with high peculiar velocities can cause an underestimation of the displacement field, due to RSD not fully taken into account. Nevertheless, the displacement is a low-scattered monotonic function of the velocity, so the displacement field well traces the true velocity field, i.e. there is not a significant velocity bias.

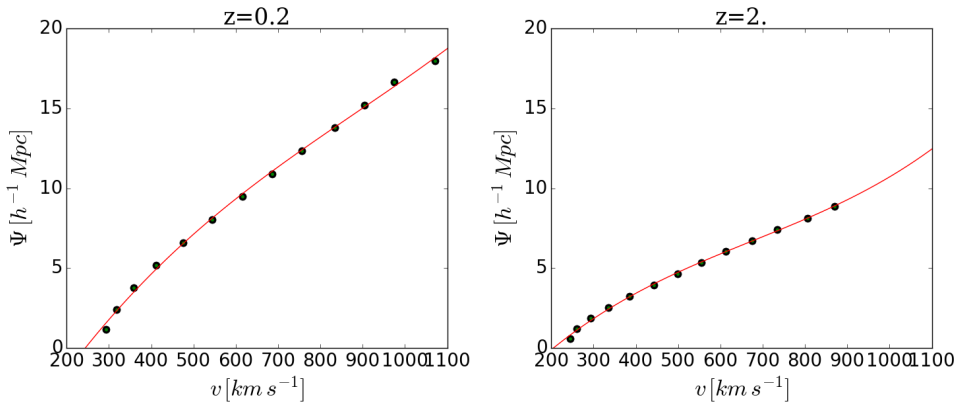

Figure 6.4: Norm of the displacement field, $\mathbf{\Psi}$, computed through the reconstruction method, averaged in bins of the norm of the true velocity field, in galaxy mocks at $z = 0.2$ (left panel) and $z = 2$ (right panel). We have fitted the data with cubic splines (red dashed lines). Error bars, too small to be appreciated, are the fraction of standard deviation over the square root of point number in each bin. Notice how both the velocity and displacement field norms are larger at low redshifts, implying that the reconstruction is more effective in the near Universe, as expected.

Figure (6.6) shows the effect of the reconstruction on the two-dimensional correlation function on the galaxy catalogue at z=0.2. In this mock sample we expect the reconstruction to be the most effective. The BAO rings are highlighted in both the unreconstructed real-space and redshift-space correlation functions. In particular, the isotropy of the BAO is clearly lost in redshift space. By reconstructing the density field, the symmetry of the BAO is approximately restored. Furthermore, the BAO is significantly enhanced, even with respect to the real-space correlation function.

6.5.1 Comparison between different reconstruction algorithms

As discussed in section 6.3, we have shifted only data catalogues for RSD correction. In fact, it has been demonstrated that the RSD correction is not effective adding the extra RSD shift on both data and random catalogues (e.g. Padmanabhan, Xu, et al., 2012, M. White, 2015). We test this, by trying both the methods. Moreover, we test our reconstruction implementation using a different algorithm, implemented by

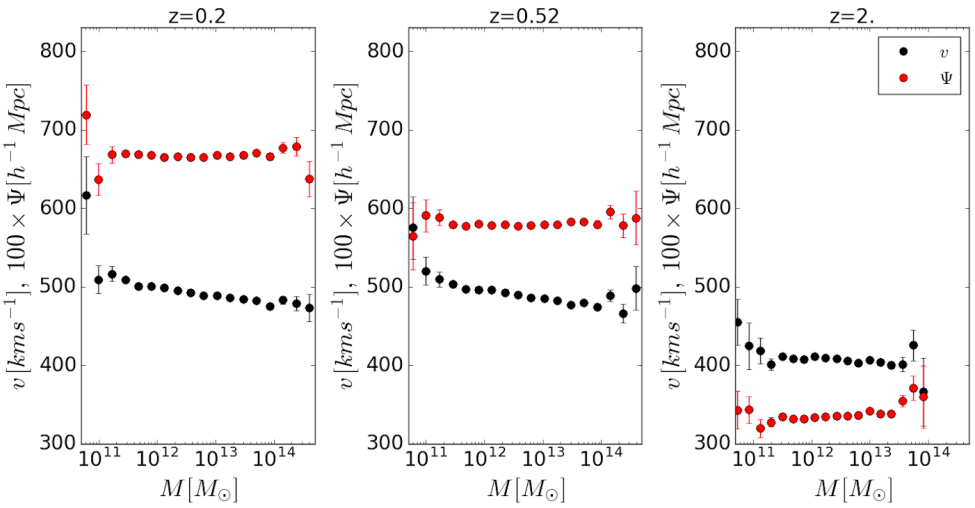

Figure 6.5: Displacement (red) and velocity (black) field norms, as a function of the mass, for galaxy clusters at $z = 0.2$ (left panel), $z = 0.52$ (middle panel) and $z = 2.$ (right panel). The error bars are computed in the same way as Figure (6.4). The displacement field is normalised at a fixed value in all the panels, to show the dependences of this quantity on the redshift.

Martin White, based on the finite difference method, and publicly available [3]. Using the reconstruction by White, both data and random are shifted for the RSD correction term.

Figure (6.7) shows the result of this test. The two-point correlation functions, reconstructed by using the "single" and "double" shifts, are overplotted to the unreconstructed ones, in both real and redshift space, for the galaxy catalogue at $z = 0.52$. The measured correlation function, after applying White's reconstruction, is almost coincident to the one measured after shifting both data and random with our algorithm. Both the correlation functions follow the redshift-space correlation function at small scales, above the real-space unreconstructed one. This overestimation of the clustering signal at small scales is due to the Fingers of God. The one-shift reconstructed correlation function, on the contrary, is quite similar to the unreconstructed real-space one, at intermediate and small scales. Notice that, even in this case, the reconstruction cannot correct for the RSD at the smallest scales. At the large scales, all the reconstructed correlation functions show a sharper BAO peak compared to both the unreconstructed ones. Thus, our test confirms that, by shifting only data, the reconstruction technique reduces the effects of RSD, while shifting both data and random not. Moreover, this test shows that our implementation of the reconstruction is fully consistent with the one in the code by White.

[3] https://github.com/martinjameswhite/recon_code/blob/master/recon.cpp

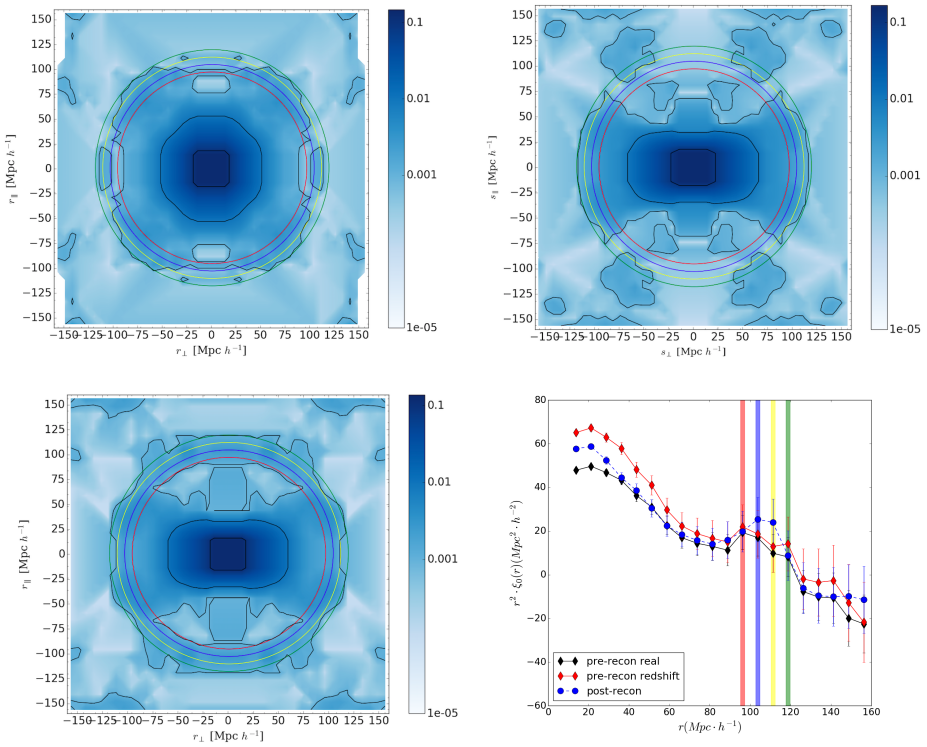

Figure 6.6: The top panels show the galaxy two-dimensional correlation function, at $z = 0.2$, in real (left) and redshift space (right). The bottom-left panel shows the reconstructed two-dimensional correlation function. The displayed contour levels of the two-dimensional correlation functions correspond to the following values: $\xi(r_\perp, r_\parallel) = [0.1, 0.01, 0.001, 0.00001]$. The bottom-right panel shows the two-point correlation functions corresponding to other panels: unreconstructed in real (black diamonds) and redshift (red diamonds) space, and reconstructed (blue circles) ones. In the latter panel we have highlighted with colored vertical lines the bins covering the BAO peak: $r = 96.25h^{-1}$ Mpc (red), $r = 103.75h^{-1}$ Mpc (blue), $r = 111.25h^{-1}$ Mpc (yellow), $r = 118.75h^{-1}$ Mpc (green). The same colour-code is used with the radii of the BAO rings in the two-dimensional correlation functions.

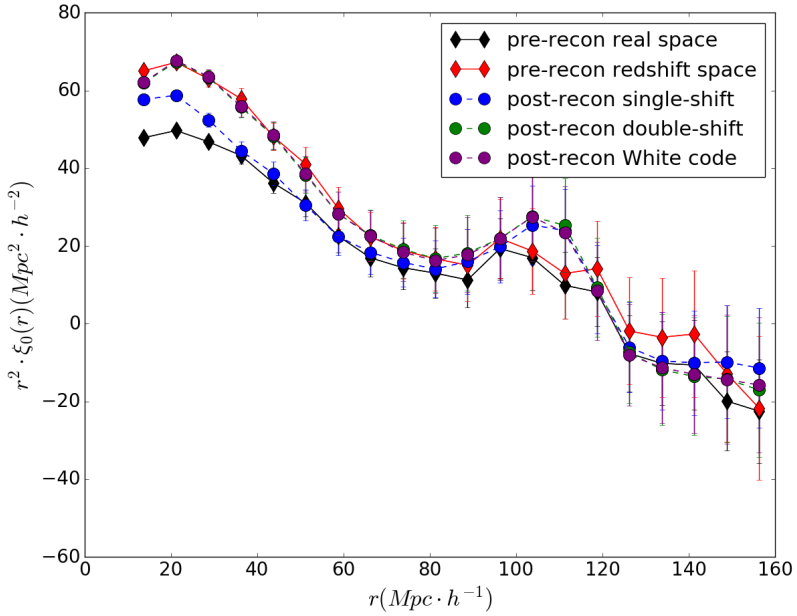

Figure 6.7: Two-point correlation function measured in Magneticum Box1amr galaxy catalogue, at $z = 0.52$. The black and red diamonds represent the real-space and redshift-space unreconstructed two-point correlation function, respectively. The circles represent the reconstructed correlation function. The reconstruction has been applied by shifting only the data (blue), both data and random (green) and with a different algorithm, that shifts both data and random, by Martin White (purple).

6.6 Modelling the BAO peak in the two-point correlation function

Once computed the reconstructed angle-averaged two-point correlation function, we can model the BAO peak to extract the cosmological information. We used the same procedure discussed in section (5.5.2). In particular, our model is

$$\xi(r) = (b\sigma_8)^2 \xi_{DM}(\alpha r) + A(r), \tag{6.14}$$

being ξ_{DM} the Fourier transform of the de-wiggle power spectrum:

$$P_{DM}(k) = [P_L(k) - P_{nw}(k)]e^{-k^2\Sigma_{NL}^2/2} + P_{nw}(k), \tag{6.15}$$

where the linear power spectrum, $P_L(k)$, is computed with CAMB (Lewis and Challinor, 2011). We modelled the two-point correlation function over the range of $60 \leq r \leq 160h^{-1}$ Mpc, not considering the scales where corrections for RSD of the reconstruction method are less effective. We have computed the posterior for the α and $(b\sigma_8)$ parameters by running 500 MCMC chains, each one sampling 150000 points. We have fixed the $A(r)$ parameter to zero, to be sure that the chains reach the convergence, and we have repeated the computation with different length of the chains, up to 30000 points. We have assumed a Gaussian likelihood, and uniform priors for both the parameters, in a range of $0.7 - 1.3$ for α and $1 - 15$ for $b\sigma_8$. The value that maximises the posterior distribution, in case of Gaussian likelihoods, is the mean over the chain samples. We have recomputed the best-fit models varying Σ_{NL} in a range of $0 \leq \Sigma_{NL} \leq 100$, with a step of $1h^{-1}$ Mpc for $\Sigma_{NL} \leq 15h^{-1}$ Mpc and $10h^{-1}$ Mpc for $\Sigma_{NL} > 15h^{-1}$ Mpc. Once we have computed the best values of the parameters for each Σ_{NL}, we determined the χ^2 of all the models. Finally, we selected the best-fit by minimising the χ^2 over the Σ_{NL}, thus obtaining a rough estimation of Σ_{NL} itself, and the best-fit parameters α and $b\sigma_8$. We show the modelled BAO peaks and the values inferred for the α parameter values in the next chapter.

6.7 Error estimation

We discussed about the different possible methods to estimate the errors, introducing the Poisson, Jackknife and Bootstrap error estimations, in section 3.7. Since CBL allows to compute all such errors, we have tested the performances of the three different methods. Figure (6.8) shows the comparison between Poisson, Jackknife and Bootstrap error estimators, with 125 Jackknife resampling and 100 Bootstrap mocks. Since we found that all the cosmic tracers show similar qualitative behaviours at the redshifts considered, we described specifically only the case of clusters at $z = 2$. Clearly, the Poisson statistic underestimates the error at large scales, with respect to Jackknife and Bootstrap, that appear quite similar to each other.

Our fiducial choice has been to use a Jackknife covariance matrix, that is faster to compute with respect to Bootstrap, and it gives similar results. Figure (6.9) shows the correlation matrices of galaxies at $z = 0.2$ and AGN at $z = 2$, before and after the reconstruction. Being $C_{ij}^{(cov)}$ the covariance matrix, described by equation (3.47), the correlation matrix $C_{ij}^{(corr)}$ is defined as follows:

$$C_{ij}^{(corr)} \equiv \frac{C_{ij}^{(cov)}}{\sqrt{C_{ii}^{(cov)} C_{jj}^{(cov)}}}. \tag{6.16}$$

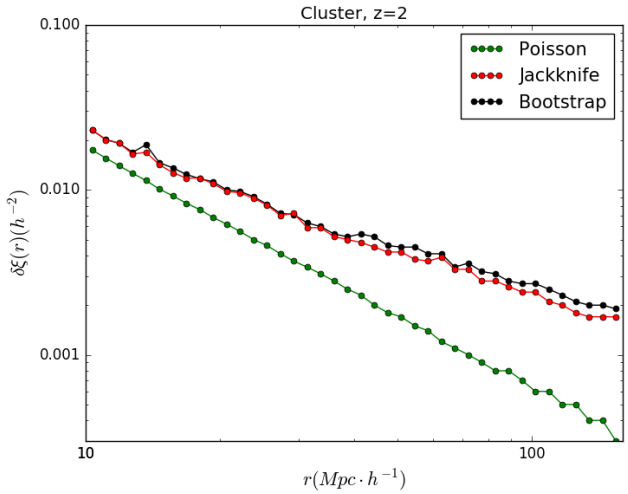

Figure 6.8: Comparison between Poisson (green), Jackknife (red) and Bootstrap (black) errors, for the mock catalogue of galaxy clusters at $z = 2$.

The highest correlations in the original matrix are in the elements close to the diagonal; the out-of-diagonal elements are more scattered, and large scales bins have in general the lowest signal. Applying the reconstruction, the elements close to the diagonal have almost the same signal, even if more definite (notice that the diagonal elements are normalised to the unity). The final effect of the reconstruction is to smooth and regularise the correlation matrix. At high redshifts, the intrinsic scatter of the correlation matrix is high, due to the lower number of objects. We can notice that the reconstruction is less effective at high redshifts, as expected, because of the small displacement field vectors: both before and after the reconstruction the correlation matrices are "blurred".
Since we want to use the same covariance matrix for a large range of redshifts and different tracers, we considered only the diagonal of the Jackknife matrix. In this way, we mitigate the noise of out-of-diagonal elements, which may affect the accuracy of the BAO modelling.

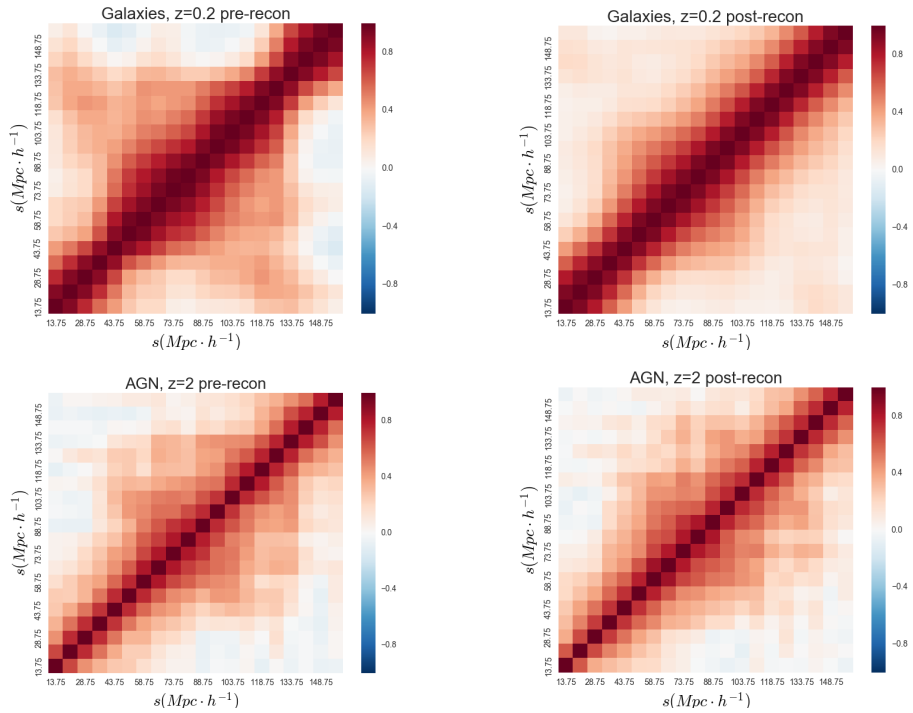

Figure 6.9: Jackknife normalised correlation matrices before (left) and after (right) the reconstruction, for galaxies at $z = 0.2$ (top) and AGN at $z = 2$ (bottom). The correlation matrices are computed in a range of $10 - 160h^{-1}$ Mpc, to encode the BAO scale. The reconstruction smooths the main contrasts in the original matrices. It is more effective at low redshifts, where the matrices are less blurred with respect to the ones at higher redshifts.

Chapter 7

Results

> "Never imagine yourself not to be otherwise than what it might appear to others that what you were or might have been was not otherwise than what you had been would have appeared to them to be otherwise. "
>
> Lewis Carroll, Alice's Adventures in Wonderland (1865)

We have reconstructed the density field traced by galaxies, galaxy clusters and AGN from Magneticum simulations, in the redshift range $0.2 \leq z \leq 2$, to estimate the reconstruction gain in different regimes. In the next sections, we present the results that we have obtained in this analysis. In particular, in the first section we show the modelling of the projected two-point correlation function, used to estimate the linear bias, that is required by the reconstruction method. Then we model the BAO peak in the monopole of the two-point correlation function, providing constraints on the α parameter. The latter is a paramount quantity, being directly related to the main cosmological parameters. Thus, it can be used to extract cosmological information. Moreover, we discuss about the Σ_{NL} parameter, that is inferred by applying a χ^2 test to the BAO model fit. We used the latter to also estimate the significance of the BAO detection. Finally, we show the result obtained by applying the mass cut $M > 10^{13} M_{\odot}$ to the cluster catalogues at redshifts $0.2 \leq z \leq 0.72$. Since the Magneticum mocks are composed also by small structures, not considerable as "real galaxy cluster", we applied this mass cut to simulate more reliable clusters. We show this further analysis in section 7.2.1, discussing the main results obtained.

7.1 Modelling the linear bias

Following the procedure described in the previous chapter, and in particular in section 6.4.2, we have modelled the projected correlation function to estimate the linear bias of the selected tracers. We used this method, instead of more direct techniques such as the modelling of the two-point correlation function in real space, to follow as close as possible the procedure with real data. Thus, we integrate the redshift-space correlation function along the line-of-sight up to up to $\pi_{max} = 50 h^{-1}\,\mathrm{Mpc}$, which ensures the robustness of the method and at the same time it excludes the noise of large bins. The biases inferred, reported in Table (7.1), will be one of the input

quantities of the reconstruction method. Figures (7.1), (7.2) and (7.3) show the best-fit models for galaxies, clusters and AGN, respectively.

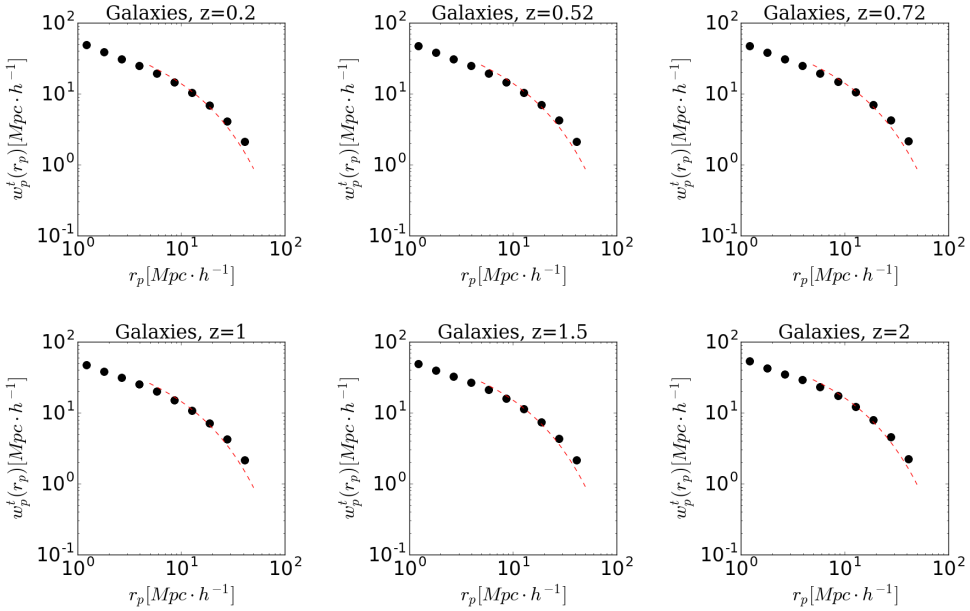

Figure 7.1: The black circles represent the measured projected correlation functions of galaxies, while the red dashed lines are their best-fit models, in the $5-50h^{-1}$ Mpc range. The redshifts of measurements are displayed on the top of the boxes.

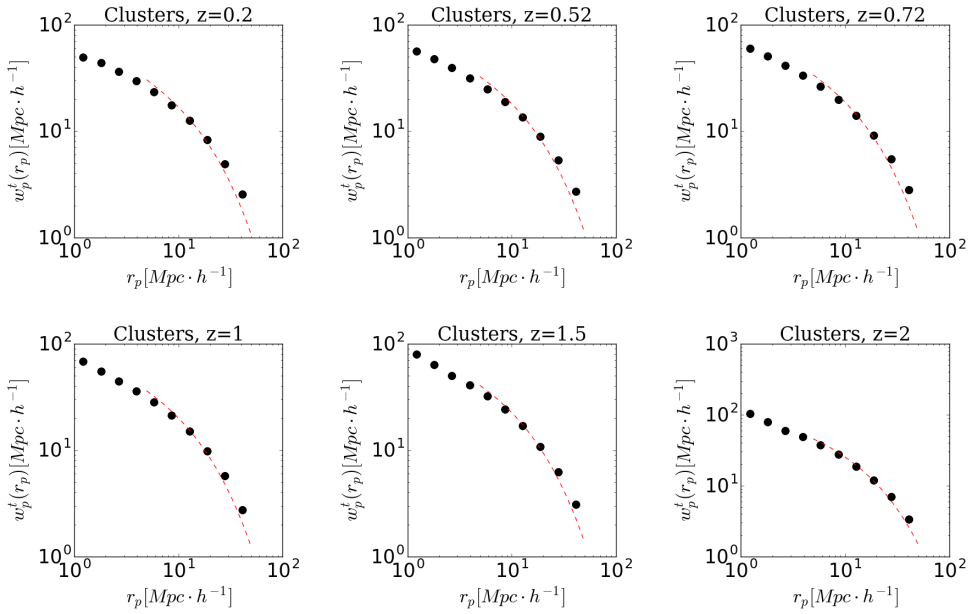

Figure 7.2: Same of Figure (7.1), but for galaxy clusters.

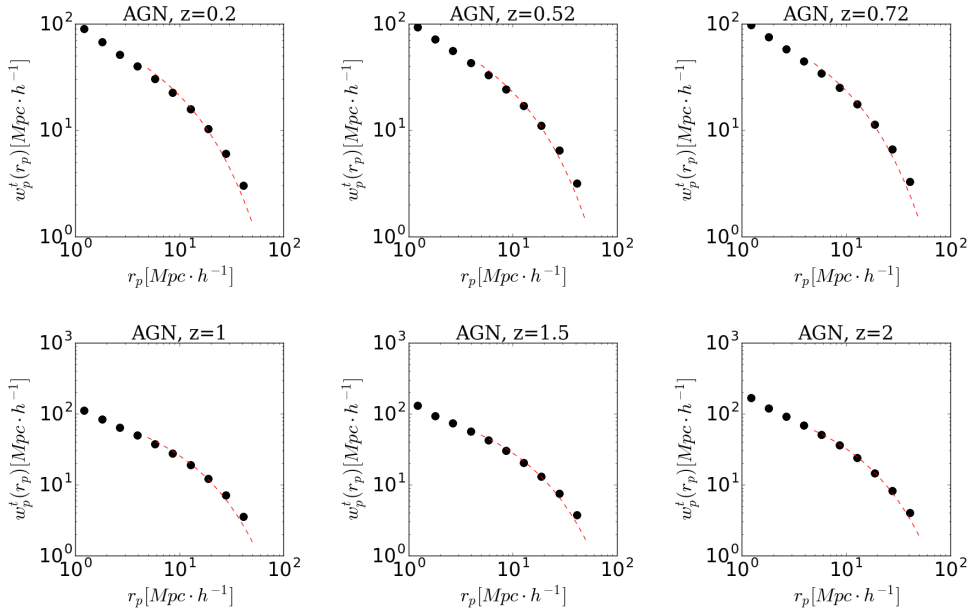

Figure 7.3: Same of Figure (7.1), but for AGN.

As expected, the bias shows a clear redshift evolution, for all the cosmic tracers considered in this analysis (Marulli, Bolzonella, et al., 2013). Notice that AGN biases are larger than the cluster ones, at all redshifts. "Real" galaxy clusters are more massive than AGN. However, according to the cluster definition in the Magneticum simulations, discussed in section 6.1, also smaller objects, such as galaxy groups or haloes, are included in this class. For this reason we have a higher number of less biased objects with respect to observable cluster catalogues. This is why, for example, we can perform clustering analyses with these tracers up to $z = 2$, while the observable clusters at those redshifts would be a few. To overcome this issue, we have applied a mass cut of $M > 10^{13} M_{\odot}$ on the catalogue, analyse more reliable cluster mock samples.

7.2 Constraints on the α parameter

To estimate the isotropic shift of the BAO peak, α, we have modelled the monopole of the two point correlation function, as described in section 6.6. Figures (7.4), (7.5) and (7.6) show the $\Delta\chi^2$ of the model fits as a function of Σ_{NL}, that is the difference between the value of χ^2 found for each model and the minimum χ^2 over all models. Our fiducial values of Σ_{NL}, inferred by selecting the ones that minimise the χ^2 (that is where the curves match the x-axis) are reported in Table (7.1). From these figures we can also estimate the significance of the BAO peak detection (see e.g. Veropalumbo et al., 2016). The Σ_{NL} parameter, in fact, represent the degradation of the BAO features in the power spectrum. This means that, for high values of Σ_{NL}, the BAO peak completely disappears (i.e. $\xi(r) \to \xi_{nw}(r)$ in equation (5.46)). Thus, for a single free parameter, that is one degree of freedom, a 1σ detection correspond to $\Delta\chi^2 = 1$, a 2σ detection to $\Delta\chi^2 = 4$, a 3σ detection to $\Delta\chi^2 = 9$, and so on. We found that, at $z = 0.2$,

the BAO detection with the galaxy and cluster catalogues have a 2σ significance before the reconstruction, and a 3σ significance after applying this technique. In an analogous way, the AGN catalogue provided a 1σ detection pre-reconstruction, that turns in a 3σ detection post-reconstruction. We can conclude that the reconstruction method, by removing part of non-linearities in the BAO peak, clearly improves the significance of the detections.

As expected, the accuracy of the detection degrades at high redshifts. At $z = 2$, the BAO peak is detected with 1σ accuracy pre-reconstruction and 2σ post-reconstruction in galaxy catalogues, while for clusters we have a 2σ detection both pre and post reconstruction. Since structures are in general more linear with respect to the near Universe, the reconstruction is less useful at high redshifts. We have a non-detection of the BAO peak for AGN at $z = 2$, both for pre- and post-reconstruction. This is due to the high shot noise of these measurements, because of the paucity of the sample (see Table 6.3).

As expected, the pre-reconstruction values of Σ_{NL} are higher at low redshifts with respect to the ones at high redshifts, in both galaxy and AGN cases. The Σ_{NL} parameters of cluster models have lower values with respect to AGN and galaxies at the same redshifts, because of their larger size, which make them be well described by the linear theory (e.g. Veropalumbo et al., 2014; Veropalumbo et al., 2016). Cluster models do not present a clear redshift evolution of the Σ_{NL} parameters. The post-reconstruction best-fit models have systematically lower Σ_{NL} values with respect to unreconstructed models. This demonstrates the effectiveness of the reconstruction method, which corrects for the non-linear evolution of structures. Figure (7.7) shows the evolution of the non-linear correction obtained with this method. Such corrections are more effective at low redshifts, and gradually degrade at higher redshift. Notice that, for this reason, post-reconstruction models do not show a Σ_{NL} redshift evolution similar to the pre-reconstruction ones.

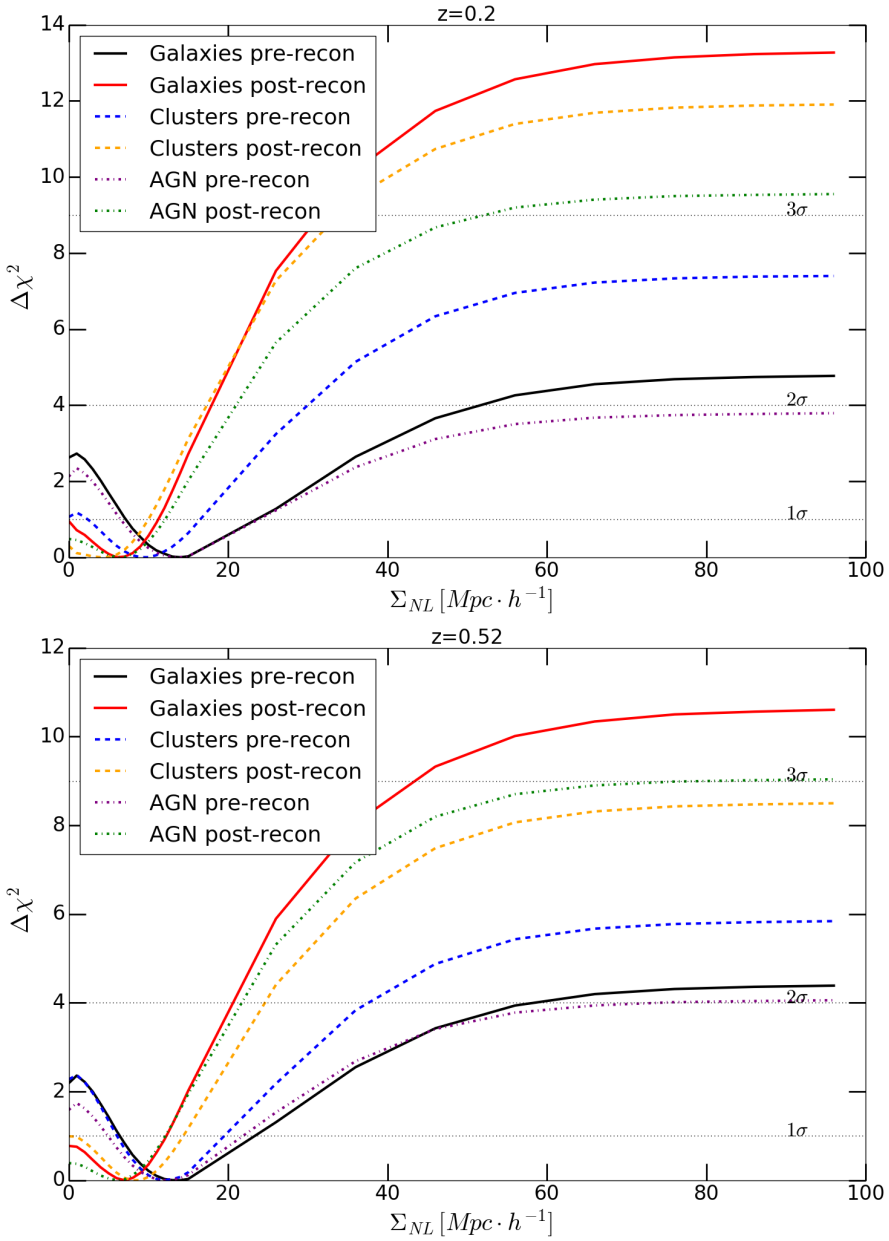

Figure 7.4: $\Delta\chi^2$ of the BAO fit models as a function of Σ_{NL}. The solid lines refer to the results obtained with galaxies, before (black) and after (red) the reconstruction; the dashed lines refer to the clusters (blue before the reconstruction, and orange after), while the dash-dotted lines to the AGN (purple before the reconstruction, and green after). These curves are referred to $z = 0.2$ (top panel) and $z = 0.52$ (bottom panel).

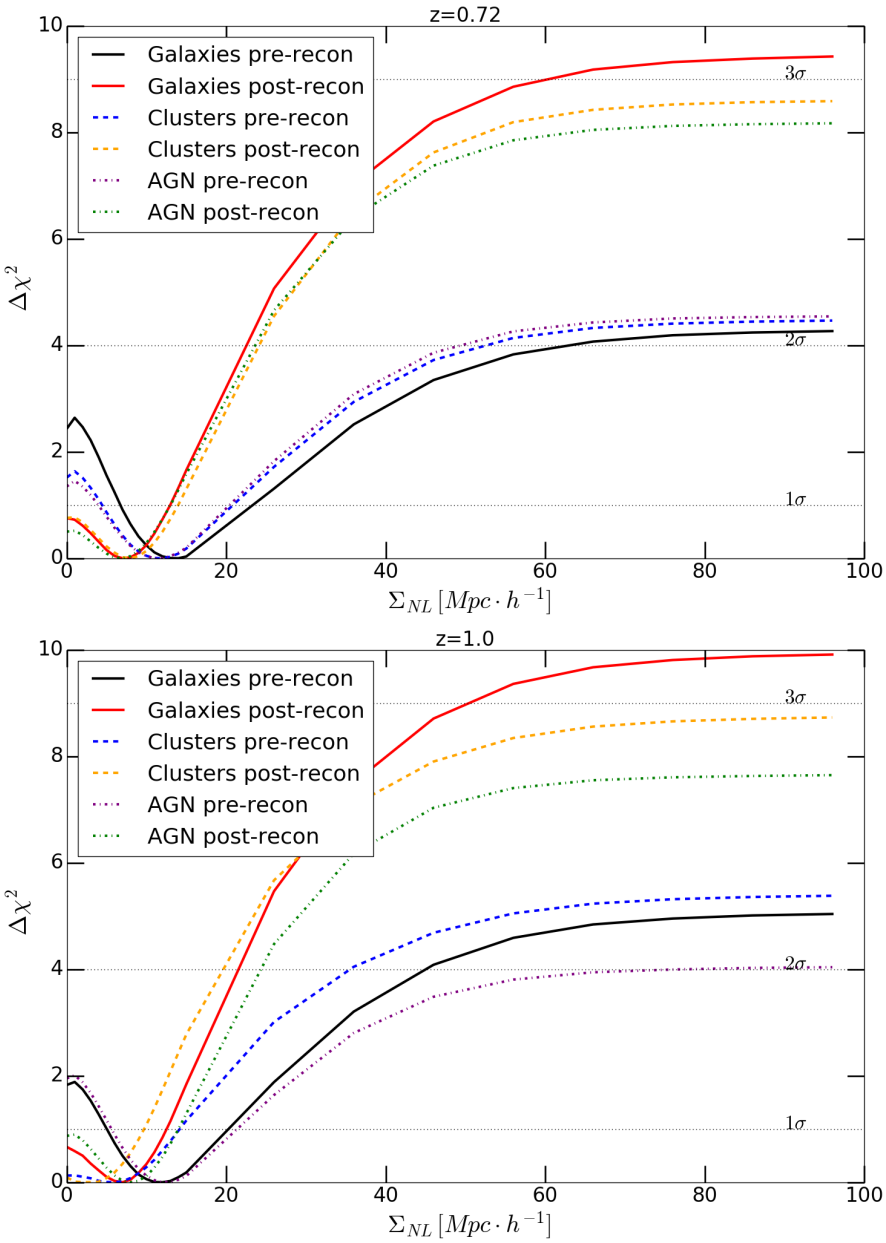

Figure 7.5: $\Delta\chi^2$ of the BAO fit models as a function of Σ_{NL}, at $z = 0.72$ (top panel) and $z = 1$ (bottom panel). The symbols are the same of Figure (7.4).

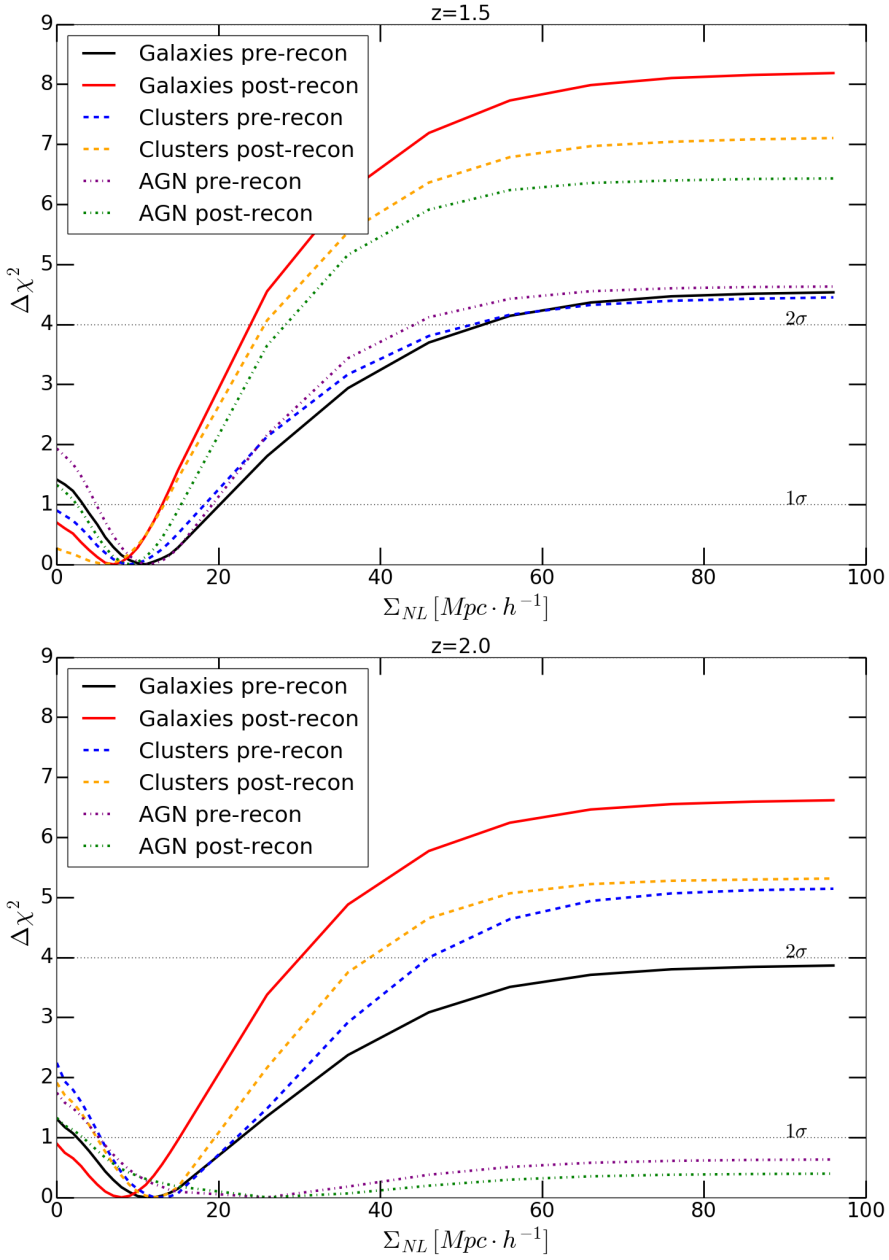

Figure 7.6: $\Delta\chi^2$ of the BAO fit models as a function of Σ_{NL}, at $z = 1.5$ (top panel) and $z = 2$ (bottom panel). The symbols are the same of Figure (7.4).

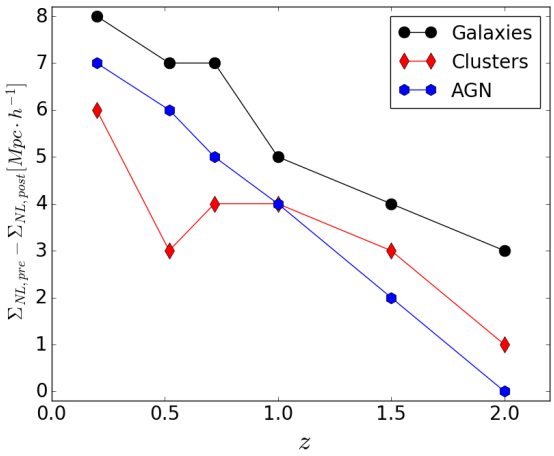

Figure 7.7: Difference between Σ_{NL} parameters of the best-fit models before and after the reconstruction, for galaxies (black circles), clusters (red diamonds) and AGN (blue hexagons).

Figures (7.8), (7.9) and (7.10) show the measured two-point correlation functions and the BAO best-fit models, for galaxies, clusters and AGN, respectively. We fit the BAO peak in the range $60 - 160\,h^{-1}$ Mpc, to use also the intermediate scales thus improving the constraint accuracy, but not considering the smallest scales, more affected by non-linear RSD effects.
The constraints on the α parameter, reported in Table (7.1), are shown in Figure (7.11). The reconstruction method clearly enhances the BAO peak at low redshifts, correcting for non-linear effects and RSD, for all the cosmic tracers considered. The offset between pre- and post-reconstruction models tends to decrease at high redshifts. This is due to the high shot noise, which makes the uncertainties larger, combined to the more linear regime of high redshift objects, which makes the reconstruction less effective.

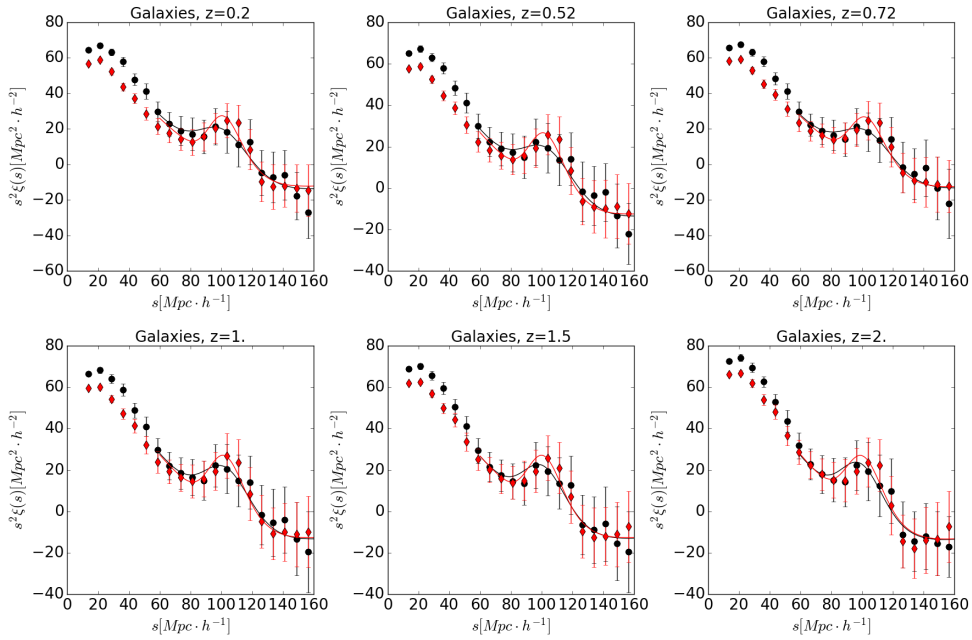

Figure 7.8: Galaxy two-point correlation functions before (black circles) and after (red diamonds) the reconstruction. The black and red solid lines are the best-fit models, before and after the reconstruction, respectively. The BAO fit was performed in the range of $60 - 160\,h^{-1}$ Mpc. Error bars are computed with the Jackknife method. The redshifts of the measurements are displayed on the top of the boxes.

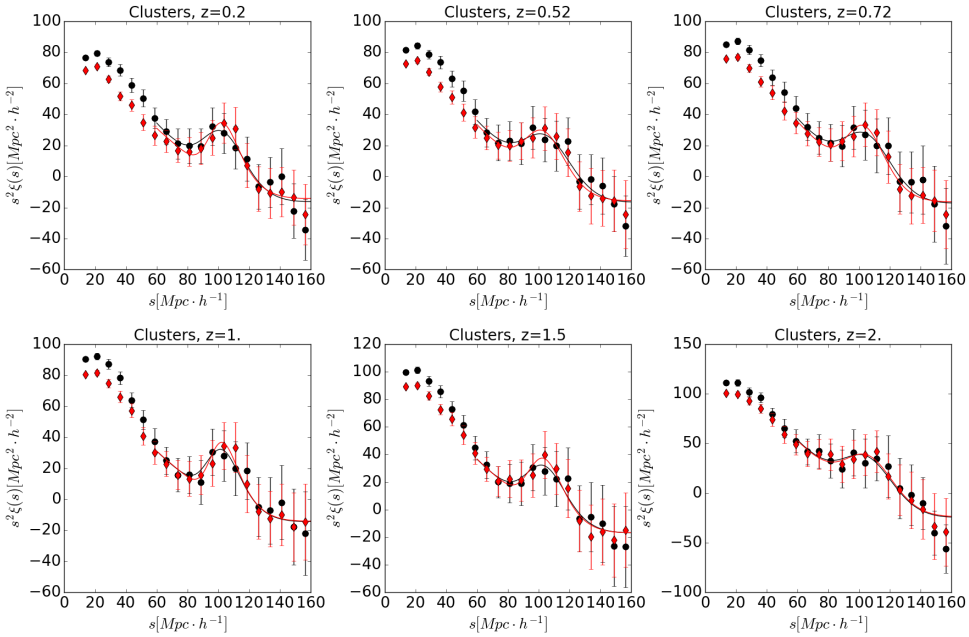

Figure 7.9: Same of Figure (7.8), but for galaxy clusters.

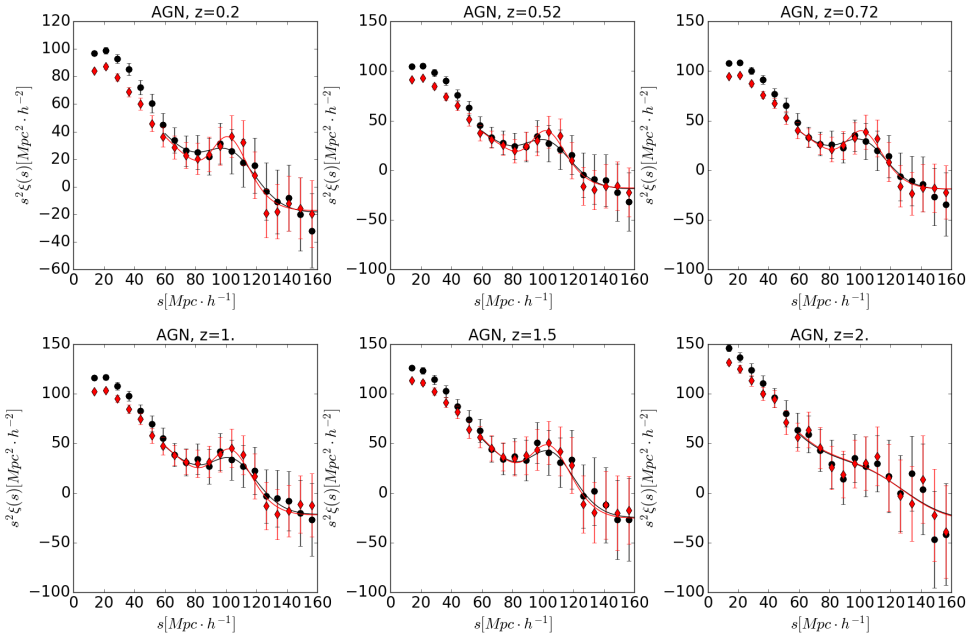

Figure 7.10: Same of Figure (7.8), but for AGN.

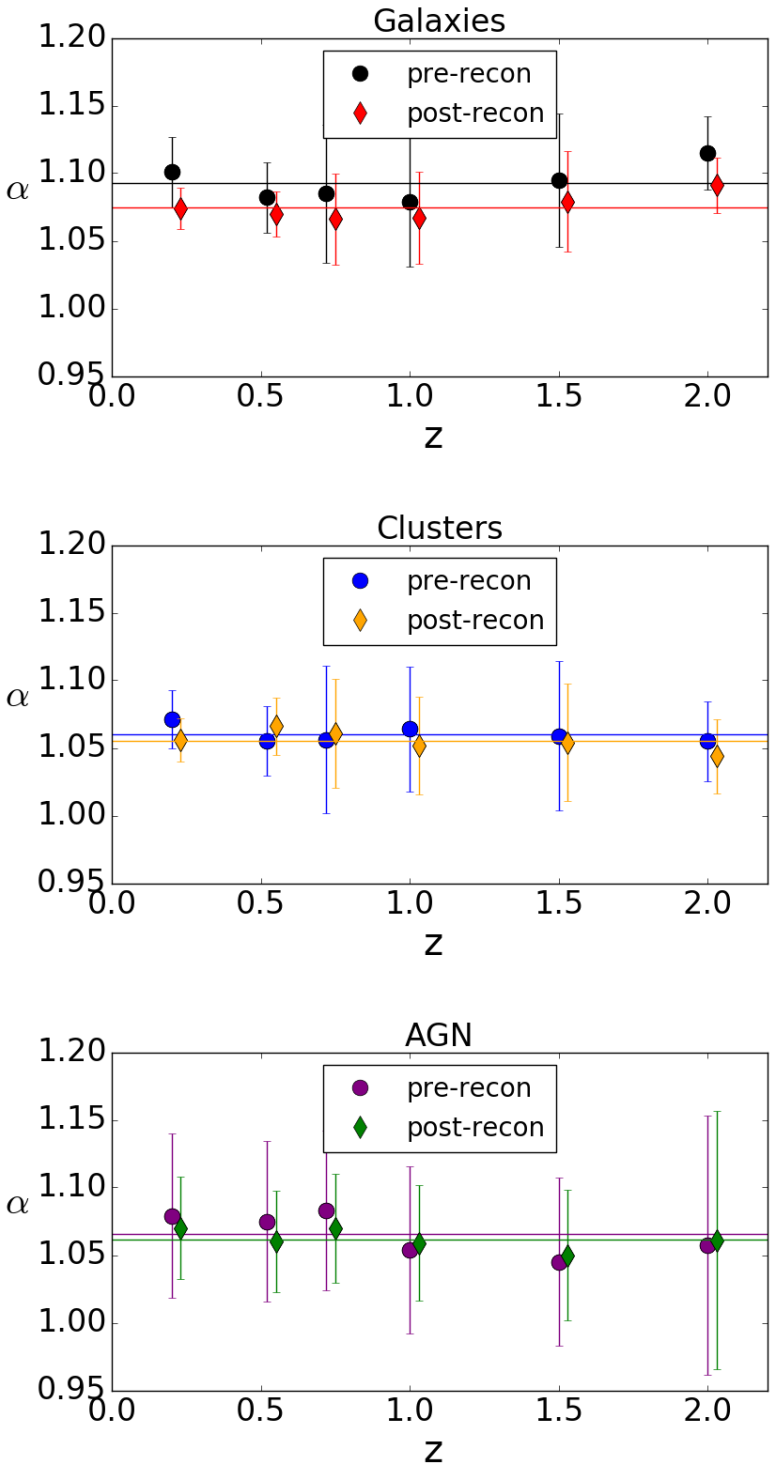

Figure 7.11: Constraints on the α parameter, estimated by using galaxies (top), clusters (middle) and AGN (bottom) as tracers. Circles and diamonds represent the values inferred pre- and post-reconstruction, respectively. The horizontal lines mark the average α values over the redshifts, before and after the reconstruction, according to the colours shown in the legend.

Galaxies	α_{pre}	α_{post}	$\Sigma_{NL,pre}$ [h^{-1}Mpc]	$\Sigma_{NL,post}$ [h^{-1}Mpc]	b
z=0.20	1.101 ±0.026	1.074 ±0.015	14	6	1.34
z=0.52	1.082 ±0.026	1.070 ±0.017	14	7	1.56
z=0.72	1.085 ±0.051	1.066 ±0.034	14	7	1.71
z=1.00	1.079 ±0.048	1.067 ±0.034	12	7	1.95
z=1.50	1.095 ±0.049	1.079 ±0.037	11	7	2.42
z=2.00	1.115 ±0.027	1.091 ±0.020	11	8	2.97
Clusters	α_{pre}	α_{post}	$\Sigma_{NL,pre}$ [h^{-1}Mpc]	$\Sigma_{NL,post}$ [h^{-1}Mpc]	b
z=0.20	1.071 ±0.021	1.056 ±0.016	10	4	1.47
z=0.52	1.055 ±0.025	1.066 ±0.021	12	9	1.77
z=0.72	1.056 ±0.054	1.070 ±0.040	12	8	1.97
z=1.00	1.064 ±0.046	1.052 ±0.036	6	2	2.30
z=1.50	1.059 ±0.055	1.054 ±0.043	9	6	2.96
z=2.00	1.055 ±0.029	1.044 ±0.027	13	12	3.72
AGN	α_{pre}	α_{post}	$\Sigma_{NL,pre}$ [h^{-1}Mpc]	$\Sigma_{NL,post}$ [h^{-1}Mpc]	b
z=0.20	1.079 ±0.060	1.070 ±0.038	14	7	1.65
z=0.52	1.075 ±0.059	1.060 ±0.037	12	6	1.99
z=0.72	1.083 ±0.059	1.060 ±0.040	12	7	2.21
z=1.00	1.054 ±0.062	1.059 ±0.042	12	8	2.61
z=1.50	1.045 ±0.062	1.050 ±0.048	11	9	3.29
z=2.00	1.057 ±0.096	1.061 ±0.095	26	26	4.18

Table 7.1: Constraints on the isotropic shift parameter α, pre- and post-reconstruction, with the corresponding values of Σ_{NL} and bias.

7.2.1 Selecting more realistic samples of galaxy clusters

Since the full Magneticum cluster catalogues include also small objects, to faint to be observed, we have selected subsamples imposing a mass threshold of $10^{13}\,M_{\odot}$, to simulate more realistic samples of groups and clusters of galaxies at $z = 0.2$, $z = 0.52$, $z = 0.72$. We found that, at higher redshifts than the ones considered, the paucity of the selected objects does not allow a BAO analysis in the simulated volume considered. By applying the same analysis method used previously, we inferred a bias $b = 2.00$ at $z = 0.2$, $b = 2.44$ at $z = 0.52$ and $b = 2.76$ at $z = 0.72$, significantly higher with respect to the catalogues previously analysed at the same redshifts. Figure (7.12) shows the $\Delta\chi^2$ of the BAO best-fit models, as a function of Σ_{NL}.

We have detected the BAO peak with an accuracy higher than 2σ in all the cases, except for the pre-reconstruction clusters at $z = 0.72$, which provided a 1σ detection. As expected, since we are considering the most massive objects, structures are more linear with respect to the whole cluster catalogue. We found that $\Sigma_{NL,pre} = 9\,h^{-1}$ Mpc and $\Sigma_{NL,post} = 4\,h^{-1}$ Mpc at $z = 0.2$, $\Sigma_{NL,pre} = 9\,h^{-1}$ Mpc and $\Sigma_{NL,post} = 5\,h^{-1}$ Mpc at $z = 0.52$, and $\Sigma_{NL,pre} = 10\,h^{-1}$ Mpc and $\Sigma_{NL,post} = 4\,h^{-1}$ Mpc at $z = 0.72$. Figure (7.13) shows the BAO best-fit models pre- and post-reconstruction, computed with these values of Σ_{NL}.

Figure (7.14) shows the resulting constraints on α. The post-reconstruction α values are moving toward the unity, i.e. to the true cosmological model, with respect to the pre-reconstruction one, even if not significantly. The α parameters at $z = 0.2$ and $z = 0.52$, both pre- and post-reconstruction, are consistent with unity. In particular, we found that $\alpha_{pre} = 1.055 \pm 0.061$ and $\alpha_{post} = 1.042 \pm 0.043$ at $z = 0.2$; $\alpha_{pre} = 1.062 \pm 0.061$

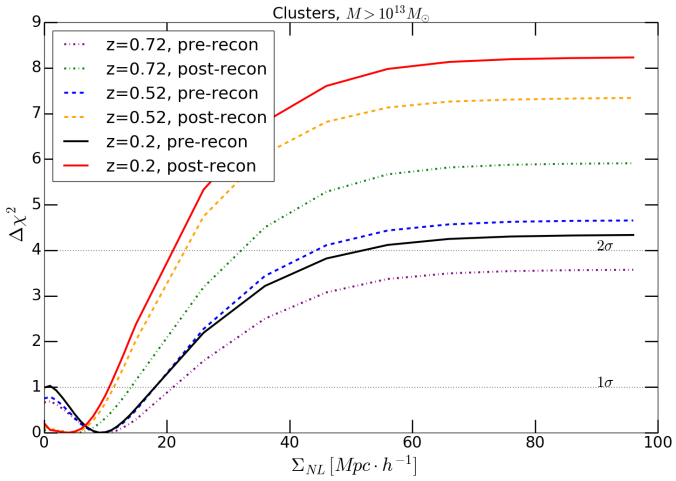

Figure 7.12: $\Delta\chi^2$ of BAO best-fit models for clusters with a mass cut of $10^{13}\,M_\odot$, at $z = 0.2$ (solid lines, red for pre and black for post reconstruction), $z = 0.52$ (dashed lines, blue for pre and orange for post reconstruction), $z = 0.72$ (dot-dashed lines, purple for pre and green for post reconstruction). The dotted lines mark the significance of the BAO peak detection: all the detections have a 2σ significance, except for the pre-reconstruction case at $z = 0.72$, which corresponds to a 1σ detection.

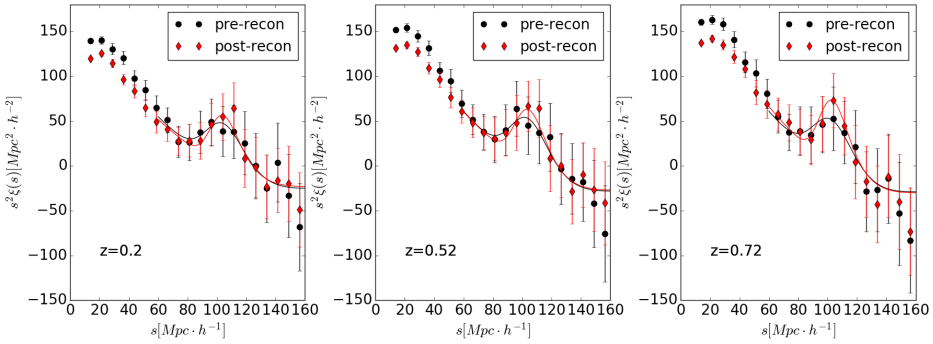

Figure 7.13: Two-point correlation functions for galaxy clusters with $M > 10^{13}\,M_\odot$, before (black circles) and after (red diamonds) the reconstruction, at $z = 0.2$ (left), $z = 0.52$(middle) and $z = 0.72$ (right). The black solid lines represent the BAO best-fit model pre-reconstruction, while the red solid lines are referred to the model post-reconstruction.

and $\alpha_{post} = 1.044 \pm 0.0442$ at $z = 0.52$; $\alpha_{pre} = 1.079 \pm 0.066$ and $\alpha_{post} = 1.052 \pm 0.042$ at $z = 0.72$.

The errors are larger compared to the whole cluster catalogue, because of the higher shot noise. Nevertheless, we found that the reconstruction provides large benefits also in these subsample, reducing α errors by a factor $\approx 1.3 - 1.5$, without a strong redshift dependence.
We plan further studies applying different cuts as a function of the redshifts, on cluster and AGN catalogues, to constrain how the reconstruction efficacy varies with a given observable used to define the selected subsample.

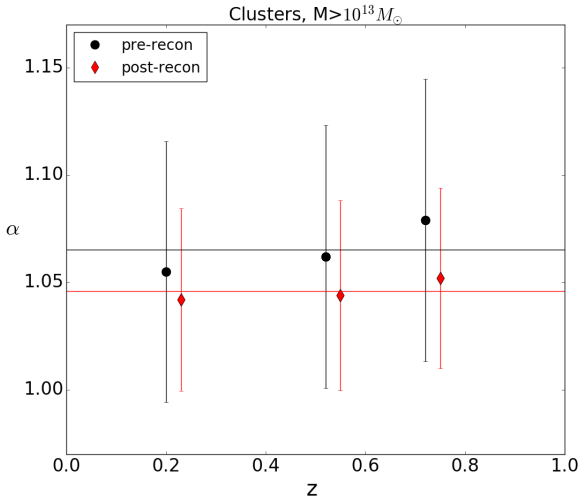

Figure 7.14: Constraints on α provided by the analysis of mock cluster catalogues with $M > 10^{13} M_\odot$, in the redshift range $0.2 \leq z \leq 0.72$. The black circles and the red diamonds represent the pre- and post-reconstruction parameters, respectively.

7.2.2 The cosmic variance effects

We are measuring the BAO peak in the two-point correlation function at scales of $r_{bao} \approx 100 - 110\, h^{-1}$Mpc. In order to analyse a large set of catalogues, spanning a wide redshifts range for several cosmic tracers, we used the Box1mr of the Magneticum simulations, which has, as discussed, a box side of $r_{box} = 896\, h^{-1}$Mpc. This box is sufficiently large to significantly detect the BAO peak, however, since the relation $r_{bao} \ll r_{box}$ is not valid, we expect to be affected by cosmic variance. However, since this thesis aims at estimating the effects of the reconstruction on the α parameter accuracy, i.e. the fraction between α errors pre- and post-reconstruction, and not at the absolute values of α and its error, cosmic variance is not a main issue.
We can notice that most of all the inferred α estimations performed in the previous sections are significantly different from unity. This is expected, though we used the fiducial cosmological model of Magneticum Simulations, due to the cosmic variance, which can shift the BAO peak.
To confirm such expectations, we have performed a simple test. We have used a galaxy cluster catalogue with the same mass cut of $M > 10^{13}\, M_\odot$ applied in the previous section, but using the Box0mr of the Magneticum Simulations. The latter is the largest simulation of the whole Magneticum set, with a $2668\, h^{-1}$Mpc box side (19.4 Gpc^3 of

cosmological volume), and a resolution of 2×4536^3 particles. This simulation has been set with an identical cosmological model of the Box1mr. Using the same methods and cosmological models, we have estimated the α parameter in the largest simulation. If the α parameter inferred using the Box0mr is found consistent to unity, the methods used is confirmed corrected, and all the deviations from $\alpha = 1$ must be attributed to cosmic variance, since the only variation between the procedures is the cosmological volume of the simulations. We have modelled the two-point correlation function of the galaxy clusters with $M > 10^{13}\, M_{\odot}$ in real space, at $z = 0.47$ (a value close to $z = 0.52$, used in the previous analyses), with the same procedure adopted in section 7.2 and described in section 6.6. We have detected the BAO peak with a 11σ significance, and the isotropic shift inferred is $\alpha = 1 \pm 0.01$. Thus, we can conclude that any deviation from the unity of the α parameter for Box1mr is mainly caused by the cosmic variance. Figure (7.15) shows the best-fit models for the galaxy clusters with $M > 10^{13}\, M_{\odot}$, in real space and before the reconstruction using the Box0mr, and in redshift space, for both pre- and post-reconstruction, using the Box1mr.

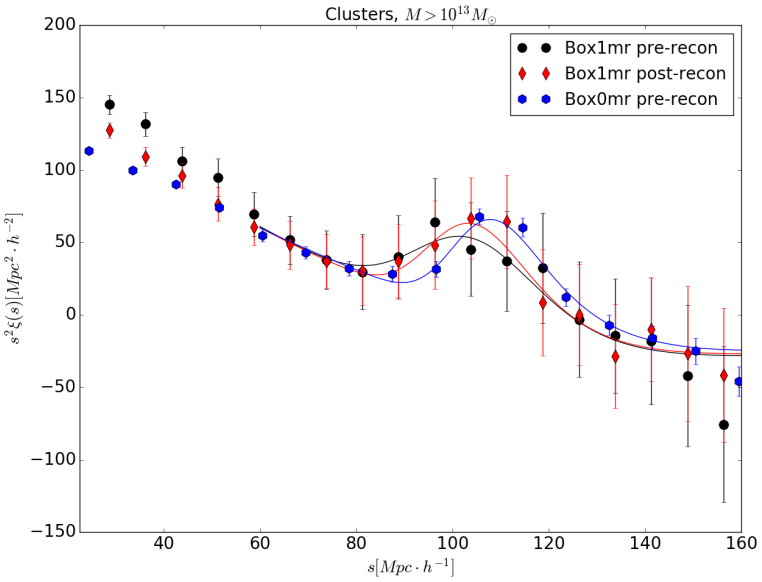

Figure 7.15: Two-point correlation function, measured in real space, at $z = 0.47$, using the Box0mr of Magneticum simulations (blue hexagons), and in redshift space, at $z = 0.52$, using the Box1mr (black circles), for galaxy clusters with a mass cut of $M > 10^{13}\, M_{\odot}$. The red diamonds represent the post-reconstruction correlation function, computed using the Box1mr at $z = 0.52$. The solid lines represent the BAO best-fit models, computed using the Box0mr (blue) and the Box1mr, both reconstructed (red) and not (black). The error bars are computed with the Jackknife method, using 125 resampling. Notice that, as expected, the correlation function computed using the Box0mr has a better accuracy with respect to the ones computed using the Box1mr.

Clearly the BAO peaks measured before the reconstruction, using the Box0mr and the Box1mr, are centered at different scales. In particular, the BAO peak measured using the largest simulation is detected at larger scales. Reconstructing the density field in the Box1mr, the BAO peak is shifted toward larger scales, because the method applied

takes into account the displacement field due to non linear evolution of structures. Nevertheless, even by reconstructing the density field we cannot take into account the cosmic variance in the smaller simulation. As a final result, the BAO peak is detected at the smaller scale in the Box1mr pre-reconstruction and at the larger scale in the Box0mr, whit respect to the post-reconstruction peak in the Box1mr, that is found between the other two.

7.3 Constraining the main cosmological parameters

The α parameter is directly related to the main cosmological parameters through equation (5.51). Thus, by constraining the α parameter, we also constrain a function of the Hubble parameter $H(z)$, and so $\Omega_{0,m}$ and $\Omega_{0,}$, where $\Omega_{0,\Lambda} = 1 - \Omega_{0,m}$. We have modelled the α parameters estimated in the previous sections, to quantify the effect of the reconstruction in increasing the accuracy of the estimation of these paramount cosmological parameters. The model used is the one described by equation (5.51). For each cosmic tracer, we have combined the α parameters, inferred by modelling the BAO peak, at all the redshifts considered, assuming that the different mock catalogues are independent. We have fixed the fiducial sound horizon, $r_{s,f}$, and volume-averaged distance, $D_{V,f}$, to the values provided by the cosmological model adopted by the Magneticum Simulations (see section 6.1). In an analogous way to the BAO modelling, explained in details in section 6.6, we have computed the posterior of the free parameter $\Omega_{0,m}$ by using a Gaussian Likelihood and the MCMC chains. As a result, we found that the reconstruction method improve the accuracy of $\Omega_{0,m}$ by a factor ≈ 1.5 using galaxies, ≈ 1.28 using clusters, and ≈ 1.12 using AGN as tracers of the cosmic density field.

7.4 Discussion

The reconstruction is expected to be more effective for small objects at low redshifts, because of the higher non-linearity of such structures (e.g. D. J. Eisenstein, H.-J. Seo, Sirko, et al., 2007). Indeed, we found that the reconstruction improves the constraints on α by a factor ≈ 1.7 for galaxies, ≈ 1.6 for AGN and ≈ 1.35 for clusters, at $z = 0.2$ in perfect agreement with the theory, and with past measurements in the galaxy case (e.g. D. H. Weinberg et al., 2013 and references therein). At this redshift, the fiducial volume distance is $D_{V,f}(z = 0.2) = 802$ Mpc. Assuming a sound horizon equal to the fiducial one, we can infer a volume averaged-distance of 862 ± 12 Mpc by reconstructing the galaxy catalogue, that is a 1.4% distance measurement, with respect to a 2.4% of pre-reconstruction. In analogous way, we found that the distance measurements before and after the reconstruction for galaxy clusters have a 2% and a 1.5% accuracy, respectively. In the AGN case it is found a 5.6% accuracy for the distance measurement before the reconstruction, and a 3.6% accuracy after applying the technique. Notice that, as expected, the reconstruction efficacy degrades at higher redshifts. The more linear behaviour of structures at high redshifts is the reason why they do not need a reconstruction of the density field. In other words, we can say that, due to the high redshift, the displacements of objects is short, thus the reconstruction method is not effective. Figure (7.16) shows the fraction between the α uncertainties before and after the reconstruction, as a function of the redshift. Linear regressions for galaxies, clusters and AGN are overplotted, excluding the AGN point at $z = 2$, that represents a non-detection. We notice that the AGN goes faster to unity, that is where the

reconstruction is ineffective, with respect to clusters and galaxies. However, at $z = 1.5$, the reconstruction can improve the constraint accuracy on α by a factor ≈ 1.3. The reconstruction technique is found to be more effective for galaxy tracers. At $z = 2$, we still expect a ≈ 1.4 factor between the pre- and post-reconstruction errors of α, having a 2.4% distance measurement pre-reconstruction and a 1.8% measurement post-reconstruction.

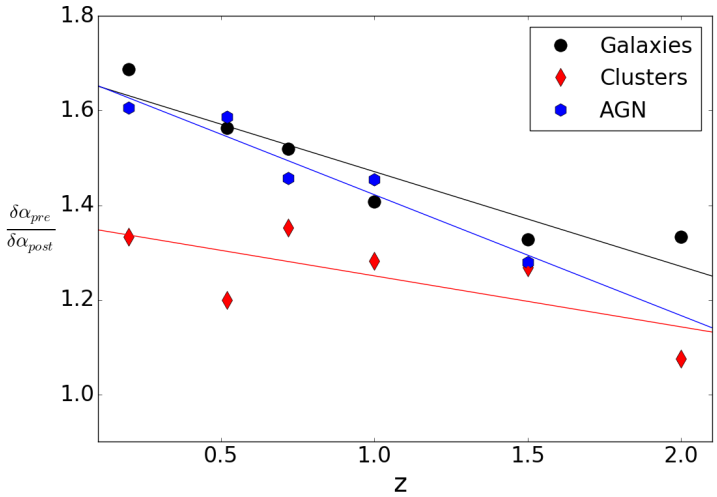

Figure 7.16: Fraction between pre- and post-reconstruction α uncertainties as a function of the redshift, for galaxies (black circles), clusters (red diamonds) and AGN (blue hexagons). The solid lines are the linear regressions of the points, black for galaxies, red for clusters and blue for AGN. The AGN point at $z = 2.$ was not considered, as it represents a non-detection of the BAO.

It is important to notice that our galaxy sample density spans from $n = 4.5 \times 10^{-3} h^3 \mathrm{Mpc}^{-3}$ at $z = 0.2$ to $n = 1.2 \times 10^{-3} h^3 \mathrm{Mpc}^{-3}$ at $z = 2$. For comparison, the CMASS sample of BOSS has a number density of $n = 3 \times 10^{-4} h^3 \mathrm{Mpc}^{-3}$, the WiggleZ $n = 2 \times 10^{-4} h^3 \mathrm{Mpc}^{-3}$ while Euclid plans to have number density in the range of $n = 0.15 - 4.8 \times 10^{-3} h^3 \mathrm{Mpc}^{-3}$ (depending on the redshift of the subsample) and J-PAS between $10^{-3} - 10^{-2} h^3 \mathrm{Mpc}^{-3}$ (see Angulo, S. D. White, et al., 2014 and references therein). On the other hand, the number density of galaxy clusters in the Box1mr goes from $n = 7 \times 10^{-4} h^3 \mathrm{Mpc}^{-3}$ at $z = 0.2$ to $n = 2 \times 10^{-4} h^3 \mathrm{Mpc}^{-3}$ at $z = 2$, while the AGN number density goes from $n = 1.3 \times 10^{-3} h^3 \mathrm{Mpc}^{-3}$ at $z = 0.2$ to $n = 1 \times 10^{-4} h^3 \mathrm{Mpc}^{-3}$ at $z = 2$.

The scatter of α constraints from galaxy clusters is higher with respect to the other objects, as expected due to shot noise. Furthermore, the cluster linear regression has a more gentle slope with respect to galaxies and AGN. This means that, even if the reconstruction is less effective for clusters compared to the other cosmic tracers, this technique can still provide some improvements on cosmological constraints. In fact, we found that, by using galaxy clusters as tracers of the cosmic density field, the reconstruction improves the accuracy of $\Omega_{0,m}$ by a factor 1.28.

Chapter 8

Conclusions and future perspectives

"Every year is getting shorter; never seem to find the time
Plans that either come to naught
or half a page of scribbled lines
Hanging on in quiet desperation is the English way
The time is gone, the song is over
Thought I'd something more to say."

Pink Floyd, Time, The Dark Side of the Moon (1973)

The BAO provides one of the most accurate probes of the accelerated expansion of the Universe, and it is paramount to investigate the Dark Energy nature. Large part of its power is in the accuracy of its theoretical modelling. By reconstructing the density field, it is possible to enlarge significantly the constraining power of the BAO. In this thesis, we have analysed galaxy, cluster and AGN mock catalogues from the Magneticum simulation Box1mr, a hydrodynamical simulation of cosmological volume of 0.719 Gpc^3, at redshifts $z = 0.2$, $z = 0.52$, $z = 0.72$, $z = 1.$, $z = 1.5$, $z = 2$. This is the most extensive investigation on the BAO reconstruction method for redshift range and cosmic tracers used. The density of our mock samples are consistent with the ones of the main BAO near-future projects, such as Euclid and J-PAS. We have implemented and tested a reconstruction code, and we have used it to reconstruct the density field of Magneticum mocks. We have modelled the BAO peak in the angle-averaged two-point correlation function, finding the constraints on the isotropic shift, α, before and after the reconstruction.
The main results presented in this thesis can be summarized as follows.

- The bias was estimated by exploiting the projected correlation function, a method which ensures results as close as possible to the ones obtainable with real data.
- The density field of cosmic tracers obtained from the considered mock catalogues was reconstructed by using a brand new algorithm, that we have implemented in the CBL and tested.
- We have modelled the BAO peak in the redshift space, both before and after the application of the reconstruction method.

- The fraction between the constraint accuracies before and after the reconstruction has a linear-like dependency on the redshift, with different slopes for the different cosmic tracers considered. In particular, AGN have a steeper slope, and galaxy clusters a more gentle slope, with respect to galaxies.

- The reconstruction reduces the value of the Σ_{NL} parameter of the BAO best-fit models up to $8h^{-1}$Mpc for galaxies at $z = 0.2$. The reducing factor of Σ_{NL} for different cosmic tracers has a redshift evolution similar to the reducing factor of the α constraints accuracy. This is a clear confirmation that the reconstruction method improves the constraints on the cosmological parameters, by partially correcting the non-linearities of cosmic structures. We found that also the value of Σ_{NL} for galaxy clusters is reduced by the reconstruction technique, even if a little less than the other two tracers considered in this work.

- By reducing the Σ_{NL} of the model, the reconstruction technique improves the significance of the BAO peak detection. We found that the BAO peak detection in the AGN catalogue at $z = 0.2$ has a 1σ significance before the reconstruction, while it has a 3σ significance after. We found several other improvements on the significance of the BAO detection, above all for AGN and galaxies. Galaxy clusters, due to their large size, are quasi-linear structures. As expected, we found that they have already a lower Σ_{NL} with respect to the other tracers, thus the application of the reconstruction technique, in this case, is less necessary.

- The reconstruction technique is more effective with galaxies, because of their strong non-linear evolutions. This technique can improve the α constraints by a factor 1.8 at $z = 2$, and 1.4 at $z = 2$. This, combined to the higher number of galaxies with respect to AGN and galaxy clusters, makes the distance measurements inferred with galaxy catalogues the most accurate.

- The reconstruction has a similar effect on AGN and galaxies, although the efficacy on AGN seems to degrade a little faster with respect to galaxies.

- The reconstruction, as said, is less important for galaxy clusters, due to their intrinsic linearity. Thus, these tracers do not strictly need the use of such techniques, confirming the results of previous works, e.g. Veropalumbo et al. (2014); Veropalumbo et al. (2016). This is a further demonstration of the power of galaxy clusters as tracers of the cosmic density field. Nevertheless, we found that even the cluster performances are a little improved by using the reconstruction. In particular, imposing a cluster mass threshold of $M = 10^{13} M_{\odot}$, the reconstruction improves the constraints on the isotropic shift by a factor $1.3 - 1.5$ in a redshift range $0.2 \leq z \leq 0.72$. Interesting, this factor seems to have a weak dependency on the redshift.

- By modelling the α parameters obtained by the BAO analysis, we have constrained the paramount cosmological parameter $\Omega_{0,m}$. We found that, by reconstructing the density field, the accuracy on the estimation of $\Omega_{0,m}$ improves by a factor ≈ 1.5 using galaxies, ≈ 1.28 using clusters, and ≈ 1.12 using AGN as cosmic tracers.

We plan to extend this analysis to anisotropic clustering, modelling the clustering wedges and multipoles to fully exploit the BAO cosmological potential. To do this, we will use the Box0mr of the Magneticum simulations, which has a cosmological volume

of 19.4 Gpc^3, ensuring an extraordinary statistical precision. Moreover, we want to apply further cuts on AGN and cluster catalogues, to investigate how the effects of the reconstruction vary for the different sample selections. Finally, we aim at analysing real data catalogues. In particular, we want to extend the analysis by Veropalumbo et al. (2016), performed on galaxy cluster catalogues within the redshift range considered in this thesis. Since we found that reconstruction improves the constraints in α, and then in the main cosmological parameters, also in cluster catalogues, we want to try our reconstruction code on the cluster samples selected from BOSS and SDSS DR7. Moreover, we want to apply the BAO reconstruction analysis to the incoming J-PAS survey. This is the natural combination of the theoretical work, performed with mock samples, discussed in this thesis, with the work carried out at the Centro de Estudios de Física del Cosmos de Aragón (CEFCA) thanks to a summer fellowship, using data from the J-PLUS survey (Cenarro et al., 2015). This survey is a J-PAS precursor, useful for both the photometric calibrations of the incoming bigger survey and the scientific investigation of the near Universe. In particular, at CEFCA we have performed galaxy clustering measurements, in both configuration and Fourier space. Moreover, we have investigated how systematics errors, such as stellar contamination, star density, seeing, signal-to-noise ratio, atmospheric conditions, etc., could affect the measurements. As a final result of the work, we have developed a pipeline for the analysis of systematic errors in clustering measurements. The J-PLUS survey does not allow to perform BAO analyses, however the familiarity with the J-PLUS facility is a good starting point on the perspective of the incoming J-PAS, that is one of the most promising BAO survey in the very next future.

Bibliography

Abazajian, K. N., J. K. Adelman-McCarthy, M. A. Agüeros, S. S. Allam, C. Allende Prieto, et al. (2009). "The Seventh Data Release of the Sloan Digital Sky Survey". In: *The Astrophysical Journal Supplement* 182, 543-558, pp. 543–558. DOI: 10.1088/0067-0049/182/2/543. arXiv: 0812.0649 (cit. on p. 76).

Abbott, B. P., R. Abbott, T. D. Abbott, M. R. Abernathy, F. Acernese, K. Ackley, C. Adams, T. Adams, P. Addesso, R. X. Adhikari, et al. (2016). "Observation of Gravitational Waves from a Binary Black Hole Merger". In: *Physical Review Letters* 116.6, 061102, p. 061102. DOI: 10.1103/PhysRevLett.116.061102. arXiv: 1602.03837 [gr-qc] (cit. on pp. xiii, 3).

Abdalla, F. B. and S. Rawlings (2005). "Probing dark energy with baryonic oscillations and future radio surveys of neutral hydrogen". In: *Monthly Notices of Royal Astronomical Society* 360, pp. 27–40. DOI: 10.1111/j.1365-2966.2005.08650.x. eprint: astro-ph/0411342 (cit. on p. 81).

Achitouv, I. and C. Blake (2015). "Improving reconstruction of the baryon acoustic peak: The effect of local environment". In: *Physical Review D* 92.8, 083523, p. 083523. DOI: 10.1103/PhysRevD.92.083523. arXiv: 1507.03584 (cit. on p. 69).

Ade, PAR, N Aghanim, M Arnaud, M Ashdown, J Aumont, C Baccigalupi, AJ Banday, RB Barreiro, JG Bartlett, N Bartolo, et al. (2016). "Planck 2015 results-XIII. Cosmological parameters". In: *Astronomy and Astrophysics* 594, A13 (cit. on pp. xiv, 14).

Alam, S., M. Ata, S. Bailey, F. Beutler, D. Bizyaev, et al. (2016). "The clustering of galaxies in the completed SDSS-III Baryon Oscillation Spectroscopic Survey: cosmological analysis of the DR12 galaxy sample". In: *ArXiv e-prints*. arXiv: 1607.03155 (cit. on pp. 79, 80, 83–85).

Alcock, C. and B. Paczynski (1979). "An evolution free test for non-zero cosmological constant". In: *Nature* 281, p. 358. DOI: 10.1038/281358a0 (cit. on p. 40).

Anderson, L., E. Aubourg, S. Bailey, D. Bizyaev, M. Blanton, et al. (2012). "The clustering of galaxies in the SDSS-III Baryon Oscillation Spectroscopic Survey: baryon acoustic oscillations in the Data Release 9 spectroscopic galaxy sample". In: *Monthly Notices of Royal Astronomical Society* 427, pp. 3435–3467. DOI: 10.1111/j.1365-2966.2012.22066.x. arXiv: 1203.6594 (cit. on p. 72).

Anderson, L., É. Aubourg, S. Bailey, F. Beutler, V. Bhardwaj, et al. (2014). "The clustering of galaxies in the SDSS-III Baryon Oscillation Spectroscopic Survey: baryon acoustic oscillations in the Data Releases 10 and 11 Galaxy samples". In: *Monthly Notices of Royal Astronomical Society* 441, pp. 24–62. DOI: 10.1093/mnras/stu523. arXiv: 1312.4877 (cit. on p. 72).

Angulo, R. E. et al. (2005). "Constraints on the dark energy equation of state from the imprint of baryons on the power spectrum of clusters". In: *Monthly Notices of*

Royal Astronomical Society 362, pp. L25–L29. DOI: 10.1111/j.1745-3933.2005.00067.x. eprint: astro-ph/0504456 (cit. on p. 75).

Angulo, R. E., C. M. Baugh, C. S. Frenk, and C. G. Lacey (2008). "The detectability of baryonic acoustic oscillations in future galaxy surveys". In: *Monthly Notices of Royal Astronomical Society* 383, pp. 755–776. DOI: 10.1111/j.1365-2966.2007.12587.x. eprint: astro-ph/0702543 (cit. on p. 60).

Angulo, R. E., S. D. M. White, V. Springel, and B. Henriques (2014). "Galaxy formation on the largest scales: the impact of astrophysics on the baryonic acoustic oscillation peak". In: *Monthly Notices of Royal Astronomical Society* 442, pp. 2131–2144. DOI: 10.1093/mnras/stu905. arXiv: 1311.7100 (cit. on p. 122).

Ansari, R., J. -. Le Goff, C. Magneville, M. Moniez, N. Palanque-Delabrouille, J. Rich, V. Ruhlmann-Kleider, and C. Yèche (2008). "Reconstruction of HI power spectra with radio-interferometers to study dark energy". In: *ArXiv e-prints*. arXiv: 0807.3614 (cit. on p. 75).

Aubourg, É., S. Bailey, J. E. Bautista, F. Beutler, V. Bhardwaj, et al. (2015). "Cosmological implications of baryon acoustic oscillation measurements". In: *Physical Review D* 92.12, 123516, p. 123516. DOI: 10.1103/PhysRevD.92.123516. arXiv: 1411.1074 (cit. on pp. 79, 83, 85).

Bagla, J. S., H. K. Jassal, and T. Padmanabhan (2003). "Cosmology with tachyon field as dark energy". In: *Physical Review D* 67.6, 063504, p. 063504. DOI: 10.1103/PhysRevD.67.063504. eprint: astro-ph/0212198.

Bamba, K., M. W. Hossain, R. Myrzakulov, S. Nojiri, and M. Sami (2014). "Cosmological investigations of (extended) nonlinear massive gravity schemes with nonminimal coupling". In: *Physical Review D* 89.8, 083518, p. 083518. DOI: 10.1103/PhysRevD.89.083518. arXiv: 1309.6413 [hep-th] (cit. on p. 19).

Bandura, K., G. E. Addison, M. Amiri, J. R. Bond, D. Campbell-Wilson, et al. (2014). "Canadian Hydrogen Intensity Mapping Experiment (CHIME) pathfinder". In: *Ground-based and Airborne Telescopes V*. Vol. 9145. proc.SPIE, p. 914522. DOI: 10.1117/12.2054950. arXiv: 1406.2288 [astro-ph.IM] (cit. on p. 81).

Barnes, J. and P. Hut (1986). "A hierarchical O(N log N) force-calculation algorithm". In: *Nature* 324, pp. 446–449. DOI: 10.1038/324446a0 (cit. on p. 51).

Benitez, N., R. Dupke, M. Moles, L. Sodre, J. Cenarro, et al. (2014). "J-PAS: The Javalambre-Physics of the Accelerated Universe Astrophysical Survey". In: *ArXiv e-prints*. arXiv: 1403.5237 [astro-ph.CO] (cit. on p. 80).

Benítez, N., E. Gaztañaga, R. Miquel, F. Castander, M. Moles, et al. (2009). "Measuring Baryon Acoustic Oscillations Along the Line of Sight with Photometric Redshifts: The PAU Survey". In: *The Astrophysical Journal* 691, pp. 241–260. DOI: 10.1088/0004-637X/691/1/241. arXiv: 0807.0535 (cit. on p. 74).

Bennett, C. L., M. Halpern, G. Hinshaw, N. Jarosik, A. Kogut, et al. (2003). "First-Year Wilkinson Microwave Anisotropy Probe (WMAP) Observations: Preliminary Maps and Basic Results". In: *The Astrophysical Journal Supplement Series* 148, pp. 1–27. DOI: 10.1086/377253. eprint: astro-ph/0302207 (cit. on p. 58).

Bertone, G., D. Hooper, and J. Silk (2005). "Particle dark matter: evidence, candidates and constraints". In: *Physics Reports* 405, pp. 279–390. DOI: 10.1016/j.physrep.2004.08.031. eprint: hep-ph/0404175 (cit. on p. 14).

Beutler, Florian, Shun Saito, Hee-Jong Seo, Jon Brinkmann, Kyle S Dawson, Daniel J Eisenstein, Andreu Font-Ribera, Shirley Ho, Cameron K McBride, Francesco Montesano, et al. (2014). "The clustering of galaxies in the SDSS-III Baryon Oscillation Spectroscopic Survey: testing gravity with redshift space distortions

using the power spectrum multipoles". In: *Monthly Notices of Royal Astronomical Society* 443.2, pp. 1065–1089 (cit. on p. 43).

Blake, C. and K. Glazebrook (2003). "Probing Dark Energy Using Baryonic Oscillations in the Galaxy Power Spectrum as a Cosmological Ruler". In: *The Astrophysical Journal* 594, pp. 665–673. DOI: 10.1086/376983. eprint: astro-ph/0301632 (cit. on p. 58).

Blake, C., E. A. Kazin, F. Beutler, T. M. Davis, D. Parkinson, et al. (2011). "The WiggleZ Dark Energy Survey: mapping the distance-redshift relation with baryon acoustic oscillations". In: *Monthly Notices of Royal Astronomical Society* 418, pp. 1707–1724. DOI: 10.1111/j.1365-2966.2011.19592.x. arXiv: 1108.2635 (cit. on pp. 73, 80).

Bojowald, M. (2008). "Loop Quantum Cosmology". In: *Living Reviews in Relativity* 11, 4, p. 4. DOI: 10.12942/lrr-2008-4 (cit. on p. 17).

Bond, J. R. and G. Efstathiou (1984). "Cosmic background radiation anisotropies in universes dominated by nonbaryonic dark matter". In: *The Astrophysical Journal Letters* 285, pp. L45–L48. DOI: 10.1086/184362 (cit. on p. 58).

Bondi, H. and T. Gold (1948). "The Steady-State Theory of the Expanding Universe". In: *Monthly Notices of Royal Astronomical Society* 108, p. 252. DOI: 10.1093/mnras/108.3.252 (cit. on p. 3).

Bondi, Hermann and Fred Hoyle (1944). "On the mechanism of accretion by stars". In: *Monthly Notices of Royal Astronomical Society* 104.5, pp. 273–282 (cit. on p. 89).

Bondi, HJ (1952). "On spherically symmetrical accretion". In: *Monthly Notices of the Royal Astronomical Society* 112.2, pp. 195–204 (cit. on p. 89).

Buchert, Th (1993). "Lagrangian perturbation theory-A key-model for large-scale structure". In: *Astronomy and Astrophysics* 267, pp. L51–L54 (cit. on p. 30).

Burden, A., W. J. Percival, and C. Howlett (2015). "Reconstruction in Fourier space". In: *Monthly Notices of Royal Astronomical Society* 453, pp. 456–468. DOI: 10.1093/mnras/stv1581. arXiv: 1504.02591 (cit. on pp. 64, 65).

Burden, A., W. J. Percival, M. Manera, A. J. Cuesta, M. Vargas Magana, and S. Ho (2014). "Efficient reconstruction of linear baryon acoustic oscillations in galaxy surveys". In: *Monthly Notices of Astronomical Royal Society* 445, pp. 3152–3168. DOI: 10.1093/mnras/stu1965. arXiv: 1408.1348 (cit. on pp. 64, 65).

Busca, N. G., T. Delubac, J. Rich, S. Bailey, A. Font-Ribera, et al. (2013). "Baryon acoustic oscillations in the Lyα forest of BOSS quasars". In: *Astronomy and Astrophysics* 552, A96, A96. DOI: 10.1051/0004-6361/201220724. arXiv: 1211.2616 [astro-ph.CO] (cit. on p. 75).

Campanelli, L., P. Cea, G. L. Fogli, and A. Marrone (2011). "Testing the isotropy of the Universe with type Ia supernovae". In: *Physical Review D* 83.10, 103503, p. 103503. DOI: 10.1103/PhysRevD.83.103503. arXiv: 1012.5596 [astro-ph.CO] (cit. on p. 3).

Cao, F. J., H. J. de Vega, and N. G. Sánchez (2004). "Quantum inflaton, primordial perturbations, and CMB fluctuations". In: *Physical Review D* 70.8, 083528, p. 083528. DOI: 10.1103/PhysRevD.70.083528. eprint: astro-ph/0406168 (cit. on p. 53).

Cenarro, J., A. Marin-Franch, M. Moles, D. Cristobal-Hornillos, C. Mendes de Oliveira, and L. Sodre (2015). "J-PLUS: The Javalambre Photometric Local Universe Survey". In: *IAU General Assembly* 22, 2257478, p. 2257478 (cit. on p. 125).

Chabrier, Gilles (2003). "Galactic Stellar and Substellar Initial Mass FunctionThe page charges for this Review were partially covered by a generous gift from a PASP supporter." In: *Publications of the Astronomical Society of the Pacific* 115.809, p. 763 (cit. on p. 89).

Chang, T.-C., U.-L. Pen, J. B. Peterson, and P. McDonald (2008). "Baryon Acoustic Oscillation Intensity Mapping of Dark Energy". In: *Physical Review Letters* 100.9, 091303, p. 091303. DOI: 10.1103/PhysRevLett.100.091303. arXiv: 0709.3672 (cit. on p. 75).

Christodoulou, L., C. Eminian, J. Loveday, P. Norberg, I. K. Baldry, et al. (2012). "Galaxy And Mass Assembly (GAMA): colour- and luminosity-dependent clustering from calibrated photometric redshifts". In: *Monthly Notices of Royal Astronomical Society* 425, pp. 1527–1548. DOI: 10.1111/j.1365-2966.2012.21434.x. arXiv: 1206.0943 (cit. on p. 35).

Chuang, C.-H. and Y. Wang (2012). "Measurements of H(z) and $D_A(z)$ from the two-dimensional two-point correlation function of Sloan Digital Sky Survey luminous red galaxies". In: *Monthly Notices of Royal Astronomical Society* 426, pp. 226–236. DOI: 10.1111/j.1365-2966.2012.21565.x. arXiv: 1102.2251 (cit. on p. 73).

Cimatti, A, R Laureijs, B Leibundgut, A Reéfrégier, N Thatte, R Nichol, M Steinmetz, E Valentijn, P Rosati, and S Lilly (2009). *Euclid assessment study report for the ESA cosmic visions*. Tech. rep. (cit. on p. 81).

Cole, S., W. J. Percival, J. A. Peacock, P. Norberg, C. M. Baugh, et al. (2005). "The 2dF Galaxy Redshift Survey: power-spectrum analysis of the final data set and cosmological implications". In: *Monthly Notices of Royal Astronomical Society* 362, pp. 505–534. DOI: 10.1111/j.1365-2966.2005.09318.x. eprint: astro-ph/0501174 (cit. on p. 58).

Coles, P. and F. Lucchin (2002). *Cosmology: The Origin and Evolution of Cosmic Structure, Second Edition*. John Wiley and Sons, p. 512 (cit. on pp. 4, 11, 34, 35).

Crocce, M. and R. Scoccimarro (2008). "Nonlinear evolution of baryon acoustic oscillations". In: *Physical Review D* 77.2, 023533, p. 023533. DOI: 10.1103/PhysRevD.77.023533. arXiv: 0704.2783 (cit. on pp. 60, 61).

Crocce, Martín and Román Scoccimarro (2006). "Renormalized cosmological perturbation theory". In: *Physical Review D* 73 (6), p. 063519. DOI: 10.1103/PhysRevD.73.063519. URL: http://link.aps.org/doi/10.1103/PhysRevD.73.063519 (cit. on p. 60).

Davis, M. and M. J. Geller (1976). "Galaxy Correlations as a Function of Morphological Type". In: *The Astrophysical Journal* 208, pp. 13–19. DOI: 10.1086/154575 (cit. on p. 35).

Davis, M. and P. J. E. Peebles (1977). "On the integration of the BBGKY equations for the development of strongly nonlinear clustering in an expanding universe". In: *Astrophysical Journal Supplement Series* 34, pp. 425–450. DOI: 10.1086/190456 (cit. on p. 41).

Dawson, K. S., J.-P. Kneib, W. J. Percival, S. Alam, F. D. Albareti, et al. (2016). "The SDSS-IV Extended Baryon Oscillation Spectroscopic Survey: Overview and Early Data". In: *The Astrophysical Journal* 151, 44, p. 44. DOI: 10.3847/0004-6256/151/2/44. arXiv: 1508.04473 (cit. on p. 80).

Dawson, K. S., D. J. Schlegel, C. P. Ahn, S. F. Anderson, É. Aubourg, et al. (2013). "The Baryon Oscillation Spectroscopic Survey of SDSS-III". In: *The Astrophysical Journal* 145, 10, p. 10. DOI: 10.1088/0004-6256/145/1/10. arXiv: 1208.0022 (cit. on p. 76).

de la Torre, S. and L. Guzzo (2012). "Modelling non-linear redshift-space distortions in the galaxy clustering pattern: systematic errors on the growth rate parameter". In: *Monthly Notices of Royal Astronomical Society* 427, pp. 327–342. DOI: 10.1111/j.1365-2966.2012.21824.x. arXiv: 1202.5559 (cit. on p. 44).

de la Torre, S., L. Guzzo, J. A. Peacock, E. Branchini, A. Iovino, et al. (2013). "The VIMOS Public Extragalactic Redshift Survey (VIPERS) . Galaxy clustering and redshift-space distortions at z $\simeq$ 0.8 in the first data release". In: *Astronomy and Astrophysics* 557, A54, A54. DOI: 10.1051/0004-6361/201321463. arXiv: 1303.2622 (cit. on p. 44).

Delubac, T., J. E. Bautista, N. G. Busca, J. Rich, D. Kirkby, et al. (2015). "Baryon acoustic oscillations in the Lyα forest of BOSS DR11 quasars". In: *Astronomy and Astrophysics* 574, A59, A59. DOI: 10.1051/0004-6361/201423969. arXiv: 1404.1801 (cit. on pp. 75, 77, 82).

Di Matteo, Tiziana, Volker Springel, and Lars Hernquist (2005). "Energy input from quasars regulates the growth and activity of black holes and their host galaxies". In: *Nature* 433.7026, pp. 604–607 (cit. on p. 89).

Dolag, K, S Borgani, G Murante, and V Springel (2009). "Substructures in hydrodynamical cluster simulations". In: *Monthly Notices of the Royal Astronomical Society* 399.2, pp. 497–514 (cit. on p. 89).

Dolag, K, F Vazza, Gf Brunetti, and G Tormen (2005). "Turbulent gas motions in galaxy cluster simulations: the role of smoothed particle hydrodynamics viscosity". In: *Monthly Notices of Royal Astronomical Society* 364.3, pp. 753–772 (cit. on p. 88).

Efstathiou, G. and J. R. Bond (1986). "Microwave background fluctuations and dark matter". In: *Philosophical Transactions of the Royal Society of London Series A* 320, pp. 585–594. DOI: 10.1098/rsta.1986.0139 (cit. on p. 58).

Efstathiou, George, M Davis, SDM White, and CS Frenk (1985). "Numerical techniques for large cosmological N-body simulations". In: *The Astrophysical Journal Supplement Series* 57, pp. 241–260 (cit. on p. 51).

Einstein, A. (1905). "Zur Elektrodynamik bewegter Körper". In: *Annalen der Physik* 322, pp. 891–921. DOI: 10.1002/andp.19053221004 (cit. on p. 1).

— (1915). "Zur allgemeinen Relativitätstheorie". In: *Sitzungsberichte der Königlich Preußischen Akademie der Wissenschaften (Berlin), Seite 778-786.* (Cit. on p. 1).

Eisenstein, D. (2002). "Large-Scale Structure Future Surveys". In: *Next Generation Wide-Field Multi-Object Spectroscopy*. Ed. by M. J. I. Brown and A. Dey. Vol. 280. Astronomical Society of the Pacific Conference Series, p. 35 (cit. on p. 58).

Eisenstein, D. J. (2005a). "Dark energy and cosmic sound [review article]". In: *New Astronomy Reviews* 49, pp. 360–365. DOI: 10.1016/j.newar.2005.08.005 (cit. on p. 58).

— (2005b). *The Acoustic Peak Primer*. URL: https://www.cfa.harvard.edu/~deisenst/acousticpeak/spherical_acoustic.pdf (cit. on p. 57).

Eisenstein, D. J., J. Annis, J. E. Gunn, A. S. Szalay, A. J. Connolly, et al. (2001). "Spectroscopic Target Selection for the Sloan Digital Sky Survey: The Luminous Red Galaxy Sample". In: *The Astrophysical Journal* 122, pp. 2267–2280. DOI: 10.1086/323717. eprint: astro-ph/0108153 (cit. on p. 74).

Eisenstein, D. J. and W. Hu (1998). "Baryonic Features in the Matter Transfer Function". In: *The Astrophysical Journal* 496, pp. 605–614. DOI: 10.1086/305424. eprint: astro-ph/9709112 (cit. on pp. 57, 58, 72).

Eisenstein, D. J., H.-J. Seo, E. Sirko, and D. N. Spergel (2007). "Improving Cosmological Distance Measurements by Reconstruction of the Baryon Acoustic Peak". In: *The Astrophysical Journal* 664, pp. 675–679. DOI: 10.1086/518712. eprint: astro-ph/0604362 (cit. on pp. xiv, 62, 65–67, 69, 70, 121).

Eisenstein, D. J., H.-J. Seo, and M. White (2007). "On the Robustness of the Acoustic Scale in the Low-Redshift Clustering of Matter". In: *The Astrophysical Journal* 664,

pp. 660–674. DOI: 10.1086/518755. eprint: astro-ph/0604361 (cit. on pp. 55, 60, 72).

Eisenstein, D. J., D. H. Weinberg, E. Agol, H. Aihara, C. Allende Prieto, et al. (2011). "SDSS-III: Massive Spectroscopic Surveys of the Distant Universe, the Milky Way, and Extra-Solar Planetary Systems". In: *The Astrophysical Journal* 142, 72, p. 72. DOI: 10.1088/0004-6256/142/3/72. arXiv: 1101.1529 [astro-ph.IM] (cit. on p. 76).

Eisenstein, D. J., I. Zehavi, D. W. Hogg, R. Scoccimarro, M. R. Blanton, et al. (2005). "Detection of the Baryon Acoustic Peak in the Large-Scale Correlation Function of SDSS Luminous Red Galaxies". In: *The Astrophysical Journal* 633, pp. 560–574. DOI: 10.1086/466512. eprint: astro-ph/0501171 (cit. on pp. xiv, 58, 59, 74).

Evrard, Guillaume and Peter Coles (1995). "Getting the measure of the flatness problem". In: *Classical and Quantum Gravity* 12.10, p. L93 (cit. on p. 14).

Ferland, G. J., K. T. Korista, D. A. Verner, J. W. Ferguson, J. B. Kingdon, and E. M. Verner (1998). "CLOUDY 90: Numerical Simulation of Plasmas and Their Spectra". In: *The Publications of the Astronomical Society of the Pacific* 110, pp. 761–778. DOI: 10.1086/316190 (cit. on p. 88).

Friedmann, A. (1922). "Über die Krümmung des Raumes". In: *Zeitschrift fur Physik* 10, pp. 377–386. DOI: 10.1007/BF01332580 (cit. on p. 9).

Fry, J. N. (1996). "The Evolution of Bias". In: *The Astrophysical Journal Letters* 461, p. L65. DOI: 10.1086/310006 (cit. on p. 36).

Gaspari, Matteo (2016). "Vincoli cosmologici dalle distorsioni geometriche della funzione di correlazione". MA thesis. Alma Mater Studiorum, University of Bologna. URL: http://amslaurea.unibo.it/9855/ (cit. on pp. 45, 46).

Gingold, Robert A and Joseph J Monaghan (1977). "Smoothed particle hydrodynamics: theory and application to non-spherical stars". In: *Monthly Notices of Royal Astronomical Society* 181.3, pp. 375–389 (cit. on p. 52).

Glazebrook, K. and C. Blake (2005). "Measuring the Cosmic Evolution of Dark Energy with Baryonic Oscillations in the Galaxy Power Spectrum". In: *The Astrophysical Journal* 631, pp. 1–20. DOI: 10.1086/432497. eprint: astro-ph/0505608 (cit. on p. 75).

Gong, Yungui, Mustapha Ishak, Anzhong Wang, et al. (2009). "Growth factor parametrization in curved space". In: *Physical Review D* 80.2, p. 023002 (cit. on p. 96).

Guth, A. H. (1981). "Inflationary universe: A possible solution to the horizon and flatness problems". In: *Physical Review D* 23, pp. 347–356. DOI: 10.1103/PhysRevD.23.347 (cit. on p. 18).

Guth, Alan H, David I Kaiser, and Yasunori Nomura (2014). "Inflationary paradigm after Planck 2013". In: *Physics Letters B* 733, pp. 112–119 (cit. on p. 18).

Guzzo, L., M. Scodeggio, B. Garilli, B. R. Granett, A. Fritz, et al. (2014). "The VIMOS Public Extragalactic Redshift Survey (VIPERS). An unprecedented view of galaxies and large-scale structure at $0.5 < z < 1.2$". In: *Astronomy and Astrophysics* 566, A108, A108. DOI: 10.1051/0004-6361/201321489. arXiv: 1303.2623 (cit. on p. 36).

Haardt, F. and P. Madau (2001). "Modelling the UV/X-ray cosmic background with CUBA". In: *Clusters of Galaxies and the High Redshift Universe Observed in X-rays*. Ed. by D. M. Neumann and J. T. V. Tran. eprint: astro-ph/0106018 (cit. on p. 88).

Hamilton, A. J. S. (1992). "Measuring Omega and the real correlation function from the redshift correlation function". In: *Astrophysical Journal Letters* 385, pp. L5–L8. DOI: 10.1086/186264 (cit. on p. 43).

— (1998). "Linear Redshift Distortions: A Review". In: *The Evolving Universe: Selected Topics on Large-Scale Structure and on the Properties of Galaxies*. Ed. by Donald Hamilton. Dordrecht: Springer Netherlands, pp. 185–275. ISBN: 978-94-011-4960-0. DOI: 10.1007/978-94-011-4960-0_17. URL: http://dx.doi.org/10.1007/978-94-011-4960-0_17 (cit. on p. 16).

Harrison, E. R. (1970). "Fluctuations at the Threshold of Classical Cosmology". In: *Physical Review D* 1, pp. 2726–2730. DOI: 10.1103/PhysRevD.1.2726 (cit. on p. 20).

Hawkins, E., S. Maddox, S. Cole, O. Lahav, D. S. Madgwick, et al. (2003). "The 2dF Galaxy Redshift Survey: correlation functions, peculiar velocities and the matter density of the Universe". In: *Monthly Notices of Royal Astronomical Society* 346, pp. 78–96. DOI: 10.1046/j.1365-2966.2003.07063.x. eprint: astro-ph/0212375 (cit. on pp. 42–44).

Heavens, A. F., R. Jimenez, and R. Maartens (2011). "Testing homogeneity with the fossil record of galaxies". In: *Journal of Cosmology and Astroparticle Physics* 2011.09, p. 035. URL: http://stacks.iop.org/1475-7516/2011/i=09/a=035 (cit. on p. 3).

Hill, G. J. and HETDEX Consortium (2016). "HETDEX and VIRUS: Panoramic Integral Field Spectroscopy with 35k Fibers". In: *Multi-Object Spectroscopy in the Next Decade: Big Questions, Large Surveys, and Wide Fields*. Ed. by I. Skillen, M. Barcells, and S. Trager. Vol. 507. Astronomical Society of the Pacific Conference Series, p. 393 (cit. on p. 80).

Hinshaw, G., M. R. Nolta, C. L. Bennett, R. Bean, O. Doré, et al. (2007). "Three-Year Wilkinson Microwave Anisotropy Probe (WMAP) Observations: Temperature Analysis". In: *The Astrophysical Journal* 170, pp. 288–334. DOI: 10.1086/513698. eprint: astro-ph/0603451 (cit. on p. xiv).

Hirschmann, Michaela, Klaus Dolag, Alexandro Saro, Lisa Bachmann, Stefano Borgani, and Andreas Burkert (2014). "Cosmological simulations of black hole growth: AGN luminosities and downsizing". In: *Monthly Notices of Royal Astronomical Society* 442.3, pp. 2304–2324 (cit. on p. 89).

Hoyle, Fred and Raymond A Lyttleton (1939). "The effect of interstellar matter on climatic variation". In: *Mathematical Proceedings of the Cambridge Philosophical Society*. Vol. 35. 03. Cambridge Univ Press, pp. 405–415 (cit. on p. 89).

Hu, W. and N. Sugiyama (1996). "Small-Scale Cosmological Perturbations: an Analytic Approach". In: *The Astrophysical Journal* 471, p. 542. DOI: 10.1086/177989. eprint: astro-ph/9510117 (cit. on pp. 57, 58).

Hu, W. and M. White (1996). "Acoustic Signatures in the Cosmic Microwave Background". In: *The Astrophysical Journal* 471, p. 30. DOI: 10.1086/177951. eprint: astro-ph/9602019 (cit. on p. 58).

Hui, Lam and Edmund Bertschinger (1996). "Local approximations to the gravitational collapse of cold matter". In: *The Astrophysical Journal* 471.1, p. 1 (cit. on p. 29).

Hütsi, G. (2010). "Power spectrum of the maxBCG sample: detection of acoustic oscillations using galaxy clusters". In: *Monthly Notices of Royal Astronomical Society* 401, pp. 2477–2489. DOI: 10.1111/j.1365-2966.2009.15824.x. arXiv: 0910.0492 (cit. on p. 75).

Ijjas, A., P. J. Steinhardt, and A. Loeb (2013). "Inflationary paradigm in trouble after Planck2013". In: *Physics Letters B* 723, pp. 261–266. DOI: 10.1016/j.physletb.2013.05.023. arXiv: 1304.2785 [astro-ph.CO] (cit. on p. 18).

— (2014). "Inflationary schism". In: *Physics Letters B* 736, pp. 142–146. DOI: 10.1016/j.physletb.2014.07.012 (cit. on p. 18).

Jones, D Heath, Will Saunders, Matthew Colless, Mike A Read, Quentin A Parker, Fred G Watson, Lachlan A Campbell, Daniel Burkey, Thomas Mauch, Lesa Moore, et al. (2004). "The 6dF Galaxy Survey: samples, observational techniques and the first data release". In: *Monthly Notices of the Royal Astronomical Society* 355.3, pp. 747–763 (cit. on p. 80).

Jungman, G., M. Kamionkowski, A. Kosowsky, and D. N. Spergel (1996). "Cosmological-parameter determination with microwave background maps". In: *Physical Review D* 54, pp. 1332–1344. DOI: 10.1103/PhysRevD.54.1332. eprint: astro-ph/9512139 (cit. on p. 58).

Kaiser, N. (1984). "On the spatial correlations of Abell clusters". In: *The Astrophysical Journal Letters* 284, pp. L9–L12. DOI: 10.1086/184341 (cit. on p. 36).

— (1987). "Clustering in real space and in redshift space". In: *Monthly Notices of Royal Society* 227, pp. 1–21. DOI: 10.1093/mnras/227.1.1 (cit. on pp. 39, 41, 43).

Kamionkowski, M., D. N. Spergel, and N. Sugiyama (1994). "Small-scale cosmic microwave background anisotropies as probe of the geometry of the universe". In: *The Astrophysical Journal Letters* 426, pp. 57–60. DOI: 10.1086/187339. eprint: astro-ph/9401003 (cit. on p. 58).

Kazin, E. A., A. G. Sánchez, and M. R. Blanton (2012). "Improving measurements of H(z) and D_A (z) by analysing clustering anisotropies". In: *Monthly Notices of Royal Astronomical Society* 419, pp. 3223–3243. DOI: 10.1111/j.1365-2966.2011.19962.x. arXiv: 1105.2037 (cit. on pp. 44, 73).

Kerscher, M., I. Szapudi, and A. S. Szalay (2000). "A Comparison of Estimators for the Two-Point Correlation Function". In: *The Astrophysical Journal Letters* 535, pp. L13–L16. DOI: 10.1086/312702. eprint: astro-ph/9912088 (cit. on p. 38).

Kiakotou, Angeliki, Øystein Elgarøy, and Ofer Lahav (2008). "Neutrino mass, dark energy, and the linear growth factor". In: *Physical Review D* 77.6, p. 063005 (cit. on p. 96).

Kitaura, F.-S., C.-H. Chuang, Y. Liang, C. Zhao, C. Tao, et al. (2016). "Signatures of the Primordial Universe from Its Emptiness: Measurement of Baryon Acoustic Oscillations from Minima of the Density Field". In: *Physical Review Letters* 116.17, 171301, p. 171301. DOI: 10.1103/PhysRevLett.116.171301. arXiv: 1511.04405 (cit. on pp. 76, 77, 79).

Komatsu, Eiichiro, KM Smith, J Dunkley, CL Bennett, B Gold, G Hinshaw, N Jarosik, D Larson, MR Nolta, L Page, et al. (2011). "Seven-year wilkinson microwave anisotropy probe (WMAP*) observations: cosmological interpretation". In: *The Astrophysical Journal Supplement Series* 192.2, p. 18 (cit. on p. 88).

Labatie, A., J.-L. Starck, M. Lachièze-Rey, and P. Arnalte-Mur (2010). "Uncertainty in 2-point correlation function estimators and BAO detection in SDSS DR7". In: *ArXiv e-prints*. arXiv: 1009.1232 [astro-ph.CO] (cit. on p. 38).

Landy, S. D. and A. S. Szalay (1993). "Bias and variance of angular correlation functions". In: *The Astrophysical Journal* 412, pp. 64–71. DOI: 10.1086/172900 (cit. on p. 38).

Laureijs, R., J. Amiaux, S. Arduini, J. -. Augueres, J. Brinchmann, R. Cole, M. Cropper, C. Dabin, L. Duvet, A. Ealet, et al. (2011). "Euclid Definition Study Report". In: *ArXiv e-prints*. arXiv: 1110.3193 [astro-ph.CO] (cit. on p. 81).

Leclercq, Florent (2015). "Bayesian large-scale structure inference and cosmic web analysis". In: *arXiv preprint arXiv:1512.04985*. URL: https://arxiv.org/abs/1512.04985.

Lesgourgues, J. (2011). "The Cosmic Linear Anisotropy Solving System (CLASS) I: Overview". In: *ArXiv e-prints*. arXiv: 1104.2932 [astro-ph.IM] (cit. on p. 61).

Levi, M., C. Bebek, T. Beers, R. Blum, R. Cahn, et al. (2013). "The DESI Experiment, a whitepaper for Snowmass 2013". In: *ArXiv e-prints*. arXiv: 1308.0847 [astro-ph.CO] (cit. on p. 80).

Lewis, A. and A. Challinor (2011). *CAMB: Code for Anisotropies in the Microwave Background*. Astrophysics Source Code Library. ascl: 1102.026 (cit. on pp. 61, 101).

Liang, Y., C. Zhao, C.-H. Chuang, F.-S. Kitaura, and C. Tao (2016). "Measuring baryon acoustic oscillations from the clustering of voids". In: *Monthly Notices of Royal Astronomical Society* 459, pp. 4020–4028. DOI: 10.1093/mnras/stw884. arXiv: 1511.04391 (cit. on p. 76).

Lima Neto, G. B., T. F. Lagana, F. Andrade-Santos, and R. E. G. Machado (2014). "Structure in galaxy clusters". In: *ArXiv e-prints*. arXiv: 1406.1496 (cit. on p. 27).

Lin, H.-N., S. Wang, Z. Chang, and X. Li (2016). "Testing the isotropy of the Universe by using the JLA compilation of Type Ia supernovae". In: *Monthly Notices of Astronomical Society* 456, pp. 1881–1885. DOI: 10.1093/mnras/stv2804. arXiv: 1504.03428 (cit. on p. 3).

Linder, E. V. (2005). "Cosmic growth history and expansion history". In: *Physical Review D* 72.4, 043529, p. 043529. DOI: 10.1103/PhysRevD.72.043529. eprint: astro-ph/0507263 (cit. on p. 24).

Loveday, J., S. J. Maddox, G. Efstathiou, and B. A. Peterson (1995). "The Stromlo-APM redshift survey. 2: Variation of galaxy clustering with morphology and luminosity". In: *The Astrophysical Journal* 442, pp. 457–468. DOI: 10.1086/175453. eprint: astro-ph/9410018 (cit. on p. 35).

Mann, R. G., J. A. Peacock, and A. F. Heavens (1998). "Eulerian bias and the galaxy density field". In: *Monthly Notices of Royal Astronomical Society* 293, p. 209. DOI: 10.1046/j.1365-8711.1998.01053.x. eprint: astro-ph/9708031 (cit. on p. 36).

Marochnik, L. and D. Usikov (2015). "Inflation and CMB anisotropy from quantum metric fluctuations". In: *Gravitation and Cosmology* 21, pp. 118–122. DOI: 10.1134/S0202289315020061. arXiv: 1410.1416 [physics.gen-ph] (cit. on p. 53).

Marulli, F., D. Bianchi, E. Branchini, L. Guzzo, L. Moscardini, and R. E. Angulo (2012). "Cosmology with clustering anisotropies: disentangling dynamic and geometric distortions in galaxy redshift surveys". In: *Monthly Notices of Royal Astronomical Society* 426, pp. 2566–2580. DOI: 10.1111/j.1365-2966.2012.21875.x. arXiv: 1203.1002 [astro-ph.CO].

Marulli, F., M. Bolzonella, E. Branchini, I. Davidzon, S. de la Torre, et al. (2013). "The VIMOS Public Extragalactic Redshift Survey (VIPERS) . Luminosity and stellar mass dependence of galaxy clustering at $0.5 < z < 1.1$". In: *Astronomy and Astrophysics* 557, A17, A17. DOI: 10.1051/0004-6361/201321476. arXiv: 1303.2633 (cit. on pp. 35–37, 108).

Marulli, F., A. Veropalumbo, and M. Moresco (2016). "CosmoBolognaLib: C++ libraries for cosmological calculations". In: *Astronomy and Computing* 14, pp. 35–42. DOI: 10.1016/j.ascom.2016.01.005. arXiv: 1511.00012 (cit. on pp. xi, xii, 90, 91).

Marulli, F., A. Veropalumbo, L. Moscardini, A. Cimatti, and K. Dolag (2015). "Redshift-space distortions of galaxies, clusters and AGN: testing how the accuracy of growth rate measurements depends on scales and sample selections". In: *ArXiv e-prints*. arXiv: 1505.01170 (cit. on pp. 39, 90).

Matsubara, T. (2008). "Nonlinear perturbation theory with halo bias and redshift-space distortions via the Lagrangian picture". In: *Physical Review D* 78.8, 083519, p. 083519. DOI: 10.1103/PhysRevD.78.083519. arXiv: 0807.1733 (cit. on p. 64).

McBride, C., A. Berlind, R. Scoccimarro, R. Wechsler, M. Busha, J. Gardner, and F. van den Bosch (2009). "LasDamas Mock Galaxy Catalogs for SDSS". In: *American Astronomical Society Meeting Abstracts #213*. Vol. 41. Bulletin of the American Astronomical Society, p. 253 (cit. on p. 66).

McDonald, P. and D. J. Eisenstein (2007). "Dark energy and curvature from a future baryonic acoustic oscillation survey using the Lyman-α forest". In: *Physical Review D* 76.6, 063009, p. 063009. DOI: 10.1103/PhysRevD.76.063009. eprint: astro-ph/0607122 (cit. on p. 75).

McDonald, P. and A. Roy (2009). "Clustering of dark matter tracers: generalizing bias for the coming era of precision LSS". In: *Journal of Cosmology and Astroparticle Physics* 8, 020, p. 020. DOI: 10.1088/1475-7516/2009/08/020. arXiv: 0902.0991 [astro-ph.CO] (cit. on p. 35).

McQuinn, M. and M. White (2011). "On estimating Lyα forest correlations between multiple sightlines". In: *Monthly Notices of Royal Astronomical Society* 415, pp. 2257–2269. DOI: 10.1111/j.1365-2966.2011.18855.x. arXiv: 1102.1752 (cit. on p. 75).

Mehta, K. T., A. J. Cuesta, X. Xu, D. J. Eisenstein, and N. Padmanabhan (2012). "A 2 per cent distance to z = 0.35 by reconstructing baryon acoustic oscillations - III. Cosmological measurements and interpretation". In: *Monthly Notices of Royal Astronomical Society* 427, pp. 2168–2179. DOI: 10.1111/j.1365-2966.2012.21112.x. arXiv: 1202.0092.

Mehta, K. T., H.-J. Seo, J. Eckel, D. J. Eisenstein, M. Metchnik, P. Pinto, and X. Xu (2011). "Galaxy Bias and Its Effects on the Baryon Acoustic Oscillation Measurements". In: *The Astrophysical Journal* 734, 94, p. 94. DOI: 10.1088/0004-637X/734/2/94. arXiv: 1104.1178 [astro-ph.CO] (cit. on p. 61).

Meiksin, A., M. White, and J. A. Peacock (1999). "Baryonic signatures in large-scale structure". In: *Monthly Notices of Royal Astronomical Society* 304, pp. 851–864. DOI: 10.1046/j.1365-8711.1999.02369.x. eprint: astro-ph/9812214 (cit. on p. 60).

Metcalfe, N., R. Fong, T. Shanks, and D. Kilkenny (1989). "An extended galaxy redshift survey. I - The catalogue". In: *Monthly Notices of Royal Astronomical Society* 236, pp. 207–234. DOI: 10.1093/mnras/236.2.207 (cit. on p. 35).

Monaghan, Joe J (1992). "Smoothed particle hydrodynamics". In: *Annual Review of Astronomy and Astrophysics* 30.1, pp. 543–574 (cit. on p. 52).

Munshi, D., V. Sahni, and A. A. Starobinsky (1994). "Nonlinear approximations to gravitational instability: A comparison in the quasi-linear regime". In: *The Astrophysical Journal* 436, pp. 517–527. DOI: 10.1086/174925. eprint: astro-ph/9402065 (cit. on p. 29).

Newburgh, L. B., K. Bandura, M. A. Bucher, T.-C. Chang, H. C. Chiang, et al. (2016). "HIRAX: a probe of dark energy and radio transients". In: *Society of Photo-Optical Instrumentation Engineers (SPIE) Conference Series*. Vol. 9906. proc.SPIE, p. 99065X. DOI: 10.1117/12.2234286. arXiv: 1607.02059 [astro-ph.IM] (cit. on p. 81).

Norberg, P., C. M. Baugh, E. Gaztañaga, and D. J. Croton (2009). "Statistical analysis of galaxy surveys - I. Robust error estimation for two-point clustering statistics". In: *Monthly Notices of Royal Astronomical Society* 396, pp. 19–38. DOI: 10.1111/j.1365-2966.2009.14389.x. arXiv: 0810.1885 (cit. on p. 47).

Norberg, P., C. M. Baugh, E. Hawkins, S. Maddox, J. A. Peacock, et al. (2001). "The 2dF Galaxy Redshift Survey: luminosity dependence of galaxy clustering". In:

Monthly Notices of Royal Astronomy Society 328, pp. 64–70. DOI: 10.1046/j.1365-8711.2001.04839.x. eprint: astro-ph/0105500 (cit. on p. 35).

Norman, M. L., P. Paschos, and R. Harkness (2009). "Baryon acoustic oscillations in the Lyman alpha forest". In: *Journal of Physics Conference Series*. Vol. 180. Journal of Physics Conference Series, p. 012021. DOI: 10.1088/1742-6596/180/1/012021. arXiv: 0908.0964 (cit. on p. 75).

Nusser, A. and M. Davis (1994). "On the prediction of velocity fields from redshift space galaxy samples". In: *The Astrophysical Journal* 421, pp. L1–L4. DOI: 10.1086/187172. eprint: astro-ph/9309009 (cit. on p. 64).

Okumura, T., T. Matsubara, D. J. Eisenstein, I. Kayo, C. Hikage, A. S. Szalay, and D. P. Schneider (2008). "Large-Scale Anisotropic Correlation Function of SDSS Luminous Red Galaxies". In: *The Astrophysical Journal* 676, 889-898, pp. 889–898. DOI: 10.1086/528951. arXiv: 0711.3640 (cit. on p. 73).

Orban, C. and D. H. Weinberg (2011). "Self-similar bumps and wiggles: Isolating the evolution of the BAO peak with power-law initial conditions". In: *Physical Review D* 84.6, 063501, p. 063501. DOI: 10.1103/PhysRevD.84.063501. arXiv: 1101.1523 (cit. on p. 60).

Padmanabhan, N. and M. White (2008). "Constraining anisotropic baryon oscillations". In: *Physical Review D* 77.12, 123540, p. 123540. DOI: 10.1103/PhysRevD.77.123540. arXiv: 0804.0799 (cit. on p. 73).

— (2009). "Calibrating the baryon oscillation ruler for matter and halos". In: *Physical Review D* 80.6, 063508, p. 063508. DOI: 10.1103/PhysRevD.80.063508. arXiv: 0906.1198 [astro-ph.CO] (cit. on p. 60).

Padmanabhan, N., M. White, and J. D. Cohn (2009). "Reconstructing baryon oscillations: A Lagrangian theory perspective". In: *Physical Review D* 79.6, 063523, p. 063523. DOI: 10.1103/PhysRevD.79.063523. arXiv: 0812.2905 (cit. on pp. 27, 31, 69).

Padmanabhan, N., X. Xu, D. J. Eisenstein, R. Scalzo, A. J. Cuesta, K. T. Mehta, and E. Kazin (2012). "A 2 per cent distance to z = 0.35 by reconstructing baryon acoustic oscillations - I. Methods and application to the Sloan Digital Sky Survey". In: *Monthly Notices of Royal Astronomical Society* 427, pp. 2132–2145. DOI: 10.1111/j.1365-2966.2012.21888.x. arXiv: 1202.0090 (cit. on pp. 63–66, 68, 74, 94, 95, 97).

Padovani, Paolo and Francesca Matteucci (1993). "Stellar mass loss in elliptical galaxies and the fueling of active galactic nuclei". In: *The Astrophysical Journal* 416, p. 26 (cit. on p. 89).

Parker, Q. A., H. T. MacGillivray, P. W. Hill, and R. J. Dodd (1986). "Three-dimensional structure in field 349 of the southern sky survey. I - Redshifts for a magnitude-limited sample of galaxies from slit spectra". In: *Monthly Notices of Royal Astronomical Society* 220, pp. 901–925. DOI: 10.1093/mnras/220.4.901 (cit. on p. 35).

Peebles, P. J. E. (1976). "A Cosmic Virial Theorem". In: *Astrophysical Journal Letters* 205, p. L109. DOI: 10.1086/182101 (cit. on p. 41).

Peebles, P. J. E. and M. G. Hauser (1974). "Statistical Analysis of Catalogs of Extragalactic Objects. III. The Shane-Wirtanen and Zwicky Catalogs". In: *Astrophysical Journal Supplement* 28, p. 19. DOI: 10.1086/190308 (cit. on p. 38).

Peebles, P. J. E. and J. T. Yu (1970). "Primeval Adiabatic Perturbation in an Expanding Universe". In: *The Astrophysical Journal* 162, p. 815. DOI: 10.1086/150713 (cit. on p. 58).

Peebles, Phillip James Edwin (1980). *The large-scale structure of the universe*. Princeton university press (cit. on p. 37).

Penzias, A. A. and R. W. Wilson (1965). "A Measurement of Excess Antenna Temperature at 4080 Mc/s." In: *The Astrophysical Journal* 142, pp. 419–421. DOI: 10.1086/148307 (cit. on p. 3).

Percival, W. J., C. M. Baugh, J. Bland-Hawthorn, T. Bridges, R. Cannon, et al. (2001). "The 2dF Galaxy Redshift Survey: the power spectrum and the matter content of the Universe". In: *Monthly Notices of Royal Astronomical Society* 327, pp. 1297–1306. DOI: 10.1046/j.1365-8711.2001.04827.x. eprint: astro-ph/0105252 (cit. on p. 58).

Percival, Will J, Beth A Reid, Daniel J Eisenstein, Neta A Bahcall, Tamas Budavari, Joshua A Frieman, Masataka Fukugita, James E Gunn, Željko Ivezić, Gillian R Knapp, et al. (2010). "Baryon acoustic oscillations in the Sloan Digital Sky Survey data release 7 galaxy sample". In: *Monthly Notices of the Royal Astronomical Society* 401.4, pp. 2148–2168 (cit. on pp. 66, 80).

Perlmutter, S., M. S. Turner, and M. White (1999). "Constraining Dark Energy with Type Ia Supernovae and Large-Scale Structure". In: *Physical Review Letters* 83, pp. 670–673. DOI: 10.1103/PhysRevLett.83.670. eprint: astro-ph/9901052 (cit. on p. 58).

Peterson, J. B., K. Bandura, and U. L. Pen (2006). "The Hubble Sphere Hydrogen Survey". In: *ArXiv Astrophysics e-prints*. eprint: astro-ph/0606104 (cit. on p. 75).

Planck Collaboration, R. Adam, P. A. R. Ade, N. Aghanim, Y. Akrami, et al. (2016). "Planck 2015 results. I. Overview of products and scientific results". In: *Astronomy and Astrophysics* 594, A1, A1. DOI: 10.1051/0004-6361/201527101. arXiv: 1502.01582 (cit. on pp. 5, 56).

Planck Collaboration, P. A. R. Ade, N. Aghanim, C. Armitage-Caplan, M. Arnaud, et al. (2014). "Planck 2013 results. XV. CMB power spectra and likelihood". In: *Astronomy and Astrophysics* 571, A15, A15. DOI: 10.1051/0004-6361/201321573. arXiv: 1303.5075 (cit. on pp. 20, 56).

Pober, J. C., A. R. Parsons, D. R. DeBoer, P. McDonald, M. McQuinn, J. E. Aguirre, Z. Ali, R. F. Bradley, T.-C. Chang, and M. F. Morales (2013). "The Baryon Acoustic Oscillation Broadband and Broad-beam Array: Design Overview and Sensitivity Forecasts". In: *The Astrophysical Journal* 145, 65, p. 65. DOI: 10.1088/0004-6256/145/3/65. arXiv: 1210.2413 (cit. on p. 81).

Press, W. H. and P. Schechter (1974). "Formation of Galaxies and Clusters of Galaxies by Self-Similar Gravitational Condensation". In: *The Astrophysical Journal* 187, pp. 425–438. DOI: 10.1086/152650 (cit. on p. 26).

Press, WH and M Davis (1982). "How to identify and weigh virialized clusters of galaxies in a complete redshift catalog". In: *The Astrophysical Journal* 259, pp. 449–473 (cit. on p. 89).

Rees, M. J. and D. W. Sciama (1968). "Large-scale Density Inhomogeneities in the Universe". In: *Nature* 217, pp. 511–516. DOI: 10.1038/217511a0 (cit. on p. 57).

Riess, A. G., A. V. Filippenko, P. Challis, A. Clocchiatti, A. Diercks, et al. (1998). "Observational Evidence from Supernovae for an Accelerating Universe and a Cosmological Constant". In: *The Astrophysical Journal* 116, pp. 1009–1038. DOI: 10.1086/300499. eprint: astro-ph/9805201 (cit. on pp. xiii, 58).

Rowan-Robinson, M., A. Lawrence, W. Saunders, J. Crawford, R. Ellis, et al. (1990). "A Sparse-Sampled Redshift Survey of IRAS Galaxies - Part One - the Convergence of the IRAS Dipole and the Origin of Our Motion with Respect to the Microwave

Background". In: *Monthly Notices of Royal Astronomical Society* 247, p. 1 (cit. on p. 55).

Sachs, R. K. and A. M. Wolfe (1967). "Perturbations of a Cosmological Model and Angular Variations of the Microwave Background". In: *The Astrophysical Journal* 147, p. 73. DOI: 10.1086/148982 (cit. on p. 57).

Sahni, V. and P. Coles (1995). "Approximation methods for non-linear gravitational clustering". In: *Physics Reports* 262, pp. 1–135. DOI: 10.1016/0370-1573(95)00014-8. eprint: astro-ph/9505005 (cit. on p. 25).

Sakharov, A. D. (1966). "The Initial Stage of an Expanding Universe and the Appearance of a Nonuniform Distribution of Matter". In: *Soviet Journal of Experimental and Theoretical Physics* 22, p. 241 (cit. on p. 58).

Sánchez, A. G., J. N. Grieb, S. Salazar-Albornoz, S. Alam, F. Beutler, et al. (2017). "The clustering of galaxies in the completed SDSS-III Baryon Oscillation Spectroscopic Survey: combining correlated Gaussian posterior distributions". In: *Monthly Notices of Royal Astronomical Society* 464, pp. 1493–1501. DOI: 10.1093/mnras/stw2495. arXiv: 1607.03146 (cit. on p. 80).

Sánchez, A. G., E. A. Kazin, F. Beutler, C.-H. Chuang, A. J. Cuesta, et al. (2013). "The clustering of galaxies in the SDSS-III Baryon Oscillation Spectroscopic Survey: cosmological constraints from the full shape of the clustering wedges". In: *Monthly Notices of Royal Astronomical Society* 433, pp. 1202–1222. DOI: 10.1093/mnras/stt799. arXiv: 1303.4396 (cit. on pp. 73, 79, 83).

Sánchez, A. G., C. G. Scóccola, A. J. Ross, W. Percival, M. Manera, et al. (2012). "The clustering of galaxies in the SDSS-III Baryon Oscillation Spectroscopic Survey: cosmological implications of the large-scale two-point correlation function". In: *Monthly Notices of Royal Astronomical Society* 425, pp. 415–437. DOI: 10.1111/j.1365-2966.2012.21502.x. arXiv: 1203.6616.

Sawangwit, U., T. Shanks, S. M. Croom, M. J. Drinkwater, S. Fine, D. Parkinson, and N. P. Ross (2012). "Measuring BAO and non-Gaussianity via QSO clustering". In: *Monthly Notices of Royal Astronomical Society* 420, pp. 1916–1925. DOI: 10.1111/j.1365-2966.2011.19848.x. arXiv: 1108.1198 [astro-ph.CO] (cit. on p. 75).

Schmidt, B. (1999). *Investigating Type Ia Supernovae and an Accelerating Universe*. HST Proposal (cit. on p. 58).

Scoccimarro, R. (2000). "The Bispectrum: From Theory to Observations". In: *The Astrophysical Journal* 544, pp. 597–615. DOI: 10.1086/317248. eprint: astro-ph/0004086 (cit. on p. 35).

Scoccimarro, Roman (1997). "Cosmological perturbations: Entering the nonlinear regime". In: *The Astrophysical Journal* 487.1, p. 1 (cit. on p. 29).

Seo, H.-J., S. Dodelson, J. Marriner, D. Mcginnis, A. Stebbins, C. Stoughton, and A. Vallinotto (2010). "A Ground-based 21 cm Baryon Acoustic Oscillation Survey". In: *The Astrophysical Journal* 721, pp. 164–173. DOI: 10.1088/0004-637X/721/1/164. arXiv: 0910.5007 (cit. on p. 75).

Seo, H.-J., J. Eckel, D. J. Eisenstein, K. Mehta, M. Metchnik, N. Padmanabhan, P. Pinto, R. Takahashi, M. White, and X. Xu (2010). "High-precision Predictions for the Acoustic Scale in the Nonlinear Regime". In: *The Astrophysical Journal* 720, pp. 1650–1667. DOI: 10.1088/0004-637X/720/2/1650. arXiv: 0910.5005 [astro-ph.CO] (cit. on p. 72).

Seo, H.-J. and D. J. Eisenstein (2003). "Probing Dark Energy with Baryonic Acoustic Oscillations from Future Large Galaxy Redshift Surveys". In: *The Astrophysical Journal* 598, pp. 720–740. DOI: 10.1086/379122. eprint: astro-ph/0307460 (cit. on pp. 58, 74).

Seo, H.-J. and D. J. Eisenstein (2005). "Baryonic Acoustic Oscillations in Simulated Galaxy Redshift Surveys". In: *The Astrophysical Journal* 633, pp. 575–588. DOI: 10.1086/491599. eprint: astro-ph/0507338 (cit. on p. 60).

— (2007). "Improved Forecasts for the Baryon Acoustic Oscillations and Cosmological Distance Scale". In: *The Astrophysical Journal* 665, pp. 14–24. DOI: 10.1086/519549. eprint: astro-ph/0701079 (cit. on p. 74).

Seo, H.-J. and C. M. Hirata (2016). "The foreground wedge and 21-cm BAO surveys". In: *Monthly Notices of Royal Astronomical Society* 456, pp. 3142–3156. DOI: 10.1093/mnras/stv2806. arXiv: 1508.06503 (cit. on p. 76).

Seo, H.-J., E. R. Siegel, D. J. Eisenstein, and M. White (2008). "Nonlinear Structure Formation and the Acoustic Scale". In: *The Astrophysical Journal* 686, 13-24, pp. 13–24. DOI: 10.1086/589921. arXiv: 0805.0117 (cit. on p. 62).

Shakura, N I and Rashid Alievich Sunyaev (1973). "Black holes in binary systems. Observational appearance." In: *Astronomy and Astrophysics* 24, pp. 337–355 (cit. on p. 89).

Shandarin, S. F. and Y. B. Zeldovich (1989). "The large-scale structure of the universe: Turbulence, intermittency, structures in a self-gravitating medium". In: *Reviews of Modern Physics* 61, pp. 185–220. DOI: 10.1103/RevModPhys.61.185 (cit. on p. 25).

Shanks, T., D. H. Sutton, R. Fong, and N. Metcalfe (1989). "An Extended Galaxy Redshift Survey - Part Three - Constraints on Largescale Structure". In: *Monthly Notices of Royal Astronomical Society* 237, p. 589. DOI: 10.1093/mnras/237.3.589 (cit. on p. 35).

Silk, J. (1967). "Fluctuations in the Primordial Fireball". In: *Nature* 215, pp. 1155–1156. DOI: 10.1038/2151155a0 (cit. on pp. 25, 53).

Slosar, A., V. Iršič, D. Kirkby, S. Bailey, N. G. Busca, et al. (2013). "Measurement of baryon acoustic oscillations in the Lyman-α forest fluctuations in BOSS data release 9". In: *Journal of Cosmology and Astroparticle Physics* 4, 026, p. 026. DOI: 10.1088/1475-7516/2013/04/026. arXiv: 1301.3459 (cit. on p. 75).

Smoot, G. F., C. L. Bennett, A. Kogut, E. L. Wright, J. Aymon, et al. (1992). "Structure in the COBE differential microwave radiometer first-year maps". In: *The Astrophysical Journal Letters* 396, pp. L1–L5. DOI: 10.1086/186504 (cit. on pp. 3, 19).

Somerville, Rachel S, Kyoungsoo Lee, Henry C Ferguson, Jonathan P Gardner, Leonidas A Moustakas, and Mauro Giavalisco (2004). "Cosmic variance in the great observatories origins deep survey". In: *The Astrophysical Journal Letters* 600.2, p. L171 (cit. on p. 37).

Springel, V. and L. Hernquist (2003). "Cosmological smoothed particle hydrodynamics simulations: a hybrid multiphase model for star formation". In: *Monthly Notices of Royal Astronomical Society* 339, pp. 289–311. DOI: 10.1046/j.1365-8711.2003.06206.x. eprint: astro-ph/0206393 (cit. on p. 89).

Springel, Volker (2005). "The cosmological simulation code GADGET-2". In: *Monthly Notices of Royal Astronomical Society* 364.4, pp. 1105–1134 (cit. on p. 88).

Springel, Volker and Lars Hernquist (2002). "Cosmological smoothed particle hydrodynamics simulations: the entropy equation". In: *Monthly Notices of Royal Astronomical Society* 333.3, pp. 649–664 (cit. on p. 88).

Springel, Volker, Simon DM White, Adrian Jenkins, Carlos S Frenk, Naoki Yoshida, Liang Gao, Julio Navarro, Robert Thacker, Darren Croton, John Helly, et al. (2005). "Simulations of the formation, evolution and clustering of galaxies and quasars". In: *nature* 435.7042, pp. 629–636 (cit. on p. 89).

Springel, Volker, Simon DM White, Giuseppe Tormen, and Guinevere Kauffmann (2001). "Populating a cluster of galaxies–I. Results at z= 0". In: *Monthly Notices of Royal Astronomical Society* 328.3, pp. 726–750 (cit. on p. 89).

Steinhardt, P. J. (2011). "The Inflation Debate". In: *Scientific American* 304.4, pp. 36–43. DOI: 10.1038/scientificamerican0411-36 (cit. on p. 18).

Stone, James M and Michael L Norman (1992). "ZEUS-2D: A radiation magnetohydrodynamics code for astrophysical flows in two space dimensions. I-The hydrodynamic algorithms and tests." In: *The Astrophysical Journal Supplement Series* 80, pp. 753–790 (cit. on p. 52).

Sunyaev, R. A. and Y. B. Zeldovich (1970). "Small-Scale Fluctuations of Relic Radiation". In: *Astrophysics and Space Science* 7, pp. 3–19. DOI: 10.1007/BF00653471 (cit. on pp. 57, 58).

Tegmark, M. (1997). "Measuring Cosmological Parameters with Galaxy Surveys". In: *Physical Review Letters* 79, pp. 3806–3809. DOI: 10.1103/PhysRevLett.79.3806. eprint: astro-ph/9706198 (cit. on p. 58).

Tegmark, M. and P. J. E. Peebles (1998). "The Time Evolution of Bias". In: *The Astrophysical Journal Letters* 500, pp. L79–L82. DOI: 10.1086/311426. eprint: astro-ph/9804067 (cit. on p. 36).

Thielemann, F.-K., D. Argast, F. Brachwitz, W. R. Hix, P. Höflich, M. Liebendörfer, G. Martinez-Pinedo, A. Mezzacappa, I. Panov, and T. Rauscher (2003). "Nuclear cross sections, nuclear structure and stellar nucleosynthesis". In: *Nuclear Physics A* 718, pp. 139–146. DOI: 10.1016/S0375-9474(03)00704-8 (cit. on p. 89).

Tinker, Jeremy L, Brant E Robertson, Andrey V Kravtsov, Anatoly Klypin, Michael S Warren, Gustavo Yepes, and Stefan Gottlöber (2010). "The large-scale bias of dark matter halos: numerical calibration and model tests". In: *The Astrophysical Journal* 724.2, p. 878 (cit. on p. 75).

Torbet, E., M. J. Devlin, W. B. Dorwart, T. Herbig, A. D. Miller, M. R. Nolta, L. Page, J. Puchalla, and H. T. Tran (1999). "A Measurement of the Angular Power Spectrum of the Microwave Background Made from the High Chilean Andes". In: *The Astrophysical Journal Letters* 521, pp. L79–L82. DOI: 10.1086/312197. eprint: astro-ph/9905100 (cit. on p. xiv).

Trotta, R. (2017). "Bayesian Methods in Cosmology". In: *ArXiv e-prints*. arXiv: 1701.01467 (cit. on p. 71).

Van den Hoek, LB and Martin AT Groenewegen (1997). "New theoretical yields of intermediate mass stars". In: *Astronomy and Astrophysics Supplement Series* 123.2, pp. 305–328 (cit. on p. 89).

Vargas-Magaña, M., S. Ho, A. J. Cuesta, R. O'Connell, A. J. Ross, et al. (2016). "The clustering of galaxies in the completed SDSS-III Baryon Oscillation Spectroscopic Survey: theoretical systematics and Baryon Acoustic Oscillations in the galaxy correlation function". In: *ArXiv e-prints*. arXiv: 1610.03506 (cit. on pp. 76–78).

Veropalumbo, A., F. Marulli, L. Moscardini, M. Moresco, and A. Cimatti (2014). "An improved measurement of baryon acoustic oscillations from the correlation function of galaxy clusters at z
0.3". In: *Monthly Notices of Royal Astronomical Society* 442, pp. 3275–3283. DOI: 10.1093/mnras/stu1050. arXiv: 1311.5895 (cit. on pp. 75, 109, 124).

— (2016). "Measuring the distance-redshift relation with the baryon acoustic oscillations of galaxy clusters". In: *Monthly Notices of Royal Astronomical Society* 458, pp. 1909–1920. DOI: 10.1093/mnras/stw306. arXiv: 1510.08852 (cit. on pp. 72, 75, 76, 78, 95, 108, 109, 124, 125).

Wang, L. and P. J. Steinhardt (1998a). "Cluster Abundance Constraints for Cosmological Models with a Time-varying, Spatially Inhomogeneous Energy Component with Negative Pressure". In: *The Astrophysical Journal* 508, pp. 483–490. DOI: 10.1086/306436. eprint: astro-ph/9804015 (cit. on p. 24).

Wang, Limin and Paul J Steinhardt (1998b). "Cluster abundance constraints for cosmological models with a time-varying, spatially inhomogeneous energy component with negative pressure". In: *The Astrophysical Journal* 508.2, p. 483 (cit. on p. 96).

Weinberg, D. H., M. J. Mortonson, D. J. Eisenstein, C. Hirata, A. G. Riess, and E. Rozo (2013). "Observational probes of cosmic acceleration". In: *Physics Reports* 530, pp. 87–255. DOI: 10.1016/j.physrep.2013.05.001. arXiv: 1201.2434 (cit. on pp. 57, 66, 74, 121).

Weinberg, S. (1967). "A Model of Leptons". In: *Physical Review Letters* 19, pp. 1264–1266. DOI: 10.1103/PhysRevLett.19.1264 (cit. on p. 17).

Weiss, Arno G, Stefan Gottlöber, and Thomas Buchert (1996). "Optimizing higher order Lagrangian perturbation theory for standard CDM and BSI models". In: *Monthly Notices of the Royal Astronomical Society* 278.4, pp. 953–964 (cit. on p. 31).

White, M. (2010). "Shot noise and reconstruction of the acoustic peak". In: *ArXiv e-prints*. arXiv: 1004.0250 [astro-ph.CO].

— (2014). "The Zel'dovich approximation". In: *Monthly notices of Royal Astronomical Society* 439, pp. 3630–3640. DOI: 10.1093/mnras/stu209. arXiv: 1401.5466 (cit. on p. 29).

— (2015). "Reconstruction within the Zeldovich approximation". In: *Monthly Notices of Royal Astronomical Society* 450, pp. 3822–3828. DOI: 10.1093/mnras/stv842. arXiv: 1504.03677 (cit. on pp. 69, 97).

Wiersma, Robert PC, Joop Schaye, and Britton D Smith (2009). "The effect of photoionization on the cooling rates of enriched, astrophysical plasmas". In: *Monthly Notices of Royal Astronomical Society* 393.1, pp. 99–107 (cit. on p. 88).

Woosley, SE and Thomas A Weaver (1995). "The evolution and explosion of massive stars. II. Explosive hydrodynamics and nucleosynthesis". In: *The Astrophysical Journal Supplement Series* 101, p. 181 (cit. on p. 89).

Wyithe, J. S. B., A. Loeb, and P. M. Geil (2008). "Baryonic acoustic oscillations in 21-cm emission: a probe of dark energy out to high redshifts". In: *Monthly Notices of Royal Astronomical Society* 383, pp. 1195–1209. DOI: 10.1111/j.1365-2966.2007.12631.x. arXiv: 0709.2955 (cit. on p. 75).

Xu, X., A. J. Cuesta, N. Padmanabhan, D. J. Eisenstein, and C. K. McBride (2013). "Measuring D_A and H at z=0.35 from the SDSS DR7 LRGs using baryon acoustic oscillations". In: *Monthly Notices of Royal Astronomical Society* 431, pp. 2834–2860. DOI: 10.1093/mnras/stt379. arXiv: 1206.6732 (cit. on p. 73).

Xu, X., N. Padmanabhan, D. J. Eisenstein, K. T. Mehta, and A. J. Cuesta (2012). "A 2 per cent distance to z = 0.35 by reconstructing baryon acoustic oscillations - II. Fitting techniques". In: *Monthly Notices of Royal Astronomical Society* 427, pp. 2146–2167. DOI: 10.1111/j.1365-2966.2012.21573.x. arXiv: 1202.0091 (cit. on p. 72).

York, D. G., J. Adelman, J. E. Anderson Jr., S. F. Anderson, J. Annis, et al. (2000). "The Sloan Digital Sky Survey: Technical Summary". In: *The Astrophysical Journal* 120, pp. 1579–1587. DOI: 10.1086/301513. eprint: astro-ph/0006396 (cit. on pp. 58, 59).

Yoshisato, Ayako, Masahiro Morikawa, Naoteru Gouda, and Hideaki Mouri (2006). "Why is the Zel'dovich Approximation So Accurate?" In: *The Astrophysical Journal* 637.2, p. 555 (cit. on p. 30).

Zel'dovich, Y. B. (1970). "Gravitational instability: An approximate theory for large density perturbations." In: *Astronomy and Astrophysics* 5, pp. 84–89 (cit. on pp. 20, 29).

— (1972). "A hypothesis, unifying the structure and the entropy of the Universe". In: *Monthly Notices of Royal Astronomical Society* 160, 1P. DOI: 10.1093/mnras/160.1.1P (cit. on p. 19).

"A hundred years from now, people will look back on us and laugh. They'll say, 'You know what people used to believe? They believed in photons and electrons. Can you imagine anything so silly?' They'll have a good laugh, because by then there will be newer and better fantasies. And meanwhile, you feel the way the boat moves? That's the sea. That's real. You smell the salt in the air? You feel the sunlight on your skin? That's all real. You see all of us together? That's real. Life is wonderful. It's a gift to be alive, to see the sun and breathe the air. And there isn't really anything else."

Michael Crichton, The Lost World (1995)

"I don't know half of you half as well as I should like;
and I like less than half of you half as well as you deserve."

J.R.R. Tolkien, The Fellowship of the Ring (1954)

Ringraziamenti

Credo che non si possa arrivare a questo punto senza dover riempire pagine e pagine di ringraziamenti. Una lista di nomi che si dilunga per molte pagine potrebbe sembrare ai più un elenco telefonico, quindi premetto che, purtroppo, non vi citerò tutti. Ma siete comunque ben impressi nella mia mente, non temete, e avrete i miei ringraziamenti silenziosi.
Vorrei iniziare ringraziando Lauro Moscardini, Federico Marulli e Alfonso Veropalumbo, per il contributo fondamentale a questa tesi.
Rivolgo i miei più sinceri ringraziamenti a Bologna. Una città fatta di torri, di portici, di idee e musiche, di persone. Dalle prime incontrate, con cui è iniziato tutto: Francesco, Valeria, Luca, Carlo, Lorenzo, Flavia, Francesca, agli anni successivi con Daniele, Ezio, Alberto, Federico, Cristiano, Roberto, Ambra, Matilde, Cecilia, Iacopo, Simone, Matteo, Maria Francesca, Andrea, Giacomo, Giovanni, Michele, Paolo, Luca, Sarah, Emma, Giulia, Caterina, e tanti altri. Se l'Università di Bologna è riuscita nell'arduo compito di tener fede al proprio nome, *Alma Mater*, nel mio caso lo deve sopratutto a voi. Grazie ai ragazzi della scuola d'italiano, ho più imparato che insegnato.
Un ringraziamento particolare a chi mi ha sostenuto negli ultimi giorni bui (nel senso che, essendo murato in camera, non vedevo la luce del giorno) prima della consegna di questa tesi. Grazie a Sebastiano, per i consigli e le premure. L'universo è un posto pieno di musica, e cosa sono i BAO se non la prima musica suonata dall'orchestra cosmica? Francesco, il pianeta Terra è troppo piccolo per poterci dividere, il tuo supporto valica i confini nazionali. Carlo e Andrea, se il fardello è condiviso, pesa molto meno. Grazie a Cinzia, per le promesse mantenute: "*Just look over your shoulder...*".
Grazie inoltre ai Queen, ai Pink Floyd, a J.R.R Tolkien ed a Lewis Carroll, per la compagnia e l'ispirazione.
Se Bologna è ormai la mia seconda casa, la prima rinfresca i pensieri sull'Aspromonte e bagna i piedi in due mari diversi. Grazie a tutti le persone che costituiscono la mia realtà calabrese: Tonino, Gianluca, Riccardo, Francesco, Vincenzo, Marco, Shari, Martina, Alessandro, Carla, Domenico, Alfonso, Pasquale e tutti gli altri.
Grazie a tutti i professori incontrati, dal primo giorno dell'elementari all'ultimo di università. Tutti, chi più chi meno, mi avete insegnato qualcosa.
Muchas gracias a los amigos del CEFCA de Teruel, Gonzalo, Siddharta, Jonás, Victor, Ignacio, Alvaro, Raul, Silvia, Carlos, Guillaume y los otros, por el precioso verano.
Infine, un grazie immenso alla mia famiglia. Incredibile che anche voi siate troppi per potervi citare tutti. Inizio con i nonni, sono venuti prima e ne hanno diritto. Grazie per il vostro essere ponte con il passato, senza memoria il futuro non può essere costruito.

Gli zii, siete tanti, diversi, incredibili. Ringrazio in particolare il più giovane perché prima ho ringraziato i più anziani. Grazie a zio Emanuele, per la generosità e l'affetto. Giuro che un giorno restituirò tutti i fumetti ed i giocattoli che ti ho preso. Grazie ai cuginetti, dal primo all'ultimo. Vedervi crescere è un piacere. Grazie a Miriam, che nei suoi viaggi in giro per il mondo trova il tempo per passare anche da Bologna e Reggio. Grazie ad Ale, unico membro (insieme a me) di una *band* molto particolare, che non ha strumenti ma tanto *orecchio*. Grazie a mamma, per l'amore e la fiducia incondizionati. Grazie a papà, la roccia su cui è poggiato il mio mondo.

Bologna, Marzo 2017 G. A.